CHLORIDE INDUCED PITTING CORROSION FATIGUE IN REINFORCED CONCRETE STRUCTURES

A Thesis Submitted to the College of

Graduate and Postdoctoral Studies

In Partial Fulfillment of the Requirements

For the Degree of Doctor of Philosophy

In the Department of Civil, Geological, and Environmental Engineering

University of Saskatchewan

Saskatoon

By

Ming Zhu

PERMISSION TO USE

In presenting this thesis/dissertation in partial fulfillment of the requirements for a Postgraduate degree from the University of Saskatchewan, I agree that the Libraries of this University may make it freely available for inspection. I further agree that permission for copying of this thesis/dissertation in any manner, in whole or in part, for scholarly purposes may be granted by the professor or professors who supervised my thesis/dissertation work or, in their absence, by the Head of the Department or the Dean of the College in which my thesis work was done. It is understood that any copying or publication or use of this thesis/dissertation or parts thereof for financial gain shall not be allowed without my written permission. It is also understood that due recognition shall be given to me and to the University of Saskatchewan in any scholarly use which may be made of any material in my thesis/dissertation.

Requests for permission to copy or to make other uses of materials in this thesis/dissertation in whole or part should be addressed to:

Head of the Department of Civil, Geological, and Environmental Engineering
57 Campus Drive Saskatoon, Saskatchewan
University of Saskatchewan
Saskatoon, Saskatchewan S7N 5A9 Canada

OR

Dean
College of Graduate and Postdoctoral Studies
University of Saskatchewan
116 Thorvaldson Building, 110 Science Place
Saskatoon, Saskatchewan S7N 5C9
Canada

ABSTRACT

There is currently a general agreement that the long-term performance of many civil infrastructure facilities, such as bridges, tunnels, harbor facilities, nuclear power plants etc. is strongly dependent, not only on mechanical loading, but also on the harshness of their service environment. Corrosion-Fatigue (CF) is a damage mechanism commonly found in many Reinforced Concrete (RC) structures (bridges, harbor structures, oil platforms, etc.) exposed to variable loading and a corrosive environment. CF is a synergetic phenomenon between corrosion and fatigue wherein the damage caused by the simultaneous action of both mechanisms is usually greater than when either corrosion or fatigue is acting alone. Recognizing that aging of these structures may adversely impact their ability to fulfill their intended function in the future, some strategies have been developed for predicting their service life and for mitigating the effects of aging on their performance. Despite its practical importance, only a relatively small number of studies have been carried out on the CF of reinforced concrete structures. Indeed, most durability studies in RC focus on either corrosion alone or fatigue without corrosion. In the few instances where CF was considered, oftentimes only RC structural elements, such as beams, were tested. Although providing important information about the overall CF behavior of this kind of structure, such tests also make it virtually impossible to extrapolate the application of those results to other structures or loading/exposure conditions.

This study proposes a new approach for assessing the CF of reinforced concrete structures that relies on a realistic constitutive characterization of CF of steel reinforcement in simulated concrete pore solutions. The novelty of the proposed approach resides in its ability to accelerate both corrosion and fatigue loading simultaneously and independently so that a given field condition can be represented without favoring one mechanism over the other. Given the difficulty in accelerating corrosion to the required values to match the acceleration of fatigue loading, oftentimes the acceleration factor for fatigue is much higher than the one used for corrosion, making the test results not very representative of the field conditions.

The research objectives of this study were divided into two main sequential stages. In stage one, the corrosion-fatigue behavior of carbon steel reinforcement is characterized as a material

operating in a chloride-laden simulated concrete pore solution in a way that is compatible with two widely used fatigue analysis approaches (S-N curves and Fracture Mechanics). A combination of pore solution chemistry and an electrochemical method is used in this study to develop a novel corrosion fatigue cell that can accelerate, independently, both corrosion and fatigue so that the degradation rates are representative of typical in-service conditions. The simulated pore solution chemistry is chosen so that it is representative of typical concrete environments that favor pitting corrosion in the presence of chloride ions. The electrochemical method is used to overcome the limitations of the maximum corrosion rates that can possibly be achieved through the chemical composition of the simulated pore solution alone, so that CF tests (representative of field conditions) can be carried out within a reasonable time frame. In stage two, the ability of the two constitutive models, developed in stage one, to predict the fatigue life of reinforced concrete beams in a corrosive environment is assessed, as an example of a structural component.

The results of the model predictions, for both approaches (S-N curves and Fracture Mechanics), were compared with the experimental results from an independent set of RC beams tested under corrosion-fatigue. The results show that both methods can be used to estimate the service life of a RC structure subjected to corrosion-fatigue. It is worth mentioning that the S-N curve approach provided more precise estimations than those provided by fracture mechanics, with standard errors ranging from 9.0% to 23.0%, instead of ranges between 26.7% and 54.2%, respectively. However, although the estimation of the fracture mechanics approach shows a higher error range, this method provides more insight into the evolution of damage in the rebar over time. The fracture mechanics model accounts for the four main stages of the metal degradation process: pit nucleation and growth, pit-to-crack transition, crack growth state, and ultimate fracture failure. The results indicate that the pit nucleation and growth stage occupies over 79.9% of the total service life in the prediction of the tested RC beams under CF. This result suggests that unstable crack propagation would not take place before the occurrence of extensive corrosion in the material. In other words, corrosion plays a more significant role than usually reported in the corrosion fatigue life of RC under realistic conditions.

ACKNOWLEDGEMENTS

I would like to thank my supervisor Dr. Moh Boulfiza for supervising my project, giving me valuable suggestions, and encouraging me during my Ph.D. study. Anytime I had issues in my program, he always dedicated to solving them. Moreover, he offered me financial support when my scholarship from the China Scholarship Council (CSC) ended. Without his support, from both professional and financial, this project would take a longer time to complete.

I would like to thank Dr. Ikechukwuka N. Oguocha from Mechanical Engineering at the University of Saskatchewan for his valuable advice in studying or analyzing the obtained data. And he is very helpful for my access to the equipment in the Department of Mechanical Engineering.

I would like to express my thanks to Dr. Akindele G. Odeshi and Dr. Bruce F. Sparling, and to all my Advisory Committee members, for their expertise during my project.

I deeply thank the China Scholarship Council (CSC) and the Department of Civil, Geological, and Environmental Engineering for their financial support.

I would like to thank Dr. Daniel Chen and Dr. Jerzy Szpunar for the access to their equipment. And I would like to thank Brennan Pokoyoway, Helen Yin, Adam Hammerlindl, Structural Engineering Laboratory, Geotechnical Laboratory, Environmental Laboratory, Daniel Vessey, Engineering shop, and my fellow graduate students.

To my wife and my family

TABLE OF CONTENTS

LIST OF FIGURES

LIST OF TABLES

LIST OF SYMBOLS AND ABBREVIATIONS

Symbols

ΔK_{th}	Threshold stress intensity factor, MPa√m
K_{Ic}	Fracture toughness, MPa√m
W_{crit}	Critical amount of rust, g
ρ_{rust}	Rust density, g/cm^3
f_t'	Tensile strength of concrete, MPa
E_{ef}	Effective elastic modulus of the concrete, Gpa
ν_c	Poisson's ratio
W_{rust}	Amount of rust, g
k_p	Rate of rust production
C_S	Chloride concentration on the concrete surface, mol/L
D_{cl}	Chloride diffusion coefficient in concrete
M	Molecular mass of iron, g/mol
i_{corr}	The corrosion current density
n	Valence of iron
F	Faraday's constant, C/mol
ΔK	Stress intensity factor range, MPa√m
a	Crack length, mm
$\Delta\sigma$	Ctress range, MPa
d_0	Original diameter of a rebar, mm
t_c	Crack propagation period, second
Δm	Mass loss of corroded steel, g
σ_a	Fatigue strength in terms of stress amplitude, MPa
σ_m	Mean stress, MPa
σ_{fat}	Fatigue strength in terms of stress amplitude, MPa
σ_{ts} or S_u	Ultimate tensile strength, MPa
σ_{ys}	Yield strength, MPa

S_e	The actual fatigue limit, MPa
S_e'	The fatigue limit measured by the standard rotating bending test, MPa
K_f	Fatigue notch factor
K_t	Elastic stress concentration factor, MPa√m
r_n	Radius of the notch root, mm
r	Radius of the rebar, mm
K_I	Stress intensity factor of mode I cracks, MPa√m
σ	Applied stress, MPa
Q	Function of material and shape
K_{EAC}	Stress intensity factor at environmentally assisted cracking, MPa√m
d	Pit depth, mm
t_0	Pitting initiation time
ΔK_{eff}	Effective stress intensity factor range, MPa√m
K_o	Stress intensity factor at the crack opening, MPa√m
K_{max}	Maximum stress intensity factor, MPa√m
c	Half of the cord correspondent to an elliptical crack on round bar, mm
S	Half of the arc length correspondent to the cord length $2c$ on round bar, mm
ΔK_{th0}	Threshold stress intensity factor range at R=0, MPa√m
γ_{th}	A material constant

Abbreviations

CF	corrosion-fatigue
RC	reinforced concrete
FRP	fiber reinforced polymer
SEM	Scanning Electron Microscope
EDS	Energy Dispersive X-Ray Spectroscopy
ASTM	American Society for Testing and Materials
UTS	ultimate tensile strength
LEFM	linear elastic fracture mechanics
FCGR	fatigue crack growth rate
SCC	Stress Corrosion Cracking
CDF	cumulative distribution function
EPFM	Elastic Plastic Fracture Mechanics
FPFM	Fully Plastic Fracture Mechanics
LPR	Linear Polarization Resistance
SCE	Saturated Calomel Electrode
MTS	Multi-testing system
SPS	Simulated pore solution
OCP	Open circuit potential
ANOVA	Analysis of variance
PSB	Persistent slip bands
CPT	Critical pitting temperature
COD	Crack opening displacement
DDW	Double distilled water

1 Introduction

1.1 Background

Most reinforced concrete (RC) structures serve a lifespan of several decades, or even over a century in some instances (Ishida, 2009). The long-term performance of these structures highly depends on both their in-service loading and the harshness of the environment in which they operate (S. Ahmad, 2003; Mori & Ellingwood, 1993; Rodriguez, Ortega, & Casal, 1997). Corrosion-fatigue (CF), which is defined as the simultaneous action of a fluctuating load and a corrosive environment, is commonly observed in many RC structures, e.g. bridges, harbor structures, oil platforms, etc. (Jaske, Payer, & Balint, 1981; Thomas, Edyvean, & Brook, 1988; Wahab & Sakano, 2001). Realizing that the aging of these structures may adversely impact their ability to fulfill their intended functions in the future, various strategies have been developed for predicting their service life and for mitigating the effects of aging on their performance.

Despite its practical importance, only a relatively small number of studies have been carried out on the corrosion-fatigue of RC structures. Most durability studies in RC focus on either corrosion or fatigue acting alone (Harlow & Wei, 1993; S. Li, Zhang, Gu, & Zhu, 1998; Masoud & Soudki, 2006; R. E. Melchers & Jeffrey, 2008; Soudki, Rteil, Al-hammoud, & Topper, 2007). In the few instances where CF was considered, RC structural elements, such as beams or slabs, were often tested providing valuable information about the overall CF behavior of such structures (Z. Liu, Diao, & Zheng, 2015; Loo, Foster, & Smith, 2013; Yi, Kunnath, Sun, Shi, & Tang, 2011). However, it is virtually impossible to extrapolate the applicability of those results to other structures or loading/exposure conditions.

Corrosion-fatigue is particularly severe in high strength metal alloys, such as stainless steel, aluminum alloys, and titanium alloys (DeJong, Heffernan, & MacDougall, 2009; El, Palin-luc, Saintier, & Devos, 2013; Hoeppner, 2011; Khan & Younas, 1996; Menan & Hénaff, 2010; Pao, Gill, & Feng, 2000; Radian, 1989; Wei & Gangloff, 1989; Weng, Zhang, Kalnaus, Feng, & Jiang, 2013). In those metals, the microstructural flaws induced by corrosion cause stress concentration effects that typically enhance the ability of fatigue loading to further grow those defects to form macro-cracks or macro-defects which greatly accelerates the degradation process in the metallic

alloy. Corrosion and fatigue facilitate each other in a way that creates synergetic effects when acting simultaneously. Hence, corrosion-fatigue-induced damage is typically greater than the sum of damages from cyclic stresses and corrosion, acting separately (Sastri, 2012).

Most published models about corrosion-fatigue in RC involve a sequential exposure to corrosion and fatigue wherein typically pre-corroded samples are tested under cyclic loading (E. Maaddawy, Soudki, & Topper, 2006; Yi et al., 2011). Consequently, the synergetic effects of corrosion and fatigue are not adequately captured. Although this kind of tests are relatively easy to carry out, strictly speaking, their results are only applicable to situations where a corroded RC structure will no longer be exposed to a strongly corrosive environment in the future. Another class of studies involves direct exposure of a RC structural element, such as a beam or a slab, simultaneously to a cyclic load and a corrosive environment, typically seawater, and monitoring the response of the system over extended periods of time (Katwan, 1988; Sonali, 1993).

An advantage of the long-term monitoring study is that it provides valuable information about the Corrosion-Fatigue performance of RC structural elements, as a system. However, such results would be almost impossible to apply to other exposure or loading conditions that are significantly different from the tested conditions. Also, it becomes extremely difficult to quantify the evolution of damage in the concrete and reinforcing steel in a way that can provide fundamental insights into this phenomenon as a function of the major external stimuli (harshness of the corrosive environment and severity of the fatigue loading). This is a consequence of the fact that what is monitored and modeled is the response of the entire concrete-steel reinforcement system, and not the response of its individual constituents.

The CF fatigue response of a structural element is the result of a combined effect of material behavior, geometry of the structure, environmental and loading conditions (Ettouney & Alampalli, 2016). For this reason, such models are unable to provide a deep insight into the root causes of damage in the Corrosion-Fatigue of RC structures and the influence of different controlling parameters. A more advantageous approach consists in characterizing the CF behavior of the reinforcing bar at the material level as a function of applied stress and corrosion rate without consideration of the structural aspects (Milella, 2013; Schijve, 2009).

There are a few corrosion-fatigue studies where only the bare steel reinforcing rebar is tested under the simultaneous action of corrosion and fatigue. Most available data indicate that the fatigue strength of bare reinforcing bars is sharply reduced when tested in seawater as compared to the performance in air (Slater, 1983; Tilly, 1979). Placing the bars inside concrete and testing in seawater exhibits a similar fatigue behavior as for the bare rebar (Baker, Money, & Sanborn, 1977). In this kind of study, frequency is reported as an important variable, as it has a strong effect on crack propagation rates in corrosion.

The main drawback of virtually all the studies reported in the literature is that the acceleration of the two major mechanisms governing the degradation of steel under CF is not done in a way that can reproduce a given field condition without distorting it. Indeed, given the excessively long periods of time that would be required to test and characterize the behavior of a given metal under actual field conditions, accelerated laboratory tests are typically designed so that the results are obtained within a relatively short period of time (Hartt, 2012; Yu, Francois, Dang, L'Hostis, & Gagne, 2015).

Acceleration of the fatigue loading is a rather well-established technique and can be implemented relatively easily in the laboratory to simulate the effect of many decades of loading cycles within only a few days or a few weeks. On the other hand, acceleration of corrosion rates in a given environment, is typically done by altering the chemistry of the service environment (concrete pore solution or sea water, etc.) so that higher corrosion rates are achieved. However, given the solubility limits of the various chemical compounds used in the service electrolyte, there is a maximum corrosion rate that cannot be exceeded using this approach. As a consequence, there are practical difficulties one encounters when attempting to accelerate both corrosion and fatigue loading in a way that preserves the relative importance they have under a given service environment (proportional increase).

Because of the need to obtain results within a reasonable time frame, oftentimes the acceleration factor used for fatigue is much higher than the one used for corrosion, making the test results not very representative of the field conditions. For instance, one can easily imagine that in situations where corrosion and fatigue damage play comparable roles, the results of accelerated tests where the acceleration factor is increased by three times for corrosion and increased by one hundred times

for fatigue, the damage induced by fatigue may become more dominant than that induced by corrosion. Hence, it is important to find ways to characterize the CF of rebars in a way that takes place over wide ranges of both corrosion rates and loading frequencies.

1.2 Problem statement

Assessing the long-term performance of materials and structures, over many decades or even centuries in some instances, requires a good knowledge of the behavior of those materials and their degradation mechanisms over the same periods of time. Given the excessively long periods of time that would be needed to produce such performance data for the actual field conditions, various accelerated techniques have been proposed to overcome this time difficulty. However, accelerated testing methods come with their own deficiencies and great care must be taken when designing them to make sure that the simulated conditions are representative of the service conditions. The difficulty to characterize the long-term behavior of materials and structures is greatly increased when both complicated loads and environmental conditions need to be taken into consideration, simultaneously, such as in the case of corrosion-fatigue of RC structures. A particularly challenging situation occurs when there is a risk that "excessive acceleration" in the laboratory could lead to changes in the degradation mechanisms, making the results of the accelerated tests not applicable to the field conditions. Unpredicted structural failures are poised to occur and may require expensive rehabilitation or replacement costs if the long-term behavior of a structure is not represented adequately (Starke, 1996).

One major disadvantage of virtually all accelerated testing methods lies in their relative simplicity, and hence, inability to recreate very accurately all aspects of the complicated loading and environmental conditions observed in the field (Starke, 1996). The field conditions may consist of many fluctuating effects such as loading, temperature, humidity, radiation, corrosive type, corrosive content, and their synergetic effects. As a result, most accelerated tests cannot represent exactly all the service conditions and, if not designed carefully, may induce major changes in the degradation mechanisms controlling the behavior of the materials (Starke, 1996). At present, a good characterization of the aging of many construction materials and the associated constitutive equations under the action of both loading and the environment are not available for practical field conditions. In particular, the CF behavior of reinforcing bars is not understood well enough, in

quantitative terms, to be representative of many practical field conditions. This fundamental knowledge is necessary for the development of reliable numerical and physical models for assessing the service performance of structures containing such materials.

The long-term performance of an RC structure depends not only on its mechanical loading but also on the severity of its service environment. In particular, the corrosion-fatigue of RC structures, such as bridges and oil platforms, is a potential issue that can trigger great economic damage and even loss of life if it is not addressed properly. Although there have been studies focusing on CF, they mostly investigated the structural performance or the rehabilitation of specific RC structures. In other words, a general method for evaluating the corrosion-fatigue performance of a RC structure in its service environment is still lacking. Moreover, the presently available acceleration approaches for the simulating the combined action of corrosion and fatigue in RC are not versatile enough to produce CF data that is representative of the field conditions. Hence, the development of effective acceleration techniques to simulate CF in reinforced concrete structures is a topic that requires further research, especially for corrosion.

1.3 Objectives

The main focus of this research is on the development of innovative accelerated tests and constitutive modeling of the corrosion-fatigue behavior in reinforced concrete, which will enable reliable calibration of theoretical models and provide some insight on the long-term performance of such materials from short-term tests. Because of the complexity of isolating the Corrosion-Fatigue behavior of steel reinforcement inside a concrete structure from the structural response of the component where it is embedded, it is proposed in this study to proceed in three separate stages. Firstly, find a way to accelerate corrosion in such a way that CF tests can be carried out in reasonable periods of time without distortion of the relative importance of corrosion and fatigue. Secondly, once a suitable acceleration test is developed, it will be used to study the corrosion fatigue of a carbon steel rebar in a synthetic concrete pore solution. Thirdly, the constitutive models developed in Stage 2 will be used to predict the response of RC beams under corrosion-fatigue. The sub-objectives of this study are as follows:

1) To assess the possibility of achieving reliable highly accelerated corrosion rates through a combination of pore solution chemistry and electrochemical corrosion means. Both Potentiostatic and Galvanostatic modes of control will be investigated and compared.

2) To develop appropriate tests to characterize the corrosion-fatigue behavior of reinforcing steel, as a material operating in a chloride-laden simulated concrete pore solution, in a way that is compatible with two widely used fatigue analysis approaches (S-N curves and Fracture Mechanics).

3) To assess the ability of the constitutive models developed in Objective 2 to capture the fatigue life of reinforced concrete beams in a corrosive environment, as an example of a structural component. The results of the model predictions, for both approaches (S-N curves and Fracture Mechanics), will be compared with the experimental results for an independent set of RC beams tested under corrosion-fatigue. Specifically, the study addresses the following:

> 3.1) Use of the S-N curves developed in Objective 2 in a relatively simple fatigue-life-based model to predict the corrosion-fatigue of carbon steel rebar in concrete.
>
> 3.2) Development of a more sophisticated fracture-mechanics-based model to gain a better insight into the evolution of damage in the rebar over time. The model should account for the four main stages of the metal degradation process: pit nucleation and growth, pit-to-crack transition, crack growth state, and ultimate fracture failure.

4) To conduct failure analysis of specimens used in the corrosion-fatigue tests for the stress-life method, Fracture Mechanics, and reinforced concrete beams. Scanning Electron Microscope (SEM) and Energy-Dispersive X-ray Spectroscopy (EDS) are used to examine the nature of the fracture surfaces and identify the origin of pitting-induced fractures.

1.4 Scope

In practice, the electrolyte for the rebar corrosion in reinforced concrete is the actual concrete pore solution. However, a synthetic concrete pore solution was used for the rebar corrosion in the two approaches considered in this study to estimate the corrosion-fatigue life, namely, the S-N approach and the Fracture Mechanics approach.

1.5 Outline of dissertation

This dissertation contains seven chapters in addition to this Introduction Chapter (Chapter 1):

Chapter 2 contains a background review of the corrosion-fatigue phenomenon and its applications in the context of reinforced concrete structures. The advantages and disadvantages of previous studies for evaluating the service life of reinforced concrete structures are discussed in this chapter. The considered approaches include the estimation of rebar corrosion and the loss of mechanical performance in the steel reinforcement induced by corrosion.

Chapter 3 introduces the two approaches used in this study to estimate the corrosion-fatigue life of RC beams – stress-life method and fracture mechanics – and the corresponding experimental programs needed for their characterization.

Chapter 4 presents the proposed acceleration methods for rebar corrosion in both solution and concrete environments. Potentiostatic and Galvanostatic polarization techniques are investigated and compared to determine the most suitable method for high acceleration of corrosion in a CF test.

Chapter 5 discusses the CF results obtained by the stress-life approach (S-N curves) in simulated concrete pore solutions. This chapter also presents a procedure for transforming the test results obtained for a rebar in a synthetic pore solution so they can be used to predict the service life of RC beams under CF. Furthermore, the fracture surfaces of tested specimens are also analyzed by SEM and EDS.

Chapter 6 builds two fracture mechanics models for predicting the corrosion-fatigue of RC beams that take into account the following four stages of damage development: pit nucleation and growth, pit-to-crack transition, crack propagation, and fracture failure. The details of the constitutive models for each stage are presented in this chapter.

Chapter 7 introduces the test results of the RC beams that were tested directly under CF conditions and compares them with predictions based on the previously developed stress-life approach and

fracture mechanics approach. The advantages and disadvantages of each approach are also discussed in this chapter.

Chapter 8 presents the conclusions of this study, together with a discussion of contributions, and suggestions for future work.

2 Literature review

This chapter contains the reviews of the chloride-induced corrosion in reinforced concrete (RC), the fatigue phenomenon of metals, and the synergetic effect of corrosion and fatigue in metals. The methods to evaluate corrosion-fatigue are then introduced.

2.1 Corrosion, fatigue, and corrosion-fatigue

2.1.1 Chloride induced corrosion in reinforced concrete

2.1.1.1 Passivity of reinforcing steel in concrete

Steel reinforcement in concrete is usually protected by a natural barrier of concrete cover and highly alkaline concrete-pore-solution with a pH above 13 (Luca Bertolini & Polder, 2013; Broomfield, 1997). The concrete pore solution is formed by the hydration of cement, and mainly consists of sodium and potassium hydroxides. Once an RC structure is constructed, cement hydration produces a highly alkaline environment and the surface of the rebar starts to oxidize since oxygen and water are available in sufficient amounts at that time. As the oxidizing process continues, the oxide layer on the rebar starts to grow and becomes the main barrier preventing oxygen and water from reaching the surface of the bare metal beneath it. The growth of the oxide film takes place with a decreasing rate, over time, because the formation of the oxide film gradually inhibits the reactants from penetrating through the film. Beyond a critical thickness, the oxide film would greatly reduce the movement of chemical species in the pore solution, and the oxidization process almost comes to a halt (Marcus, 2002). The passivity of steel reinforcement in concrete is typically maintained by a highly alkaline environment that leads to the formation of a protective oxide film (a few nanometers).

The oxide layer develops according to the following reactions (Broomfield, 1997):

$$Fe \rightarrow Fe^{2+} + 2e^{-} \text{ (Anodic dissolution)} \qquad (2.1)$$

$$Fe^{2+} + 2OH^- \rightarrow Fe(OH)_2 \text{ (Ferrous hyroxide)} \quad (2.2)$$

$$2\ Fe(OH)_2 + O_2 \rightarrow 2FeOOH + H_2 \text{ (Ferric hyroxide)} \quad (2.3)$$

$$O_2(g) + 2H_2O + 4e^- \rightarrow 4(OH)^-(aq) \text{ (Cathodic reaction)} \quad (2.4)$$

The composition of the oxide layer is usually either Fe_2O_3 or Fe_3O_4, both of which are stable in a concrete environment. The most stable passive film in RC is Fe_2O_3 in the form of γ-FeOOH that is produced during the reaction of O_2 and $Fe(OH)_2$.

$$4Fe(OH)_2 + O_2 \rightarrow Fe_2O_3 \cdot H_2O + 2H_2O \quad (2.5)$$

Since the corrosion rate is very low, while passivating conditions are maintained, a carbon steel rebar can operate during the entire service life of a structure without any significant corrosion-induced damage. However, any factor that destroys the alkaline environment or the protective oxide layer would cause the degradation of reinforcing steel. It is reported that RC structures most often fail in environments of high humidity and high temperature, or those surrounded by hygroscopic substances (Fernandez, Bairan, & Mari, 2015; Islam & Sugiyama, 2010; Strength, Concrete, & Fly, 2010). Thus, to maintain the passivity of rebar in concrete, the quality of concrete should be rigorously specified and carefully monitored. In other words, the quality of the fresh concrete properties (workability, settlement & bleeding, plastic shrinkage, etc.) during construction, together with the hardened state properties (porosity, resistance to freeze-thaw cycles, etc.) play a major role on the long-term performance of a reinforced concrete structure.

2.1.1.2 Chloride attack in RC

The long-term degradation of concrete usually comes from two main mechanisms, chloride penetration and carbonation (Luca Bertolini & Polder, 2013; Broomfield, 1997; Kim, Boyd, Kim, & Lee, 2015; Sohail, 2013). Carbonation decreases the pH of the concrete pore solution to values that cause a destruction of the protective oxide layer on the rebar surface. Although the pH value of the pore solution in concrete remains practically constant during chloride penetration, the presence of chloride ions can produce pitting corrosion on the rebar.

Chloride induced corrosion is a type of localized corrosion. The mechanism of chloride attack in RC is usually divided into several stages: transport of chloride ions though the concrete cover, passive film breakdown on rebar, pitting corrosion (L. Bertolini & Redaelli, 2009; Luca Bertolini, 2008). In the field, two typical types of sources introduce chloride in RC, coastal environments and de-icing agents. Other sources of chloride ions may be aggregates containing chlorides, saline mixing water, and addition of chloride as a component of an admixture during the mixing process (Z. Ahmad, 2006; Broomfield, 1997).

Transport of chloride in concrete

In a concrete environment, ions have to be transported in the pore solution of the inter-connected pores. Chloride transport in concrete is mainly governed by three mechanisms: capillary suction, migration, and diffusion (Luca Bertolini, 2008; Boulfiza, Sakai, Banthia, & Yoshida, 2003; Broomfield, 1997; Martın-Pérez, Pantazopoulou, & Thomas, 2001). Capillary suction is the phenomenon that liquid enters a porous medium caused by capillary forces. Migration in concrete is defined as the movement of a substance in concrete induced by magnetic field. Diffusion is considered as the movement of a substance from high concentration to low concentration. Many scientists (Bastidas-arteaga, 2009; Luca Bertolini, 2008) approximate the chloride ingress rate by the laws of diffusion. However, depending on the exposure conditions, the ingress of chloride in concrete is typically far more complicated than through simple molecular diffusion. As chlorides appear on the concrete surface, suction usually governs the chloride ingress when the concrete surface is dry. Deeper inside concrete, the chloride ingress rate is mainly controlled by diffusion. Many factors could increase the transport rate of chloride in concrete such as wet-dry cycling, evaporation, freeze-thaw cycling, etc. However, a number of mechanisms might reduce the penetration rate of chlorides, among those one can mention bonding with the solid matrix and the reaction with hydration products (Luca Bertolini & Polder, 2013).

Breakdown of passive film

Provided that enough oxygen and moisture are available at the reinforcement location within concrete, the oxide film protecting the rebar is destroyed thorough pitting corrosion whenever the concentration of the chloride ions reaches a threshold value. The breakdown mechanisms are not

yet fully understood, e.g. localized corrosion in the presence of chlorides, and the interaction between the chloride anions and the oxide film (Szklarska-Smialowska, 2005).

Many researchers (Luca Bertolini & Polder, 2013; Landolt, 2007; Szklarska-Smialowska, 2005) studied the mechanisms of chloride-induced pitting corrosion. Their findings agree that adsorption of chlorides on the passive film is the first step in pitting corrosion while chlorides act as catalysts for pitting. The corrosion rate has been shown to depend on the amount of free chlorides available in the pore solution. The amount of bound chlorides does not affect the corrosion rate. Previous research also shows that a threshold concentration of chloride is required in order to destroy the oxide layer and initiate pitting. Below that threshold the chloride anions are simply adsorbed on the metal surface in the form of clusters and the passive layer is able to rehabilitate itself (Janik-Czachor, Szummer, & Szklarska-Smialowska, 1975; Okada, 1984).

Many scientists (Luca Bertolini & Polder, 2013; Vonezawa, Ashworth, & Procter, 1988) have characterized the critical chloride concentration in terms of the chloride/hydroxyl ratio or simply the chloride concentration. Researchers observed that the chloride/hydroxyl ratio of 0.6 or the chloride concentration of 0.05 M could break down the passive film and nucleate pits on the rebar (Hausmann, 1967; Mohamed, 2009). However, all the proposed thresholds are only approximate because: (1), pH in concrete is affected by the cement type and the concrete mixing ratio; (2), chlorides might be adsorbed both chemically and physically; (3), the activation of chlorides depends not only on the reaction environment but also on the concentration of the reactants.

Pitting corrosion

With the protective passive layer breaks down, the steel areas directly exposed to the bulk alkaline solution act as anodes (active zones, pits) while the surrounding areas, still covered with the passive layer, act as cathodes. In the anodic areas, steel corrosion takes place and produces electrons due to the dissolution of metal iron to form ferrous or ferric ions. Those electrons are then transferred to the cathode and react with oxygen and water to produce hydroxide ions. The cathodic areas surrounding the pit remain protected during the pitting process.

A schematic of pitting corrosion is shown in Figure 2.1. As soon as the passive layer is destroyed by chemicals such as chlorides, fresh steel is exposed to the pore solution. Although the pH of a chloride contaminated concrete maintains the conditions of a highly alkaline environment, which practically suppresses the corrosion rate of reinforcing steel, the presence of a sufficient amount of chlorides leads to pitting corrosion, provided that enough moisture and oxygen are available for corrosion to occur.

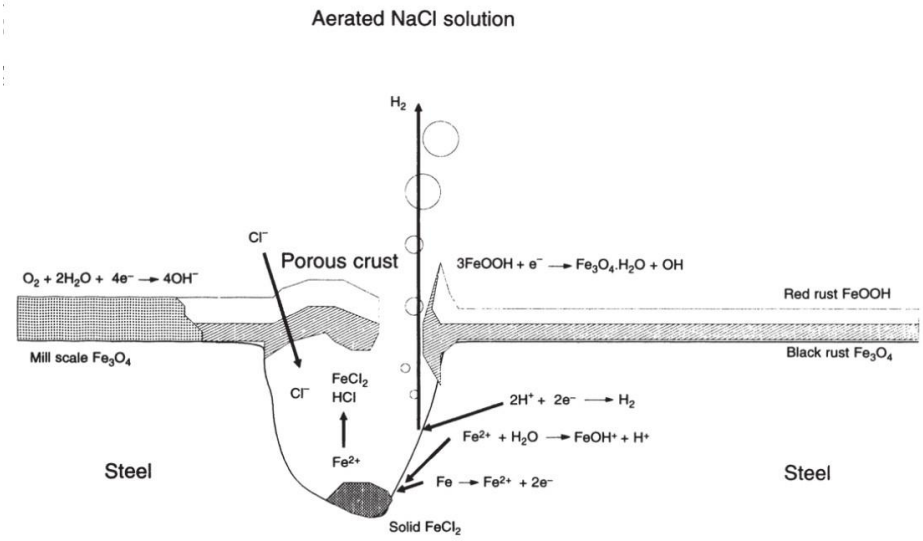

Figure 2.1. The model of pitting corrosion (Luca Bertolini & Polder, 2013)

Following its direct exposure to the bulk solution, fresh steel at the depassivated spots start to corrode and pits are nucleated. A severe form of pitting corrosion occurs when there is formation of a pit cap, which is composed by the porous rust clustered in the pit mouth. The environment within the pit is very different from the bulk alkaline solution. Due to the electrochemical features in the pitting area, the corrosion current produced in the electrochemical reactions drives the chloride ions towards the anodic zones because of their negative charge. Chlorides permeate through the porous cap, cluster in the pit, and interact with the hydrogen ions produced by the reaction between Fe^{2+} and water, producing HCl, a strong acid that produces a highly acidic micro-environment inside the pit which in turn leads to a very aggressive corrosion of steel. Some researchers reported that the pH in the pit could go down to 5, while others confirmed in the laboratory that the pH was as low as 2 (Luca Bertolini & Polder, 2013; Pacheco, Polder, Fraaij, & Mol, 2011). The corrosion rate inside the pit is rather high (up to 1 mm/year) in comparison with

the rates typically observed in general corrosion. The high penetration rates of pitting corrosion can cause a rapid reduction in the cross section of the reinforcement, and this in turn, could greatly reduce the load-bearing capacity of an RC structure.

The corrosion of a carbon steel rebar is an electrochemical reaction, which consists of anodes and cathodes. The general corrosion process of steel is seen as:

$$\text{Iron + oxygen + water} \rightarrow \text{corrosion products} \tag{2.6}$$

At the anodes, the anodic process consists of the dissolution of iron into solution and the liberation of electrons along the way. At the cathodes, the cathodic process is the reduction of oxygen and consumption of the electrons produced by the anodic process.

$$\text{Anodic reaction: } Fe(s) \rightarrow Fe^{2+} + 2e^{-} \tag{2.7}$$

$$\text{Cathodic reaction: } O_2(g) + 2H_2O + 4e^{-} \rightarrow 4(OH)^{-}(aq) \tag{2.8}$$

In the absence of oxygen, the main cathodic reaction that takes place in a typical concrete pore solution is the evolution of hydrogen gas:

$$2H_2O + 2e^{-} \rightarrow H_2(g) + 2(OH)^{-}(aq) \tag{2.9}$$

As an electrochemical reaction, an essential part of corrosion is the transport of electrons from the anodic regions (pits) to the cathodic regions (rebar surface surrounding the pits). The transport of electrons causes the flow of current from the anode to the cathode.

As shown in the anodic reaction, iron dissolves in the pore solution. However, the corrosion product is not the usual rust we would see in cracked or spalled concrete. More processes (shown from Eq. (2.10) to Eq. (2.12)) are required to form that rust:

$$Fe^{2+} + 2(OH)^{-} \rightarrow Fe(OH)_2 \tag{2.10}$$

$$4Fe(OH)_2 + O_2 + 2H_2O \rightarrow 4Fe(OH)_3 \quad (2.11)$$

$$2Fe(OH)_3 \rightarrow Fe_2O_3 \cdot H_2O + H_2O \quad (2.12)$$

Depending on the availability of oxygen and other chemicals in the electrolyte, the exact composition of the final corrosion products varies from case to case. However, the two corrosion products, Fe_2O_3 and Fe_3O_4, are often observed (Z. Ahmad, 2006).

2.1.2 Fatigue

The definition of fatigue, cited from ASTM 1823 (ASTM, 2013a) standard, can be written as – the process of progressive localized permanent structural change occurring in a material subjected to conditions that produce fluctuating stresses and strains at some point or points and that may culminate in cracks or complete fracture after a sufficient number of fluctuations. Fatigue failure is a phenomenon where a structure fails after exposure to a number of cycles of a fluctuating load, the maximum stress of which is less than the ultimate stress the structure can bear.

The process of fatigue can be divided into several phases from the fracture mechanics point of view: cyclic slip, crack nucleation, micro-crack growth, macro-crack growth, and final failure (Schijve, 2009). A schematic of this process is provided in Figure 2.2.

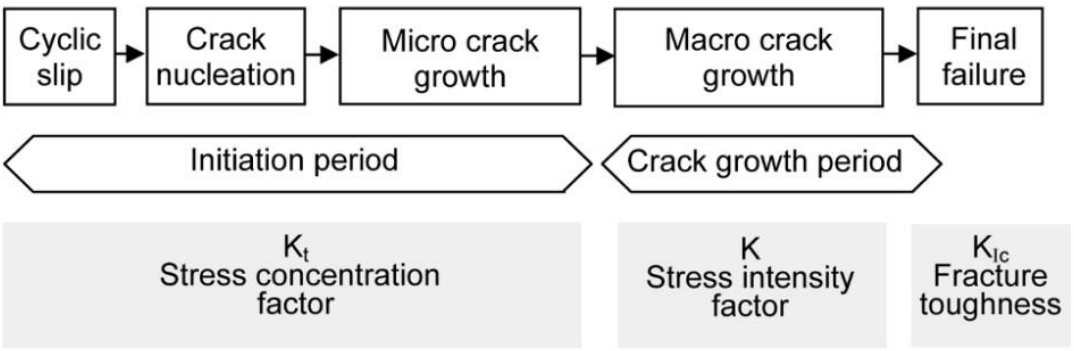

Figure 2.2. Growing stages of fatigue from initiation until failure (Schijve, 2009).

2.1.2.1 Crack initiation

The applied stress caused by the fatigue loading is usually fairly low compared with the ultimate tensile stress (UTS) of the material. For high fatigue loading (e.g. close to the UTS), a single loading cycle could cause a crack on the surface of the material. However, for most fatigue loading conditions (e.g. below the yield stress), a crack is often unable to nucleate in the early stages of cyclic loading. Each cycle of the loading produces a plastic deformation on the surface of the material since the loading is too weak to fracture the solid. A single loading cycle could be treated as a monotonic loading, which produces dislocations on the specimen's surface exhibiting a staircase morphology, as shown in Figure 2.3 (a) (Suresh, 1998). The appearance of the strain offset depends on the properties of the grains – size and shape, crystallographic orientation – and the elastic anisotropy of the material (Schijve, 2009).

With fatigue loading, the strain offset would firstly appear similarly as in the case of the monotonic loading. However, during the reverse loading period in a loading cycle, fresh strain offsets would be created instead of the complete recovery of the previous strain offsets (Hertzberg, 2012). That is because strain hardening in the slip zone is unable to fully reverse and an oxide layer might form on the previous slip tips once they have been created. Since a monotonic load creates a geometrical discontinuity on the metal surface, the dislocation spot facilitates the nucleation of new dislocations because of stress concentration. As a result, the accumulated damage of the cyclic loading is caused by the slips with extrusions and intrusions observed on the metal surface, shown in Figure 2.3 (b). These non-reversible slips are also known as persistent slip bands (Milella, 2013).

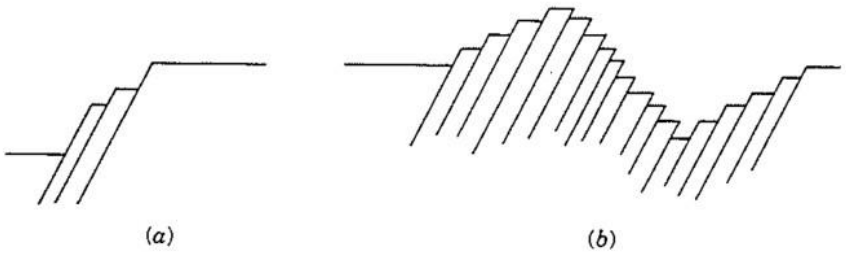

Figure 2.3. Plastic strain-induced surface offsets: (a) monotonic loading caused slip offsets; (b) fatigue loading caused extrusions and intrusions (Hertzberg, 2012).

Some researchers (Hertzberg, 2012; Milella, 2013) concluded that these slips act as fatigue crack nucleation sites. The reason can be attributed to the fact that micro-cracks usually form at these extrusions and intrusions. Alden and Backofen (Alden & Backofen, 1961) have shown that fatigue life can be improved as long as the slips on the specimen's surface are constantly polished during the testing period. Other studies (Hertzberg, 2012) illustrated the fact that the plastically deformed slip bands soften the specimen's surface and concentrate stress in the fatigue testing. Therefore, cyclic plastic deformation, caused dislocation activities, are the dominant behavior prior to crack initiation in metals. Figure 2.4 shows the cyclic slip bands in a copper specimen after two million cycles.

However, some researchers (Milella, 2013; Palin-luc et al., 2010) reported that inclusions or pre-existing flaws near the surface of a specimen may also trigger a crack. Moreover, some studies (DeJong et al., 2009; El May, Palin-Luc, Saintier, & Devos, 2013) showed that corrosion induced flaws such as pits were also an essential source to the initiation of cracks.

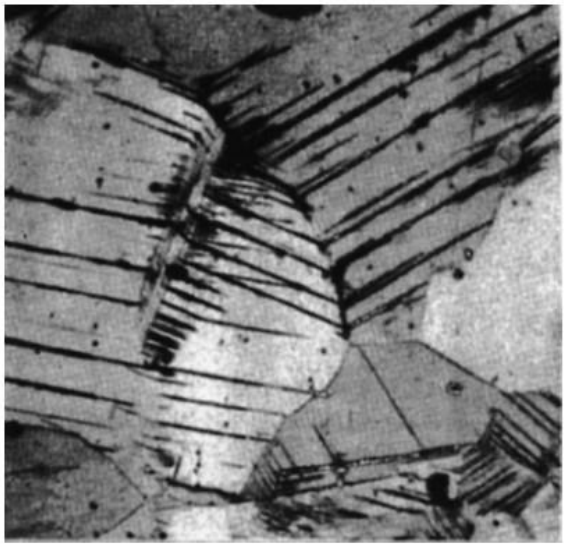

Figure 2.4. Slip bands in a copper specimen (Bullen, Head, & Wood, 1953).

2.1.2.2 Crack growth

Short crack growth

Prior to cracking, fatigue only affects the surface of the material. Hence, the material surface conditions would greatly influence the nucleation of a crack. Once a micro-crack is formed, fatigue behavior steps into a new stage.

Unlike the macro-cracks (known as large cracks or long cracks) that have steady growth rates, the growth of micro-cracks (also known as short cracks or small cracks, usually with a crack length of several grain diameters) is usually unstable and unpredictable in the same material (Lankford, 1982; Narasaiah & Ray, 2005). The growth rate of a short crack might slow down or even stop because of the change in the crack tip stress field. Thus, despite the existence of short cracks in a specimen, it may have a fairly long fatigue life or even 'infinite' life as defined in fracture mechanics (Suresh, 1998). The concept of stress intensity factor K is used in fracture mechanics to describe the stress state in a crack tip. According to the definition of stress intensity factor shown in ASTM E399 (ASTM, 2013c) standard, it is magnitude of the ideal-crack-tip stress field, for a particular mode of crack displacement, in a homogeneous, linear-elastic body. Figure 2.5, which depicts the stress intensity factor range ΔK against crack growth rate dc/dN, shows the difference in crack growth between short cracks and long cracks.

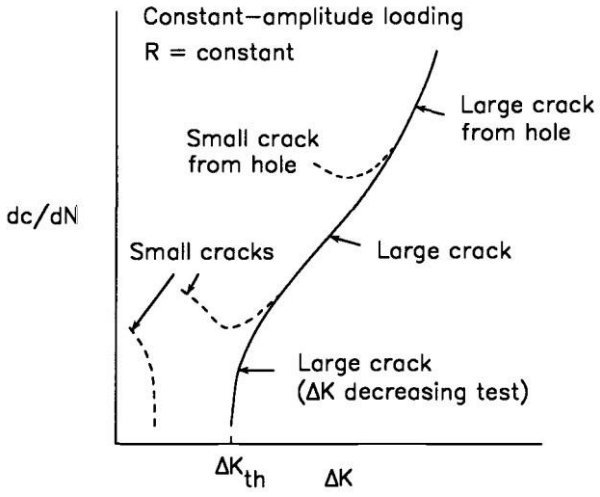

Figure 2.5. Small crack growth and large crack growth (Larsen & Allison, 1992).

The reasons for the short-crack effects have been intensively studied. Both linear elastic fracture mechanics (LEFM) and nonlinear or elastic-plastic fracture mechanics (using the concepts of J-integral and crack closure) have been proposed to explain the observed short-crack effects (Larsen & Allison, 1992). Moreover, metallurgical features are also used to explain these effects (Lankford, 1982; Newman Jr, 1983). In materials that are markedly inhomogeneous and anisotropic, the local grain orientation and grain boundary features could affect the crack propagation rate and the growth directions (Blom et al., 1986). Also, the irregularities and the inclusions of the crack front would affect the local stress distributions, and crack growth would be affected.

Long crack growth

A long crack is defined as a crack that can steadily grow from the fatigue crack growth threshold ΔK_{th}, where the da/dN closes to zero, until fracture failure as depicted in Figure 2.5. The growth of a long crack is usually governed by the loading conditions, the properties of the material, and the environmental effects. The stress intensity factor is usually used to characterize a crack geometry and the applied stress. A typical image of the logarithmic scale of the stress intensity factor range (ΔK) against the fatigue crack growth rate (FCGR, da/dN) is presented in Figure 2.6.

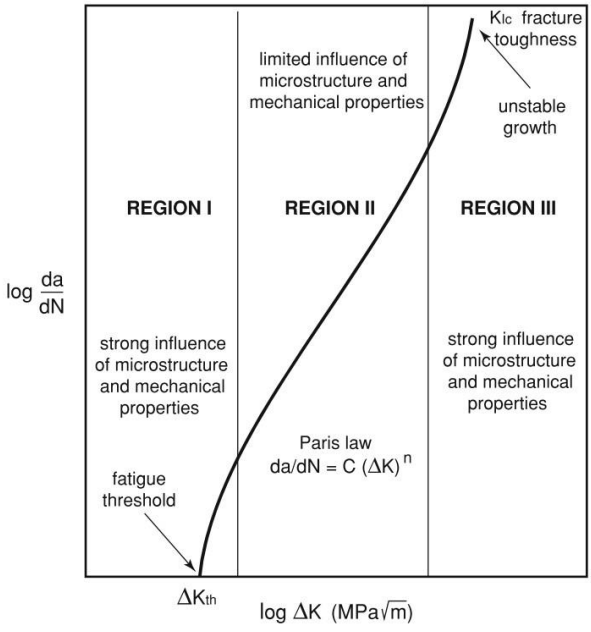

Figure 2.6. Typical crack growth curve in metals (Milella, 2013).

Three zones can be identified in the typical FCGR curve shown in Figure 2.6. The left zone, Region I, the so-called threshold zone, is characterized by a certain threshold value, ΔK_{th}, below which no apparent fatigue crack growth would occur. Cracks in this zone are strongly affected by the microstructure and mechanical properties of the material. In the central part of the curve, Region II, the fatigue crack growth rate da/dN varies linearly with ΔK in the log-log scale and it is governed by the well-known Paris law. This region is largely independent of the microstructure and the inclusions presented in the material when the metal is in a non-corrosive environment. The typical character of the final region, Region III, is the fast FCGR that causes low fatigue cycles. In this stage, the FCGR takes place very rapidly and one single cycle could cause the failure of the specimen. Furthermore, the ΔK at which failure occurs defines the fracture toughness K_{Ic} of the material. Similar to Region I, the microstructure and material properties greatly affect the FCGR in this region.

2.1.3 Synergetic effect of corrosion and fatigue

The fatigue behavior discussed in Section 2.1.2 would be affected if the material is in a corrosive environment. In general, any environment including dry air could become potentially aggressive, depending on the material and the loading conditions. The synergetic effect of corrosion and fatigue is highly complex and their interactions are greatly affected by chemical, mechanical, and metallurgical factors.

In corrosion-fatigue, the degradation of a material accounts for the singular effects of corrosion and fatigue and the interactions between the two. Hence, environmentally assisted fatigue is highly dependent on the effects of both corrosion and fatigue, acting simultaneously. However, the relative importance of corrosion and fatigue should be "close enough" for the synergetic effects to be observed. Otherwise, either corrosion or fatigue would dominate the corrosion-fatigue response and eclipse the other degradation mechanism.

2.1.3.1 Corrosion-fatigue mechanisms

During the crack initiation period, corrosion affects fatigue in two ways. First, corrosive environments such as chlorides nucleate pits that become the stress concentrators and cause short

cracks (T. Chen, 2014; Sankaran, Perez, & Jata, 2001). Second, when cyclic loading forms slip bands, the fresh slip bands could be oxidized and the products may penetrate into the specimen surface when the loading is reversed in a cycle (Zhao, Wang, Zhang, & Wang, 2012). The consequence of the oxides on the steel surface is that the oxide damage accelerates the initiation of cracks. Moreover, corrosion products embedded in the slip planes would decrease the cohesive strength of steel between two adjacent slip planes, and this would accelerate the propagation of fatigue cracks along these planes.

In the crack propagation period, many factors from both corrosion and fatigue aspects would affect the fatigue crack propagation response of a material subjected to a corrosive environment, which includes test frequency, load ratio, load profile, temperature, inclusions, and chemical species (Hertzberg, 2012; Milella, 2013). Thus, these factors somehow have an effect on either corrosion or fatigue or both.

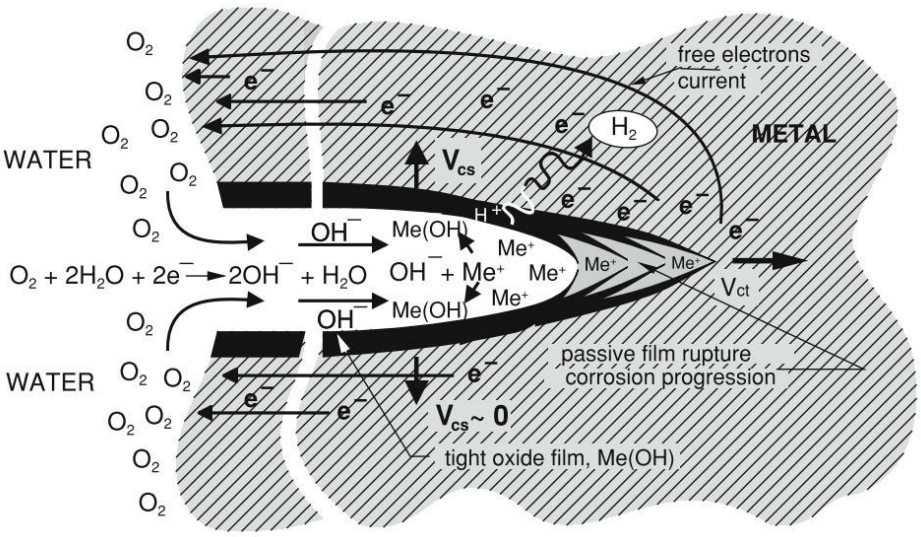

Figure 2.7. A schematic of the propagation in the crack tip (Milella, 2013).

When a crack is formed, the propagation of the crack tip is mainly governed by anodic dissolution and fatigue loading. A schematic of the propagation in crack tip is shown in Figure 2.7. The passive film might form in the crack tip front. Depending on the severity of the corrosive environment, either corrosion or some fatigue cycles could break the oxidized layer of film and produce the active anodic dissolution of the bare metal in the crack tip. The metal in the front of the crack tip

would be unable to re-passivate since the fatigue loading could break the passive film in each cycle. In corrosion-fatigue, both anodic dissolution and fatigue loading facilitate the propagation of the crack tip.

2.1.3.2 CF and stress corrosion cracking (SCC)

CF and SCC might be simultaneously triggered in an environmentally assisted fatigue testing, depending on both environment and cyclic loading. A schematic of the relationship between CF and SCC is shown in Figure 2.8. Film rupture, anodic dissolution and hydrogen embrittlement are the three typical types of SCC, and they are often activated in corrosion-fatigue testing. For instance, the reduction of the loading frequency or the increase of the stress ratio (R ratio) can activate the SCC mechanism (see Figure 2.9). The true corrosion fatigue (TCF) behavior in Figure 2.9 (a) shows that, in an aggressive environment, fatigue crack growth threshold could shift to a lower value and the shape of fatigue crack propagation curve could change. Depending on the environmentally assisted cracking threshold K_{ISCC}, it might be higher or lower than ΔK_{th}, which means a SCC mechanism might be triggered before or after the occurrence of TCF, as shown in Figure 2.9 (b) and (c), respectively.

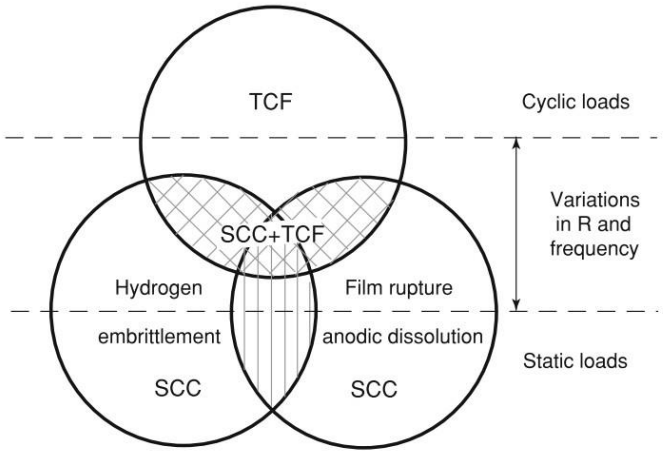

Figure 2.8. Interdependence among true corrosion fatigue (TCF), film rupture-anodic dissolution and hydrogen embrittlement of stress corrosion cracking (SCC) (Fontana, 1987).

Hydrogen embrittlement is severe in many strong metals since a hydrogen atom has a small diameter and could penetrate through the grain boundaries. The weakening of the grain boundaries greatly increases the crack propagation along them. The SCC mechanism would dominate, on the condition that the crack propagation induced by SCC is faster than what induced by true corrosion fatigue as seen in Figure 2.9 (c).

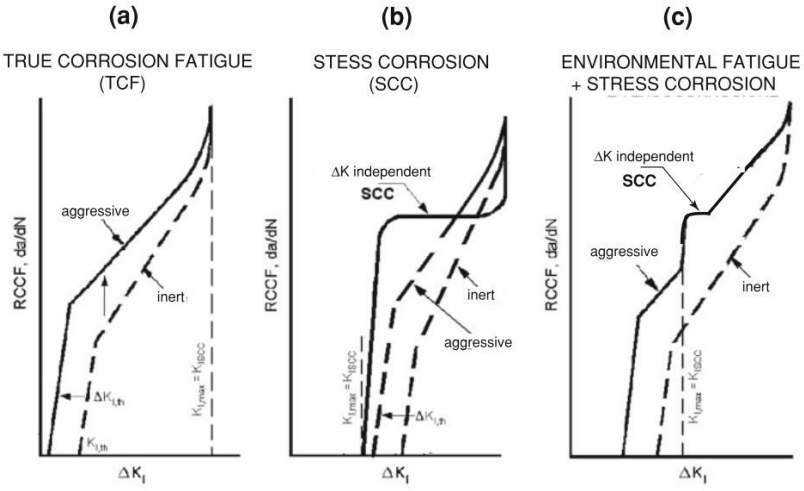

Figure 2.9. Different types of corrosion-fatigue propagation curves in terms of fatigue crack growth rate da/dN against stress intensity factor range ΔK (Milella, 2013).

2.2 Studies on corrosion-fatigue and corrosion-fatigue evaluation

This section introduces the previous studies on CF and the evaluation of CF in RC structures. Previous studies on CF can be divided into two main categories; those based on the material point of view and those based on the structural point of view. However, the vast majority of the published studies focus mostly on some aspect of the consequences of the corrosion-fatigue phenomenon in concrete rather than on a fundamental understanding of its root causes. For instance, many studies were concerned with the issues of structural rehabilitation, uncoupled corrosion and fatigue, the bonding strength between concrete and rebar, fatigue strength, and service life loss (Amleh, Mirza, & Ahwazi, 2000; Luca Bertolini, 2008; Das, Cheng, & Murray, 2006; Song & Yu, 2015). Few studies, however, have been conducted on the evaluation of CF. Corrosion-fatigue evaluation is usually studied in two ways: the transport of corrosive chemicals in concrete and the degradation of reinforcing steel. The former focuses on the transport of corrosive chemical species through

concrete and their reaction on the reinforcing steel surface. Studies on the degradation of rebar, on the other hand, concentrate on the mechanical performance loss in a rebar because of corrosion.

2.2.1 Previous studies on corrosion-fatigue

Many researchers (Al-hammoud, Soudki, & Topper, 2011; Coca, Tello, Romero, & Villafañe, 2011; S. Li et al., 1998; Oyado, Kanakubo, Sato, & Yamamoto, 2011; Soudki et al., 2007; Yi et al., 2011)(Z. Liu et al., 2015) examined the load-bearing capacity loss and reduction of fatigue life induced by pre-corrosion in RC beams. The main findings were: (1), the fatigue cycles of RC beams are increasingly reduced with an increasing mass loss of steel; (2), brittle failure of rebar is observed; (3), the yield strength of reinforcement declines with an increasing mass loss of steel; and (4), pitting will happen beyond 7% mass loss of reinforcement.

Many researchers (Masoud & Soudki, 2006; Soudki et al., 2007)(Loo et al., 2013; Song & Yu, 2015)(Feldman, Boulfiza, Zacaruk, Christensen, & Sparks, 2008) studied the response of various pre-corroded RC structures (mostly beams) for the purpose of their rehabilitation by externally bonded fiber reinforced polymers (FRP), or simply for assessing the loss of fatigue life induced by corrosion. Their research found that, with external FRP reinforcement, the fatigue strength of corroded RC beams were typically 15% higher than the beams without.

Fatigue bond strength in RC was examined by Al-Hammoud et al as well (Al-Hammoud, Soudki, & Topper, 2010). Their research showed that even a low corrosion level could reduce the fatigue bond strength by about 30% and the crushed spots in concrete induced by the expansion of corrosion products lead to a significant reduction in the bonding between concrete and rebar.

Besides studies on high cycle fatigue in steel bars, many researchers (Apostolopoulos, 2007; Apostolopoulos & Pasialis, 2009; Khan & Younas, 1996) also investigated low cycle fatigue under corrosion as it took shorter testing times in the laboratory and the results somewhat reflect corrosion-fatigue in the field. Since most corrosion-fatigue studies in RC structures are not strictly considered as corrosion-fatigue because of the separation of corrosion and fatigue processes during testing, the results they produced could not account for the synergy between these two degradation mechanisms.

From a material angle, many studies (Luca Bertolini, 2008; Rahman, Al-Kutti, Shazali, & Baluch, 2012; Ravikumar & Neithalath, 2013) have been carried out on corrosive species penetration and accumulation at the reinforcement location. In particular, chloride ions play an essential role in pitting corrosion. A critical amount of chloride ions is needed to initiate pitting and can be used as a threshold for determining the start of active corrosion. Although concrete cover in RC somewhat prevents chlorides from penetrating through concrete, the porous nature of concrete can not completely block the transport of chlorides. Scientists investigated the transport of chloride by different mechanisms in concrete cover, including diffusion, capillary suction, permeation, and migration (Bertolini, 2008; Bertolini, Elsener, Pedeferri, & Polder, 2004). By considering those mechanisms, the accumulated chloride concentration at the reinforcement location can be assessed, and used to estimate the service life of an RC structure. Although, the transport of chloride ions shows promising results in inferring estimates about the service life of RC through the use of empirical corrosion rates, this remains an indirect method with a lot of limitations, even for cases where only corrosion is present. The limitations are far more sever when used for evaluating CF life in RC.

Another class of studies that can be found in the published literature considers the CF phenomenon from the material degradation standpoint (Y. Liu & Weyers, 1998; Suwito & Xi, 2008). In this type of study, the main issues addressed included corrosion-induced crack failure in the concrete matrix, structural evaluation under fatigue loading, and pitting-corrosion-fatigue of steel bar.

The service life of reinforced concrete structures with chlorides present can be divided into three stages: chloride diffusion through concrete cover, corrosion and rust accumulation on the reinforcing steel surface, and the initiation of cracks in concrete and their propagation. Depending on the corrosion products volume expansion in RC, Suwito et al (Suwito & Xi, 2008) and Liu et al (Y. Liu & Weyers, 1998) proposed time-to-corrosion-cracking models to generate the critical amount of corrosion products to fill the space around reinforcement, and produce the required pressure to overcome the tensile strength of concrete and generate cracks in the concrete cover. The time needed to cracking is computed by the models and the service life of RC is obtained.

Oh et al. (Oh, Asce, Lew, & Choi, 2007) evaluated the CF of a bridge deck slab by the stress-life (S-N curve) relationship. Modeling the rebar cross section loss at a specified corrosion rate, the

authors combined the cross section loss with the S-N curves of a slab. The total required time was computed as the total service life an RC structure can withstand. Despite the fact that this approach did somewhat reflect the RC structure performance in the field, the synergetic effect of corrosion and fatigue was neglected.

Regarding the published studies on the pitting-induced-corrosion-fatigue crack growth of reinforcement, the process from pitting initiation to structural failure was usually divided into several stages: pit nucleation, pit-to-crack transition, small crack growth, large crack growth, unstable crack growth and structural failure. This model studied CF from a fracture mechanics point of view and was widely used in the CF life prediction of many metals, e.g. stainless steel, aluminum alloys, titanium alloys (G. S. Chen, Wan, Gao, Wei, & Flournoy, 1996; Dolley, E.J.; Lee, B.; Wei, 2000; Hoeppner, 1979, 2011; Medved, Breton, & Irving, 2004; Weng et al., 2013). Bastidas-Arteaga et al. (Bastidas-Arteaga, Sánchez-Silva, Chateauneuf, & Silva, 2008) tried the pitting-corrosion-fatigue (PCF) model for estimating the CF life of reinforcement. However, no corrosion effect was shown in the fatigue crack growth of reinforcing steel. Scott (Scott, 1983) performed fracture analyses under fatigue of structural steels in seawater. Instead of evaluating CF, the study mainly focused on the fracture behavior under various environments, i.e. stress ratios (R ratios), wet-dry cycles, and cathodic protection. The effect of corrosion was implicitly present but buried within the observed fracture behavior.

2.2.2 Corrosion assessment

In the study of rebar corrosion in concrete, researchers usually defined concrete spalling as the end of the functional service life in an RC structure (Ferro, Carpinteri, & Ventura, 2007; Yu et al., 2015). The total service life of an RC structure could be divided into three parts from the corrosion point of view: the diffusion period of chemicals, the time from corrosion initiation to crack initiation, and the period from the crack initiation to the critical crack causing spalling and delamination of concrete cover. A schematic of these three stages can be seen in Figure 2.10.

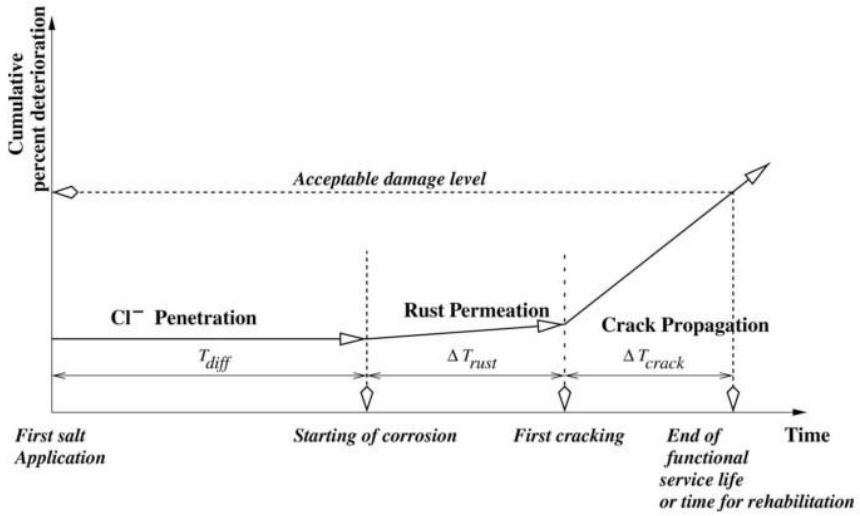

Figure 2.10. A three-stage lifespan of RC structures (Suwito & Xi, 2008).

Depending on the exposure conditions, the transport of chloride in concrete could be governed by many mechanisms, including, diffusion, capillary suction, permeation, and migration. Each mechanism has its individual governing equations. A concentration gradient causes diffusion and it might be affected by the status of the solution. Under non-stationary 1D transport conditions a unidirectional flux caused by diffusion can be described using Fick's second law shown in Eq. (2.13).

$$\frac{\partial C(x,t)}{\partial t} = D\frac{\partial^2 C(x,t)}{\partial x^2} \tag{2.13}$$

where C(x,t) is the chloride concentration (in mol/m^3) at time t (in s) and depth x (in m); and D is the diffusion coefficient (in m^2/s).

For capillary suction, the mass of liquid absorbed in a unit surface is assumed to be proportional to the square root of time. A pressure difference in solution can produce permeation and this behavior is characterized by Darcy's law presented in Eq.(2.14) (Luca Bertolini, 2008).

$$\frac{dq}{dt} = \frac{kHA}{L} \tag{2.14}$$

where $\frac{dq}{dt}$ is the flow rate (in m^3s^{-1}), H (in m) is the pressure head across the specimen, k is the coefficient of permeability (in $m \cdot s^{-1}$), A is the cross-section area (in m^2) and L is the thickness (in m).

Provided that there is an electric field, migration of chlorides also occurs because the charged ions are driven by the electrical field. Because of the electrical field, the charged ions would migrate through the porous concrete medium by the electrical force. However, unless a specific electric field is applied, the migration of chlorides in concrete is usually ignored because of the absence of such an electric field.

In the field, RC structures usually suffer from the penetration of chlorides by dual or multiple mechanisms mentioned above. For the purpose of approximation, some scientists (Hartt, 2012; Suwito & Xi, 2008) used the diffusion model – the main transport mechanism of chloride – to represent the penetration of chlorides into concrete.

Many research findings (Alonso, Castellote, & Andrade, 2002; Jiang, Huang, Xu, Zhu, & Mo, 2012; Maslehuddin, Al-Zahrani, Ibrahim, Al-Mehthel, & Al-Idi, 2007) indicated that a threshold chloride concentration existed in order to produce chloride-induced-pitting. Upon reaching the threshold concentration, chloride-induced corrosion occurs. Depending on the curing conditions and the mix proportions, concrete shrinks somewhat during the hardening period; hence, creating a porous zone between the concrete matrix and rebar. Because of the volume expansion of corrosion products in comparison with the reactants in the corrosion reactions, they would firstly fill up this porous zone, then generate pressure on the surrounding concrete, and finally cause cracks in the concrete cover.

The time-to-cracking from the initial corrosion in rebar to spalling or delamination of the concrete cover are studied by examining the volume expansion of corrosion products and the resultant pressure on the concrete cover (Y. Liu & Weyers, 1998; Suwito & Xi, 2008). The composition of the corrosion products are firstly analyzed and their volume ratios are examined. The total amount of corrosion products in the three corrosion stages – free expansion around the steel/concrete interface, stress in the concrete cover, cracking in the concrete cover – is estimated by the

quantitative approximation of the total volume of the interconnected pores around the steel/concrete interface and the amount of corrosion products needed to overcome the concrete and generate cracks. The critical amount of rust can be evaluated by Eq. (2.15) and the growth of corrosion products can be approximated by Eq. (2.16) (Y. Liu & Weyers, 1998). Therefore, the amount of time required to produce the critical cracking of concrete can be estimated.

$$W_{crit} = \rho_{rust}\left(\pi\left[\frac{C_c f_t'}{E_{ef}}\left(\frac{a^2+b^2}{b^2-a^2}+v_c\right)+d_0\right]D+\frac{W_{st}}{\rho_{st}}\right) \quad (2.15)$$

where W_{crit} is the critical amount of rust (in kg/m), ρ_{rust} is the rust density (in kg/m^3), C_c is the concrete cover depth (in m), f_t' is the tensile strength of the concrete (in MPa), E_{ef} is the effective elastic modulus of the concrete (in MPa), a and b are the two radii of the assumed thick-wall concrete cylinder around the rebar (in m), v_c is Poisson's ratio of the concrete, d_0 is the thickness of the porous zone around the steel/concrete interface (in m), D is the diameter of steel reinforcement (in m), W_{st} is the amount of corroded steel (in kg/m), ρ_{st} is the density of steel (in kg/m^3). The rate at which the rust increases is given by:

$$\frac{dW_{rust}}{dt} = \frac{k_p}{W_{rust}} \quad (2.16)$$

where W_{rust} is the amount of rust (in kg/m), t is the corrosion time (in years), k_p is the rate of rust production (in kg/(m^2 year)).

2.2.3 Deterioration of reinforcement performance

The corrosion-fatigue study of reinforcement usually focuses on the fracture mechanics point of view. In this approach, the service life of rebar is evaluated from the initial corrosion until fracture failure.

Bastidas-Arteaga et al (Bastidas-Arteaga, Bressolette, Chateauneuf, & Sánchez-Silva, 2009) and Zhang et al (Zhang & Mahadevan, 2001) proposed a pitting corrosion fatigue (PCF) model to predict the service life of an RC structure that suffers both chloride-induced corrosion and fatigue

damage. The PCF model consists of three stages: corrosion initiation and pitting nucleation, pit-to-crack transition, and crack growth.

To simplify the corrosion initiation process, Fick's second law is used to estimate the transport of chloride in concrete. At any depth x, from the concrete surface, the instantaneous chloride concentration C(x,t) (in kg/m^3) could be expressed as a function of the parameters: depth in concrete x, exposure time t, chloride concentration on the concrete surface C_s, and the chloride diffusion coefficient in concrete D_{cl}, as seen in Eq. (2.17) (Zhang & Mahadevan, 2001).

$$C(x,t) = C_s\left[1 - erf\left(\frac{x}{2\sqrt{D_{cl}t}}\right)\right] \tag{2.17}$$

where C_s is the chloride concentration on the concrete surface (in kg/m^3), erf() is the error function, D_{cl} is the chloride diffusion coefficient in concrete (in m^2/s), x is the depth in the chloride path (in m), t is the diffusion time (in years).

The pit is assumed to volumetrically grow according to the uniform corrosion current density. Hence, the growth rate of a pit in volume can be estimated by the Faraday's law, as presented in Eq. (2.18) (Harlow & Wei, 1998; Kondo, 1989):

$$\frac{dV}{dt} = \frac{Mi_{corr}}{nF\rho} \tag{2.18}$$

where M is the molecular mass of iron (in kg/mol), i_{corr} is the corrosion current density (in A/m^2), n is the valence of iron, F is Faraday's constant (in C/mol), and ρ is the density of iron (kg/m^3).

Even though fatigue crack propagation in Region I and III of the crack growth curve depends on the microstructure and the properties of the material, fatigue crack propagation is not governed by the Paris law, which is found to govern the crack propagation in Region II. The entire crack growth is assumed to be governed by the Paris law presented in Eq. (2.19):

$$\frac{da}{dN} = C_p(\Delta K)^m \tag{2.19}$$

where a is the crack length (in mm), N is the number of cycles, ΔK is the stress intensity factor range (in MPa√m), and C_p and m are material constants.

The stress intensity factor of crack propagation in rebar is computed by Eq. (2.20) (Bastidas-Arteaga et al., 2009):

$$\Delta K = \Delta\sigma\, Y\left(\frac{a}{d_0}\right)\sqrt{\pi a} \tag{2.20}$$

where Δσ is the stress range (in MPa), a is the crack length (in mm), d_0 is the original diameter of the rebar (in mm), and $Y(a/d_0)$ is a dimensionless geometry function.

The pit-to-crack transition is calculated by equating the pit growth rate with the equivalent crack growth rate in which the pit depth substitutes the crack length in Eq. (2.20). Therefore, the time required to develop the critical pit and the beginning of a crack can be obtained. As a crack in rebar grows, the rupture point of a rebar is calculated by the remaining cross section of rebar that will yield to the applied load. Following the Paris law in Eq. (2.19), the cycles of a growing crack until fracture failure can be computed, and the service time during crack propagation can be obtained by the division of the calculated cycles and the loading frequency.

A cumulative distribution function (CDF) of the total corrosion-fatigue life is used by many researchers (Bastidas-Arteaga et al., 2009)(Zhang & Mahadevan, 2001). Integrating the mechanical model of pitting corrosion fatigue into a probabilistic framework, the probability function is presented in Eq. (2.21) (Zhang & Mahadevan, 2001):

$$F_T(t) = Pr\{T \le t\} = \int_{t_p + t_c \le t} f(x)dx \tag{2.21}$$

where $F_T(t)$ is the cumulated probability, x is the vector of the involved random variables and f(x) is the joint probability density function of x, t_p is the pit growth period (in years), t_c is the crack propagation period (in years).

With the help of the limit-state-based reliability method, the failure probability of a structure can be estimated on the condition that the critical crack size is defined.

3 Methodology and experimental design

The methods used to characterize corrosion-fatigue, and describes the corresponding experimental design are discussed in this chapter. Prior to introducing the characterization approaches, a fast corrosion acceleration method is firstly reviewed and two corrosion-fatigue (CF) characterization methods – stress-life (S-N) relationship and Fracture Mechanics – are then demonstrated. Finally, CF studies in reinforced concrete (RC) beams are introduced in order to confirm the validity in the evaluation of CF by the stress-life (S-N) relations and the Fracture Mechanics model.

3.1 Electrochemical corrosion acceleration

Due to the fact that CF in RC structures is a long lasting process (decades, or even enduring the entire lifespan), both corrosion and fatigue have to be accelerated. Regarding fatigue, increasing the loading frequency is the optimal option. The generally used cyclic loading machines usually tolerate a frequency up to several Hz, which allows millions of cycles to be completed in a few days, hence fast enough for fatigue testing. Corrosion acceleration, on the other hand, is more difficult to achieve at the same rate as the fatigue acceleration.

Electrochemical acceleration takes the advantage of the electrochemical corrosion in metals. In metal corrosion, the process is usually governed by an electrochemical mechanism. Metal in corrosion serves as both anode and cathode depending on the different locations on metal surface, and a humid or liquid environment surrounding the metal acts as an electrolyte. A potential difference is then generated between the two electrodes because of the electrochemical mechanism. In the electrochemical corrosion in this project, a potential is applied between the rebar – the anode – and an externally added cathode. Simulated concrete pore solution or actual concrete serves as the electrolyte. Hence, rebar corrodes actively with an adjustable corrosion rate depending on the potential applied.

There are two ways to manage the electrochemical corrosion: Potentiostatic, which controls a constantly applied potential, and Galvanostatic, which controls a constantly applied current. In this project, a comparison between these two approaches was firstly performed and the approved with superior performance was implemented in the corrosion acceleration of CF in the S-N relations,

the fracture mechanics approach, and the validation of RC beams. The corresponding reinforcing steel mass loss at a corrosion current density can be computed by Eq. (3.1) (T. A. El Maaddawy & Soudki, 2003):

$$\Delta m = \frac{M i_{corr} A t}{zF} \tag{3.1}$$

where Δm is the mass loss of corroded steel (in g); M is the molar mass of steel (in g/mol); i_{corr} is the corrosion current density (in A/cm^2); A is the corrosion area (in cm^2); t is corrosion time (in seconds); z is the ionic charge, 2 for Fe; F is Faraday's constant, 96,500 $A \cdot S/mol$.

3.2 Stress-life (S-N) relationship

The stress-life diagrams (S-N curves), also known as Wöhler's diagram, depict the relationship between the applied stress amplitudes or the stress ranges and the number of fatigue cycles to failure in a log-log scale. Two types of S-N curves are seen in Figure 3.1. This figure shows that ferrous alloys and titanium have a stress amplitude below which a specimen exhibits infinite fatigue life; hence, this stress amplitude is defined as the fatigue limit of a metal. For nonferrous alloys, on the other hand, the fatigue limit has to be defined at a number of cycles (e.g. 10^8 cycles) since these alloys only have fatigue strength rather than fatigue limit as ferrous alloys. Between 10^3 cycles and the cycles at the fatigue limit of ferrous metals and titanium, a linearly logarithmic S-N relationship often exists with the fitted equation indicated by Eq. (3.2). Given the S-N curve and a stress amplitude, the fatigue life corresponding to that stress amplitude can easily be calculated from the linear regression of the curve:

$$\frac{logS - logS_0}{logN - logN_0} = \frac{logS_1 - logS_0}{logN_1 - logN_0} \tag{3.2}$$

where N_0 is 1000 cycles, S_0 is the applied stress at N_0 (in MPa), S_1 is the fatigue limit (in MPa), N_1 is the cycles at S_1.

The laboratory test for S-N curves is usually produced by the rotating bending test with a completely reversed loading at a mean stress of zero. However, in most field loading environments,

the mean stress is usually non-zero; therefore, the mean stress effect has to be corrected. Generally, there are three empirical equations proposed to correct the mean stress effect in S-N curves: the Goodman relation, the Gerber relation, and the Soderberg relation. The equations of these relations are seen from Eq. (3.3) to Eq. (3.5), respectively, (Hertzberg, 2012; Milella, 2013) and a schematic of these three relations is presented in Figure 3.2.

$$\text{Goodman relation: } \sigma_a = \sigma_{fat}\left(1 - \frac{\sigma_m}{\sigma_{ts}}\right) \tag{3.3}$$

$$\text{Gerber relation: } \sigma_a = \sigma_{fat}\left(1 - \left(\frac{\sigma_m}{\sigma_{ts}}\right)^2\right) \tag{3.4}$$

$$\text{Soderberg relation: } \sigma_a = \sigma_{fat}\left(1 - \frac{\sigma_m}{\sigma_{ys}}\right) \tag{3.5}$$

where σ_a is fatigue strength in terms of stress amplitude (in MPa), where $\sigma_m \neq 0$; σ_m is mean stress (in MPa); σ_{fat} is fatigue strength in terms of stress amplitude (in MPa), where σ_m = 0; σ_{ts} = ultimate tensile strength (in MPa); σ_{ys} is yield strength (in MPa).

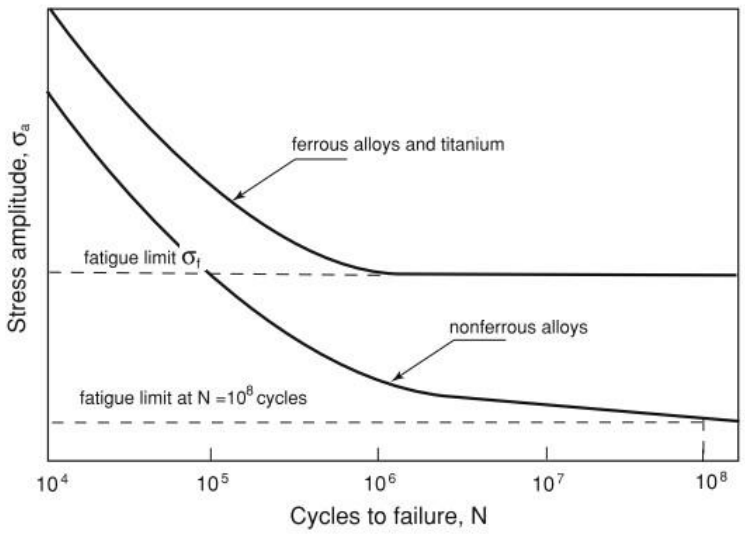

Figure 3.1. Two types of S-N curves (Milella, 2013).

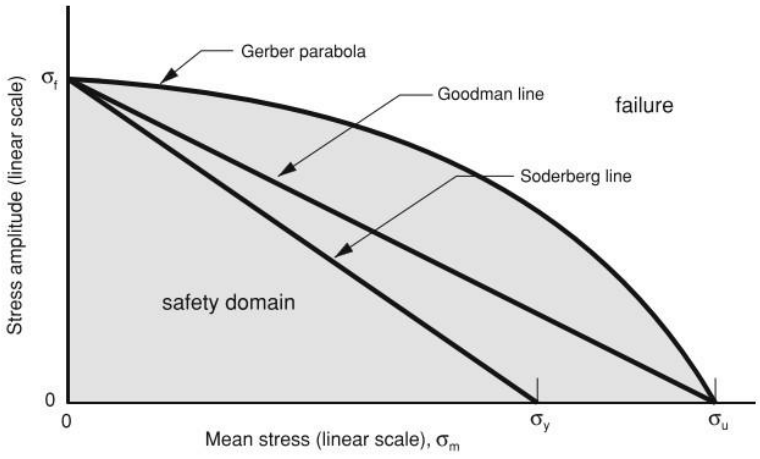

Figure 3.2. Goodman, Gerber, and Soderberg diagrams illustrating the relationships between fatigue limit and mean stress (Schijve, 2009).

The empirical data demonstrate that the testing results usually fall between the Goodman line and the Gerber parabola. Accounting for the mean stress effect, the Goodman line is a more conservative criterion in comparison with the Gerber parabola; the Soderberg line, on the other hand, is the most conservative among the three.

Besides the mean stress effect, there are many other factors influencing the fatigue limit or fatigue strength of an S-N curve, i.e. the notch effect, sample size effect, surface finish, surface treatment, temperature, loading type, etc. Eq. (3.6) (Schijve, 2009) accounts for these effects in the fatigue endurance calculation by adding modifying factors for each effect:

$$S_e = S'_e C_{notch} C_{size} C_{load} C_{surface\ finish} C_{surface\ treatment} C_{temperature} \qquad (3.6)$$

where S_e = the actual fatigue limit for a real component (in MPa)

S'_e = the fatigue limit measured by the standard rotating bending test (in MPa)

$C_{notch}, C_{size}, C_{load}, C_{surface\ finish}, C_{surface\ treatment} C_{temperature}$ = the effects of notch, component size, loading type, surface finish, surface treatment, and temperature, respectively.

However, the drawback of the correction of the endurance limit in Eq. (3.6) is that it only applies to the modification of the fatigue limit, not to all fatigue strengths in an S-N curve. Since this study focuses on the fatigue life prediction at a specific fatigue load, the application of Eq. (3.6) in estimating CF of a structure is limited.

In a corrosive environment, the S-N curves usually shift to the left of those generated in a non-corrosion environment, indicating that fewer fatigue cycles are required to cause the failure of a specimen. Moreover, the fatigue limit disappears because of the corrosion damage accumulated on the specimen surface with time, thus a fatigue strength replaces the fatigue limit at a tested stress amplitude. Even though little research has been conducted on corrosion effects on S-N curves, corrections are required in considering the corrosion effect, as well as other factors such as temperature, notches, loading type, surface treatment, etc.

In a chloride environment, the fatigue failure of a specimen usually derives from chloride-induced pits. A specimen with smooth surface possesses a longer fatigue life than one with a notch. Thus, this study proposes that the presence of pits are considered as notches on specimen surfaces. The notch effect is modified by the fatigue notch factor, which is then added to correct the resultant fatigue strength in S-N curves. The formula used to calculate the notch factor is seen in Eq. (3.7) (Stephens, Fatemi, Stephens, & Fuchs, 2000):

$$K_f = 1 + \frac{K_t - 1}{1 + a/r_n} \tag{3.7}$$

where K_f is the fatigue notch factor (in MPa√m), K_t is the elastic stress concentration factor (in MPa√m) which can be cited from a literature review or obtained from experimental measurement, a is another material characteristic length (in mm), r_n is the radius of the notch root (in mm). An empirical equation relating the ultimate tensile strength S_u and a for steels is given as:

$$a = 0.0254\ (\frac{2070}{S_u})^{1.8} \text{ with } S_u \text{ in MPa and } a \text{ in mm} \quad (3.8)$$

In Eq. (3.7), K_t, which is the elastic stress concentration factor (in MPa$\sqrt{m}$) of the material, could be obtained either by conducting an experiment or by citing from literature. The radius of the notch root r_n in Eq. (3.7) could be calculated by the stress intensity factor equation (K~a formula) according to the geometry of a specimen. Therefore, the fatigue notch factor could be calculated based on the known material properties and the specimen geometry.

Taking into account the notch effect, the Goodman and Gerber relations can then be rewritten as (Stephens et al., 2000):

$$\text{Goodman relation: } \sigma_a = \frac{\sigma_{fat}}{K_f}\left(1 - \frac{\sigma_m}{\sigma_{ts}}\right) \quad (3.9)$$

$$\text{Gerber relation: } \sigma_a = \frac{\sigma_{fat}}{K_f}\left(1 - \left(\frac{\sigma_m}{\sigma_{ts}}\right)^2\right) \quad (3.10)$$

where σ_a is fatigue strength in terms of stress amplitude (in MPa), with $\sigma_m \neq 0$; K_f is the fatigue notch factor; σ_m is mean stress (in MPa); σ_{fat} is fatigue strength in terms of stress amplitude (in MPa), with $\sigma_m = 0$; σ_{ts} = ultimate tensile strength (in MPa); and σ_{ys} is yield strength (in MPa).

Therefore, transforming both the mean stress and notch effect, the fatigue life at a tested stress amplitude can be estimated by the Goodman and the Gerber relations.

3.3 Fracture Mechanics

From the Fracture Mechanics point of view, the fatigue life of a metal structure (shown in Figure 3.3) consists of four stages: crack formation or nucleation; micro-structurally dominated crack propagation; crack propagation governed by Linear Elastic Fracture Mechanics (LEFM), Elastic Plastic Fracture Mechanics (EPFM), or Fully Plastic Fracture Mechanics (FPFM); and final instability of crack propagation. In a chloride environment, cracks are repeatedly reported to initiate from chloride-induced pits (Huang & Xu, 2013; Kondo, 1989; Rokhlin, Kim, Nagy, &

Zoofan, 1999). As a result, the four stages of fracture mechanics are divided into seven phases in the presence of chlorides: pit nucleation, pit growth, pit-to-crack transition, short crack growth, short crack to long crack transition, long crack growth, and fracture failure. Currently available studies are unable to model each stage with models. Hence, in this study, a four-stage model is used: pit nucleation and growth, pit-to-crack transition, crack growth, and fracture failure.

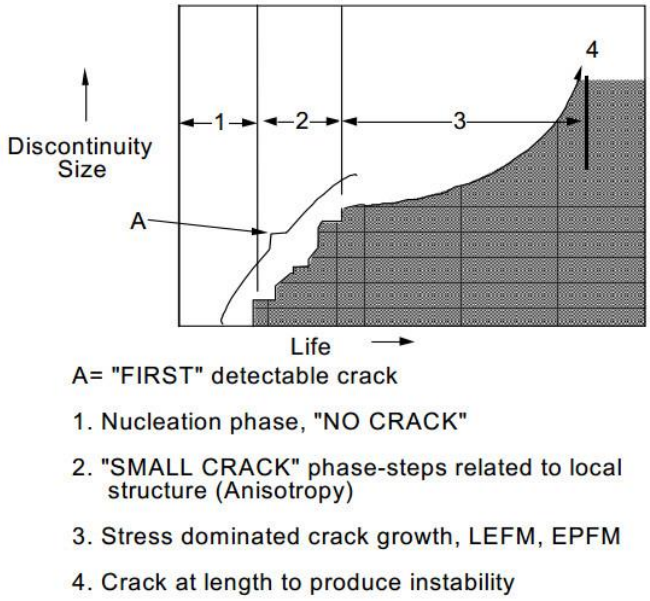

Figure 3.3. A depiction of the degradation process of a material (Hoeppner, 1979).

A typical logarithmic relationship of the crack growth rate against the stress intensity factor range is shown in Figure 2.6, and the fatigue life of a specimen is computed by the four-stage model mentioned above. Prior to the threshold of stress intensity factor range ΔK_{th}, the fatigue life is considered as pit nucleation and growth, and pits transit to cracks at ΔK_{th}. In other words, the crack length a is the same as the pit depth at ΔK_{th}; thus, the maximum pit depth can be calculated by the ΔK~a relation in fracture mechanics. In the pit-to-crack transition, the pit growth rate may be higher than the initial crack propagation rate at ΔK_{th}. In this case, the pit would keep growing until its propagation agrees with the calculated crack propagation rate. Therefore, two rules govern the pit-to-crack transition, the stress intensity factor range threshold ΔK_{th} and a higher crack growth rate at any ΔK than the correspondent pit growth rate. The number of fatigue cycles in pit growth until pit-to-crack transition is calculated according to the pit growth from the initiation of a pit

until ΔK_{th} or a ΔK, at which the crack growth rate equals pit growth rate. The growth of pit depth is documented as a function of time as shown in Eq (3.11) (R E Melchers, 2006; Robert E. Melchers, 2012):

$$d = \begin{cases} A(t - t_0)^B, & t \geq t_0 \\ 0, & t < t_0 \end{cases} \tag{3.11}$$

where d is the pit depth (in mm), t_0 is the pit nucleation time (in hours), t is the pitting time (in hours), A and B are the constants associated with the material and the corrosive environment.

Given the pit depth growth function, the critical pit size, and the loading frequency, the number of cycles in pit nucleation and propagation can be estimated by dividing the frequency by the time to nucleate the critical pit.

In the crack propagation stage, the initiated crack grows from the threshold of the stress intensity factor range ΔK_{th} until the fracture toughness K_{Ic}. In order to estimate the fatigue life between ΔK_{th} and K_{Ic}, the crack growth rate da/dN against ΔK is required. The crack length a from ΔK_{th} to K_{Ic} can be calculated by the ΔK~a relation. The total number of fatigue cycles from pitting nucleation to fracture failure is the sum of the cycles to produce the critical pit and the cycles allowing a crack growth from its formation until the final fracture failure.

Many equations are proposed for the ΔK~a relationships, depending on the geometry of the metal and the shape of cracks. Eq. (3.12) and Eq. (3.13) (Milella, 2013) account for two circumstances: the general plate metal with a small flat crack in the center of a specimen and the cylindrical metal accompanied with a semi-elliptical crack on sample edge. Although rebar has ribs, this study assumes the geometry of rebar is round, hence, Eq. (3.13) is used to calculate the ΔK~a relation:

$$K_I = 1.1\ \sigma \sqrt{\pi(\frac{a}{Q})} \tag{3.12}$$

$$K_I = \sigma\sqrt{\pi S}\, f(\frac{a}{c}) \tag{3.13}$$

$$S = r \cdot arcsin(\frac{c}{r}) \tag{3.14}$$

$$f\left(\frac{a}{c}\right) = 0.7433(\frac{a}{r})^2 - 0.2194\left(\frac{a}{r}\right) + 0.6757 \tag{3.15}$$

where K_I is the stress intensity factor of mode I cracks (in MPa√m), σ is the applied stress (in MPa), a is the critical pit depth or crack length (in m), Q is the function of material and shape, and 2S is the length of the arc (in m) corresponding to the two axis 2c and r (in m) of the surface crack in the specimen. A schematic of the growth of semi-elliptical crack in the cylindrical sample is seen in Figure 3.4.

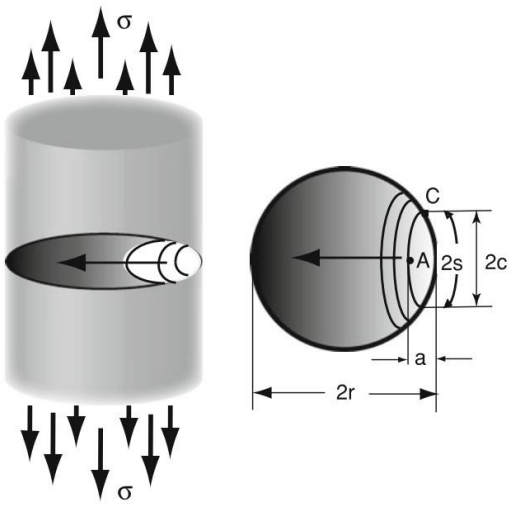

Figure 3.4. Semi-elliptical crack growth in round specimen (Milella, 2013).

The required parameters and the procedures to properly estimate fatigue life in pitting corrosion fatigue are:

- The critical pit size (the initial crack size) assessment: The threshold of stress intensity factor range ΔK_{th} must be measured. The critical pit size can be examined by three approaches. Firstly, the critical pit depth is calculated by the ΔK~a equations, e.g. Eq. (3.12)

and Eq. (3.13). Moreover, the critical size is also able to be determined by experiments in the laboratory. By applying a series of stress patterns to pitted specimens, the critical pits that transform to a crack can be identified and their sizes can be measured. The final approach is to cite from literature where fracture analysis has been conducted and the initial crack size identified. In this study, Eq. (3.13) is used to estimate the critical pit size.

- The critical crack size for instability examination: The critical crack size at the fracture toughness can be calculated by the ΔK~a relations with an experimentally measured fracture toughness K_{Ic}. Another approach performs failure analysis of the failure surfaces, on which the critical crack size is obtained of the same size rebar as long as the final fracture failure could be identified on the corroded fracture surface. In this study, due to the fact that intense corrosion products are produced on fracture surface during CF, the unstable crack size is calculated by Eq. (3.13) with a measured K_{Ic}.
- Crack growth rate (da/dN) vs stress intensity factor range ΔK curves: This study examines the (da/dN) ~ ΔK relations at different corrosion degrees in the laboratory. Based on the ΔK~a equation and the range of crack length (from ~ ΔK_{th} to K_{Ic}), the number of cycles that causes a crack from its initiation until failure is integrated in a reverse manner using the (da/dN) ~ ΔK curves. This study implements experimental tests to produce the da/dN ~ ΔK curves from the non-corrosive exposure to the significantly aggressive corrosive.
- Pit-depth vs. time equation: Parameters in the pit growth equation are either obtained from literature or examined through experiments in the laboratory. The number of service cycles from pit nucleation to the critical pit resulting in the 'first' crack is estimated by the division between the time required to produce the critical pit size and the loading frequency. This study examines the pit-depth vs. time curves by measuring the development of pit depth with time at various corrosives.
- Depending on the pit growth rate at the critical pit size and the crack growth rate at the ΔK_{th}, the cycles in the pit nucleation and propagation stage is evaluated by the pit size at ΔK_{th} or the above mentioned equivalent ΔK.
- The total number of cycles is the sum of cycles calculated in pit growth and crack propagation.

3.4 Experimental setup

3.4.1 Materials and corrosive environment

The material studied in this project is general-use 400R structural rebar, the chemical composition of which is listed in Table 3.1, as cited from the mill certificate of the manufacturer. The yield strength and the ultimate tensile strength of the used steel rebar were determined according to ASTM E8 standard and their values were 440 MPa and 666 MPa, respectively.

Table 3.1. Rebar chemical composition

Composition	Percentile (%)	Composition	Percentile (%)
C	0.38	Ni	0.10
Mn	0.95	Cr	0.16
P	0.015	Mo	0.020
S	0.051	V	0.100
Si	0.22	Cb	0.003
Cu	0.32	CEA706*	0.57

*CEA706: A706 CARBON EQUIVALENT

Except for the CF test in RC, other tests involving corrosion were carried out in chloride concentration(s) mixed in a base solution, defined as a simulated pore solution (SPS) environment. The pore solution in concrete has a high pH value – usually above 13 – which protects reinforcement. The pore solution has a complicated composition and many scientists have proposed combinations of chemicals to simulate concrete pore solutions (Ghods, Isgor, McRae, & Miller, 2009; Moreno, Morris, Alvarez, & Duffó, 2004; Poursaee, 2010; Schmidt & Rostasy, 1993; Vonezawa et al., 1988). This study simulated concrete pore solution by mixing 1 g/L $Ca(OH)_2$, 8 g/L Na(OH), and 22.44 g/L K(OH) as proposed by Ghods (Ghods et al., 2009). The pH was found to be 13.60 after 7 days of mixing.

3.4.2 Corrosion acceleration

The specimen used for the corrosion acceleration test was a disk-shaped cross-section, with a thickness around 2 mm cut from of a Φ15 mm rebar. The disk specimens were polished on one side in the following order of sandpapers: 80 grit, 150 grit, 240 grit, 360 grit, and 600 grit. Then the disks were covered with Gamry sample masks and 1 cm^2 of the polished surfaces was exposed to both pure chloride corrosion and electrochemical corrosion. Figure 3.5 gives a photo of a polished disk, which is covered with a sample mask and ready for test.

Figure 3.5. A photo of a polished specimen covered with sample mask.

The corrosion rate of pure chloride corrosion acceleration was measured by both linear polarization resistance (LPR) and Potentiodynamic (Tafel) scan to ensure the accuracy of the measurement. Electrochemical corrosion was divided into a Potentiostatic scan and a Galvanostatic scan, the mass losses of which were weighted to compare with the estimated mass losses by the Faraday's law.

3.4.2.1 Pure chloride corrosion acceleration

Linear Polarization Resistance (LPR)

In order to stabilize the corrosion potential of specimen in the tested solution environment, a specimen was exposed to the corrosive solution for an hour prior to a LPR test. The test parameters were:

- Initial E: defines the potential prior to any potential step. The value was set at – 0.02 V vs the open circuit potential E_{OC}.
- Final E: This defines the ending potential after the potential step. The Final E value was set at + 0.02 V vs E_{OC}.
- Scan Rate: This defines the speed of the potential sweep during data acquisition. The scan rate was 0.125 mV/sec.
- Sample period: This defines the spacing between data points. The sample period was 1 second.
- Beta Anodic / Beta Cathodic: These are the Tafel constants and depend on many parameters such as electrode material and solution.
- Initial delay: This defines the starting time of a test in order to keep a relatively steady varying rate of the corrosion potential. The initial delay was set at 300 seconds unless the varying rate of the open circuit potential was less than 0.1 mV/sec.

Potentiodynamic (Tafel) scan

The Potentiodynamic scan was performed after an hour of exposure to the designed corrosive environments. The parameters in the Tafel scan were:

- Initial E: This defines the potential prior to any potential step. The Initial E was set at – 0.15 V vs E_{OC}.
- Final E: This defines the ending potential after the potential step. The value was set at + 0.20 V vs E_{OC}.
- Scan Rate: This defines the speed of the potential sweep during data acquisition. The scan rate was set at 0.167 mV/sec.
- The sample period: This defines the spacing between data points. The value was set at 1 second.
- Initial delay: This defines the starting time of a test in order to keep a relatively steady varying rate of the corrosion potential. The Initial delay value was 600 seconds unless the varying rate of the open circuit potential was less than 0.1 mV/sec.

3.4.2.2 Potentiostatic scan

The Potentiostatic scan utilized the disk-shape specimens as the working electrode, a graphite rod as the counter electrode, and a saturated calomel electrode (SCE) as the reference electrode. The electrolyte used in the test was the simulated pore solution mixed with 0.6 M NaCl. A Gamry Interface 1000 applied a constant potential between the working electrode and the counter electrode, and the machine recorded the corresponding current vs time data for 600 seconds. The applied potential (vs SCE) levels were selected at 0.1 V, 0.3 V, 0.5 V, and 0.7 V. Prior to testing, a 300 seconds initial delay was implemented after the setup of a test (see Figure 3.6) in order to obtain a steady open circuit potential (OCP).

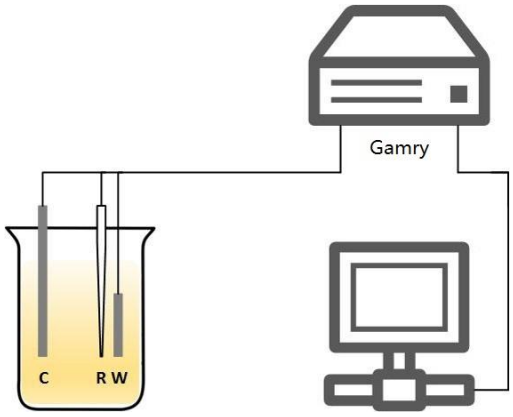

Figure 3.6. A schematic of the testing setup of both Potatiostatic and Galvanostatic scans. C, R, W in the beaker represent the counter, reference, and working electrodes, respectively.

3.4.2.3 Galvanostatic scan

Sharing the same specimen preparation and test setup as the Potentiostatic scan, the Galvanostatic scan differed in applying a constant current between the anode and cathode and in recording the instantaneous potential over time. In this study, the testing conditions (e.g. the applied current, chloride concentration, and the applied duration) are listed in Table 3.2. ASTM G1 (ASTM, 2011) standard describes the procedures to remove the corrosion products from the sample surface when a test is done. The mass differences of the specimens (listed in Table 3.2) before and after the Galvanostatic scan were measured and compared to the calculated values.

Table 3.2. Galvanostatic scan test parameters

Sample No.	Applied current /mA	[Cl] in simulated pore solution /M	Duration /min
0.1 M1mA30 Min	1	0.1	30
0.6 M1mA60 Min	1	0.6	60
0.6 M10 MA60 Min	10	0.6	60
1.5 M10 MA60 Min	10	1.5	60

3.4.2.4 Corrosion acceleration in pure solution environment

Prior to any CF test (e.g. CF examination of rebar in SPS and of RC beams), the verification of electrochemical acceleration was performed and a schematic of the testing setup is presented in Figure 3.7. In a pure solution environment, the disk-shaped specimens, whose exposed area was controlled at 1 cm^2, were connected to the positive pole of an output-current controllable GW Instek DPD 4303S DC power supply, while the negative pole was connected to a graphite rod. Simulated pore solution plus chlorides (0.6 M or 1.5 M NaCl) acted as the electrolytes in the test. Currents of 10 mA or 20 mA were applied individually in the electric circuit for 30 minutes each time, for a total of 60 minutes. Mass differences before and after the test of all specimens were measured by the same procedures as those in Potentiostatic and Galvanostatic scans. The actual mass loss of the specimens was plotted and compared to the theoretical mass loss.

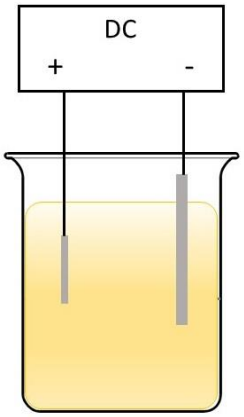

Figure 3.7. A schematic of corrosion acceleration in a pure solution environment.

3.4.2.5 Corrosion acceleration in RC

Due to the concrete cover, electrochemical corrosion in RC was performed slightly different than the previous corrosion acceleration examinations. The presence of porous concrete prohibits chlorides contacting rebar at the moment that a potential was being applied between the rebar in concrete and the counter electrode. Even though concrete is a porous media and some pores are connected through the concrete cover, it requires time to transport chloride from the concrete surface to the embedded rebar.

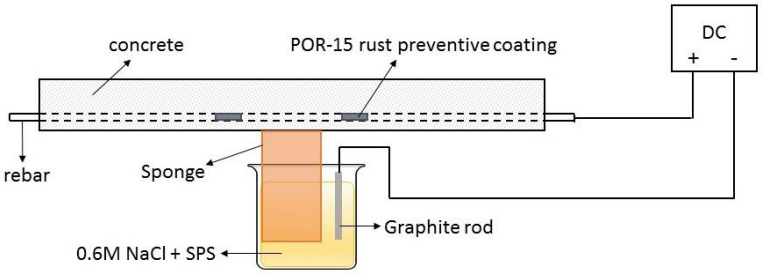

Figure 3.8. A schematic of RC corrosion acceleration

When a potential is applied, the electric field drives chlorides from the concrete cover surface to the rebar, hence chloride transport is not governed by diffusion, which takes months, even years, to travel through the concrete cover. Because of the complex porous structure in concrete, a period of time is required for the migration process at an applied potential. Aguayo et al (Aguayo, Yang, Vance, Sant, & Neithalath, 2014) studied the transport behavior of electrically driven chlorides in concrete. Their results showed that chlorides migrated a depth of 20 mm after 24 hours of applying a potential of 60V. In the RC beams with a concrete cover thickness of 20 mm in this study, the potential was applied 24 hours prior to counting the actual corrosion time of rebar.

Another issue in applying potential on rebar is their ribs that help to increase the bonding between concrete and rebar. Since the accurate calculation of rebar surface area is almost impossible, this study assumes rebar to be round. The corrosion length of rebar was controlled to 20 cm with a coating width of 5 cm on both ends of the controlled corrosion length. A schematic of the acceleration is shown in Figure 3.8. Rebar was connected to the positive pole of a GW Instek DPD 4303S DC power supply and a graphite rod was connected to the negative pole. A piece of 10 cm

wide cotton towel was attached to the bottom of the RC beam that covered the center of the uncoated 20-cm length portion. Both ends of the towel were immersed in SPS mixed with 0.6 M NaCl.

El Maaddawy and Soudki (T. A. El Maaddawy & Soudki, 2003) studied the impressed current technique for rebar corrosion in concrete and concluded that an applied current density above 200 $\mu A/cm^2$ exaggerated strain and crack width in concrete due to the quick corrosion of reinforcement. Therefore, the corrosion acceleration of rebar in concrete was controlled at an applied current density below 200 $\mu A/cm^2$ and the tests were performed as shown in Table 3.3.

Table 3.3. Electrochemical corrosion in RC testing parameters.

Sample No.	Applied current /mA	[Cl] in externally simulated pore solution /M	Duration /days
10 MA9d	10	0.6	9
20 MA9d	20	0.6	9
20 MA18d	20	0.6	18
15mA13d	15	0.6	13
15mA45d	15	0.6	45

3.4.3 Stress-life (S-N) relationship

3.4.3.1 Specimen preparation

The standard rotating bending test specimen in ASTM E466 (ASTM, 2002) standard and the draft of specimens used in this study are shown in Figure 3.9 (a) and (b), respectively. The central neck section of the standard sample was around 25.4 mm wide, while the sample used in this study had a 17.8 mm length in the neck region. The smaller neck width was used to leave space in the sample; hence, a corrosion chamber can be mounted to apply accelerated corrosion. The specimen diameter

was machined to 6 ± 0.001mm with a surface roughness around 0.3 μm. Figure 3.10 provides a photo of the machined rotating bending test specimen.

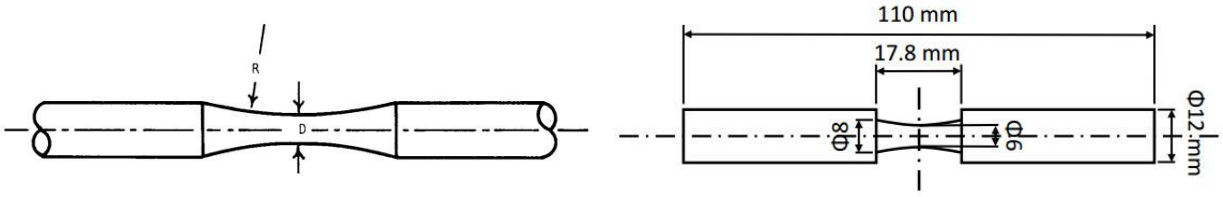

(a) (b)

Figure 3.9. Draft of rotating bending test samples: (a) standard test sample; (b) the sample tested in this project.

Figure 3.10. A machined rotating bending test specimen.

3.4.3.2 Testing procedures

Three groups of rotating bending tests were conducted: a fatigue test in air (reference group), under an accelerated corrosion environment produced by chloride concentrations, and under electrochemical corrosion. A fatigue test at atmospheric condition seeks to find the linear stress-fatigue life relationship (S-N curve) and the fatigue limit of the metal. Tests were manually terminated when the number of cycles reached 10 million, the stress amplitude of which was considered as the fatigue limit in this study.

Prior to both types of corrosion-fatigue test, around 2 mm of width in the central neck region of a specimen was left blank, and the rest of the neck zone was coated with rust preventative in order to prevent corrosion in undesired regions. Specimens were then attached to a specially designed

corrosion chamber, which had an open mouth on the top. The fatigue test was carried out using a Krouse machine (Figure 3.11). The spinning rate for both CF tests was 1000 rpm.

Figure 3.11. The Krouse machine used to conduct rotating bending test.

In the chloride-controlled CF test, 0.1 M and 0.6 M NaCl mixed in synthetic pore solution were selected to increase the corrosion rate. The specimens were required to undergo 24 hours of pre-pitting under a moist 0.6 M NaCl environment. In the electrochemical corrosion-fatigue test, a current-controllable DC power supply was connected by its anode to the test sample while the cathode was connected to a graphite rod. The electrolyte was a synthetic concrete pore solution mixed with 0.6 M NaCl.

A schematic of the pre-test process and the test setup are shown in Figure 3.12. The designed fatigue cycle levels were introduced from AASHTO (AASHTO, 1977) for a service life of 75 years at different traffic loadings: 500,000, 2 million, and above 2 million cycles. Three corrosion rates were chosen: 0.05 $\mu A/cm^2$, 0.15 $\mu A/cm^2$, and 0.32 $\mu A/cm^2$, which stood for low, moderate, and severe aggressiveness, respectively. The required current for the specimen was evaluated from the total corrosion current lasting 75 years and the fatigue cycles at each stress amplitude in the reference group. At the tested stress amplitude below the fatigue limit, the maximum number of tested cycles were selected at 2 million and 5 million, above which the test was manually terminated.

The obtained fatigue cycles tested at the combinations of stress levels and corrosion rates were recorded and these data were plotted as the S-N curve graph while the fracture surface was

analyzed by Scanning Electron Microscope (SEM) and Energy-Dispersive X-ray Spectroscopy (EDS). SEM is a type of microscope that provides the image of a surface by scanning the surface with a beam of electrons. EDS, on the other hand, gives the elemental mapping or chemical characterization of a scanned sample.

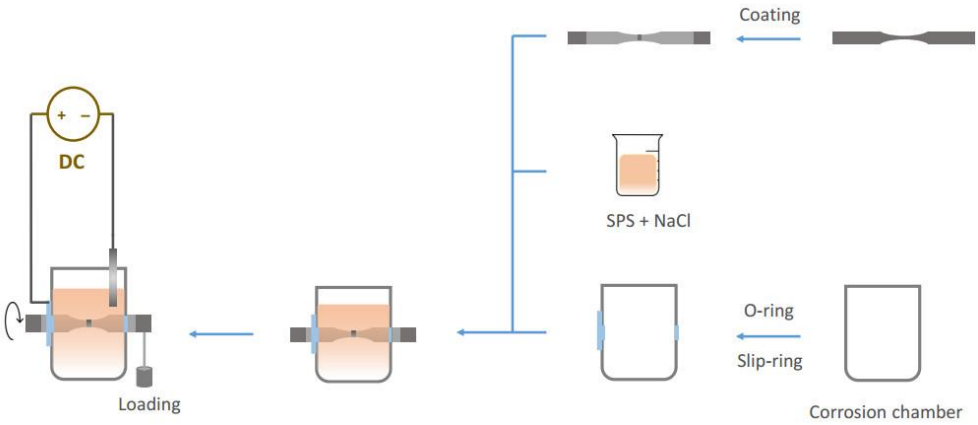

Figure 3.12. A schematic of rotating bending test flow under electrochemical corrosion.

3.4.4 Fracture Mechanics

Even though the Fracture Mechanics approach is divided into four stages from pit nucleation to final fracture failure as introduced before, the corresponding experimental part in this study mainly consisted of three sections in the experimental design: pit growth, crack propagation, and the measurement of K_{EAC}, K_{Ic}, and ΔK_{th}. During crack propagation, a fracture grows from initiation until the fracture failure. However, many researchers (Milella, 2013; Schijve, 2009) reported that environmentally assisted cracking (K_{EAC}) may affect the crack propagation curves. That was the reason why K_{EAC} had to be measured.

3.4.4.1 Pit growth test

The specimens used in the pit growth test had the same disk-shape as the specimens used to determine the corrosion rate by LPR and Tafel scans. One side of the specimen was polished in the following order of sandpapers: 80 grit, 150 grit, 240 grit, 360 grit, 600 grit, 1000 grit, and 2000 grit. For the short term pit growth test, the specimens were further polished using 0.3 µm and 0.1 µm polishing solutions to obtain a finely polished mirror surface finish. In terms of the long-term

pit growth test, two types of surface roughness were examined, 1 μm and 15 μm. Prior to each test, the specimen was immersed in the SPS for 12 hours to produce a passive layer on the exposed rebar surface.

Short term pit growth

The effect of chloride on corrosion was investigated at three chloride levels, 0.1 M, 0.6 M, and 1.5 M. In order to prevent corrosion from occurring on the unpolished area, a layer of rust preventative was applied to the unpolished area, leaving only the polished plate surface exposed to the corrosive. The short term pit growth test was conducted in an ambient environment and the samples were immersed in the SPS mixed with chlorides for a period of 2 hours, 12 hours, and 24 hours. After each corrosion period, the tested specimens were washed off with double distilled water and then viewed using a Scanning Electron Microscope (SEM) to observe the nucleation of pits.

Long-term pit growth

A schematic of the testing procedure is shown in Figure 3.13. Prior to the immersion of specimens in the corrosive medium, specimens were coated by rust preventative to leave only one side of exposure. The tested specimen was placed upside down on a piece of sleeve to prevent rust deposit on the corrosion surface. Air was entrained in the solution. Slow stirring was introduced in the solution to evenly distribute the reactants on the reacting area, including oxygen, hydroxide, and chloride. To maintain the pH of the solution, the corrosive was replaced semi-monthly. The tested environments are listed in Table 3.4; two specimens were exposed to each condition. In addition, specimens were cleaned monthly by the procedures described in ASTM G1 (ASTM, 2011) standard and then scanned by a Vantage50 profilometer to examine the maximum depth on the sample surface for a total of six months. Many scientists (Jarrah et al., 2011; R. E. Melchers, 2004; Rob E. Melchers, 2005) studied the occurrence of the maximum pit depth at a certain corrosion duration. They concluded that that was a possibility that a certain pit depth would occur. In other words, a pit with a rather large depth would not happen in each tested specimen. In the trial tests and the formal tests of this project, differences (0.005 mm – 0.015 mm) were observed in the depths of the deepest pits in both specimens. Hence, the average depth of the top three

measurements of the two specimens was considered as the equivalent maximum pit depth in a corrosion period.

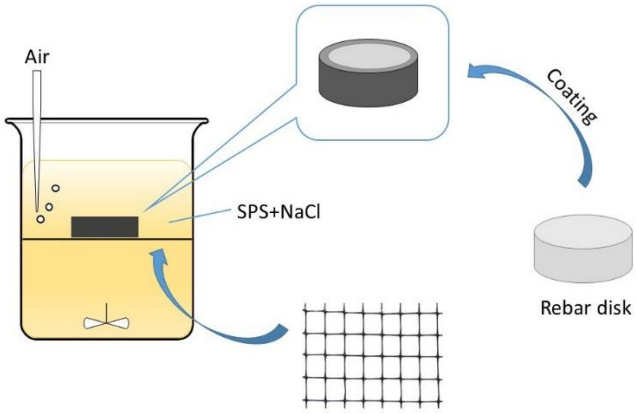

Figure 3.13. A schematic of pit growth test flow chart.

Table 3.4. Pit depth test parameters.

Sample NO.	Cl / M	pH	Surface / μm
1-1, 1-2	0.6	13.3	1
1-3, 1-4	0.6	9.3	1
15-1, 15-2	0	13.3	15
15-3, 15-4	0.1	13.3	15
15-5, 15-6	0.6	13.3	15
15-7, 15-8	1.5	13.3	15
15-9, 15-10	0	9.3	15
15-11, 15-12	0.1	9.3	15
15-13, 15-14	0.6	9.3	15
15-15, 15-16	1.5	9.3	15

3.4.4.2 General information about crack-propagation related testing

Specimens

Compact tension (CT) specimens with a longitudinal transverse (LT) orientation of the material were machined for the fatigue-crack-propagation related study. All specimens were machined from a piece of 45M rebar. The thickness of the disk-shaped specimen (B in ASTM E399) was 4.0 mm, and the width of the specimens (W in ASTM E399) was 30.0 mm. The surface roughness of the machining was measured at Ra 0.85. Notches were cut using a profile metal slitting saw and the angle of the notch was 60°. The entire machining process was performed under a coolant environment in order to prevent heat treatment of specimens because of the heat produced in the machining process. Figure 3.14 presents a schematic with dimensions (in mm) of the specimen for testing environmentally assisted cracking K_{EAC}, threshold stress intensity factor range ΔK_{th}, fracture toughness K_{Ic}, and the fatigue crack growth curves.

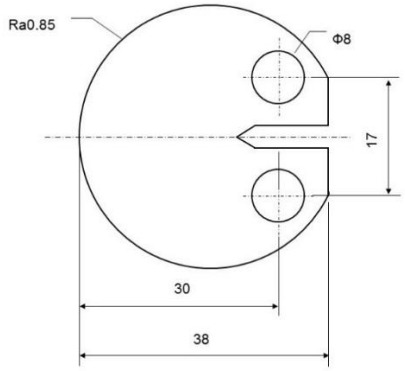

Figure 3.14. A schematic with dimensions of the specimen in measuring K_{EAC}, K_{Ic}, ΔK_{th}, and the fatigue crack growth curves.

Multi-testing system (MTS) loading frame and corrosion chamber

The general setup for all three tests is presented in Figure 3.15. The setup was composed of a fatigue loading cell, a corrosion chamber, a data acquisition system, and an optical microscope for monitoring crack growth.

All three tests were conducted by an IPC Global universal testing system with a 50 kN capacity load cell. The loading system consisted of a loading controller, a hydraulic power supply, and an actuator.

The corrosion chamber, with a volume of two litres and an open mouth on the top, was machined from transparent plastic material and the side view of the chamber is presented in Figure 3.16. The entire corrosion chamber was attached to the base of the hydraulic loading frame. The loading arms, used to apply loads to specimens during testing, were machined from SS316 stainless steel to prevent corrosion on the arms. The bottom loading arm was sealed and attached to the fixed corrosion chamber base.

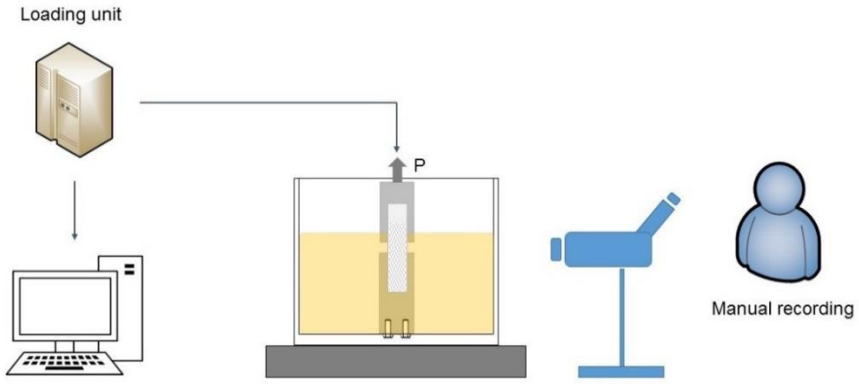

Figure 3.15. A general schematic of the experimental setup of the threshold stress intensity factor

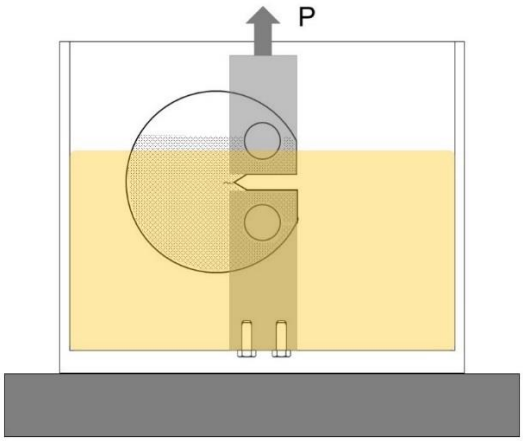

Figure 3.16. A side view of the testing specimen setup in the corrosion chamber.

The optical microscope used was a Zeiss microscope with a magnification range from 8 to 50 times. A built-in rule was embedded in the microscope; the crack length and the corresponding number of cycles were recorded manually every 0.10 mm increment of the crack length.

Table 3.5. Testing parameters for fatigue tests involved in fracture mechanics.

Measurement	Method	Stress ratio	Max Load / kN	Frequency / Hz	Corrosive environment
Pre-cracking		0.1	0.7	20	NA
ΔK_{th}	Stepped load	0.1	0.7, 0.8, 0.9, 1.0, 1.1, 1.2, 1.3	10	SPS + 0.6 M NaCl
Corrosion-fatigue crack propagation	Electrochemical corrosion	0.1	1.2, 1.6, 2.0	10	Air; SPS + 0.6 M NaCl; SPS + 0.6 M NaCl with 1 mA or 5 mA applied current
	Acidic corrosion	0.1	0.9	1	0.6 M NaCl mixed in double distilled water, 0.1 M H_3PO_4, and 1.0 M H_3PO_4
R ratio effect on crack propagation	CF crack propagation	0.1, 0.3, 0.5, 0.7	1.6	1	SPS + 0.6 M NaCl with 1 mA applied current

Pre-cracking

Prior to pre-cracking, specimens were washed with 95% methanol to clean the residual oil or coolant left on the specimen surfaces during the sample machining process. All specimens were pre-cracked according to ASTM (ASTM, 2013b) standard to the maximum stress intensity factor of 7.0 MPa√m at a tested stress ratio of 0.1. All pre-crack processes were conducted in air at a testing frequency of 20 Hz. Table 3.5 lists the general testing parameters for the fatigue tests

involved in the fracture mechanics approach, some of which are introduced in the following sections.

3.4.4.3 K_{EAC} measurement

In order to measure K_{EAC}, two approaches were tried: the constant loading displacement method and the constant loading rate method. The testing conditions are listed in Table 3.6. In the measurement of K_{EAC}, the corrosive environment was SPS mixed with 0.6 M NaCl. Prior to the K_{EAC} test, specimens were immersed in the corrosive solution for 24 hours of pre-corrosion.

Table 3.6. Loading and environment in K_{EAC} measurement.

Methods	Loading	Corrosive environment
Constant loading rate	0.1 N/sec	SPS + 0.6 M NaCl
Constant loading displacement	2E-4 mm/s, 1E-4 mm/s, 5E-5 mm/s	SPS + 0.6 M NaCl

Constant loading rate

In the constant load approach, the applied load started from zero and the loading rate of the MTS system was set at 0.1 N/sec. The applied load and the corresponding testing time was automatically recorded by the data acquisition system. The crack length, on the other hand, was recorded manually every 15 minutes until the crack length increment was above 0.1 mm, beyond which the crack length was recorded every 5 minutes until fracture failure.

Constant loading displacement

In the constant loading displacement method, the loading displacement rates were controlled at 2E-4 mm/s, 1E-4 mm/s, and 5E-5 mm/s. The corresponding crack lengths were recorded every 15 minutes.

3.4.4.4 Threshold stress intensity factor range ΔK_{th} measurement

Multi-stepped load

The stepped load approach was cyclically loaded at a stress ratio of 0.1 and the loading frequency was 10 Hz. The load level was in the order of 0.7 kN, 0.8 kN, 0.9 kN, 1.0 kN, 1.1 kN, 1.2 kN, and 1.3 kN. Every load level was tested for a maximum period of three hours, while the crack length was recorded every 30 minutes.

3.4.4.5 K_{Ic} measurement

Fracture toughness K_{Ic} was measured in an air environment and the testing procedures were conducted according to ASTM E399 (ASTM, 2013c) standard. The loading rate was set as 0.1 kN/s. The crack mouth displacement was replaced by the displacement recorded in the loading cell. Triple tests were conducted, and the average value was used to calculate the fracture toughness.

3.4.4.6 CF crack propagation

CF crack propagation tests were conducted according to ASTM E647 (ASTM, 2013d) standard in two types of corrosion environments, SPS and acidic corrosive solutions. CF crack growth in SPS required electrochemical corrosion on rebar disks; hence, the validity of this acceleration approach had to be determined.

Electrochemically accelerated corrosion in pre-cracked rebar disks

The electrochemically accelerated corrosion approach was used in the rebar crack growth under CF. Although this method was introduced and used for rebar corrosion in SPS and in concrete environments, corrosion acceleration in the crack still required further trials and modifications. Two types of coating – rust preventative and high-pressure vacuum grease – were used to prevent corrosion outside the crack surface. A two mA current was applied between the coated specimen and the SPS mixed with 0.6 M NaCl (pH 13.3) for four hours. Figure 3.17 and Figure 3.18 give the views of the pre-crack after ten minutes of corrosion and four hours of corrosion, respectively.

Figure 3.17 clearly shows that corrosion occurs in the crack. Figure 3.18 shows that the corrosion products in both samples mainly appear on the pre-cracks and the surrounding area (circled by red ellipses). Therefore, both coatings worked well. Because the rust preventative required 24 hours to dry, high vacuum grease was chosen in this study for rebar crack growth under CF.

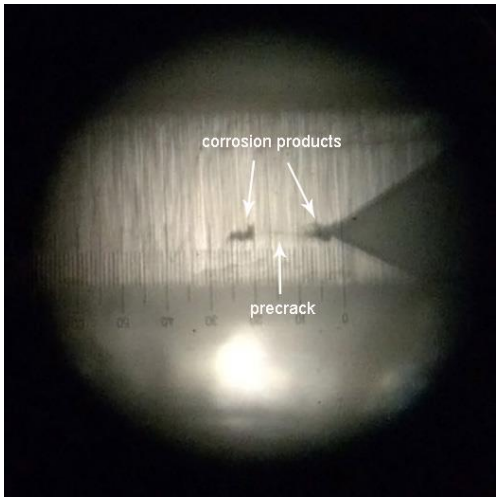

Figure 3.17. Corrosion in pre-crack after applying electrochemical corrosion.

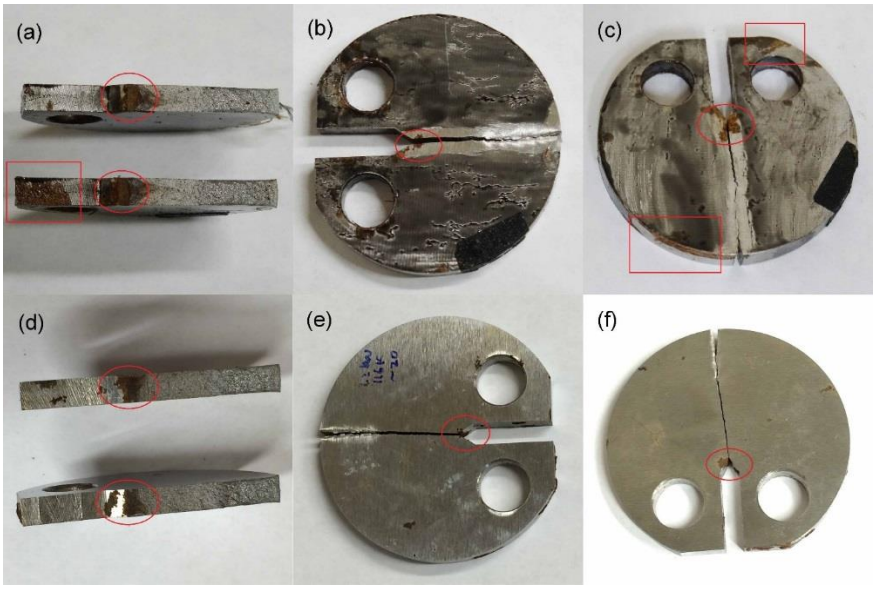

Figure 3.18. Two types of coating are used on rebar disks exposed to 2 mA to accelerate corrosion: the specimen coated by rust preventative, (a), fracture view, (b), top view, (c), rear view; the specimen coated by high vacuum grease, (d), fracture view, (e), top view, (f), front view.

CF crack propagation in SPS

The crack propagation test in the SPS solution consisted of two types of corrosion, pure solution corrosion and electrochemical corrosion. The corrosive solution in this test was SPS mixed with 0.6 M NaCl and the test frequency was 10 Hz. The stress ratio of the applied loading in the SPS environments was 0.1 while the maximum loads were 1.2 kN, 1.6 kN, and 2.0 kN. Two types of reference tests were used, specimens tested in air and in pure solution. Electrochemical corrosion tests were conducted by applying a constant current – 1 mA or 5 mA – between the tested specimen and the SPS. Specimens were coated with Dow high-pressure vacuum grease. A GW Instek DPD 4303S DC power supply was used to apply the required current. The disk-shaped sample acted as an anode and a graphite bar acted as the cathode. A schematic of the test setup and the actual testing frame in the laboratory are shown in Figure 3.19 and Figure 3.20, respectively. Figure 3.21 shows a magnified figure of the loading cell, corrosion chamber, specimen, and microscope.

Prior to applying current, a drop of the SPS solution was placed on the notch side of the pre-crack for a period of 30 minutes in order to induce corrosion on the pre-crack surface. The crack length was recorded prior to the start of a test and periodic measurements – crack length and the corresponding number of cycles – by the optical microscope were taken for every 0.25 mm increment in the crack length, as suggested in ASTM E647 standard. Specimens were tested until complete fracture failure.

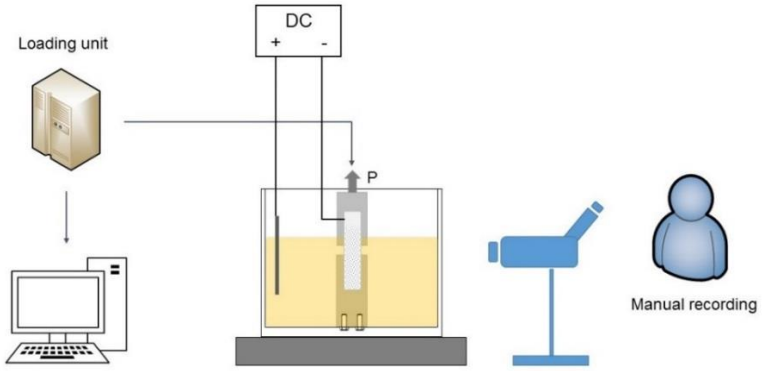

Figure 3.19. CF crack propagation test by electrochemical corrosion acceleration.

Figure 3.20. A layout of CF crack propagation test frame.

Figure 3.21. A magnified figure showing the loading cell, corrosion chamber, specimen, and microscope

CF crack propagation in acidic solutions

Prior to each test, the specimen was coated with Dow high-pressure vacuum grease. Three types of acidic solutions were used: 0.6 M NaCl mixed in double distilled water (DDW), 0.1 M H_3PO_4,

and 1.0 M H_3PO_4. The load range was 0.09 kN to 0.9 kN and the loading frequency was 1 Hz. Periodic measurements of the crack length taken every 0.10 mm increment of the crack length from the beginning of a test until the final fracture failure of the sample.

Crack propagation affected by R ratio effect

The maximum load in this test was chosen at 1.6 kN with a loading frequency of 1 Hz. The R ratios were selected at 0.1, 0.3, 0.5, and 0.7. The corrosive environment is SPS + 0.6 M NaCl with an applied current at 1 mA. Crack length was recorded every 0.10 mm increment until the failure of the sample.

3.4.5 Corrosion-fatigue testing of reinforced concrete beams

Specimen dimension and concrete specifications

Prior to RC beam casting, a layer of rust preventative with a width of 5 cm was applied on both ends of the central 20 cm length of a 10 M rebar. The dimensions of the RC beam were 10 × 10 × 100 cm with the concrete mix ratio listed in Table 3.7. The center of the rebar was placed 2.0 cm above the bottom of the concrete cover. The cast RC beams were cured in > 90% relative humidity and a temperature of 23 ± 2 °C for 28 days prior to CF tests. The average compressive strength of three cylinder specimens was measured at 39.95 MPa.

Table 3.7. Concrete mixing ratio in RC beams.

Cement	Sand	Gravel, size 4-13 mm	water	Daracem-19 Superplasticizer
1	1.65	2.92	0.4	1000 ml / 100 kg concrete

Testing frame compositions

A schematic of the entire test system is presented in Figure 3.22 and the actual testing fame is presented in Figure 3.23. A hydraulic cylinder accompanied by a hydraulic pump supplied the cyclic loading in the RC beams. A cooling fan was located near the hydraulic pump to prevent the pump from overheating. The data acquisition system was connected to the hydraulic system and the displacement sensors on the RC beam to collect instantaneous data, i.e. loading cycles, testing time, loads, and displacements.

Fatigue testing was conducted using a Sheffer 1 1/8 HH hydraulic cylinder at a loading frequency of 1.0 Hz. The average bending test capacity of three RC beams after 28 days of curing was measured at 18.05 kN. The applied load range of RC beam was 0.9 kN to 9 kN. Electrochemical corrosion was implemented in a similar manner to that in tests of the validation of corrosion acceleration of rebar in concrete as indicated in Section 3.4.2.5.

Specimens were tested in an air environment – as a reference – and three designed corrosion current densities, 0.05 $\mu A/cm^2$, 0.15 $\mu A/cm^2$, and 0.32 $\mu A/cm^2$. In calculating the required current, the rebar was assumed to be a cylindrical bar with a diameter of 11.2 mm (for 10 M rebar). Electrochemical corrosion was designed for a period of 75 years of corrosion in the three levels of corrosion current densities. The three applied corrosion current densities were computed at the testing frequency of 1 Hz and the applied current was further calculated at a fixed corrosion area on rebar.

Prior to applying fatigue loading to the RC beams, the potential was applied for 24 hours. RC beams were tested until the fracture failure of the RC beam or manually terminated when the number of cycles reached the two-million limit.

Post-test examinations

Once the RC beam failed, the number of cycles was recorded for each corrosion condition. The crack maps on the RC beam surface were recorded and analyzed. The morphology of the fracture

surface was examined using SEM and the failure mode would be analyzed. Moreover, the rebar cross section loss along the corroded length was estimated and analyzed.

In this study, the cross section loss was estimated by the mass difference of a small piece of rebar before and after the CF test. As the test was completed, the central 20 cm of corroded rebar was cut and cleaned according to the rust cleaning procedures listed in ASTM G1 (ASTM, 2011) standard. The corroded rebar was then cut into pieces at a width around 1 cm. The weights of these corroded pieces were examined and their original weights were computed by the width of those pieces and the unit weight of the entire piece of rebar prior to CF test. The unit weight (g/cm) of the rebar was examined by dividing the mass of the entire rebar prior to casting the RC beam by the rebar length. Since the original cross section area of the rebar was 100 mm^2 and the density of the rebar was constant, the cross section after corrosion could be computed according to the weights prior to and after corrosion.

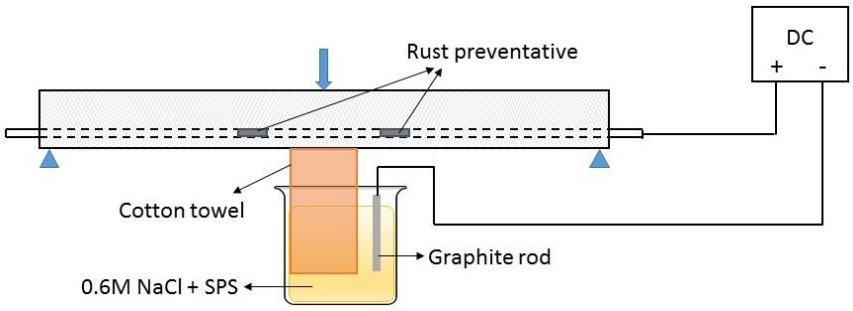

Figure 3.22. A schematic of the CF test in RC beams.

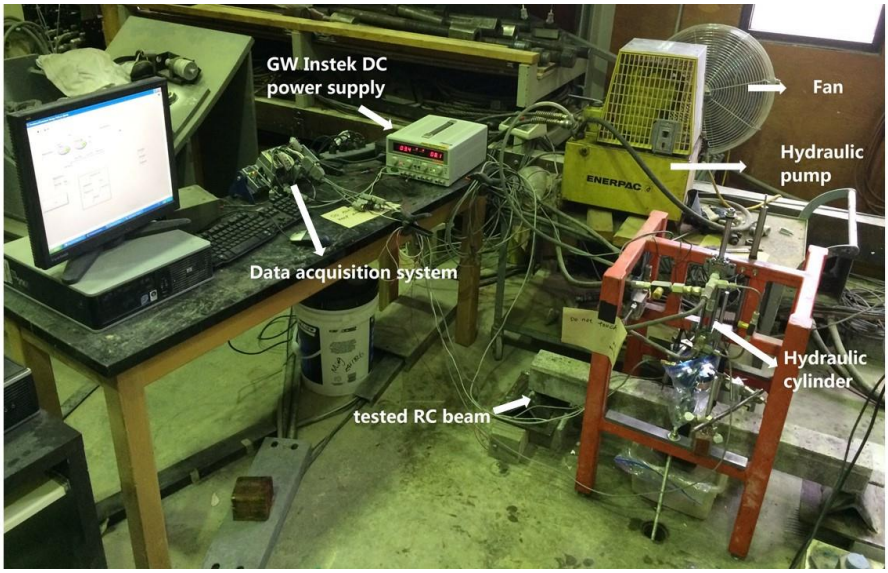

Figure 3.23. The actual testing frame of RC beams.

4 Rebar corrosion acceleration

It is critical to accelerate both the corrosion and fatigue processes in the laboratory since a natural corrosion-fatigue process usually takes decades to happen. Sufficient corrosion acceleration is rather difficult to achieve and control. Previous studies usually have estimated the corrosion-fatigue of metals under chloride solutions with high concentrations or investigated the fatigue behavior of reinforcing steel after a certain period of salt sprays (Apostolopoulos & Michalopoulos, 2006; Apostolopoulos & Pasialis, 2009; El et al., 2013; Fernandez et al., 2015; Palin-luc et al., 2010). In this chapter, Linear Polarization Resistance (LPR) and Tafel scans are applied to measure the accelerated corrosion rates in different chloride-added simulated pore solutions (SPS). The accelerated corrosion rate of this electrochemical corrosion approach is verified via the mass losses of rebar with both Potentiostatic and Galvanostatic scans. The approach producing faster corrosion rates was subsequently validated by examining the mass loss of rebar corrosion in both an SPS and concrete environments with the DC power supply.

4.1 Rebar corrosion in simulated-concrete-pore-solutions containing NaCl

Prior to the LPR and Tafel scans, an open circuit potential (OCP) was measured. Figure 4.1 shows a typical group of the tested data. The OCP increased immediately when exposed to the chloride contaminated SPSs, which indicated a passivation process in the rebar – the formation of a thin layer of oxide film in a chloride environment. After one hour, the OCP became steady, which implied that one-hour of standing was suitable for the measurement of corrosion current densities. The OCP of the sample immersed in a chloride free solution maintained a slow but steady increase, as the absence of chloride failed to induce a quick passivation. Figure 4.1 also shows that: the OCP had a higher value in the chloride environment than in the non-chloride environment; as chloride concentration increases, there was no observable shift of the OCP values in a more positive direction.

4.1.1 Linear polarization resistance (LPR)

Figure 4.2 presents the LPR curves of one group of specimens. The linear increments in and around the zero current density validated the tests. Figure 4.3 shows all the acquired corrosion current

densities, and presents the the data range (box range in the figure), mean value (hollow circle in the box), and the median (line in the box). The mean corrosion current density, which presumably increases with an increasing content of chloride, rose at first and then declined to as low as 124.2 nA/cm^2 at 1.5 M NaCl + SPS. This was probably because of the drawback of the LPR regarding the low corrosion current density in 1.5 M NaCl + SPS. Fontana (Fontana, 1987) pointed out that the approximation involved in the LPR calculations could introduce errors up to 50%. Therefore, LPR should always be compared with the other measurement techniques of corrosion rate to ensure the accuracy of LPR.

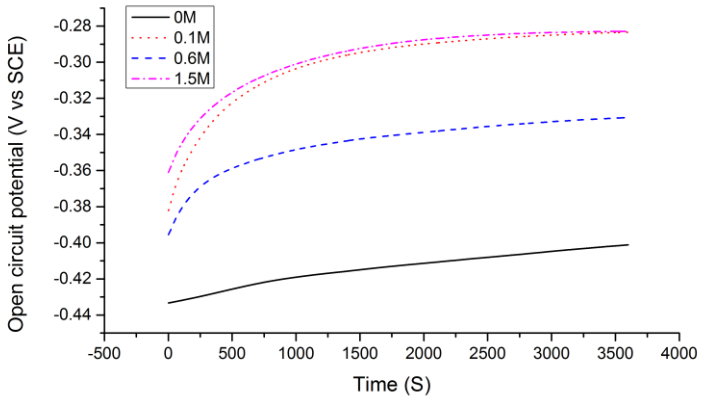

Figure 4.1. Open circuit potential of mixed simulated pore solutions with NaCl

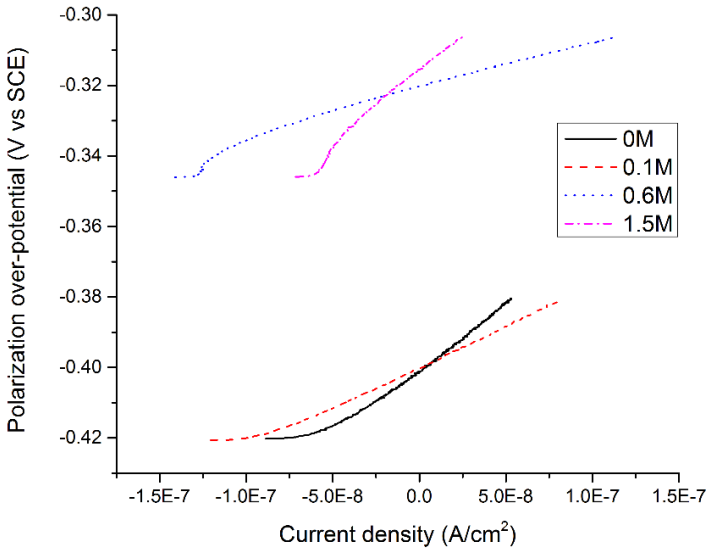

Figure 4.2. Linear polarization resistance data plot

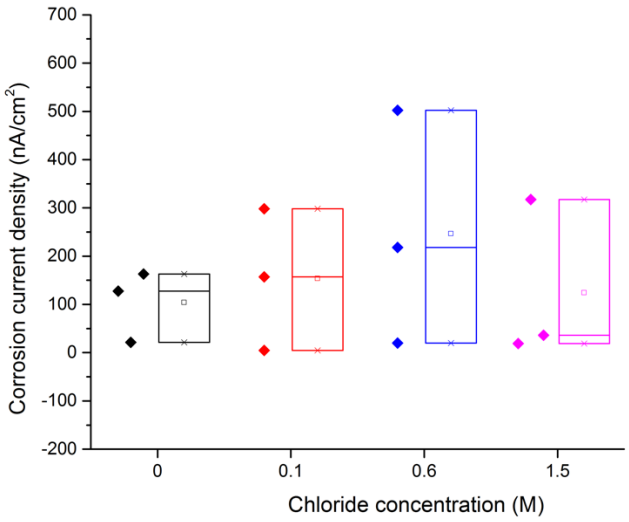

Figure 4.3. Corrosion current densities of mixed simulated pore solutions with NaCl

4.1.2 Tafel scan

The Tafel scan is the second technique used in this project for the measurement of corrosion rate. A typical group of scan curves is shown in Figure 4.4. In the figure, chloride content has little effect on the corrosion potential. Moreover, in the four repeated testing groups, the corrosion current densities in one group tests clearly showed that the corrosion rate increased with increasing chloride content. To ensure the accuracy of the corrosion rate results, four replicate tests were carried out. The collected corrosion current densities are plotted in Figure 4.5, showing the data range, quarter range data (box range in the figure), mean value (hollow circle in the box), and the median (line in the box). The correspondent descriptive statistics of Figure 4.5 are shown in Table 4.1. Both the box chart and the statistical table presented that the mean corrosion current density increased with the increase of chloride concentration. Furthermore, the coefficients of variation (CV) of current densities were rather high – 27.3%, 37.0%, and 29.7% – at 0.1 M NaCl, 0.6 M NaCl, and 1.5 M NaCl, respectively, when compared to the chloride free environments, whose CV was 20.5%. This is probably because of the occurrence of unstable electrochemical reactions on the rebar surfaces in the chloride contaminated solutions as these three environments are more likely to initiate a pit than the chloride free environment.

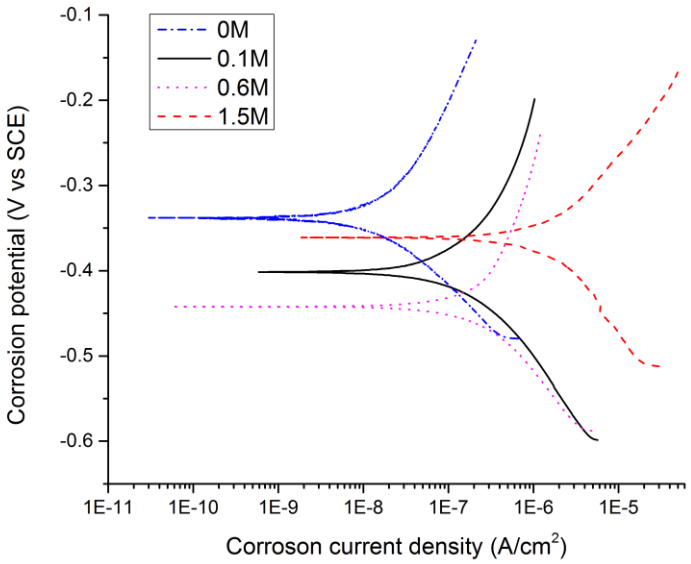

Figure 4.4. Tafel scans of simulated pore solutions with NaCl

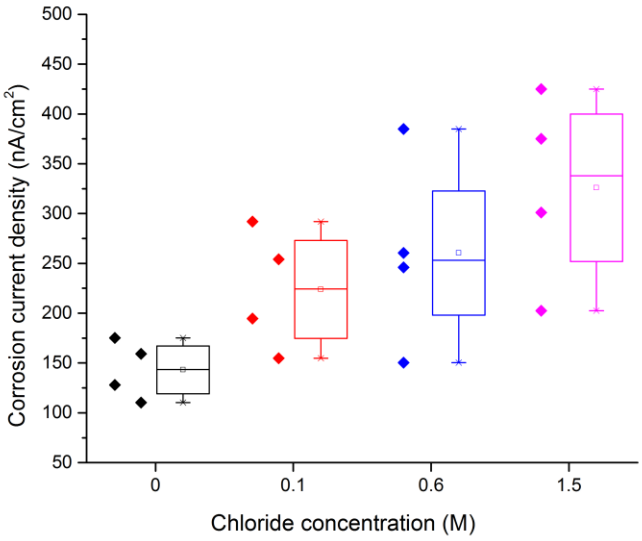

Figure 4.5. Rebar corrosion current densities of simulated pore solutions with NaCl

Table 4.1 Descriptive statistics of rebar corrosion current densities in simulated pore solutions with NaCl

Chloride concentration /M	Corrosion current densities mean value / nA/cm^2	Standard deviation / nA/cm^2
0	143.15	29.38
0.1	223.80	61.04
0.6	260.45	96.32
1.5	325.90	96.70

4.1.3 Validity of chloride corrosion acceleration

The results of LPR and Tafel show that the corrosion current densities in the chloride contaminated solutions were higher than in the non-chloride simulated pore solution, even though LPR results individually could not be used to quantitatively analyze the current density in a specific chloride environment. Compared to the corrosion current density in the non-chloride environment of 103.98 nA/cm^2 measured by LPR and 143.15 nA/cm^2 tested by Tafel, the most severe corrosion current densities were 246.75 nA/cm^2 and 325.90 nA/cm^2 measured by LPR and Tafel, respectively. In other words, a heavily chloride-contaminated simulated-pore-solution only lead to an increased corrosion rate by several times. However, this program aimed at shortening the corrosion duration from 75 years to several days, even hours, which means that the corrosion rate should have been enhanced by hundreds, even thousands, of times. Therefore, simply mixing a high concentration of chlorides would likely have failed to effectively accelerate the corrosion rate to achieve this target.

4.2 Electrochemical corrosion acceleration

4.2.1 Potentiostatic scan

The Potentiodynamic polarization curves of the structural steel under a simulated pore solution mixed with 0 M, 0.1 M, 0.6 M, and 1.5 M NaCl are shown in Figure 4.6. The corrosion potential

and current density from the Tafel region in this figure are presented in Table 4.2. The table provides that, compared with the chloride entrained solutions, the non-chloride solution had the highest corrosion potential (-0.430 V/SCE) and the highest corrosion current density (0.708 $\mu A/cm^2$). Nevertheless, compared with a non-chloride testing environment, chloride bearing solutions had slightly lower corrosion potential ranging from -0.406 V/SCE to -0.420 V/SCE, and corrosion current density ranging from 0.501 $\mu A/cm^2$ to 0.687 $\mu A/cm^2$. In other words, chlorides had no apparent impact on the corrosion potential and corrosion current.

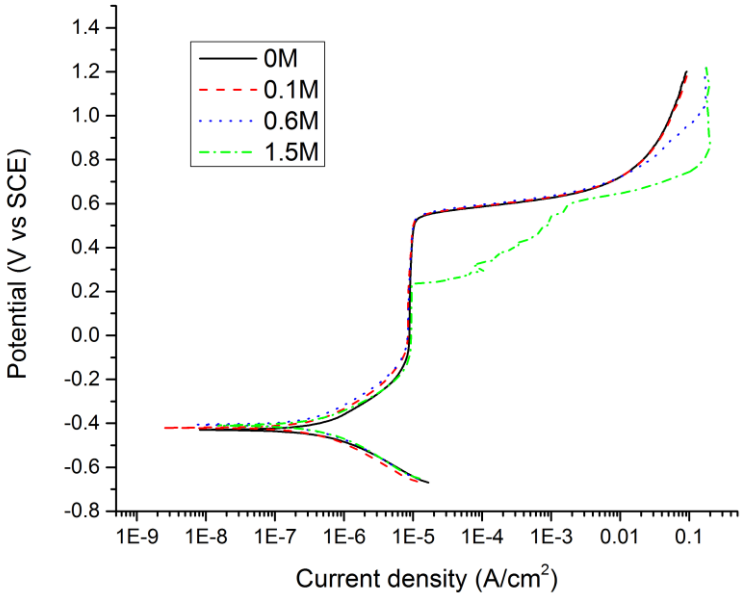

Figure 4.6. Rebar potentiodynamic polarization curves in simulated pore solution mixed with chlorides

Above the Tafel zone in the polarization curves, the Potentiodynamic scan firstly goes through the passivation region and then enters the trans-passive region. Figure 4.6 shows no significantly observable differences in the passivation breakdown potentials of +0.57 V/SCE, +0.57 V/SCE, and +0.58 V/SCE in the 0 M, 0.1 M and 0.6 M NaCl solutions, respectively. However, the specimen tested in 1.5 M Cl had a much lower passivation breakdown potential of +0.26 V/SCE than the other three solutions, and this may be attributed to a higher pitting ability in 1.5 M NaCl. Therefore, based on the chloride content in SPS, an applied potential on the reinforcing steel

between +0.26 V/SCE and +0.58 V/SCE increased the corrosion to reach the trans-passive region and generate a fast corrosion rate.

Table 4.2. Corrosion potential and corrosion current density from potentiodynamic polarization curves

Chloride concentration in simulated concrete pore solution /M	Corrosion potential, E_{corr} / V vs SCE	Corrosion current density, i_{corr} / $\mu A/cm^2$
0	-0.430	0.708
0.1	-0.420	0.524
0.6	-0.406	0.501
1.5	-0.409	0.687

In order to explore the relationship between the current density and time at a designated potential, Potentiostatic scans were performed at four potentials (+0.1 V/SCE, +0.3 V/SCE, +0.5 V/SCE, and +0.7 V/SCE). The results are presented in Figure 4.7, which shows that the corrosion current densities exponentially declined with time at +0.1 V/SCE and +0.3 V/SCE. By applying a constant potential in the passivation region, the corrosion process is viewed as the applied potential steps from the open circuit potential to a passive potential (Bard & Faulkner, 2001). The Potentiostatic process demands a great amount of current since it happens instantly, which leads to a high current value in the circuit. However, the initial reduction also creates a number of ferrous ions that adhere to the sample surface, which subsequently start to form a passive film because of the high concentration of hydroxyl ions in the alkaline solution. The thin film grows, and the enlarging passive film gradually prevents the steel surface from contacting with the corrosive solution. This process depletes the amount of current, and thus the measured current value declines sharply (Figure 4.7) in the curves of +0.1 V/SCE and +0.3 V/SCE, and in the curves of +0.5 V/SCE and +0.7 V/SCE at the first 15 seconds.

Figure 4.7 also shows that the current densities decrease at the beginning but then increase afterwards and fluctuate with time at +0.5 V/SCE and +0.7 V/SCE. The initial decline in current

density is probably due to the depletion of current as discussed above. The +0.5 V/SCE and +0.7 V/SCE were located at the trans-passive zone of the steel (Figure 4.6), which could break down the passive film and generate a trans-passive dissolution. Hence, after the first 15 seconds of passivation, the specimens de-passivates and the corresponding current rises and violently fluctuates with time (Figure 4.7). The Potentiostatic curves also reveal that destroying the passive layer under +0.5 V/SCE takes around 10 minutes, longer than that under +0.7 V/SCE by roughly four minutes.

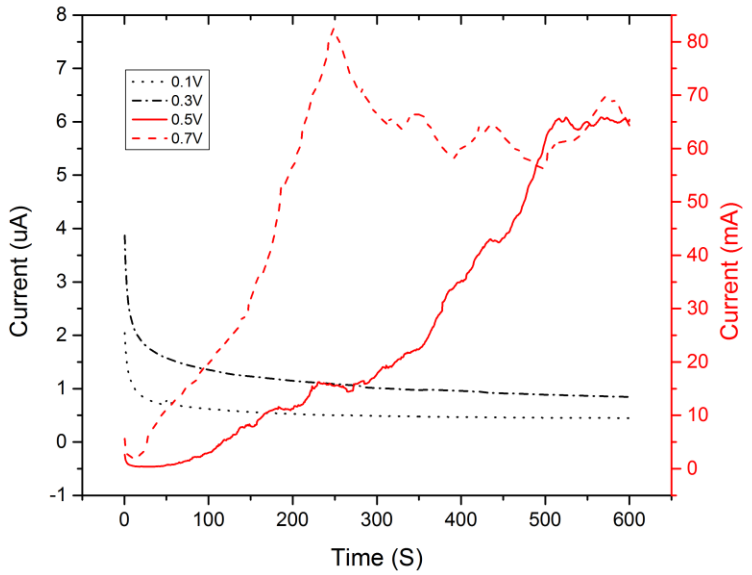

Figure 4.7. Potentiostatic scans of structural steel immersed in SPS + 0.6 M Cl at four potentials: +0.1 V/SCE, +0.3 V/SCE, +0.5 V/SCE, and +0.7 V/SCE.

Two one-hour Potentiostatic scans were performed at two potentials (+0.5 V/SCE and +0.7 V/SCE) and the results are given in Figure 4.8. The graph suggests that the responding currents fluctuate violently with time for both potential levels, and +0.7 V/SCE breaks down the passive film sooner than +0.5 V/SCE. Both points agree with the results presented in Figure 4.7.

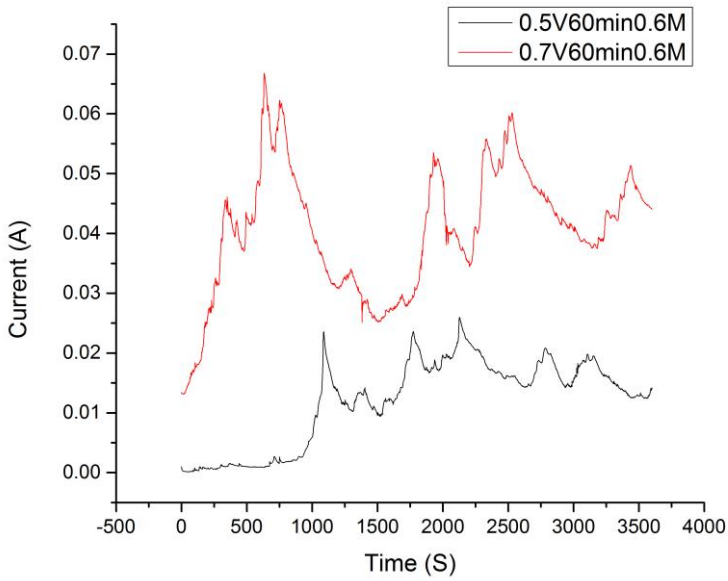

Figure 4.8. Ten minutes of Potentiostatic scan of rebar disks at 0.5 V/SCE and 0.7 V/SCE in SPS + 0.6 M Cl.

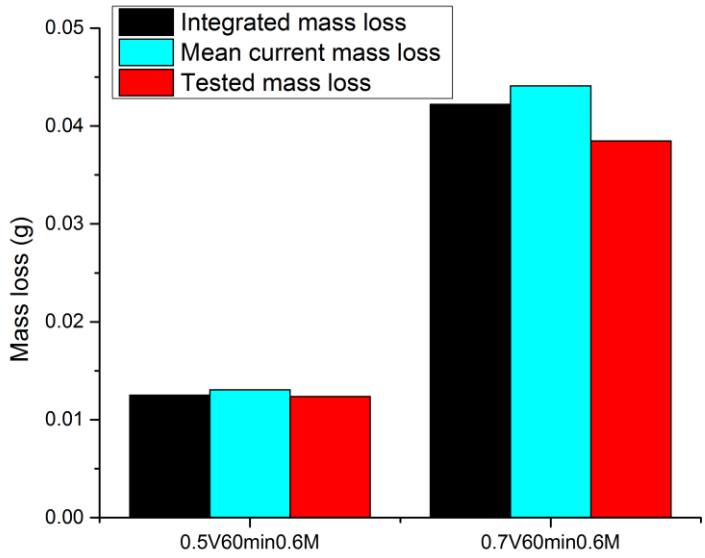

Figure 4.9. Rebar disk mass losses after exposure to 0.5 V and 0.7 V for 1 hour under 0.6 M NaCl mixed with simulated concrete pore solution.

After the Potentiostatic scans, the mass losses of specimens were determined by three approaches: the actually weighed mass loss; the computed mass losses using the corrosion mass formula by

integrating the current-time curve; and by the mean current value. The results in Figure 4.9 illustrate that, compared to the measured mass loss after a Potentiostatic scan, the integrated mass loss (total current is integrated by the area under the current curves in Figure 4.8) and the mean-current-calculated mass loss are 1.1% and 5.2% higher at +0.5 V/SCE, but 8.8% and 12.8% higher at +0.7 V/SCE. Thus, estimating of the corroded mass loss found by using the mean current density introduces an error in comparison with the integrated weight loss. Therefore, an instantaneous current acquiring device was required to precisely procure the total current during the electrochemical process.

4.2.2 Galvanostatic scan

Figure 4.10 (a) shows the results of Galvanostatic scan results of the two levels of applied current in SPS (1 mA and 10 mA) mixed with 0.1 M, 0.6 M, and 1.5 M NaCl. By controlling 1 mA at 0.1 M NaCl, the potential suddenly jumped between 180 s and 320 s but then remained steady. However, the other three combinations present a steep drop of potentials at the beginning and then a randomly oscillating potential that maintains a constant output current. Theoretically, under a constant current output, the applied potential between the anode and cathode should increase at the beginning, then reach a plateau, and finally grow exponentially to an extremely high value (Bard & Faulkner, 2001). The reason is that, as iron is oxidized to ferrous iron, the divalent iron forms a thin layer of passive film at the iron surface that blocks the corrosive solution from contact with the iron. Thus, the applied potential should increase in order to maintain a constantly applied current. As the passive film grows and finally covers the entire sample surface, less and less ferrous irons can be produced and the applied potential increases dramatically to supply a constant current.

In Figure 4.10 (b), the 0.1 mA curve fits the theoretical format with no observable final dramatic increment that could be attributed to the incomplete formation of a passive film. Figure 4.10 (b) also shows that the 1 mA curve gradually climbed at first, then underwent a short period of fluctuated potential, and finally reached a steady state. The fluctuating potential may have been caused either by electromagnetic interference or by the formation of metastable pits. Both explanations agree with the optical observation, with no visible corrosion product observed with a 10X optical microscope after the Galvanostatic scan. Therefore, the 1 mA curve also fit in the theoretical format. The 10 mA curve in Figure 4.10 (b) rose slightly at the start, but went through

random fluctuation over the rest of the scan. This indicates that the passivation layer is formed beforehand and destroyed afterward.

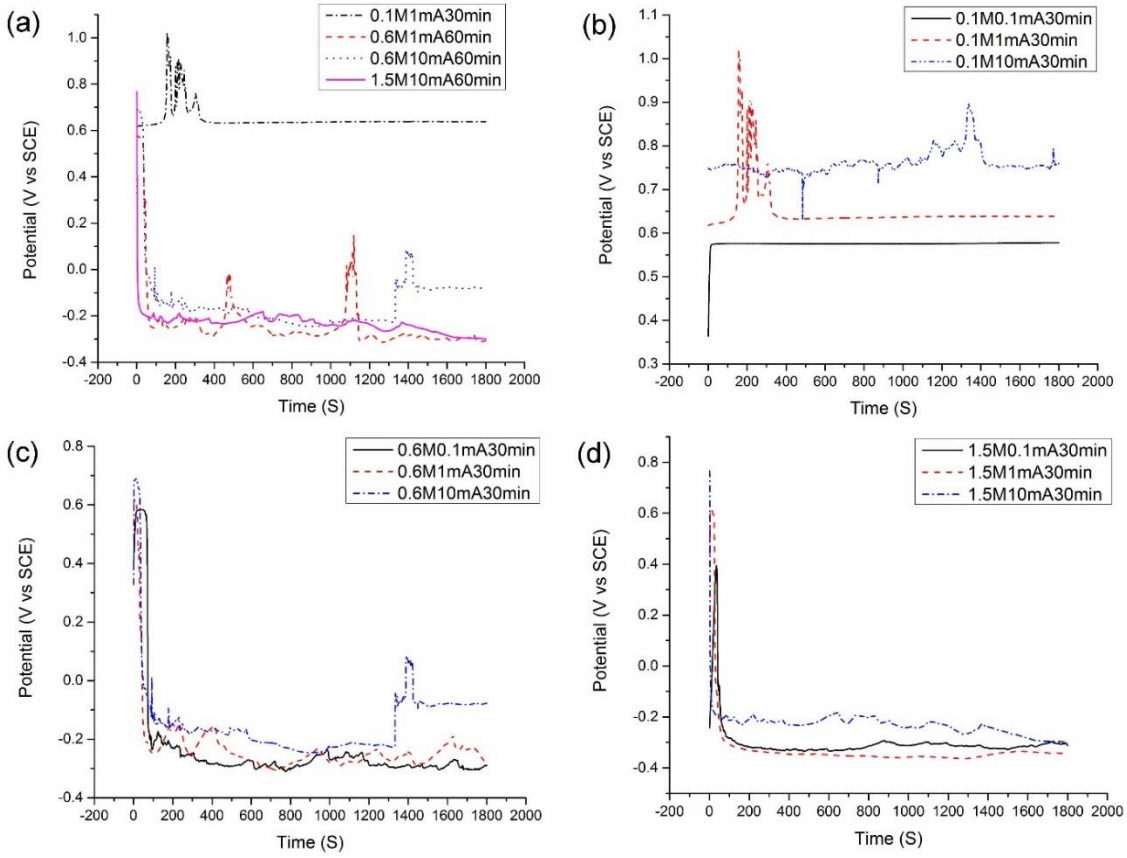

Figure 4.10. Galvanostatic scan results of specimens tested under: (a), a combination of chloride concentration, applied current, and corrosion time; (b) 0.1 M NaCl, three current levels for 30 minutes; (c) 0.6 M NaCl, three current levels for 30 minutes; (d) 1.5 M NaCl, three current levels for 30 minutes.

All curves in Figure 4.10 (c) and (d) show that the applied potentials grew in the beginning, then dropped sharply to negative values, and randomly oscillated until the end of the tests. The short increment at the beginning of a test may be triggered by the quick formation of the passive film at a high current density, as described in the typical above-mentioned process (Bard & Faulkner, 2001; Landolt, 2007).

In a Galvanostatic scan, a current density higher than the critical current of passivation provokes the formation of a passivation film that rapidly increases the anode potential. The higher applied the current density, the more a potential could be elevated (Szklarska-Smialowska & Janik-Czachor, 1971). This phenomenon was confirmed in this study with three applied current levels (0.1 mA, 1 mA, and 10 mA) as shown in Figure 4.10 (b), (c), and (d). In Figure 4.10 (c) and (d), the potential declined dramatically beyond a short rise at the beginning. The same phenomenon was observed in the study by Frangini and De Cristofaro; Smialowska believed that the formation of a passive layer facilitates the decline of potential in the anode (Frangini & De Cristofaro, 2003; Szklarska-Smialowska & Janik-Czachor, 1971).

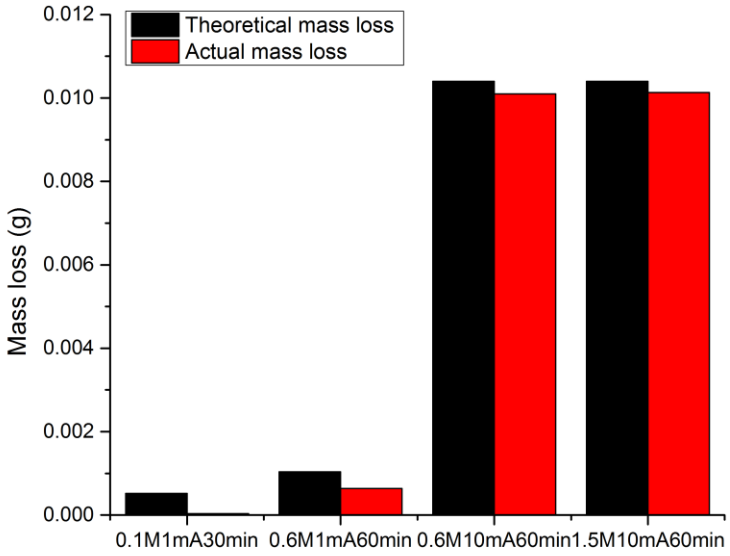

Figure 4.11. Rebar mass losses after Galvanostatic scans

Figure 4.11 compares the theoretical mass losses that are calculated based on the applied current and duration, the actual mass losses, weight difference before and after the test in Figure 4.10 (a). The results illustrate that the tested mass loss in rebar specimens was in line with the theoretical mass loss at 0.6 M and 1.5 M NaCl solutions. However, there was no detectable mass loss from the sample in the 0.1 M NaCl solution with the applied current. This is probably because of the passive film breakdown potential (E_b) and the oxygen revolution potential ($E_{rev,O2}$). In the environment without aggressive anions, $E_b > E_{rev,O2}$, oxygen formation dominates the trans-passive zone, and iron dissolution barely exists at low current densities (Landolt, 2007). Although the rebar

sample was tested in 0.1 M NaCl solution, the highly alkaline background suppressed the pitting potential to a value shown in the non-NaCl polarization curve (Figure 4.6). In other words, the oxygen revolution dominated the competition, and the rebar dissolution contributed little current to the transpassive corrosion.

4.2.3 Comparison between Potentiostatic and Galvanostatic scans

The scan data and the corrosion weight losses of Potentiostatic and Galvanostatic scans were introduced in the previous paragraphs. From the mass loss in both approaches, the rebar corrosion could be greatly accelerated either by a potential-controlled device or by a current-controlled output equipment. However, an instant current acquisition system was necessarily installed in the potential-controlled device in order to integrate a more precise total current. Moreover, a small potential difference could result in a large current difference in the trans-passive region, as shown in Figure 4.6. Thus, an automatic setting is required of the potential-controlled device. However, it is usually hard to access such equipment. The current-controlled method, on the other hand, can easily manage the current in the circuit and produce a more precisely designed corrosion rate. In addition, these current-controlled DC power supplies are more readily accessible, depending on the required accuracy of measurement. Consequently, the current-controlled output approach is preferred to accelerate the corrosion of rebar.

4.3 Corrosion mass loss examination

In the Galvanostatic scans of Chapter 4.2, applying a current on rebar was found to produce the designed corrosion current density with the assistance of the delicate Gamry testing frame. However, there were some concerns regarding use of the general DC power supply to apply current. Thus, a mass loss validation of electrochemical corrosion acceleration was carried out, not only in a solution environment, but also in a concrete environment.

4.3.1 Corrosion mass loss in simulated pore solution

By using a laboratory GW Instek GPD 4303S DC power supply to control the output current in rebar corrosion, the theoretical and actual mass losses are provided in Figure 4.12. The overall tested weight loss because of the anodic dissolution matches the theoretical values.

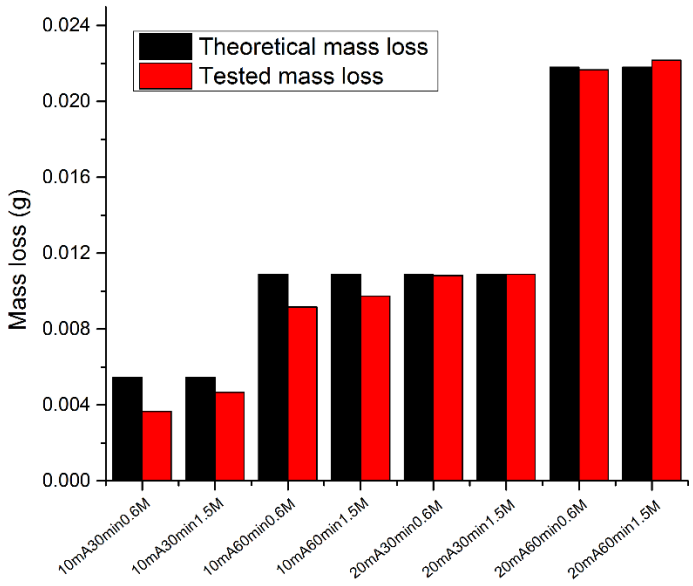

Figure 4.12. Theoretical and tested mass losses under electrochemical corrosion

The differences between the two mass losses in 10 mA samples varied from 10.7% to 32.7%. In comparison to an applied current of 20 mA, 10 mA had a lower correspondent potential in Galvanostatic polarization, therefore, oxygen reduction may have contributed to the current production in the competition between the transpassive dissolution and oxygen reduction. On the other hand, equipment resolution may have also caused the errors. The current output resolution of GPD 4303S is 1 mA, therefore, it may have also raised the error to the total current difference in the 10 mA tests. Moreover, the error of the scale was magnified by the small mass loss.

4.3.2 Rebar corrosion mass loss in concrete environment

Many studies (Al-hammoud et al., 2011; El-Zeghayar, Topper, & Soudki, 2011; E. Maaddawy et al., 2006) simplify the electrochemical corrosion in reinforced concrete by entraining chloride ions in concrete during the casting process of RC beams, and use the concrete pore solution as the electrolyte. However, an extra counter electrode has to be embedded in the concrete to complete the electrochemical corrosion loop, and the electrode usually interferes with the properties of RC beams, e.g. an additional reinforcement (counter electrode) in the compression zone or tension zone. In this study, chlorides are placed externally and they have to transport through the concrete cover to reach the rebar. Due to the three-phase property of a concrete cover, the concrete

environment is complicated rather than simply a solution or a solid environment, hence concrete itself has an effect on the corrosion acceleration in rebar by applying the same electrochemically accelerated corrosion in a homogeneous SPS condition. Since the transport rate of chloride ions in concrete is slow, a period of pre-applying current is required. The study of Aguayo et al (Aguayo et al., 2014) concluded that 24 hours of electric field drove chloride ions to 20 mm depth in concrete, the same value as the concrete cover thickness in this test. The actual and theoretical mass losses after 24 hours of pre-applying current are plotted in Figure 4.13. The results show that the mass losses were in a good agreement with the theoretical values, with the errors range from 8.8% to 34.29%.

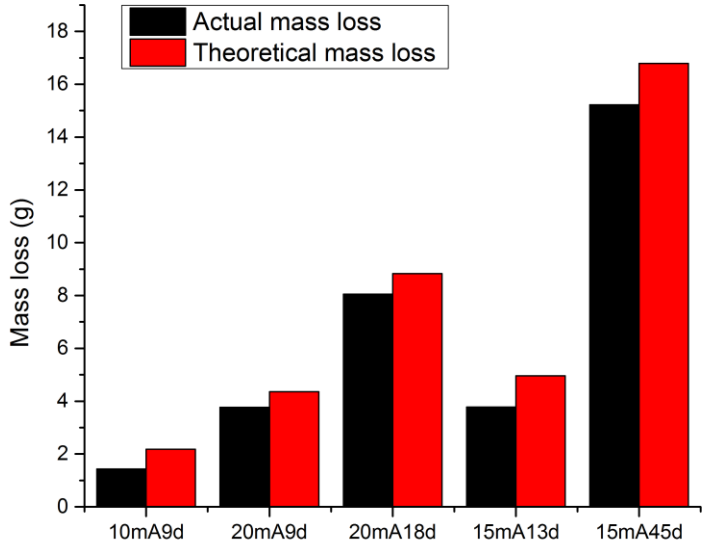

Figure 4.13. Rebar actual and theoretical mass losses after electrochemical corrosion in concrete environment

Table 4.3 lists the detailed mass loss percentages after corrosion, and the results indicate a mass loss of 3.98% occurred in approximately 18 days. As it might take months to years for the diffusion of chloride from the concrete surface to the rebar in field, therefore, one is able to conclude that electrochemical corrosion greatly reduces the corrosion time. Moreover, the mass loss errors of the measured specimens were fairly small except sample 10MA9d with a mass loss of 0.72% and

an error of 34.29%. The error might have been introduced by residual, unremoved corrosion products and concrete on the rebar. Because of the low applied current and the short corrosion time, the mass loss of the rebar was small, thus the resultant tiny mass difference could provoke a large error in the mass loss determination. Overall, the actual mass loss agreed well with the theoretical mass loss, indicating that the Galvanostatic corrosion acceleration is applicable to reinforcement in concrete.

Table 4.3. Applied corrosion current, duration and the resultant corrosion degree of steel

Sample No.	Applied current /mA	Corrosion time /hr	Theoretical mass loss percentage /%	Actual mass loss percentage /%	Mass loss error /%
10MA9d	10	209	1.09	0.72	34.29
20MA9d	20	209	2.11	1.83	13.53
20MA18d	20	424	4.36	3.98	8.80
15mA13d	15	317.5	2.46	1.87	23.87
15mA45d	15	1074	8.21	7.44	9.30

5 Stress-life (S-N) approach to estimate corrosion-fatigue of rebar

The fatigue life of a structure represents the total number of cycles from the beginning of its service until its final failure. In a non-corrosion environment, several approaches are available that evaluate the fatigue life of a material. Among them, the stress-life (S-N) approach depicts the relationship between the applied stresses and the corresponding number of fatigue cycles to failure. Provided that the S-N curves of a material are generated, the fatigue life of a structure fabricated from the same material can be directly or indirectly obtained from the curve for a given applied stress.

In this chapter, the electrochemical corrosion acceleration approach was used for rapid corrosion of rebar during the rotating bending test in air and in NaCl solutions as references. In the rotating bending test, the stress amplitudes were selected at five levels: specifically, 366.47 MPa, 329.82 MPa, 302.48 MPa, 272.83 MPa, and 243.17 MPa. The corrosion degrees were selected to present 75 years of corrosion under three corrosion levels of 0.05 $\mu A/cm^2$, 0.15 $\mu A/cm^2$, and 0.32 $\mu A/cm^2$, respectively. The fatigue life of each stress amplitude in the designed corrosion rate was obtained by the rotating bending test in the combined environment of a stress amplitude and a corrosion condition. In a chloride corrosion environment, the rebar under cyclic loading usually generates pitting-induced corrosion-fatigue. Hence, a fracture analysis by SEM and EDS was carried out to determine the fracture failure mode of specimens. Thereafter, the S-N curves were analyzed to extrapolate the corrosion-fatigue at a different mean stress.

5.1 S-N curves

Tests in non-corrosion and SPS + NaCl environments

Figure 5.1 (a) shows the results from the rotating bending test in air and in SPSs mixed with two NaCl concentrations (0.1 M and 0.6 M). The reference test in air indicates that the fatigue life almost linearly increased with a decreasing stress amplitude from 659.6 MPa to 329.8 MPa. By conducting a linear fitting, the linear equation was found as $\log S = 3.14 - 0.10 \log N$. Table 5.1 provides the Analysis of Variance (ANOVA) results from the linear fitting of the logarithmic S-N data of the reference test in air. The total sum of squares (245,091.29 $cycle^2$) equaled to the sum

of squares of the model (239,579.64 cycle^2) plus the sum of squares of the error (5,511.65 cycle^2). The F value of the predicted model was 695.49, which equaled to the division of mean square of the model 239,579.64 cycle^2 and the mean square of error 344.48 cycle^2. The P-value, which indicates the area to the right of the calculated F value in a designed confidence level, was determined at 1.30E-14. Thus, this P value was significantly less than the confidence interval of 0.05. The adjusted R-squared was 0.976, indicating a well-fitted regression in the data. Therefore, it was concluded that a linear relationship dominates the S-N above the stress amplitude of 329.8 MPa. In the same curve, the average numbers of cycles at 329.8 MPa and 326.2 MPa were 1.08E6 and 1.04E7, respectively. The small decrement in stress with a sharp increment in the fatigue cycles suggested the existence of a fatigue limit (endurance limit) in the material at 326.2 MPa. The entire curve showed a typical S-N relationship for a mild steel: a linear S-N relation with a fatigue limit.

Since the corrosion-fatigue data are compacted in Figure 5.1 (a) (encircled in gray), a magnified graph is provided in Figure 5.1 (b). Compared with the reference test in air, the results from the corrosive environments clearly showed that both chloride concentrations had a negative impact on the fatigue life. At 366.5 MPa, the clustered data in 0.1 M and 0.6 M NaCl indicated similar damages from both corrosives. Since the specimens were tested at 1000 cpm, a rough duration of two hours was required to complete the test. In contrast, the pre-pitting occurred in 24 hours. Therefore, the pre-pitting period dominated the damage to the fatigue life. Corrosion damage from both corrosives could be distinguished at 329.8 MPa and 311.5 MPa because of the observable differences in the average cycles of the two stress amplitudes. At the descending stresses from 366.5 MPa to 293.2 MPa, the correspondent cycles gradually increased until 10 million, which was defined as the fatigue limit for a non-corrosion group in this study. Thus, it was concluded that a chloride environment can shorten the service life of the pre-pitted reinforcing steel, though a fatigue limit still exists.

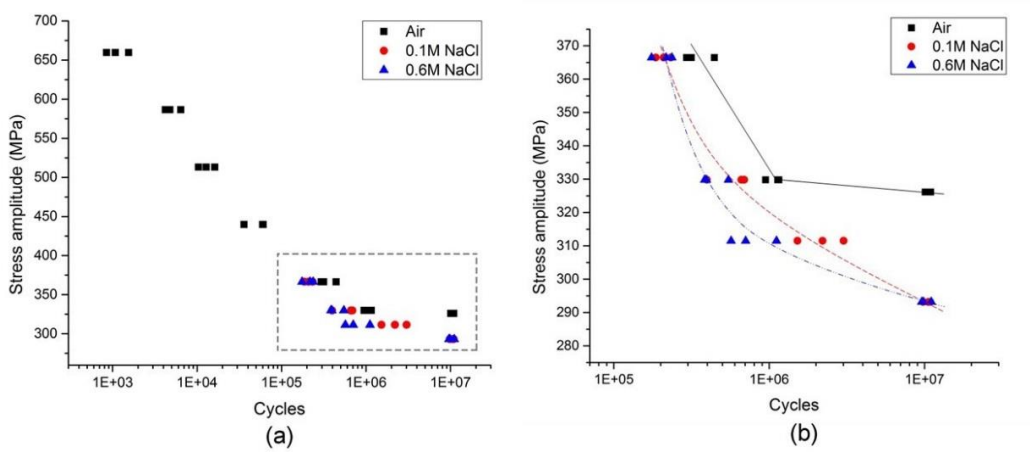

Figure 5.1. Stress-life (S-N curve) of rebar tested in corrosive environments: (a), all data; (b), data near fatigue limit.

Table 5.1. ANOVA table for linear regression of the data tested in air with a logarithmic S-N relationship above the stress of 329.8 MPa.

	Degree of Freedom	Sum of Squares / cycle^2	Mean Square / cycle^2	F Value	Probability > F
Model	1	239579.64	239579.64	695.49	1.30E-14
Error	16	5511.65	344.48		
Total	17	245091.29			

Tests under corrosion acceleration of electrochemical approach

Both corrosion and fatigue have to be accelerated during corrosion-fatigue in the rotating bending examination. In this test, the fatigue life of a stress amplitude tested in air presumably requires 75 years (AASHTO, 1977). For the same duration, corrosion is assigned for different corrosion rates, 0.05 μA/cm^2, 0.15 μA/cm^2, and 0.32 μA/cm^2. With these parameters, the applied current can be calculated by the Faradaic formula for the stresses above the endurance limit. Below the endurance limit, a number of fatigue cycles have to be defined as the maximum fatigue cycles of testing,

otherwise, the steps of corrosion and fatigue cannot be matched in CF testing. At stress amplitudes of 366.5 MPa and 329.8 MPa, the applied currents were computed according to the mean fatigue cycles at these two stress levels. Below 326.2 MPa, though, the maximum fatigue cycles were chosen to be 2 million and 5 million.

Figure 5.2 (a) presents the results of the electrochemically controlled CF tests, the CF tests in background solution, and the fatigue test in air. Due to the high density of CF data in Figure 5.2 (a), a corresponding magnified plot (enclosed by the dashed box) is presented in Figure 5.2 (b). Compared with the fatigue cycles obtained from the reference tests in air at 366.5 MPa and 329.8 MPa, the fatigue lives of specimens tested in electrochemical corrosion were shorter than those in the chloride environment, which indicated that the corrosion acceleration by an applied current was faster than by a pure chloride. Furthermore, no fatigue limit was observed in current-applied specimens.

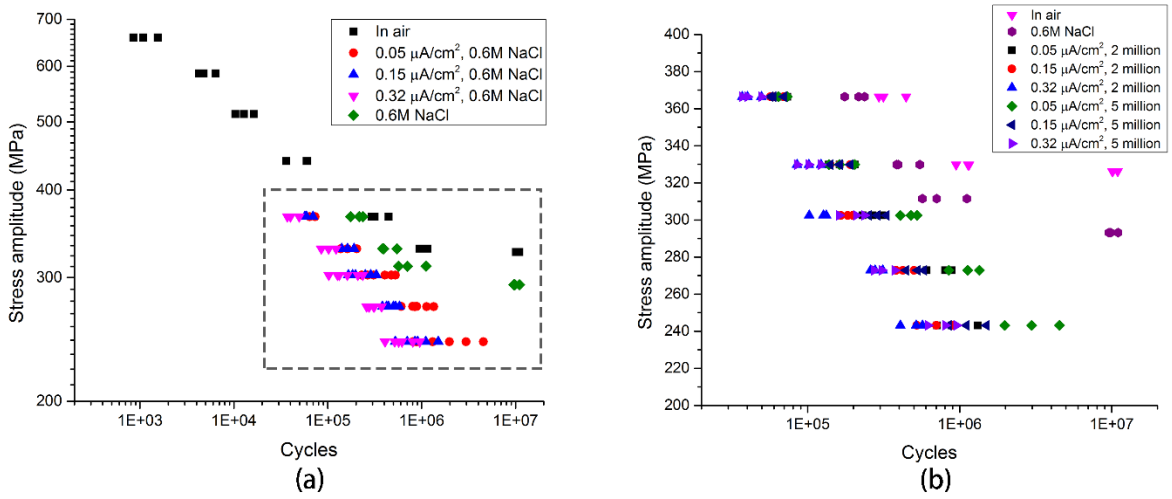

Figure 5.2. S-N curves of rebar in electrochemically accelerated corrosion environments: (a), all tested data; (b), magnification of condensed data.

The results of electrochemical corrosion seemed to have linear relations; hence, the linear regressions are carried out, and the regression lines, the summary and the ANOVA of the fittings are shown in Figure 5.3, Table 5.2, and Table 5.3, respectively. The summary of the linear regressions in Table 5.2 provides that the adjusted R-squared of these six regressions in Figure 5.3 were all above 0.931, suggesting that the linear models closely fit the selected data. To confirm

that linear fitting was the optimal fit of the CF S-N data, ANOVA tests were executed between the actual data and the modeled linear relations. The results of the ANOVA presented in Table 5.3 illustrated that all the P-values (probability > F) were smaller than 3.74E-9 and far less than the confidence interval – 0.05, and therefore demonstrated little probability of a non-linear relationship between load and cycle life. Therefore, not only the adjusted R-squared but also the results of ANOVA test results suggested that linear relationships governed the corrosion-fatigue S-N results.

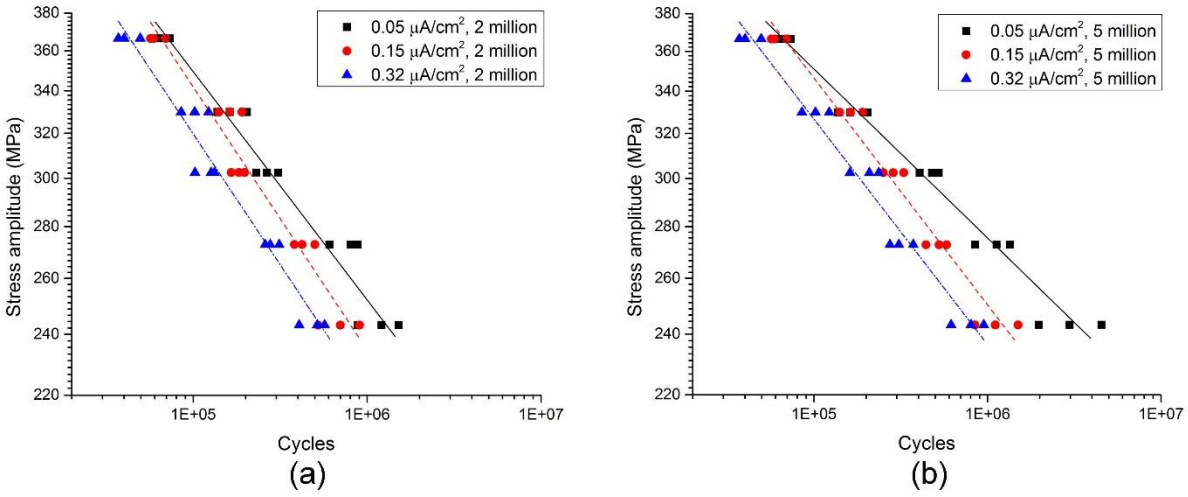

Figure 5.3. Corrosion-fatigue life at a pre-designed 0.05 μA/cm^2, 0.15 μA/cm^2, and 0.32 μA/cm^2 for 75 years and the linear regression of S-N: (a) pre-designed maximum 2 million cycles at stress amplitude of 302.5 MPa and below; (b) pre-designed maximum 5 million cycles at stress amplitude of 302.5 MPa and below

In the results of two million and five million groups, Figure 5.3 (a) and (b) show that: the higher the applied current, the lower the respondent fatigue cycles were at all stress amplitudes. In addition, the fitted parameters of the linear regressions are explored in Table 5.2. In the group of two million cycles, the fitted line of 0.05 μA/cm^2 had a slope of – 0.142, higher than – 0.163 for the other two lines, suggesting a decreasing effect of corrosion in CF. Due to the fact that the two corrosion rates (0.15 μA/cm^2 and 0.32 μA/cm^2) shared the same slope value and close standard errors in the regressions of 0.011 and 0.009, it was concluded that both corrosion rates had a similar increment rate of fatigue life on CF at decreasing stresses. The similar relationship of slopes was also observed in the results obtained from test with the maximum cycles of five million. Compared with the tests at two million cycles, tests assigned with the five million cycles actually prolonged

the corrosion duration. Thus the corrosion effect was less severe than the damage resulting from the same stress, and the corresponding slopes in the S-N relations were lower shown in Table 5.2.

Table 5.2. Summary of linear regressions of S-N data in both 2 million and 5 million groups

	Intercept		Slope		Statistics
	Value	Standard Error	Value	Standard Error	Adjusted R-Square
0.05 μA/cm^2, 2 million	3.252	0.056	-0.142	0.010	0.931
0.15 μA/cm^2, 2 million	3.351	0.0600	-0.163	0.011	0.938
0.32 μA/cm^2, 2 million	3.317	0.048	-0.163	0.009	0.956
0.05 μA/cm^2, 5 million	3.071	0.026	-0.105	0.005	0.974
0.15 μA/cm^2, 5 million	3.246	0.037	-0.141	0.007	0.968
0.32 μA/cm^2, 5 million	3.216	0.037	-0.140	0.007	0.967

Table 5.3. ANOVA of linear regressions of S-N data in both 2 million and 5 million groups

		Degree of Freedom	Sum of Squares	Mean Square	F value	Prob>F
0.05 μA/cm^2, 2 million	Model	1	0.0542	0.0541	191.28	3.74E-9
	Error	13	0.0037	2.83E-4		
	Total	14	0.0578			
0.15 μA/cm^2, 2 million	Model	1	0.0545	0.0545	213.61	1.90E-9
	Error	13	0.0033	2.55E-4		
	Total	14	0.0578			
0.32 μA/cm^2, 2 million	Model	1	0.0555	0.0555	304.78	2.10E-10
	Error	13	0.0024	1.82E-4		
	Total	14	0.0578			
0.05 μA/cm^2, 5 million	Model	1	0.0564	0.0564	516.52	7.53E-12
	Error	13	0.0014	1.09E-4		
	Total	14	0.0578			
0.15 μA/cm^2, 5 million	Model	1	0.0561	0.0561	429.88	2.41E-11
	Error	13	0.0017	1.31E-4		
	Total	14	0.0578			
0.32 μA/cm^2, 5 million	Model	1	0.0561	0.0561	406.25	3.44E-11
	Error	13	0.0018	1.38E-4		
	Total	14	0.0578			

5.2 Fracture analysis

Fatigue fracture failure usually initiates from the fracture origin – persistent slip bands (PSB), and their presence nucleates a micro-crack that grows to a macro-crack until the critical fracture failure. Pits presumably nucleate on the PSBs if chlorides exist (Zhao et al., 2012). As pits propagate, stress concentrates in them which finally results in the first crack. Thereafter, cracks propagate with the cyclic loading until fatigue failure (Medved et al., 2004; Organization, 2011; Rokhlin et al., 1999).

A typical fracture surface of a specimen under CF testing was observed by SEM as shown in Figure 5.4 (a). Similar to most of non-corroded rotating bending fracture surfaces, the presence of multiple ratchet lines illustrated that multiple origins initiate cracks before the final ductile fracture failure of a specimen. The elliptical zone encircled by the dashed line near the center was the final unstable fracture failure of the sample. The magnified morphologies of the elliptical zone are magnified in Figure 5.4 (b), (c), and (d). These microstructural figures clearly showed the dimples during the ductile tensile fracture that confirmed the encircled zone as the final fractural surface.

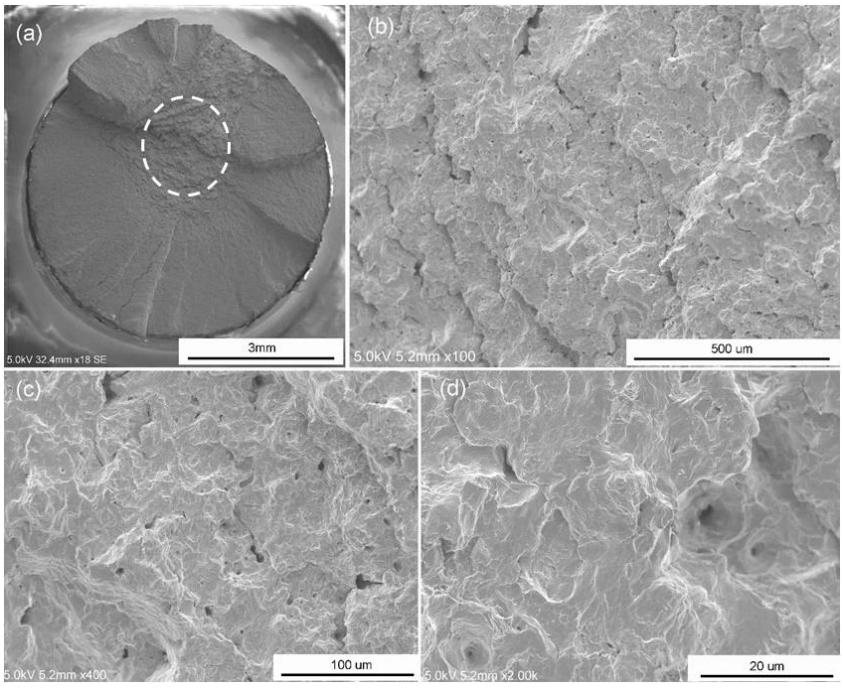

Figure 5.4. SEM of fracture surface after corrosion-fatigue test: (a), entire fracture surface; (b), dimple zone 100X; (c), dimple zone 400X; (d) dimple zone 2000X.

After fatigue failure, the fracture surface was scanned to identify the fracture origins. On the edge of the sample surface after the CF test, the radiation feature marked by the solid black arrowheads in Figure 5.5 (a) and (b) provided two fractural initiation sites – two typical pits – along the tips of both white arrowheads. Cracks were initiated from both pits until the fracture failure.

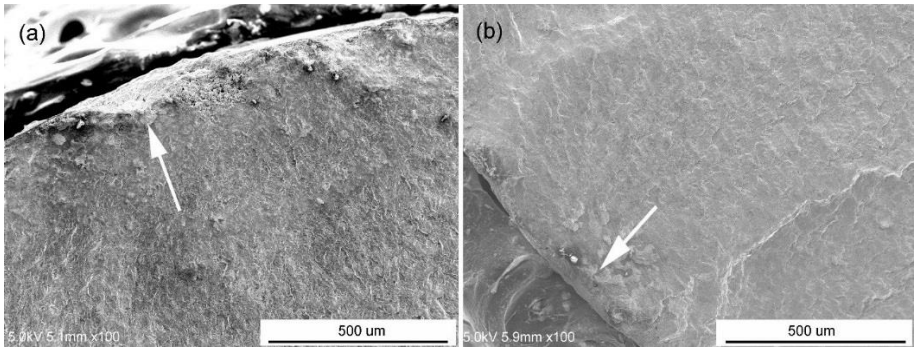

Figure 5.5. Pits on the fracture surface of a failed specimen: (a) crack origin from a pit; (b) crack origin from another pit.

Striations, another typical feature of fatigue failure in BCC, HCP, and FCC metals, are usually observed only on a magnified fracture surface because of their small sizes. Thousands or even tens of thousands of striations form a single clamshell marking on the service failure fracture surfaces of metals. The clustered clamshell markings are visible by naked eye on the fracture surfaces, however, their visibility is highly correlated with the material/environment. Due to the environmental and/or metallurgical or the service situations, striations may appear clearly or poorly. Hence, it is hard to have visible clamshell markings with unclear striations.

Each fatigue loading cycle advances the increment of the crack tip and leaves a mark of the loading on the fracture surface as a striation (Hertzberg, 2012). A striation usually grows perpendicular to the crack growth, and the width of a striation depends on the stress range. In this test, some suspicious and broken clamshell markings could be observed perpendicular to the ratchet lines in Figure 5.6 (a). At higher magnifications near the pit in Figure 5.6 (a) and (b), the clearer microscopic striations are seen in Figure 5.6 (c) and (d). Even though these striations were discontinuous and some were corroded – seen in the dashed box in Figure 5.6 (d), their appearance strongly implied the existence of striations because of the fatigue loading. In addition, Figure 5.6

(d) also shows that a broken striation was observed caused by corrosion (enclosed in the dashed box).

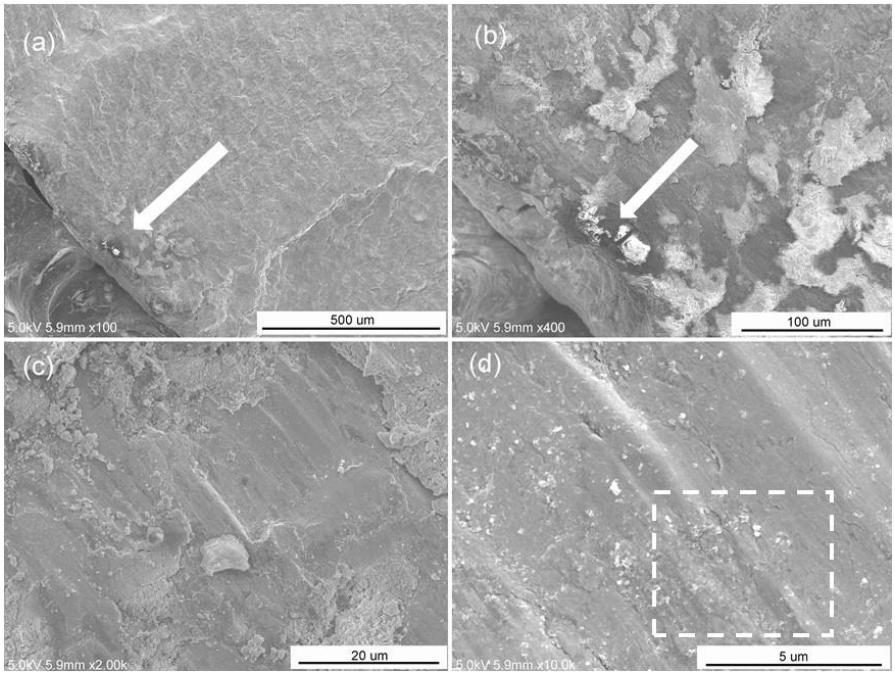

Figure 5.6 Pit on fracture surface and corroded striations: (a), crack origin from a pit; (b), 400X of the pit; (c), 2000X of the striations around the pit; (d), broken striations (indicated by the dashed box).

In the fatigue failure process without corrosion, stress concentrates on the PSB and initiates tiny cracks. Although the small cracks are mainly unstable, some of them propagate thereafter at steady growth rates. Finally, the growth of cracks becomes unstable, reaches the critical rate, and then results in fracture failure. Without corrosion, the existing crack surface before fracture failure is exposed to air, thus no corrosion products would deposit on the surface.

Furthermore, in the CF test, specimens were immersed in chloride-contaminated simulated concrete pore solutions with a dynamic potential applied between the specimen and corrosive. Thus, before the fracture failure, the existing cracks in specimens underwent accelerated corrosion. In other words, corrosion products could be examined on the fracture surface prior to the final fracture failure, especially surrounding the fractural origins or pits. Since iron accounts for 97.925% of the content in the tested rebar (Table 3.1), the elemental distributions around the fractural origin

implied the existence of iron and oxygen beyond the CF test. In the same scanned region of EDS, Figure 5.7 and Figure 5.8 provide the all-layered mapping and the atomic spectrum, respectively. Figure 5.8 shows that: the atom content of iron and oxygen were 51.2% and 43.1% respectively; therefore, the sum of iron and oxygen was 94.3%. Hence, iron and its oxidation products dominated the compounds around the pit. Moreover, the element mapping of iron and oxygen presented in Figure 5.9 showed that both elements were almost evenly distributed around the pit.

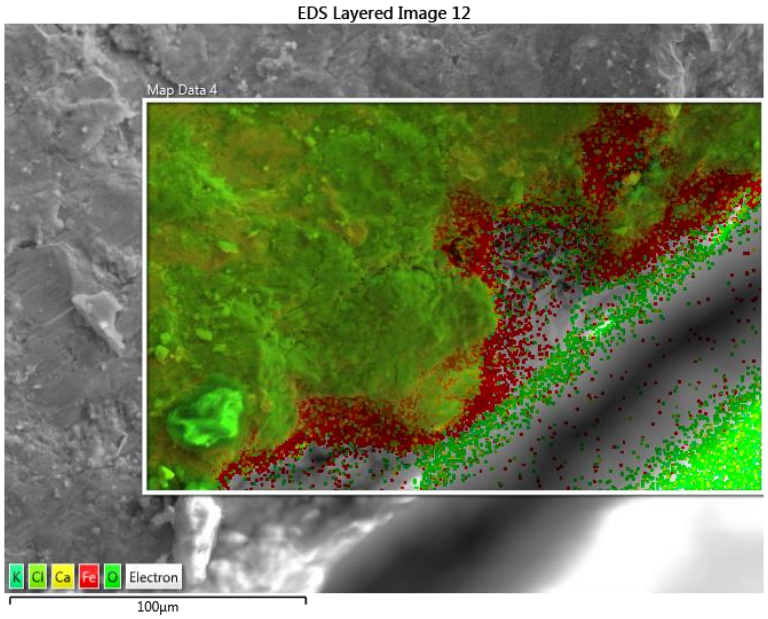

Figure 5.7. Fracture surface layered EDS mapping after rotating bending test

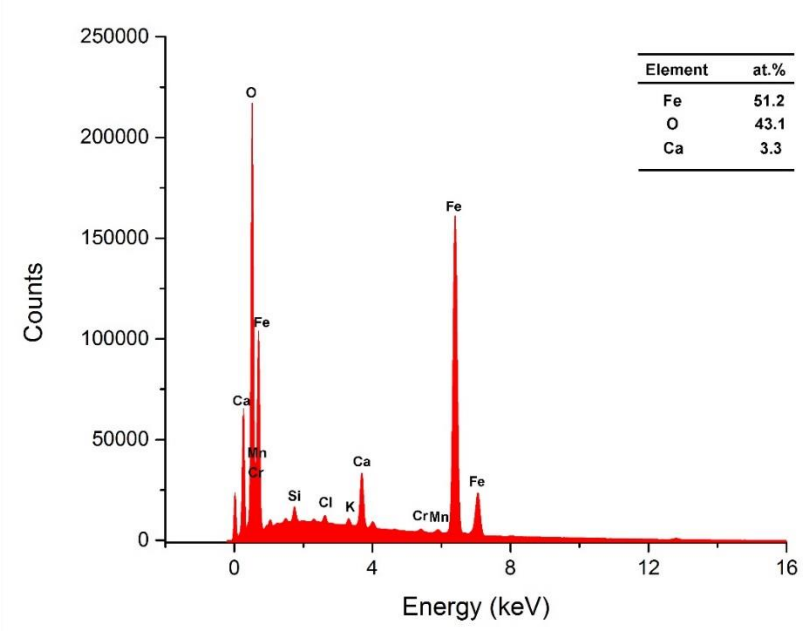

Figure 5.8. Rotating bending test specimen fracture surface element spectrum-EDS

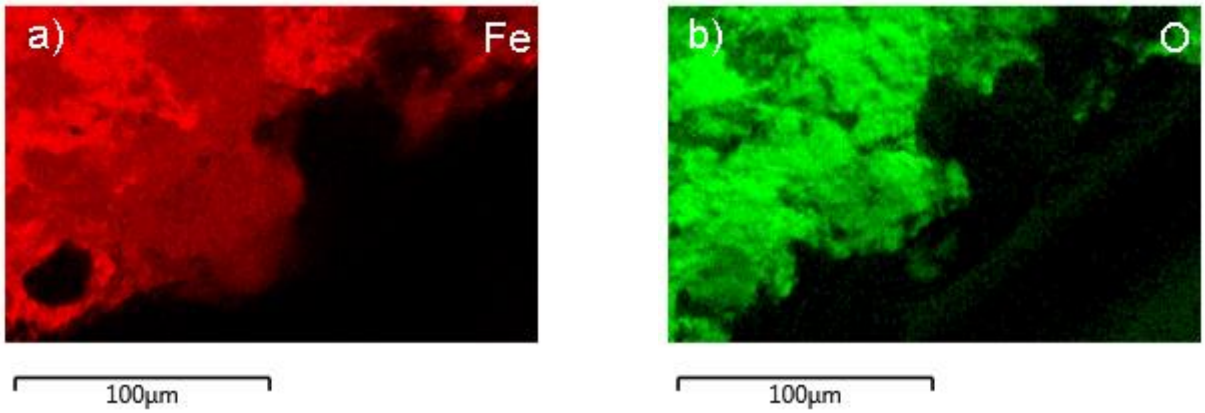

Figure 5.9. Rotating bending test specimen fracture surface element mapping

5.3 Service life prediction by S-N curves

The fundamental idea behind using the S-N curves to estimate fatigue life of a metal under a certain load is based on the property of metals, especially steels, that a linearly logarithmic relationship

exists between the stress and the number of cycles from the fatigue limit to 90% of the ultimate tensile strength (UTS). In other words, given this linear relationship and the applied stress amplitude, the approximate fatigue cycles could be found from the linear relationship after a few corrections of the tested parameters. The main procedures of this approach are: firstly use the UTS to estimate the fatigue limit, then build the linear function of S-N data, and finally find the fatigue cycles at the desired stress amplitude.

The evaluation of the fatigue limit starts with assessing the effect of the applied mean stress and then other factors such as component size, loading type, notch, surface finish, and surface treatment. However, the corrections for these factors are applied to the fatigue limit rather than the S-N curves. Thus, this study firstly applied the mean stress effect modification on S-N curves according to the testing conditions of RC beams. Goodman and Gerber relations shown in Eq. (3.3) and (3.4) were utilized in the correction, and the corrected stresses were then plotted to the new S-N curves:

$$\text{Goodman relation: } \sigma_a = \sigma_{fat}\left(1 - \frac{\sigma_m}{\sigma_{ts}}\right) \tag{3.3}$$

$$\text{Gerber relation: } \sigma_a = \sigma_{fat}\left(1 - \left(\frac{\sigma_m}{\sigma_{ts}}\right)^2\right) \tag{3.4}$$

Referring to the S-N curves in Figure 5.3, with the given the mechanical properties of reinforcing steel (yield strength of 440 MPa and tensile strength of 666 MPa), and an applied stress ranging from 22 MPa to 220 MPa, Figure 5.10 gives the corrected mean stress effect according to Eq. (3.3) and (3.4). Figure 5.10 presents that, for both the Goodman and Gerber corrections, a positive mean stress degrades the fatigue strength, agreeing with the results of past studies (Hertzberg, 2012; Milella, 2013).

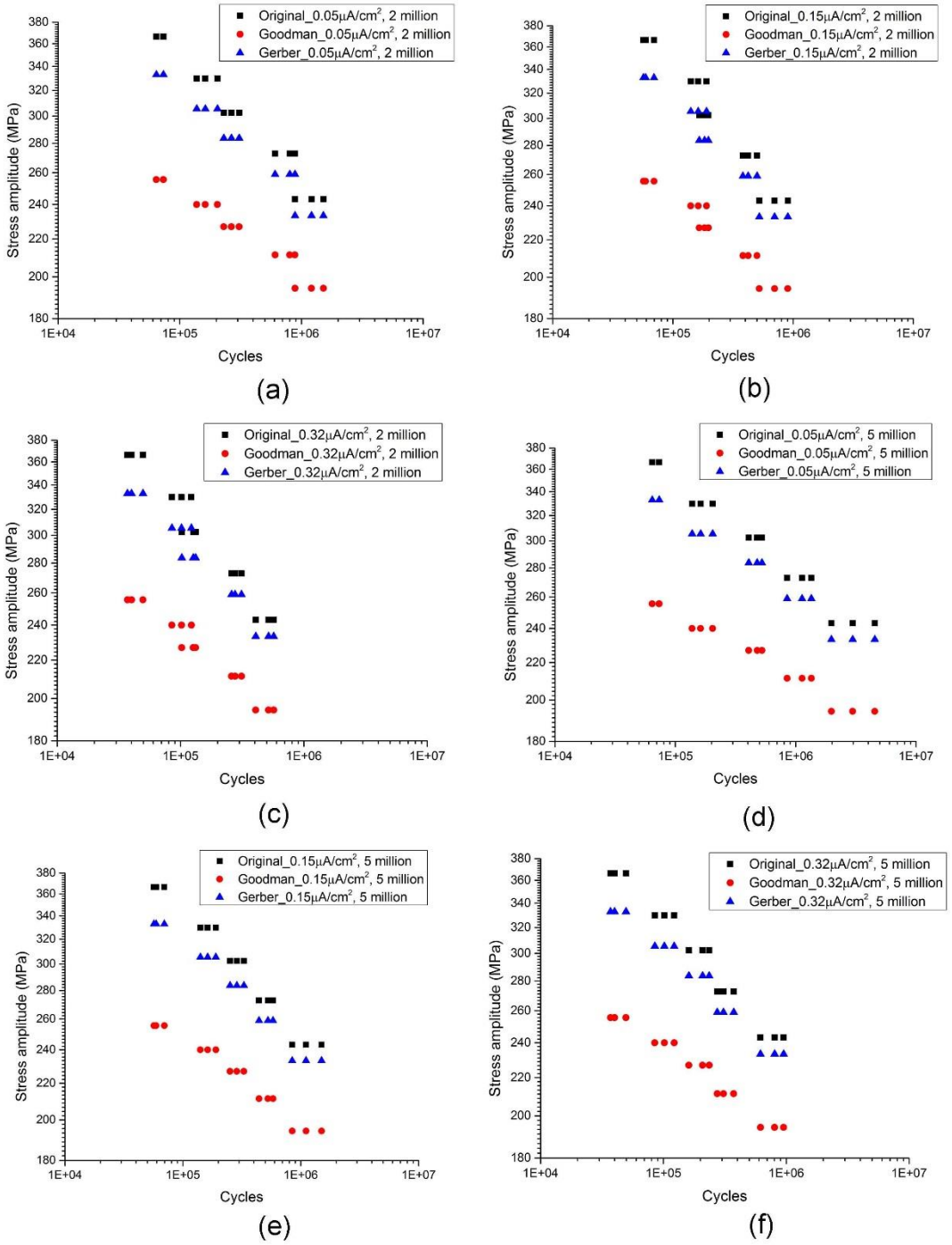

Figure 5.10. The fatigue cycles with the corrected mean stress effect at three pre-designed corrosion rate for a duration of 75 years and the two types of limit cycles: (a), 0.05 μA/cm^2, 2 million cycles; (b), 0.15 μA/cm^2, 2 million cycles; (c), 0.32 μA/cm^2, 2 million cycles; (d), 0.05 μA/cm^2, 5 million cycles; (e), 0.15 μA/cm^2, 5 million cycles; (f), 0.32 μA/cm^2, 5 million cycles.

Besides the mean stress, the corrosion effect should also be taken into account for the correction of S-N curves as a form of notch effect because of the chloride-induced pits on the specimen surface. A notch factor was calculated according to the stress concentration factor and the geometry of the notch as shown in Eq. (3.7):

$$K_f = 1 + \frac{K_t - 1}{1 + a/r} \tag{3.7}$$

$$a = 0.0254\ (\frac{2070}{S_u})^{1.8} \text{ with } S_u \text{ in MPa and } a \text{ in mm} \tag{3.8}$$

The notch effect was then used to modify the mean stress using Goodman line and Gerber parabola. From the literature (J. Newman, 1999), the elastic stress concentration factor is 3.0 MPa√m for a reinforcing steel. The radius of the notch root is calculated by the stress intensity factor formula Eq. (3.13) with an elastic stress concentration factor:

$$K_I = \sigma\sqrt{\pi S}\, f(\frac{a}{c}) \tag{3.13}$$

Given the metal properties, e.g. the ultimate tensile strength, the notch factor K_f can be determined. Since K_t is 3.0 MPa√m, a and r are positive values, the value of K_f is larger than 1 in reinforcing steel. A notch in the specimen causes the reduction of the fatigue strength after adding the notch factor to Goodman and Gerber relations as shown in Eq. (3.9) and (3.10):

$$\text{Corrected Goodman relation: } \sigma_a = \frac{\sigma_{fat}}{K_f}\left(1 - \frac{\sigma_m}{\sigma_{ts}}\right) \tag{3.9}$$

$$\text{Corrected Gerber relation: } \sigma_a = \frac{\sigma_{fat}}{K_f}\left(1 - \left(\frac{\sigma_m}{\sigma_{ts}}\right)^2\right) \tag{3.10}$$

After the corrections of mean stress and notch effect, the newly obtained S-N curves can be applied to predict the fatigue cycles of RC beam under a CF environment.

6 Pitting-corrosion-fatigue approach for estimating corrosion-fatigue of rebar in simulated concrete pore solution

Engineering failure usually causes enormous economic damage and possible loss of life. Scientists (Clark, 2001; Hoeppner, 1979; Murtaza & Akid, 2000; Wang, 2003; Zhang & Mahadevan, 2001) performed abundant studies on the development of stress concentrations on structure surfaces that nucleate cracks, the propagation of which causes final fracture failure. They also developed models of the entire degradation process in order to estimate the fatigue life of a structure in service.

This chapter presents the test data for estimating corrosion-fatigue (CF) of rebar in simulated pore solution (SPS) by the fracture mechanics approach, which includes the four stages of this model: pit nucleation and pit growth, pit-to-crack transition, crack growth, and fracture failure. Prior to thoroughly presenting the service life evaluation by fracture mechanics, the growth of a pit in chloride contaminated concrete pore solution and the propagation of a crack in a corrosion-fatigue environment have to be determined. Pit growth consists of the nucleation of a pit and its propagation rate over time. Crack propagation, on the other hand, includes the nucleation of a crack, the instable propagation of a small crack, the stable propagation of a long crack, and the final unstable growth of a crack near fracture failure.

In this study, pit growth is composed of two types of investigations, short term pitting and long-term pitting. Short term pitting examines the initiation of a pit and the difference in pit sizes in SPS mixed with 0.1 M, 0.6 M, and 1.5 M NaCl. Long-term pitting, on the other hand, mainly evaluates the development of the maximum pit depth over time in a combination of chloride concentration and pH of the solution.

The crack propagation determines a crack on the rebar from the threshold of the stress intensity factor ΔK_{th} until the stress toughness K_{Ic}. In this study, both ΔK_{th} and K_{Ic} of a rebar disk were measured in an SPS environment mixed with 0.6 M NaCl. Crack growth behavior of rebar disks were examined in diverse environments, such as in air, 0.6 M NaCl + SPS, applied current (1 mA and 5 mA), 0.6 M NaCl, 0.1 M H_3PO_4, and 1.0 M H_3PO_4.

Finally, two types of Fracture Mechanics models, the direct approach and indirect approach, were introduced to predict the service life of a corrosive environment by computing fatigue cycles involving all four stages of fracture mechanics.

6.1 Pitting growth test results

6.1.1 Pitting initiation

Figure 6.1 shows the morphology evolution of pit initiation in chloride contaminated SPSs. Figure 6.1 (a) shows that, the rebar surface contained flaws prior to corrosion since entrained air bubbles with various sizes were observed. After two hours of corrosion, polygon-shaped pits are seen in Figure 6.1 (b). Regular elliptical pits shown in usual publications (Landolt, 2007; Szklarska-Smialowska, 2005) were found in Figure 6.1 (c) and (d) under a corrosion period of 12 hours and 24 hours, respectively.

The polygonal 2-hour-corrosion pit shapes in Figure 6.1 (b) indicated that chlorides in 13.3 pH solution corrode reinforcing steel lightly on the surface. Light corrosion usually happened at low corrosion potentials and short corrosion periods. According to the previously measured corrosion current of high pH SPS mixed with 0.1 M chloride, the corrosion current was 0.115 $\mu A/cm^2$, which is much lower than the corrosion current density in low pH solutions of around 100 $\mu A/cm^2$ (Marcus, 2002). Because high pH usually prevents corrosion from occurring and the SPS used in the test had a pH of 13.3, it was reasonable to conclude that it was the SPS resulting in light corrosion on reinforcement surface, at least for the duration of the tests.

Shape change of the pits was observed from a polygon shown in Figure 6.1 (b) to an ellipse shown in Figure 6.1 (c) and (d). This could be explained by a change in corrosion potential as discussed in Sundaresan's study (Sundaresan, 1989). Marcus (Marcus, 2002) holds the view that a high corrosion potential leads to a high local current density, which thereafter increases the corrosion production on the surface of pits resulting in a round pit configuration. Low corrosion potentials may not have sufficient corrosion current to form a round pit even over an accumulated corrosion period. Figure 6.1 clearly shows that the corrosion potential at the beginning (2-hour corrosion) could not reach the necessary potential to produce elliptical corrosion pits. However, at 12 and 24

hours corrosion, the pitting ability could produce elliptically shaped pits because of the longer corrosion periods.

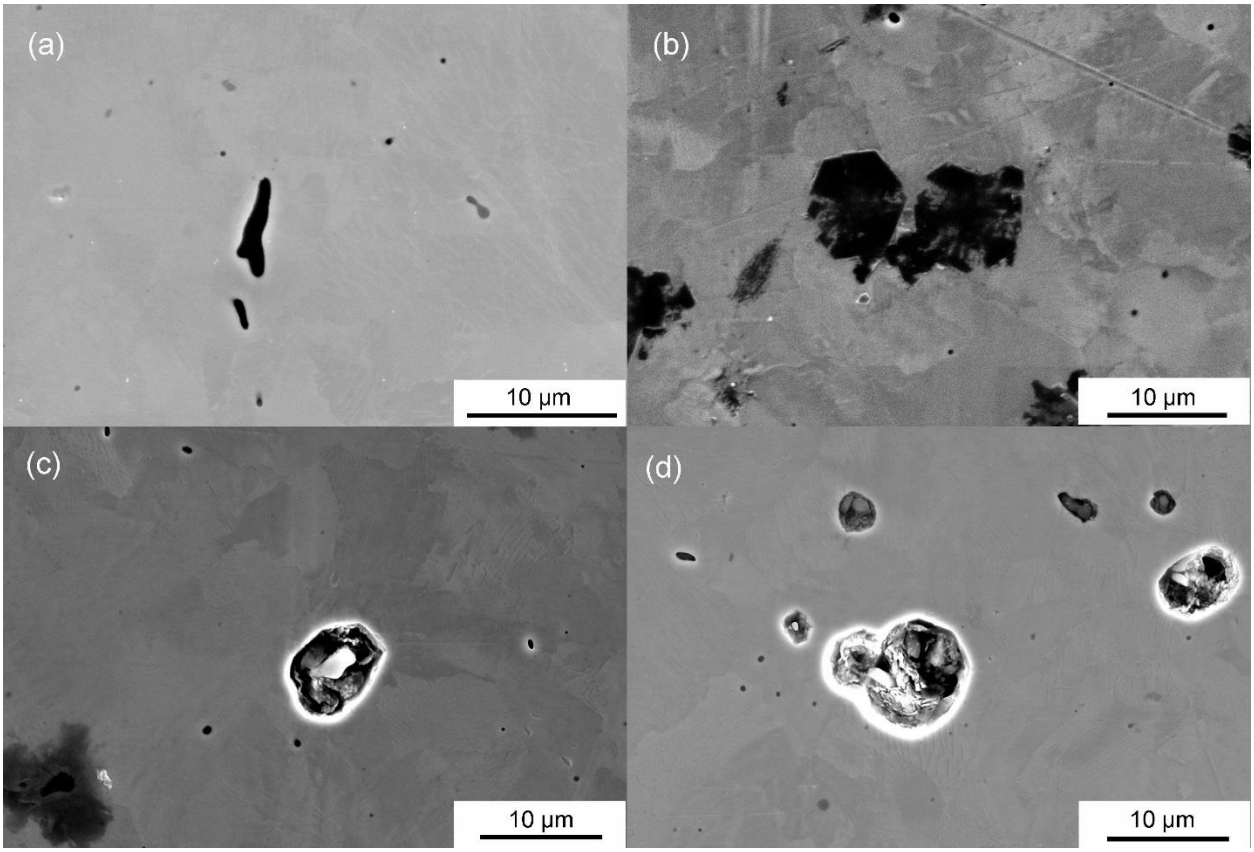

Figure 6.1. Pit initiation in chloride contaminated high pH environment: (a), 0 hour; (b), 2 hours; (c), 12 hours; (d), 24 hours.

Figure 6.2 to Figure 6.4 represent the SEM images of pits at high pH (pH 13.3) SPS mixed with 0.1 M, 0.6 M, 1.5 M chloride after a corrosion period of 2 hours, 12 hours, and 24 hours, respectively. As can be seen from these three figures, the number of pits increased with an increase of chloride concentrations from 0.1 M to 1.5 M at a pitting period of 12 hours and 24 hours but not at two hours.

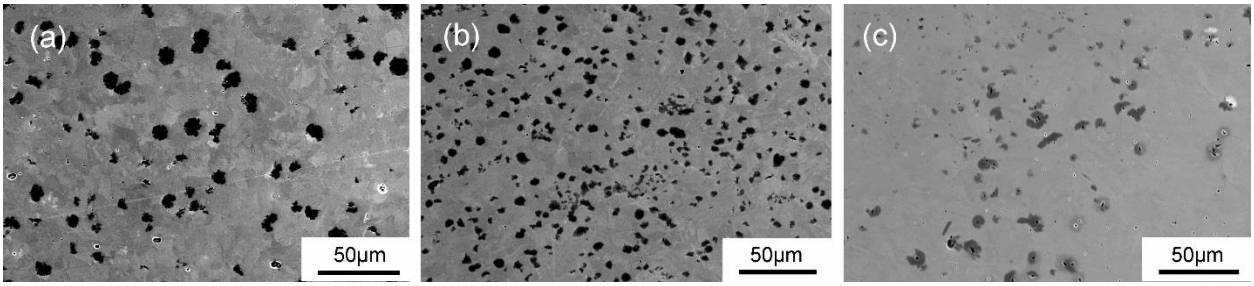

Figure 6.2. Pit size at 0.1 M, 0.6 M, 1.5 M chloride mixed high pH SPS after 2 hours of corrosion: (a), 0.1 M; (b), 0.6 M; (c), 1.5 M.

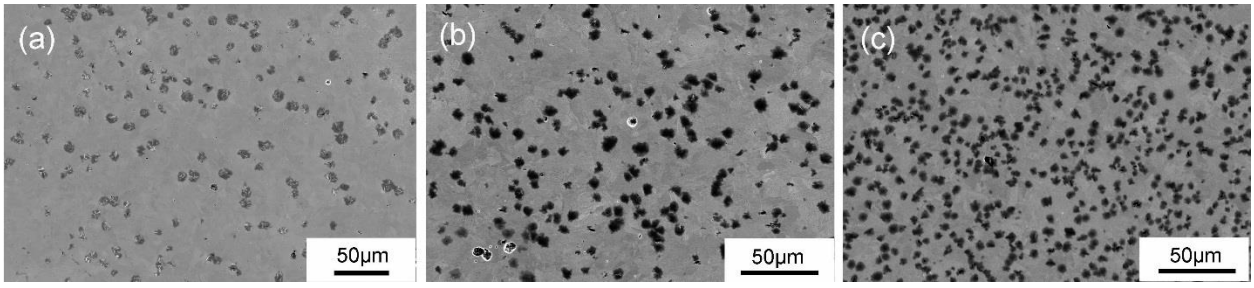

Figure 6.3. Pit size at 0.1 M, 0.6 M, 1.5 M chloride mixed high pH SPS after 12 hours of corrosion: (a), 0.1 M; (b), 0.6 M; (c), 1.5 M.

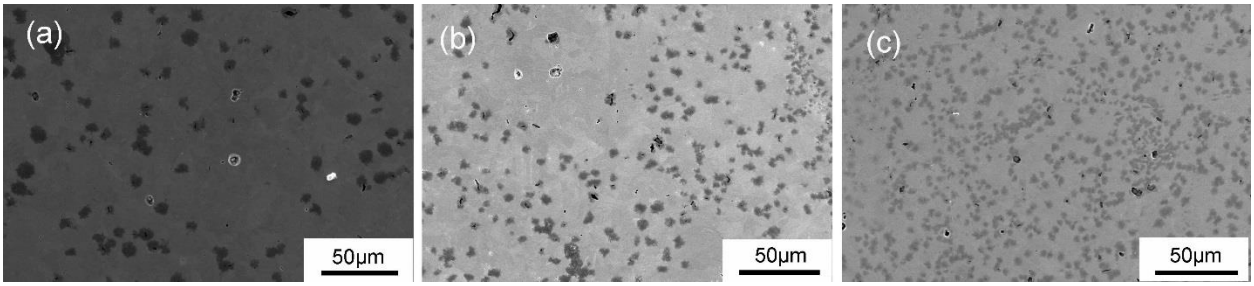

Figure 6.4. Pit size at 0.1 M, 0.6 M, 1.5 M chloride mixed high pH SPS after 24 hours of corrosion: (a), 0.1 M; (b), 0.6 M; (c), 1.5 M.

Based on the assumption that pits are elliptical, the major and the minor axes of each pit were measured and the area of each pit was computed. Table 6.1 provides the statistics of the pit sizes at a combination of pitting time (2 hours, 12 hours, 24 hours) and chloride concentration (0.1 M, 0.6 M, 1.5 M). The pit sizes data indicated that, the pit diameter difference between the major axis and the minor axis was small, ranging from 0.14 μm to 2.50 μm, under all combinations. However,

the deviations of the diameters were relatively large, ranging from 1.81 μm to 4.78 μm. In comparison, the diameter values ranged from 4.69 μm to 8.35 μm. The large deviation in diameter generated a large deviation in the average area of a single pit, ranging up to 28.47 μm^2.

Table 6.1. Statistics of pits size after 2 hours, 12 hours, and 24 hours of pitting in 0.1 M, 0.6 M, and 1.5 M chloride mixed high pH SPS

Corrosion period (hour)	Chloride concentration (M)	Average elliptical pit dimensions		Single pit average area (μm^2)
		Major axis (μm)	Minor axis (μm)	
2	0.1	8.35±3.38	5.85±3.43	40.16±27.46
	0.6	7.16±2.46	5.55±1.81	31.83±16.95
	1.5	6.99±4.78	4.69±2.69	25.72±20.9
12	0.1	7.41±4.05	6.97±4.04	40.88±28.47
	0.6	6.89±3.14	6.64±3.83	36.57±26.09
	1.5	5.94±2.65	5.80±1.95	26.95±14.16
24	0.1	8.17±2.87	7.49±3.33	49.42±26.42
	0.6	7.36±2.70	5.38±1.95	31.19±14.32
	1.5	6.15±3.17	5.21±2.64	24.98±16.58

Comparing the dimensions and the average area of pits at a pitting time of 2 hours, 12 hours, and 24 hours, one finds out that pit size fluctuated with the increase of corrosion time. However, the size and the average area of a pit decreased with the increase of chloride content at chloride levels of the same pitting period. Figure 6.2 to Figure 6.4 show that the density of pits rose along with chloride concentration. This phenomenon might be attributed to the competitive behavior of pitting under a chloride environment. A higher chloride concentration or a longer pitting period gives the corrosive a higher capacity to generate pits on metal surface. From the electrochemical standpoint, the pitted area of the micro-pit acts as an anode while the area surrounding the pit acts as a cathode

that is protected from corrosion. In a corrosive contaminated by a low chloride concentration but still above the critical threshold, the size of a pit could expand to a large size since the distance between two pits is far enough to guarantee the required cathodic area for sustaining the development of pitting. At high chloride content, for example 1.5 M in this study, the potential of pitting is more severe than what it is in 0.1 M NaCl and this causes the competition of pitting areas including both the anode and the cathode, the result of which leads to smaller pits in 1.5 M NaCl solutions.

Pitting initiation time

Even though some researchers (Acuña-González, González-Sánchez, Dzib-Pérez, & Rivas-Menchi, 2012) propose that the empirical pit-depth growth equation should be written as $d = At^B$, where *d* is the pit depth, *t* is the pitting time, *A* and *B* are the constants associated with the material and the corrosive environment, some other scientists (C. Q. Li, Yang, & Melchers, 2008; R E Melchers, 2005) suggest the equation should be written as $d = A(t - t_0)^B$, where t_0 is the pitting initiation time. In terms of t_0 in this study, Figure 6.2, Figure 6.3, and Figure 6.4 show pits with visible depth. Thus, it may be concluded that the pitting initiation time of rebar in SPS mixed with chlorides was less than two hours. Although two hours is a short time in the service life of an RC structure, e.g. 75 years, it is unclear whether or not if it should be ignored in the development of pits so far since the growth rate of a pit is unknown.

6.1.2 Long-term pit growth

In order to generate the relationship between the pit depth on rebar and the corrosion time under the concrete environment, this study simulated the process by immersing polished rebar samples in a simulated concrete pore solution. Several possible factors were also taken into consideration, e.g. chloride content, pH, and surface treatment.

Morphological examination with SEM

Figure 6.5 shows the one-month pitted specimen surfaces under the combined environment of two SPSs – the normal high pH (13.3) SPS and the carbonated SPS (pH 9.3) – and four types of chloride

contamination – 0 M, 0.1 M, 0.6 M, and 1.5 M. Figure 6.5 (a) and (e) present the specimens immersed in non-chloride SPSs. Both figures show no visible pits or corrosion product on the exposed surfaces.

In the high pH SPS mixed with a chloride concentration of 0.1 M, 0.6 M, and 1.5 M, the morphology of the pitted samples for a month are seen from Figure 6.5 (b) to (d). Little difference was observed on the pitted sample surfaces from these images. In the carbonated SPS mixed with the same order of chloride concentrations, the one-month pitted sample surfaces are presented from Figure 6.5 (f) to (h). Clearly, severe pitting was observed in 0.6 M and 1.5 M NaCl; however, no apparent pitting is seen in 0.1 M NaCl, suggesting that the pitting ability of 0.6 M and 1.5 M NaCl is higher than that in 0.1 M NaCl. Compared with the corroded specimens in high pH SPS, the specimens immersed in 0.6 M and 1.5 M NaCl in the carbonated SPS had rougher surfaces, suggesting that a lower pH facilitated the occurrence of pitting.

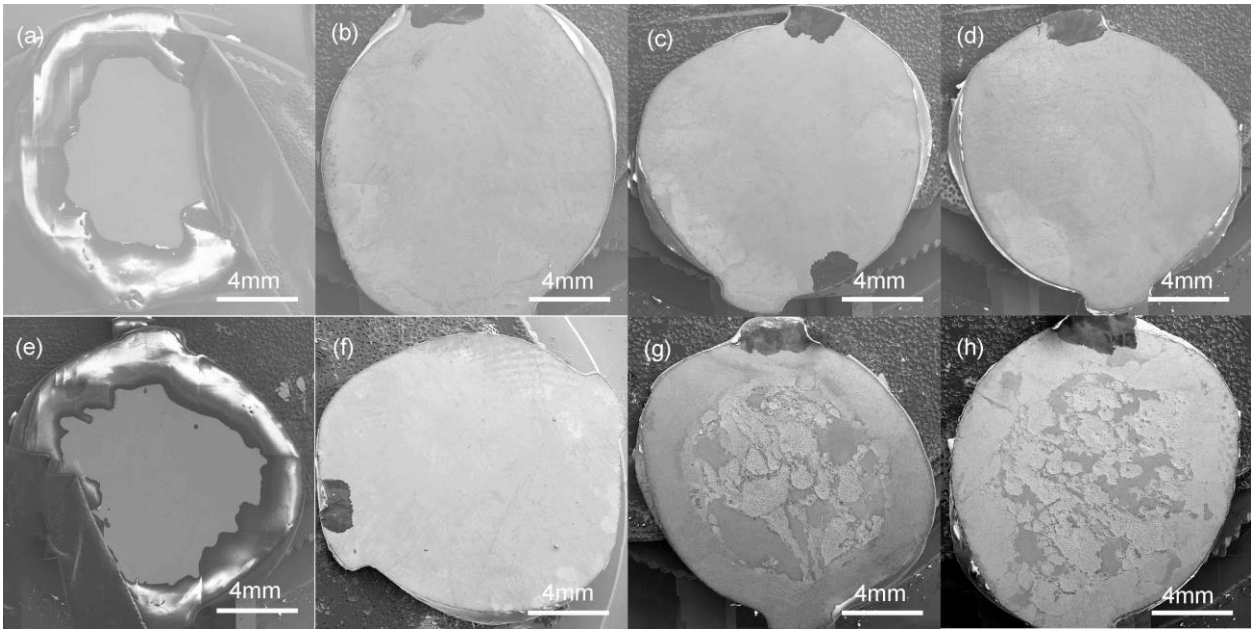

Figure 6.5. Specimens' surfaces after one-month pitting: a, 0 M Cl + pH 13.3 SPS; b, 0.1 M Cl + pH 13.3 SPS; c, 0.6 M Cl + pH 13.3 SPS; d, 1.5 M Cl + pH 13.3 SPS; e, 0 M Cl + pH 9.3 SPS; f, 0.1 M Cl + pH 9.3 SPS; g, 0.6 M Cl + pH 9.3 SPS; h, 1.5 M Cl + pH 9.3 SPS.

Besides pitting corrosion, another type of corrosion was also observed beneath some of the coated specimen surfaces: crevice corrosion. In the dash-box of Figure 6.6 (a), magnified in (b), two spots with honeycomb-shaped crevice corrosion were detected. Even though the rust preventative adhered tightly with the rebar disk surface, some gaps may still occur between the coating and the specimen surface, and crevice corrosion was nucleated in the presence of oxygen.

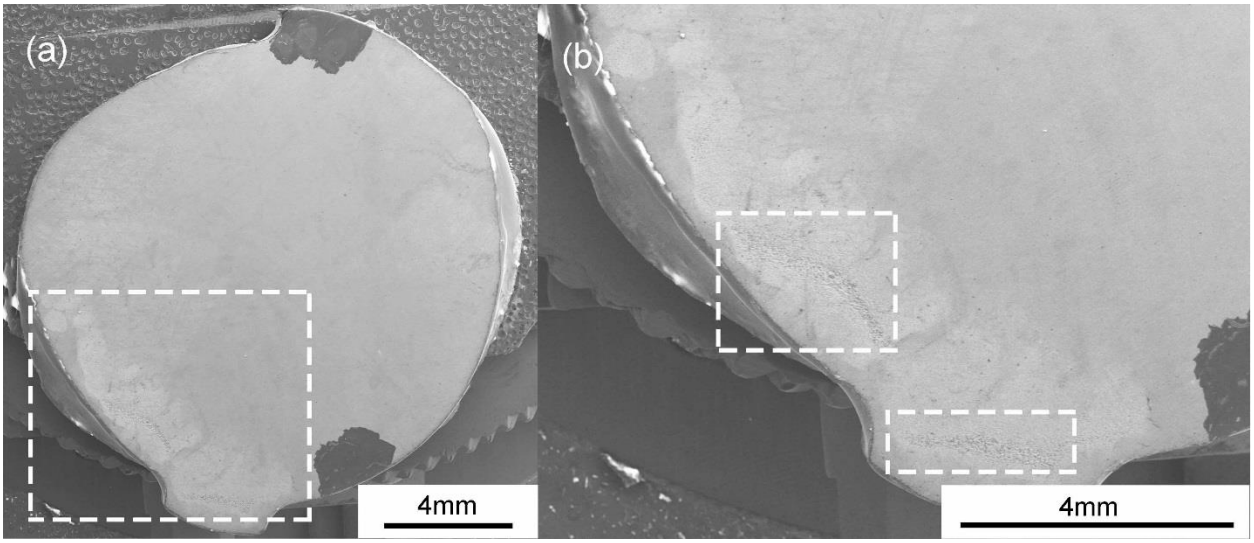

Figure 6.6. Crevice corrosion at a corrosive combination of one-month corrosion and high pH SPS mixed with 0.6 M NaCl: (a), a large area of crevice corrosion (dashed box); (b), two spots of crevice corrosion (two dashed boxes).

Figure 6.7 shows the specimen surfaces after a corrosion period of one month for coupled effects of the surface polish and the aggressiveness of solutions. For specimens immersed in pH 13.3 SPS, light pitting was seen on specimens with their surfaces polished to 1 μm and 15 μm, as shown in Figure 6.7 (a) and (b), respectively. In terms of specimens immersed in pH 9.3 SPS, severe pitting was observed on specimens with a surface treatment of 1 μm and 15 μm seen in Figure 6.7 (c) and (d). Hence, the visual examination of samples indicated that there was no obvious difference between the two types of surface treatments at a corrosion period of one month. The actual pitted depth in the combined effect of surface treatment and the pH of the corrosives was further examined by a profilometer; the data of pit depth were analyzed later.

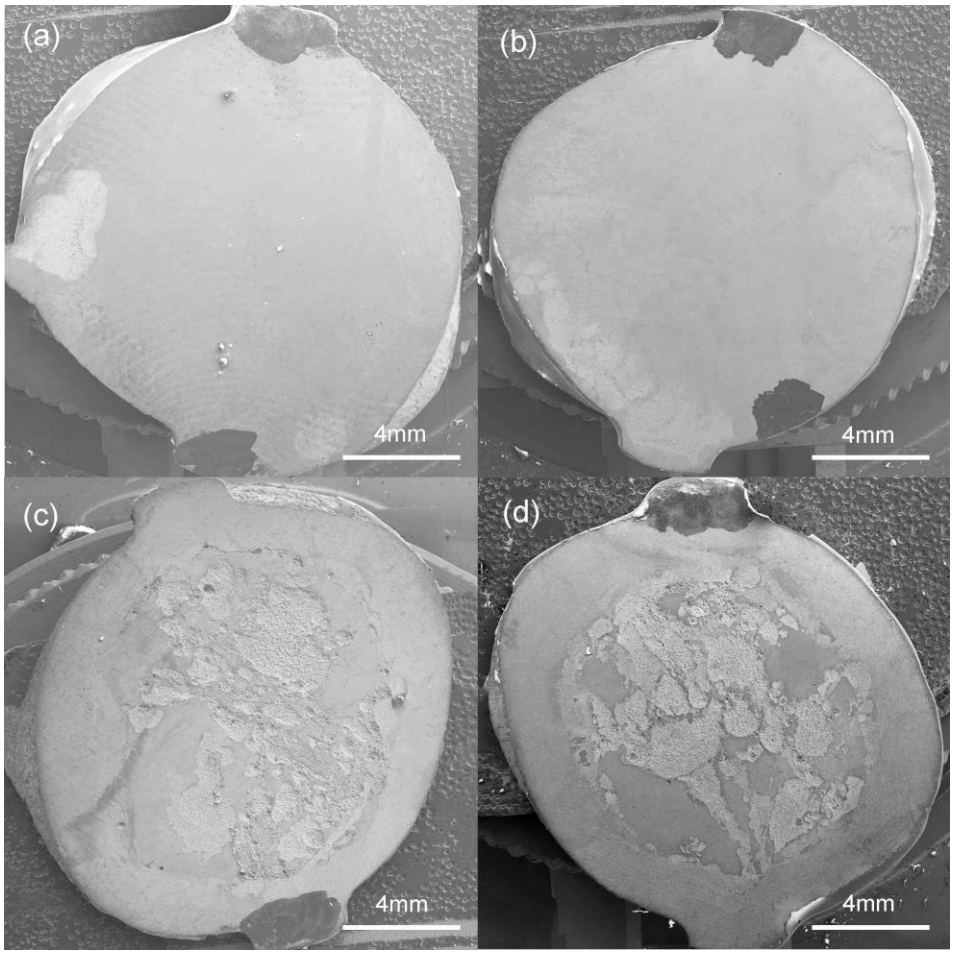

Figure 6.7. Specimens' surfaces after one-month of pitting under a combination of surface treatment and pH of the corrosive: a, 1 µm, 0.6 M Cl + pH 13.3 SPS; b, 15 µm, 0.6 M Cl + pH 13.3 SPS; c, 1 µm, 0.6 M Cl + pH 9.3 SPS; d, 15 µm, 0.6 M Cl + pH 9.3 SPS.

Figure 6.8 provides the comparison of two groups of specimens corroded for a four-month pitting in two types of SPS and four levels of chloride contaminations, similar to those in the one-month pitting. No apparent corrosion was seen on the specimen surfaces immersed in non-chloride SPSs, shown in Figure 6.8 (a) and (e). In addition, little corrosion product was observed during the test. Compared to the one-month pitted specimens shown in Figure 6.5, the pitted samples in Figure 6.8 were "messier" at both high pH and carbonated SPSs, indicating that pitting was more severe in both types of solutions beyond four months of immersion. Moreover, more severe pitting damage was observed in the carbonated SPS mixed with 0.6 M and 1.5 M NaCl than that in 0.1 M NaCl. Overall, both low pH corrosive and long corrosion period facilitated the development of pits.

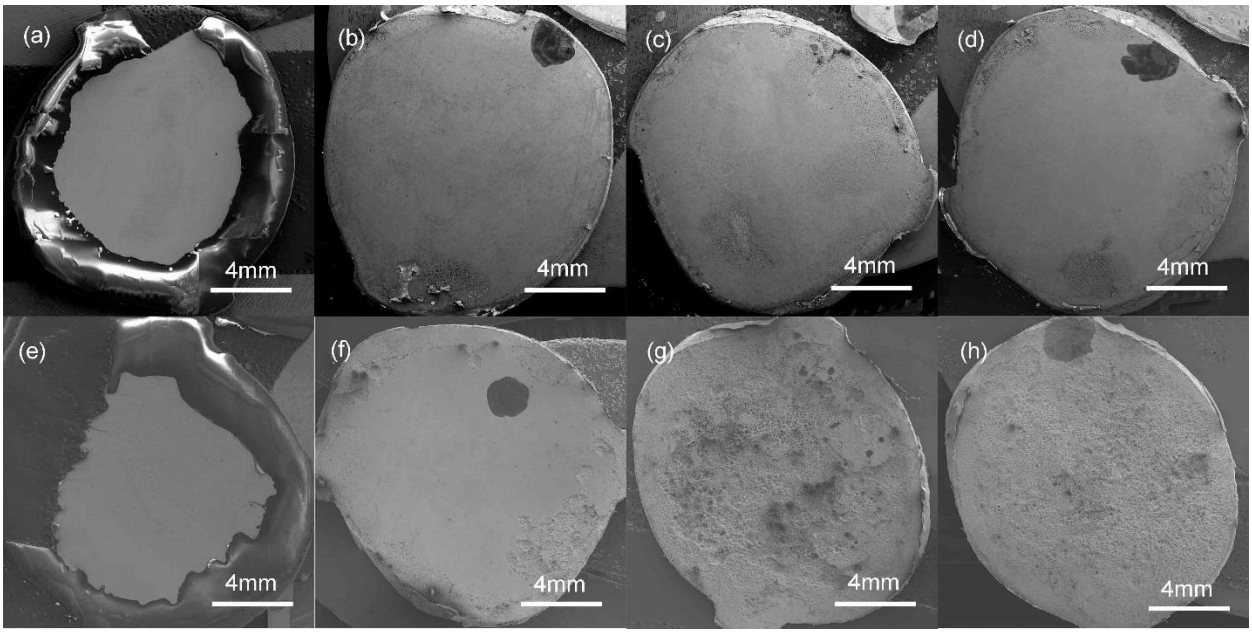

Figure 6.8. Specimen surfaces after four-month pitting: a, 0 M Cl + pH 13.3 SPS; b, 0.1 M Cl + pH 13.3 SPS; c, 0.6 M Cl + pH 13.3 SPS; d, 1.5 M Cl + pH 13.3 SPS; e, 0 M Cl + pH 9.3 SPS; f, 0.1 M Cl + pH 9.3 SPS; g, 0.6 M Cl + pH 9.3 SPS; h, 1.5 M Cl + pH 9.3 SPS.

Figure 6.9 displays the effect of surface treatment on the corroded surfaces of specimens after four months of corrosion at two pH levels, pH 13.3 and pH 9.3. As can be seen in specimens polished to 1 μm and 15 μm, these two samples had similarly corroded surfaces as shown in Figure 6.9 (a) and (b). Severe pitting was observed in specimens immersed in carbonated SPS shown in Figure 6.9 (c) and (d). Hence, the SEM images led to the conclusion that the polish of specimen surface had a negligible effect on the corrosion behavior in the four-month corrosion in both carbonated and non-carbonated SPSs. The effect of surface polish on pit depth was analyzed in later chapters.

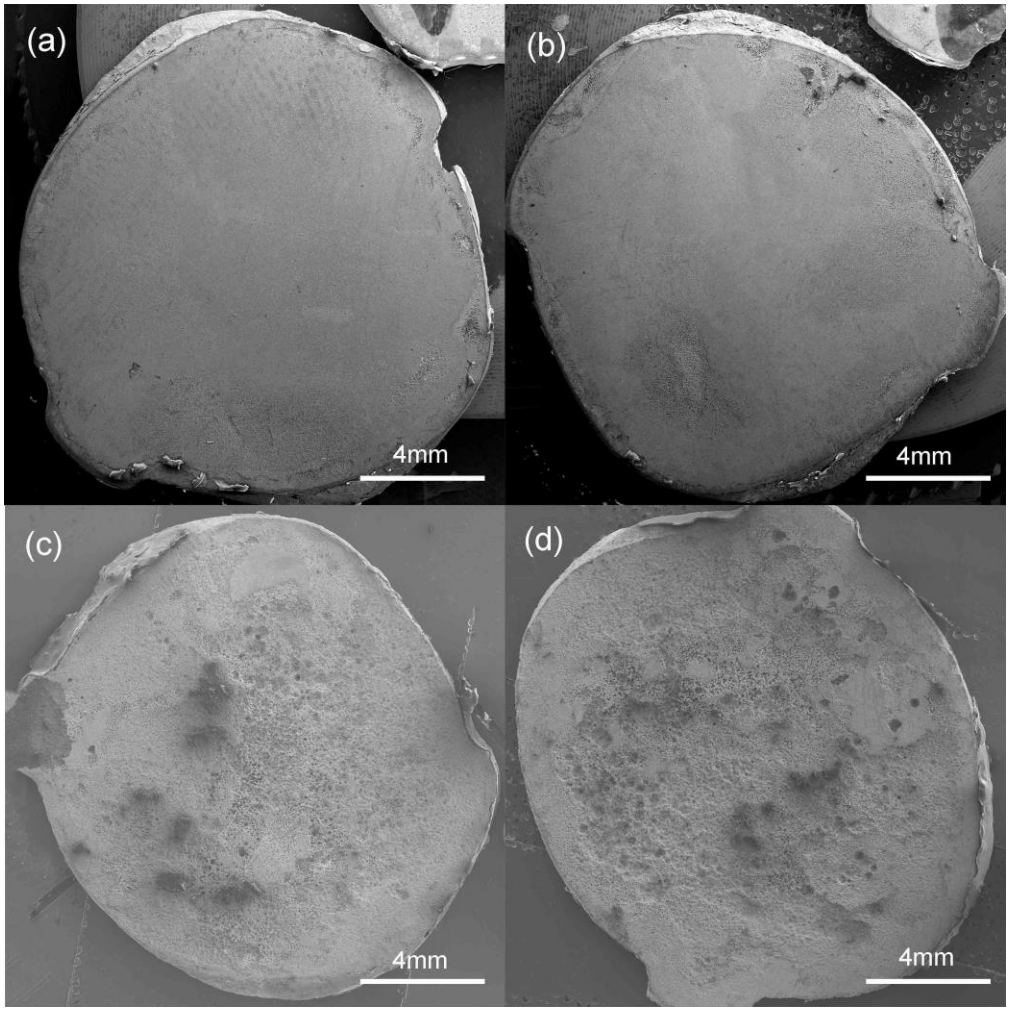

Figure 6.9. Specimen surfaces after four-month pitting under a combination of surface treatment and pH of the corrosive: a, 1 µm, 0.6 M Cl + pH 13.3 SPS; b, 15 µm, 0.6 M Cl + pH 13.3 SPS; c, 1 µm, 0.6 M Cl + pH 9.3 SPS; d, 15 µm, 0.6 M Cl + pH 9.3 SPS.

Pit depth data analysis

In the pit depth test, the maximum depth of the pits on each specimen was measured by the Vantage 50 profilometer. Figure 6.10 presents a 3D plot of the pit depth of the specimens with coupled effect of pH value in SPS and chloride concentration. This image clearly demonstrates that: pit depth increases with time in both chloride-contaminated SPSs, and carbonated SPS overall produces more severe pitting damage than high pH SPS. Two separate 2D graphs plotted using the same data as Figure 6.10 are shown in Figure 6.11.

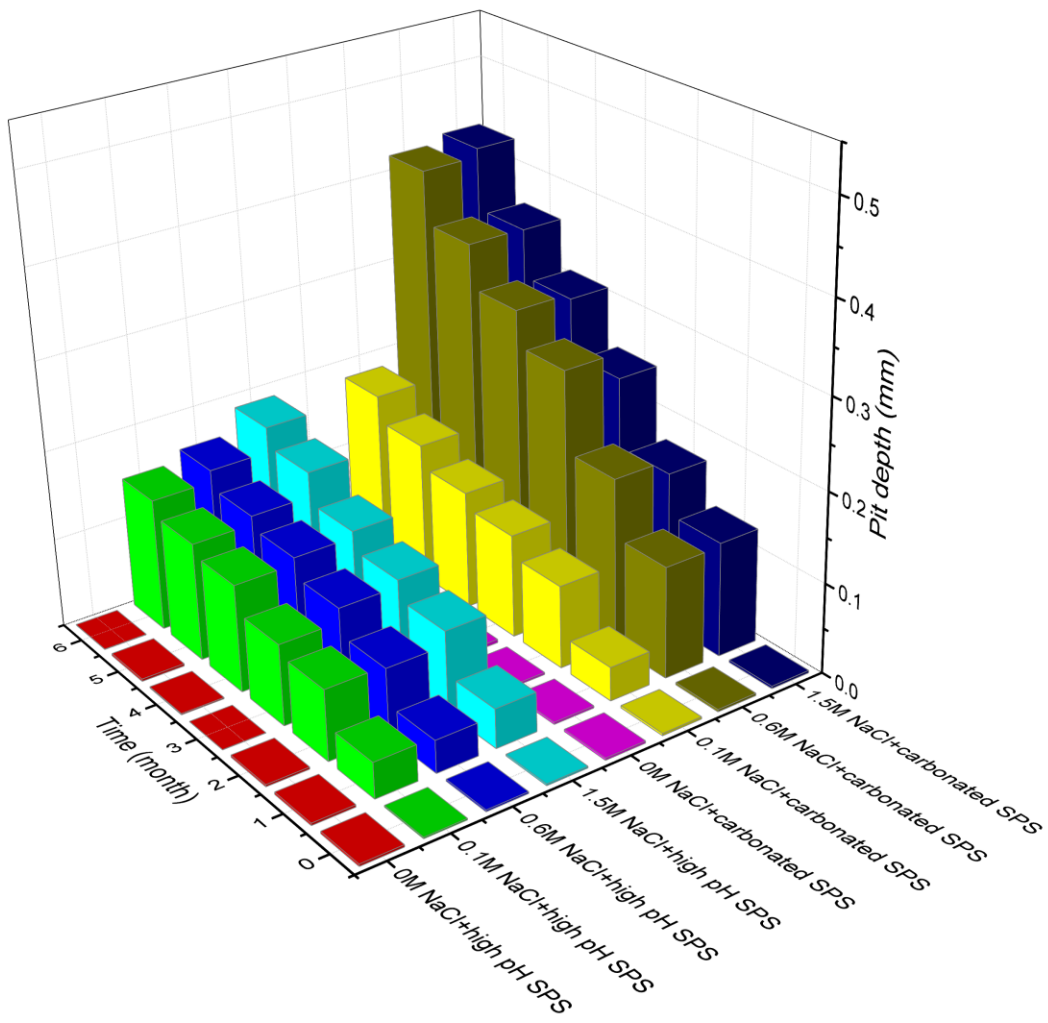

Figure 6.10. Pitting growth bar chart of rebar in the corrosive solution at the combination of chloride and simulated concrete pore solution

Figure 6.11 (a) depicts the development of pit depth in high alkaline (pH 13.3) SPS. The data indicate no pitting in non-chloride SPS. The maximum pit depth of these three chloride levels increased steadily with time, and the maximum pit depth generally decreased from 1.5 M NaCl to 0.1 M NaCl in an SPS solution.

It is documented (Luca Bertolini & Polder, 2013) that a higher chloride concentration usually becomes more competitive in introducing pitting. Hence, high chloride concentration promotes the total pitting area, which was confirmed by the short term pitting results in this study. The pit depth, however, depends on the microenvironment in and around the pit. The formation of a pit cap could

isolate the pit from the bulk environment and this usually facilitates a decrease in the pH of the microenvironment in the pit, even from an alkaline condition to an acidic environment.

Many researchers (Landolt, 2007; Szklarska-Smialowska, 2005) reported that the isolated microenvironment causes the quick growth of pit depth. Due to the fact that the corrosion current density is higher in an SPS mixed with higher chloride concentration, it is probable that the breakdown of the passivation film and the formation of the cap on a pit are faster in the higher chloride-concentrated solution. Furthermore, chlorides could transport through the porous cap into the pit because of the chloride concentration difference between the pit interior and the bulk solution. The higher the concentration of chloride in the bulk solution, the more chlorides penetrate to a pit. The concentration of hydrochloride acid increases as the chloride concentration increases, and this phenomenon increases the acidity of the corrosive environment, which facilitates the growth of pit depth. Therefore, the corrosive environment mixed with a higher chloride concentration requires a shorter time to develop a pit in comparison with the solution mixed with a lower chloride concentration. This explains why the maximum pit depth in the SPS solutions was descending in the order of 1.5 M, 0.6 M, and 0.1 M NaCl.

In the carbonated SPS shown in Figure 6.11 (b), the growth pattern of pit depth was mostly different from that in non-carbonated SPS. In SPS with non-chlorides, both Figure 6.11 (a) and (b) showed no pit growth in either high pH SPS or carbonated SPS. In the carbonated SPS with added 0.1 M NaCl, pits grew slower than that mixed with 0.6 M and 1.5 M NaCl. As can be seen in Figure 6.11 (b), the maximum pit depth in the SPSs with 0.6 M and 1.5 M NaCl was similar at all corrosion durations. Hence, a one-way ANOVA analysis was performed to identify whether chloride has an effect on the pit growth. The results in Table 6.2 show that the P value was 0.952 (much larger than 0.05), which means chloride concentration had no effect on the maximum pit depth. Overall, unlike the growing pattern of pit depth in a high pH SPS, a pit in the carbonated SPS grew slower in 0.1 M NaCl than in 0.6 M and 1.5 M NaCl, and there was no apparent pit depth difference between the corrosives mixed with 0.6 M and 1.5 M NaCl.

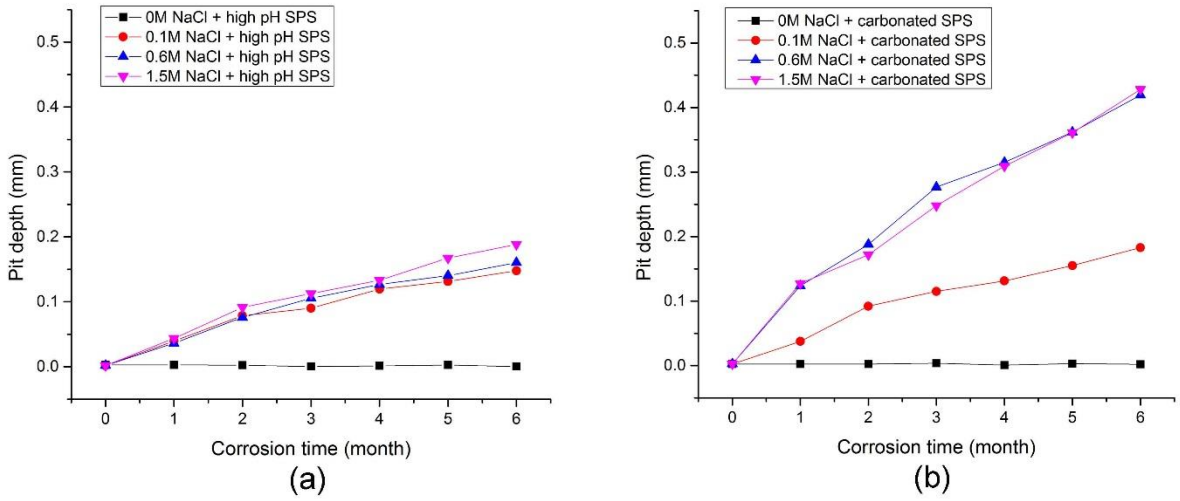

Figure 6.11. Pit depth growth of rebar in 0 M, 0.1 M, 0.6 M, and 1.5 M chloride mixed with: (a), high pH (pH 13.3) SPS; (b), carbonated (pH 9.3) SPS.

Table 6.2. Chloride concentration effect (0.6 M and 1.5 M) of the max pit depth in carbonated SPS solutions.

	DF	Sum of Squares	Mean Square	F Value	Prob>F
Model	1	8.76E-5	8.76E-5	0.0037	0.952
Error	12	0.284	0.0237		
Total	13	0.284			

Figure 6.12 depicts the effect of surface treatment – 1 µm and 15 µm – on the growth of pit depth on the rebar disks in both carbonated and high pH SPSs. Little difference between the two surface treatments was seen at all six corrosion periods. The surface quality of a metal is essential for the nucleation and the development of pits, including both metastable and stable pits. Many scientists have reported that both the pitting potential and the critical pitting temperature (CPT) are lower on

rougher surfaces than on smoother ones (Burstein & Pistorius, 1995; Burstein & Sasaki, 2000; G. E. Coates, 1990; Moayed, Laycock, & Newman, 2003; Sasaki & Burstein, 1996). In other words, the initiation time of a pit is significantly influenced by the surface. However, the nucleation time of a pit varies from minutes to hours in most commonly used metals and alloys. This nucleation period is rather short in comparison with the corrosion duration of one-month interval, which was used for measurement in this study. Hence, the effect of surface fails to be reflected in a long-term test as shown in Figure 6.12.

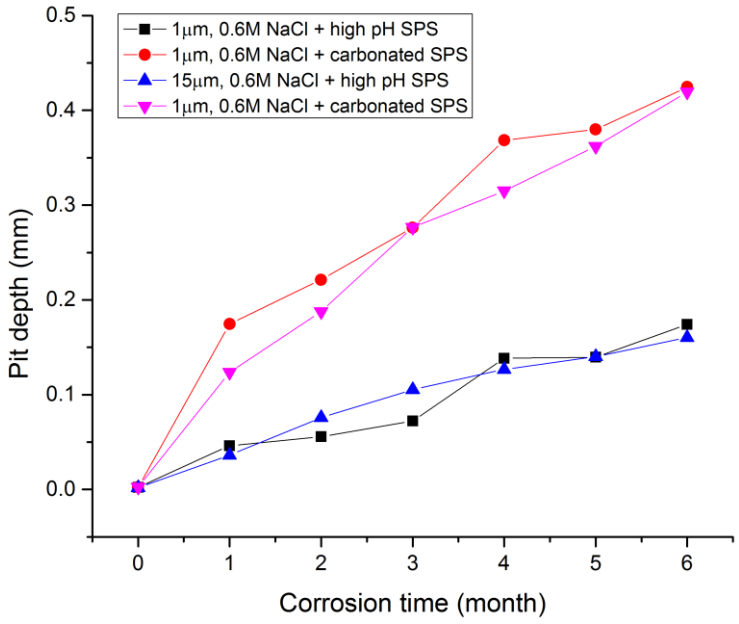

Figure 6.12. Pitting growth of rebar specimens polished by 1μm and 15μm sandpapers and tested in the 0.6 M chloride mixed with high alkaline and carbonated SPSs.

Since multiple factors, such as chloride concentration, pH, and surface treatment, influence pit growth, their individual effects and synergetic contributions were both investigated in this study. The interactions of chloride and pH were firstly compared by the two-way ANOVA in Table 6.3 with a confidence level of 0.05. This table shows that chloride and pH individually had a P value of 2.60E-6 and 0.008, suggesting that both factors had an effect on the growth of pit depth. The interaction of Cl and pH had a P value of 0.094, hence, no significance was presented in the interaction since the P value was above 0.05. A one-way ANOVA was performed on the effect of surface treatment as shown in Table 6.4. The generated P value was 0.873, which exceeded 0.05;

therefore, it was concluded that surface treatment had no effect on the long-termed development of pit depth. Therefore, ANOVA results confirmed the observation and discussion of Figure 6.12. Moreover, a two-way ANOVA was executed to examine the interaction effect of pH and surface treatment as seen in Table 6.5. At the 0.05 confidence level, both the P-values of surface treatment and the interaction in the table were higher than 0.05, denoting that both null hypotheses should be rejected and both surface treatment and the interaction had little influence on the growth of pit depth.

Table 6.3. ANOVA table for pH, Cl, and their synergetic effects influencing pit depth

	DF	Sum of Squares	Mean Square	F Value	P Value
Cl	3	0.363	0.121	12.046	2.60E-6
pH	1	0.075	0.075	7.458	0.008
Interaction	3	0.067	0.022	2.230	0.094
Model	7	0.550	0.079	7.817	9.23E-7
Error	62	0.624	0.010		
Corrected Total	69	1.174			

Table 6.4. ANOVA for the pit growth at 1μm and 15μm polished surface under both high pH and carbonated SPS mixed with 0.6 M NaCl

	Degree of freedom	Sum of squares	Mean square	F value	Probability > F
Model	1	4.790E-4	4.790E-4	0.026	0.873
Error	26	0.479	0.0184		
Total	27	0.480			

Table 6.5. ANOVA for the pit growth data between pH of SPS and surface treatment

	DF	Sum of Squares	Mean Square	F Value	P Value
pH	1	0.136	0.136	9.543	0.005
Surface treatment	1	4.790E-4	4.790E-4	0.034	0.856
Interaction	1	3.467E-4	3.467E-4	0.0243	0.877
Model	3	0.137	0.046	3.200	0.041
Error	24	0.343	0.014		
Corrected Total	27	0.479			

Pit growth data fitting

Many researchers (Kawai & Kasai, 1985; R E Melchers, 2006) have studied the relationship between the maximum pit depth and exposure time. Their statistical results suggested that pit depth growth is governed by an empirical power formula Eq. (3.11).

$$d = \begin{cases} A(t - t_0)^B, & t \geq t_0 \\ 0, & t < t_0 \end{cases} \tag{3.11}$$

In the short term pitting analysis of Section 6.1.1, it was concluded that pit initiation time was less than two hours. In comparison with the pit growth test period – six months, a two-hour (0.00278 months) pit initiation time in the empirical power equation might be ignored. In order to illustrate that the initiation time can be ignored, a power equation is fitted with a boundary condition that $0 \leq t_0 \leq 0.00278$ in both SPSs mixed with three chloride levels. The fitted parameters turned out such that four out of six t_0 were regressed at 0 and the other two t_0 are regressed at 0.00278. Due to the fact that t_0 had to be constant for all fitted pit growth equations, a t_0 value of zero was chosen for all regressions in this study.

Thus, a simplified equation, seen in Eq. (6.1), was used to regress the data obtained in Figure 6.11. The corresponding fitting curves and regression parameters are shown in Figure 6.13 and Table 6.6, respectively:

$$d = At^B \tag{6.1}$$

where d is pitting depth (in mm), t is pitting time (in hour), A and B are both empirical parameters which depend on the material and the environment.

Figure 6.13 (a) reveals that the growth of pits gradually increased from 0.1 M to 1.5 M NaCl in the high pH SPS. Figure 6.13 (b), on the other hand, demonstrates pit growth was faster in 0.6 M and 1.5 M NaCl than in 0.1 M NaCl in the carbonated SPS. The pit growth rates for the first four months were higher in the carbonated SPS mixed with 0.6 M NaCl than 1.5 M NaCl. From the long run in both non-carbonated and carbonated SPSs, the pit growth rate climbed along with increasing chloride concentration. Moreover, the adjusted R-squared values in Table 6.6 were above 0.970 and the standard error for both constants – A and B – were fairly small in comparison to the regressed values, denoting that the predicted models closely agreed with the collected data.

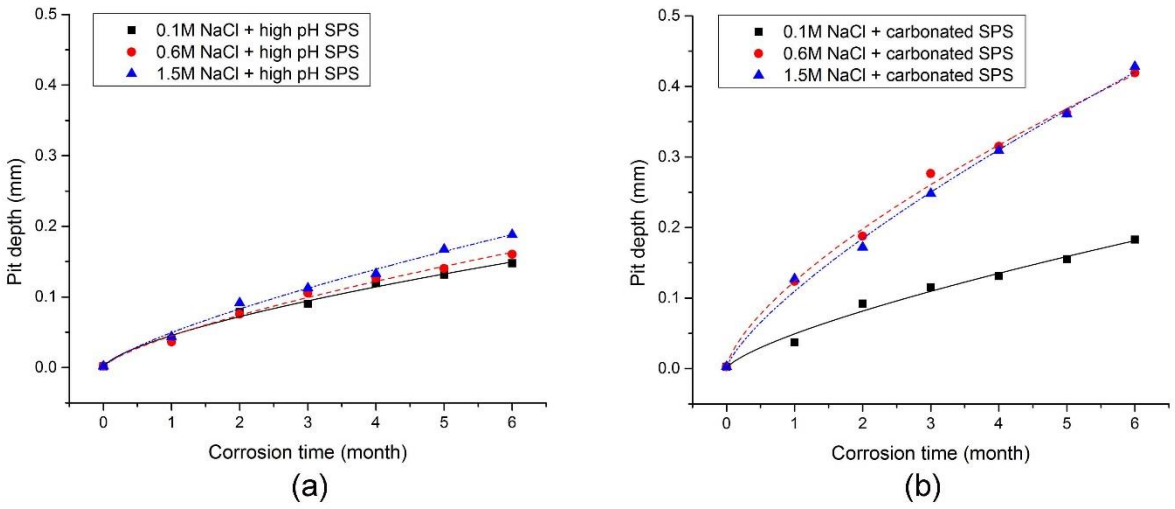

Figure 6.13. Empirical fitting of pit growth data in two types of SPS: (a), high pH SPS; (b), carbonated SPS

Table 6.6. Fitting parameters of pit growth data in both high pH SPS and carbonated SPS

Corrosion conditions	A		B		Statistics
	Value	Standard Error	Value	Standard Error	Adj. R-Square
0.1 M Cl, high pH SPS	0.047	0.004	0.670	0.044	0.983
0.6 M Cl, high pH SPS	0.051	0.004	0.707	0.043	0.980
1.5 M Cl, high pH SPS	0.053	0.005	0.719	0.042	0.991
0.1 M Cl, carbonated SPS	0.049	0.005	0.728	0.072	0.970
0.6 M Cl, carbonated SPS	0.124	0.006	0.678	0.034	0.991
1.5 M Cl, carbonated SPS	0.110	0.007	0.749	0.043	0.989

6.2 K_{EAC}, K_{Ic}, and rebar crack growth under CF

6.2.1 Fracture toughness (K_{Ic})

Fracture toughness was measured using the disk-shaped rebar specimen according to ASTM E399 (ASTM, 2013c) standard. The applied loading was within the range from 0.55 to 2.75 MPa√m/s and the resultant load-crack-opening-displacement relationship is seen in Figure 6.14. The curves denote that the tested metal was a ductile material because of the non-linear increment beyond the linear portion of load-crack opening relationship. Following the steps in the ASTM E399 standard to obtain the correct maximum load in calculating the fracture toughness, this study determined three calculated K_{Ic} values shown in Table 6.7. The resultant average fracture toughness of rebar was 29.92 MPa√m.

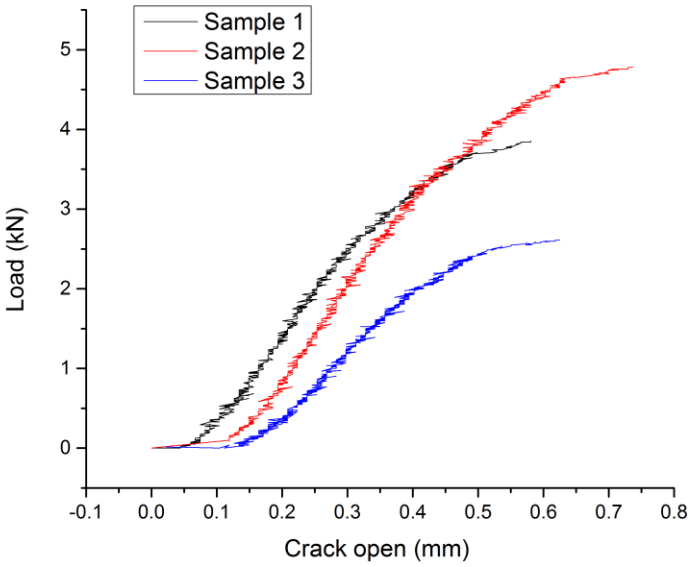

Figure 6.14. Load and crack opening relationship in measuring fracture toughness.

Table 6.7. Reinforcing steel fracture toughness measured by ASTM E399 standard

	Sample 1	Sample 2	Sample 3	Average
Fracture toughness / MPa√m	29.45	29.82	30.29	29.92

6.2.2 Stress intensity factor threshold for environment-assisted cracking (K_{EAC})

The stress intensity factor is used in the field of fracture mechanics to represent the stress distribution near the crack tip which is produced by a remotely applied load or a residual stress (Schijve, 2009). The stress intensity factor threshold for environment-assisted cracking (K_{EAC}) refers to the highest value of the stress intensity factor (K), below which crack growth cannot be observed for a specific combination of static load and environment (ASTM, 2013a, 2013b).

The standard measurements of K_{EAC} (ASTM, 2013b) involve several methods for various shapes of specimens. All approaches share the same idea that the specimen has to be loaded with a certain mass in a corrosion chamber containing a 3% NaCl aqueous solution. The crack development is examined beyond an incubation time, depending on the tested metal and the testing environment.

The incubation time for steels with yield strength less than 1200 MPa is 10,000 hours as cited in the ASTM (ASTM, 2013b) standard. Considering that the incubation time is fairly long for a test, this study examined the K_{EAC} of reinforcing steel by experiment using a constant load rate-control or constant displacement rate-control as proposed by Kalnaus et al (Kalnaus, Zhang, & Jiang, 2010).

Constant load rate-control method

The constant load rate test controlled the loading rate at 0.1 N/sec on a disk-shaped specimen, which was immersed in an SPS mixed with 0.6 M NaCl. The applied load verses the correspondent crack length was recorded by the data acquisition system. The test data is shown in Figure 6.15, which reveals that crack growth initiated around 17 MPa√m prior to crack propagation in both tests. Hence, the measured K_{EAC} by this approach was 17 MPa√m.

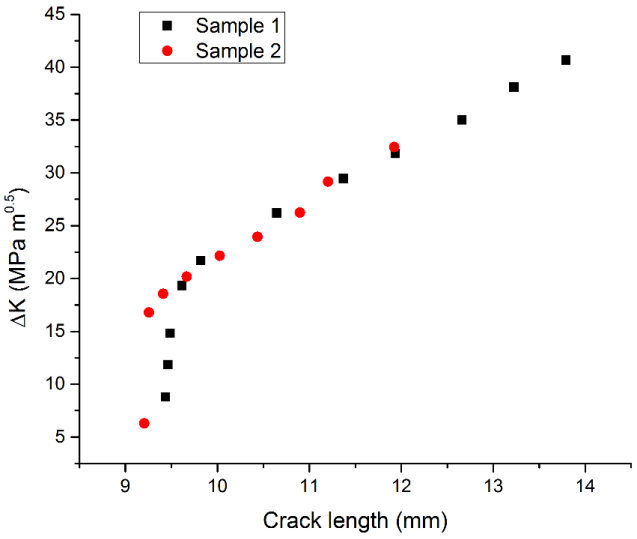

Figure 6.15. Crack length against stress intensity factor range at a constant loading rate of 0.1 N/sec.

Constant displacement rate-control method

The constant displacement rate test controls three displacement rates (2E-4 mm/s, 1E-4 mm/s, and 5E-5 mm/s) and records the instant data of load and the corresponding crack length. The test results are shown in Figure 6.16.

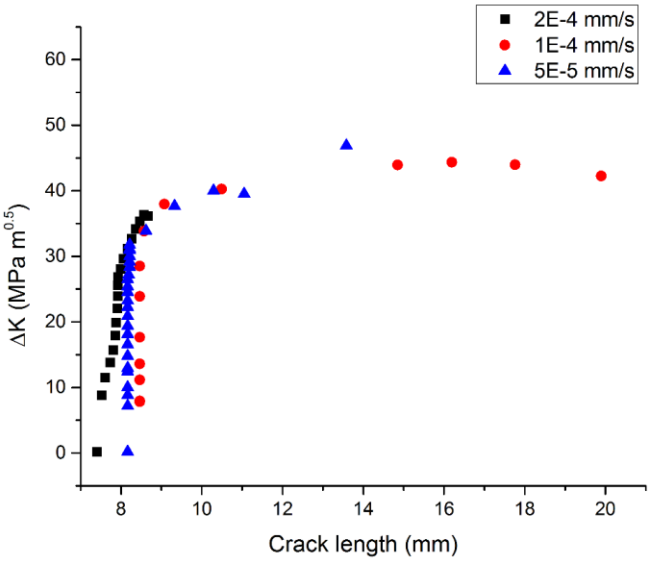

Figure 6.16. Variation of the stress intensity factor in load rate-controlled test and displacement rate-controlled tests.

Unlike the data of Kalnaus et al (Kalnaus et al., 2010) shown in Figure 6.17, in which the stress intensity factor threshold appears as the COD rate decreases, the results indicated in Figure 6.16 showed little difference in the growth pattern of the stress intensity factors at the three declining displacement rates. During the test, the observed opening of a crack mouth enlarged with an increasing applied load; however, the crack tip had little increment. As the climbing of applied load, plastic deformation in front of the crack tip was observed. As long as the plastic deformation reached the critical value, rapid crack growth occurred with a sudden drop of the applied load, resulting in a jump in crack length at an almost constant stress intensity factor in Figure 6.16.

Since the displacement being rate-controlled in the test and reinforcing steel being ductile, sudden crack growth until failure is impossible. After the first quick increment of crack length, another round of plastic zone deformation initiates and continues until the next jump in crack length. This process proceeds in a cycle until the complete failure of the specimen. Even though a plateau was seen in Figure 6.16 in the relationship between the stress intensity factor and the crack length, the observation in the test demonstrates this phenomenon to be caused by the slow rate of loading displacement. In reality, the sample would fail immediately after reaching the critical plastic deformation. Thus, the plateau is completely different from that in Figure 6.17, in which the

threshold stress intensity factor was obtained by a combination effect of corrosion and loaded displacement rate.

The reason why the displacement rate-controlled approach fails to examine the stress intensity factor threshold is attributed to the insensitivity of small flaws in low strength metal. Unlike the high strength metals, in which flaws in the metal (e.g. chloride induced pit and grain boundary corrosion) could lead to crack propagation, low strength metals are insensitive to the flaws caused by corrosion.

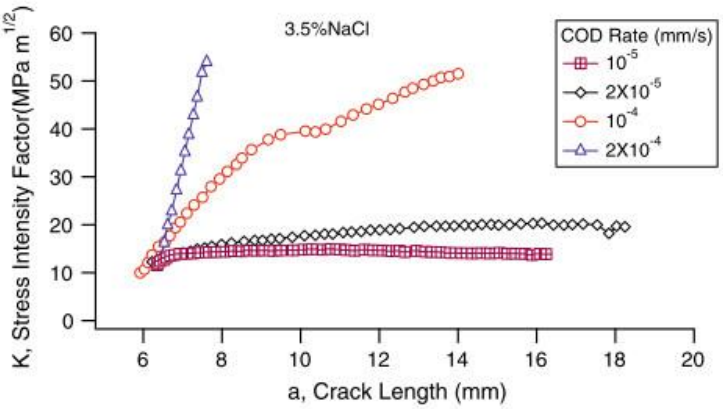

Figure 6.17. Variation of stress intensity factor in COD rate-controlled experiments (Kalnaus et al., 2010).

6.2.3 The threshold of fatigue stress intensity factor ΔK_{th}

In order to examine the threshold stress intensity factor range under environment-assisted cracking, the multi-stepped fatigue loading approach was executed in this study. Samples were exposed to the maximum fatigue loads in the order of 0.7 kN, 0.8 kN, 0.9 kN, 1.0 kN, 1.1 kN, 1.2 kN, and 1.3 kN. Each fatigue load sustained a period with the R ratio at 0.1. The growth of crack length was recorded along with cycles, and the data were then transferred to the logarithmic relationship between crack growth rate and stress intensity factor range as plotted in Figure 6.18.

Figure 6.18 clearly demonstrates the three stages of the growth of a crack indicated in Figure 2.6, and data in Region I provide that the average ΔK_{th} of three examinations was 5.70 MPa$\sqrt{m}$. The

measured ΔK_{th} was much lower in comparison to the K_{EAC}, 17 MPa$\sqrt{m}$, which was reasonable since stress corrosion cracking usually happens at a higher stress intensity factor in steels.

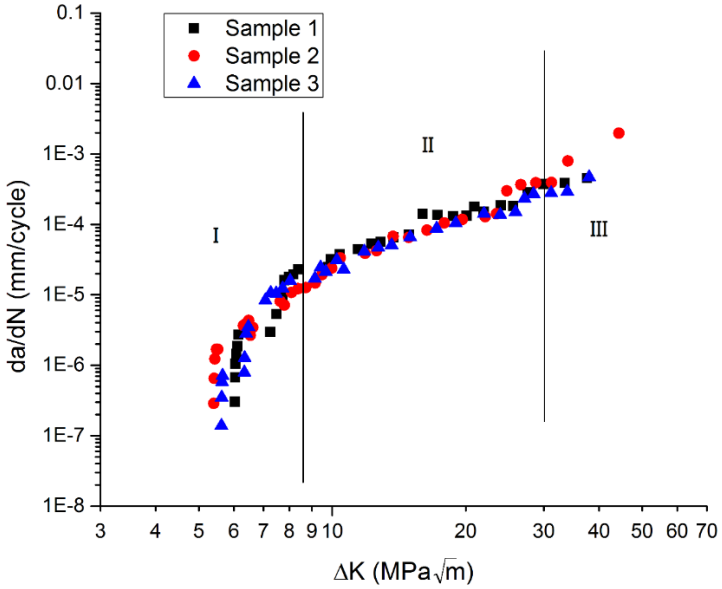

Figure 6.18. Fatigue crack propagation behavior in reinforcing steel for stepped fatigue loads.

6.2.4 Rebar crack growth under electrochemically accelerated CF

FCGR under corrosion was studied by many researchers in different metals, e.g. low-alloy steels, stainless steels, aluminum alloys, and titanium alloys (G. S. Chen et al., 1996; Gregory, 1999; Hu, Meng, Liu, Song, & Wang, 2015; Kalnaus et al., 2010; Ostash, Kostyk, & Makoviichuk, 1999; Seifert, Ritter, & Leber, 2012a, 2012b; Sivaprasad, Tarafder, Ranganath, Tarafder, & Ray, 2006; Werner & Koliasinsky, 2003). However, few studies have been conducted on the FCGR of structural steel. In this section, the rebar crack growth under CF is examined with the coupled effect of corrosion environments (in air, in Cl mixed SPS, 1 mA and 5 mA electrochemical corrosion) and fatigue loads (1.2 kN, 1.6 kN, and 2.0 kN), and the results are plotted in Figure 6.19. Figure 6.19 shows that the data were condensed; hence, the plot was separately plotted by the maximum load amplitude in Figure 6.20, Figure 6.21, and Figure 6.22.

Because of the crack closure effect in crack propagation, this effect must be corrected. In this study, the effective stress intensity factor range ΔK_{eff} replaces ΔK in the ΔK~da/dN curves, and the transformation between ΔK and ΔK_{eff} is provided in Eq. (6.2) (J. C. Newman & Annigeri, 2012).

$$\Delta K_{eff} = \frac{1 - K_0/K_{max}}{1 - R} \Delta K \tag{6.2}$$

$$\frac{K_0}{K_{max}} = 0.343 + 0.027R + 0.917R^2 - 0.287R^3 \tag{6.3}$$

where K_0 is the stress intensity factor at the crack opening, K_{max} is the maximum stress intensity factor, R is the stress ratio.

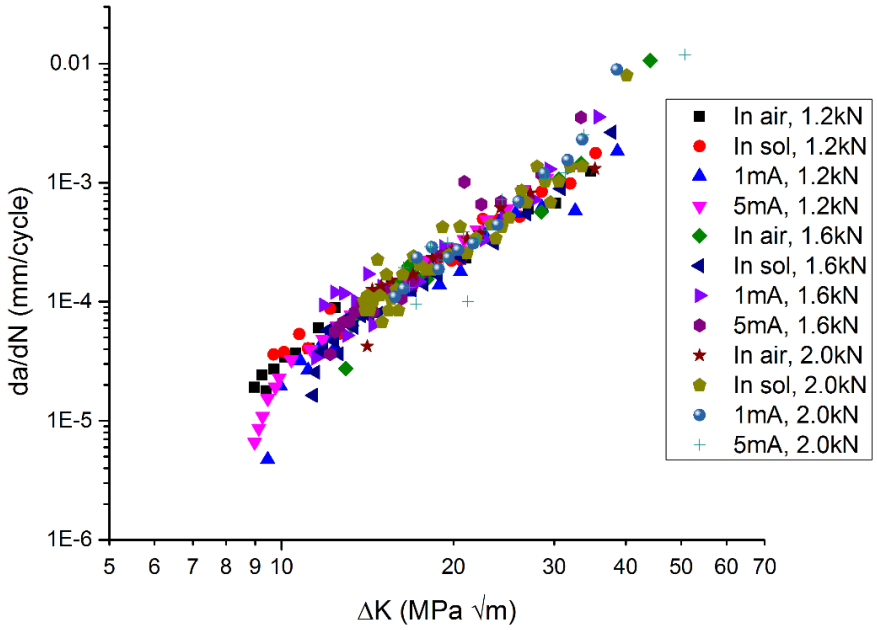

Figure 6.19. FCGR at the combination of load (1.2kN, 1.6kN, 2.0kN) and environment (in air, in SPS+0.6 M Cl solution, an electrochemical corrosion of 1mA and 5 mA)

Figure 6.20 shows the FCGR curves tested under different environments at the maximum load of 1.2 kN. Obviously, a ΔK_{th} was observed from all four test environments – in air, in 0.6 M Cl mixed SPS, in electrochemical corrosion of 1 mA and 5 mA – and the four ΔK_{th} values seemed to approach 9 MPa√m. Like the crack propagation of many metals governed by the Paris law, a linear relationship between da/dN and ΔK was seen on the plot at the ΔK range from 10 MPa√m to 30 MPa√m. Compared to the data tested in air, FCGR was barely affected by CF and this might be attributed to the fact that structural steel is mild steel which is insensitive to chloride-induced corrosion in comparison with high strength steel, e.g. stainless steel.

Figure 6.21 and Figure 6.22 provide the FCGR curves tested under different environments at the maximum load of 1.6 kN and 2.0 kN, respectively. Similar to the FCGR curves tested at the maximum load of 1.2 kN, ΔK_{th} was observed in the curves of 1.6 kN and 2.0 kN with a value of 11.2 MPa√m and 13.4 MPa√m, respectively. Extracting data from 13 MPa√m to 32 MPa√m in Figure 6.21 and from 14 MPa√m to 32 MPa√m in Figure 6.22, the relationships between da/dN and ΔK looked linear in both ranges.

To sum up the results in Figure 6.20, Figure 6.21, and Figure 6.22, a higher load amplitude enhanced the ΔK_{th} from 9 MPa√m to 13.4 MPa√m with respect to the maximum load amplitude from 1.2 kN to 2.0 kN. Figure 6.23 provides the comparison of the maximum load effect on FCGR curves, and the plots indicated that the ΔK_{th} rose with the increasing tested maximum load under all four environments, including both non-corrosive and corrosive circumstances. The Paris law seemed to govern the stable crack growth region in all figures; however, further analysis was required to identify the CF effects on FCGR. Thus, linear regressions were required to perform in the suspicious region to examine the postulated linearity of FCGR curves.

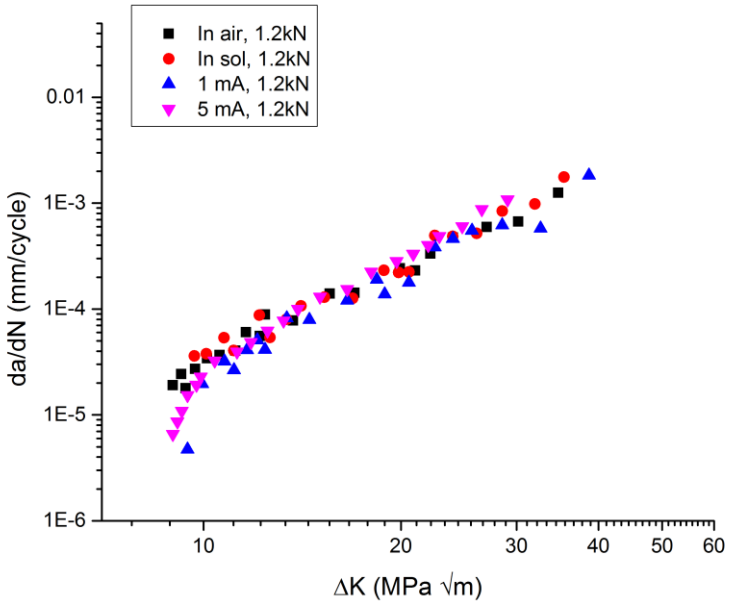

Figure 6.20. FCGR curves tested under different environments at a maximum load of 1.2 kN.

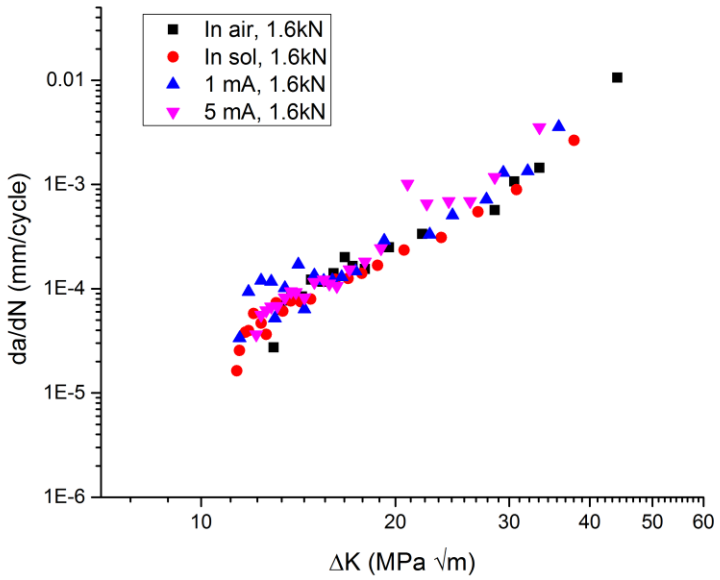

Figure 6.21. FCGR curves tested under different environments at a maximum load of 1.6 kN.

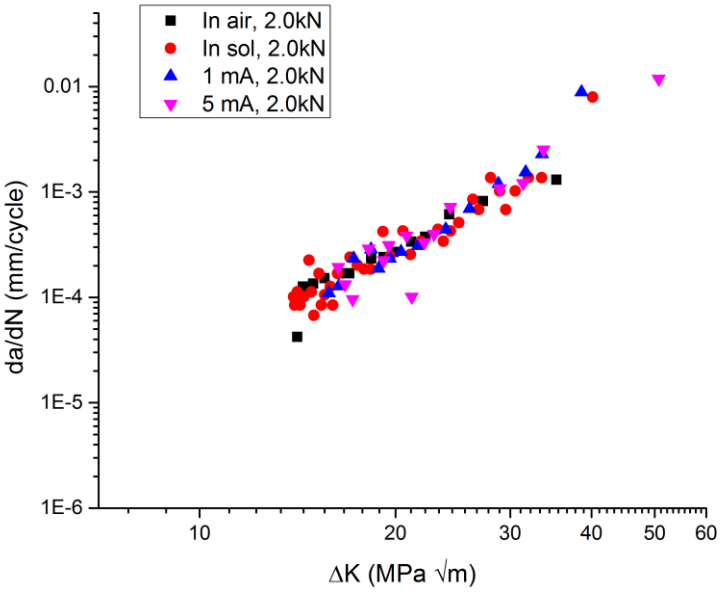

Figure 6.22. FCGR curves tested under different environments at a maximum load of 2.0 kN.

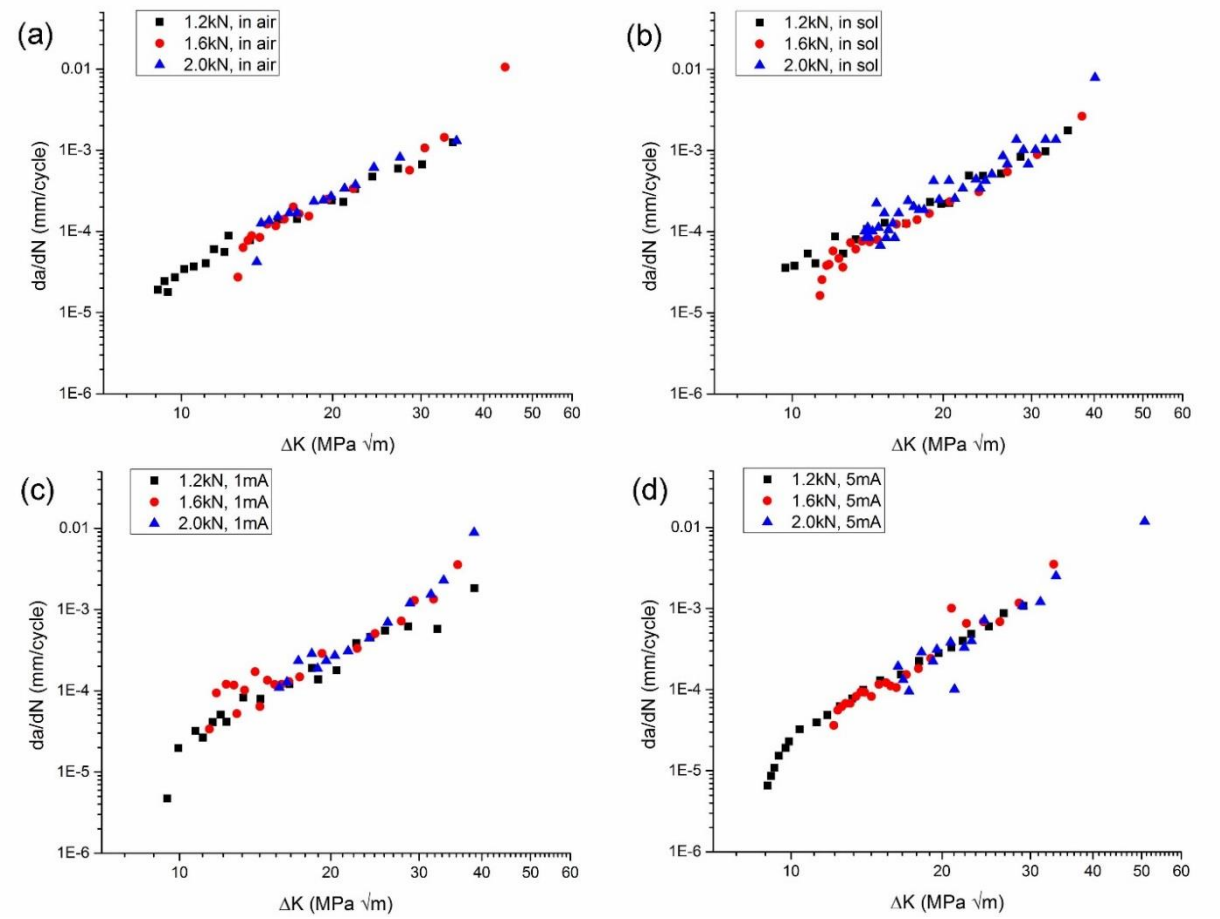

Figure 6.23. FCGR in different environments: (a) in air; (b) in SPS+0.6 M Cl solution; (c) electrochemically applied 1 mA; (d) electrochemically applied 5 mA.

Table 6.8 provides the linear fitting parameters of the FCGR under various CF environments. Most of the adjusted R-squared values in the table exceeded 0.9 and the minimum was 0.828, denoting that the postulated linear regressions fit well with the original data. The effect of CF on the Paris postulation was reflected mainly in the slope or the intercept of an FCGR curve.

In comparison with the in-air group data, Table 6.8 showed a slight increase in the slope with the increase of the aggressiveness of the corrosive at all three load amplitudes – 1.2 kN, 1.6 kN, and 2.0 kN. In the data of the 1.2 kN group, slopes gently climbed from 2.86 to 3.41 with an average standard error of 0.12. The same phenomenon was observed in the data of the 1.6 kN group and the 2.0 kN group. Hence, unlike many metals where the slopes of the Paris law remain constantly in corrosive environments, corrosion in reinforcing steel marginally increases the FCGR by electrochemically accelerated corrosion.

As can be seen in Table 6.8, the intercepts of the FCGR curves tested in air, solution, 1mA corrosion, and 5 mA corrosion were -7.32, -7.33, -7.89, and -7.95 for the load level of 1.2 kN. The same descending order was also observed in the data of 1.6 kN and 2.0 kN in spite of small deviation. Therefore, two conclusions could be made: (a), electrochemical corrosion was more severe than the corrosiveness of SPS mixed with 0.6 M NaCl; (b), a higher applied current by electrochemical corrosion had a greater effect on the intercept of the logarithmic Paris equation.

Overall, even though differences were observed in both slope and intercept of the logarithmic Paris's law, the effect of electrochemically accelerated corrosion was limited in promoting the corrosion rate of the crack surface. The possible reason attributes to that an applied corrosion current produces the expansion of corrosion on the crack surface however not necessary the crack tip, the corrosion on which causes the synergetic effect of corrosion and fatigue.

Table 6.8. Linear fitting of the Paris postulation governed region in the logarithmic FCGR curves under CF environments

CF conditions	Intercept		Slope		Statistics
	Value	Standard Error	Value	Standard Error	Adj. R-Square
In air, 1.2 kN	-7.32	0.15	2.86	0.13	0.976
In sol, 1.2 kN	-7.33	0.18	2.89	0.15	0.961
1mA, 1.2 kN	-7.89	0.17	3.26	0.14	0.972
5mA, 1.2 kN	-7.95	0.06	3.41	0.05	0.997
In air, 1.6 kN	-7.24	0.24	2.79	0.20	0.943
In sol, 1.6 kN	-7.43	0.15	2.88	0.12	0.981
1mA, 1.6 kN	-7.49	0.43	3.00	0.35	0.862
5mA, 1.6 kN	-8.50	0.38	3.86	0.31	0.907
In air, 2.0 kN	-7.37	0.18	2.96	0.14	0.976
In sol, 2.0 kN	-7.66	0.34	3.16	0.26	0.841
1mA, 2.0 kN	-8.10	0.45	3.49	0.34	0.912
5mA, 2.0 kN	-8.26	0.68	3.63	0.52	0.828

The effect of stress ratio – R-ratio – was evaluated at the maximum load amplitude of 1.6 kN with four levels – 0.1, 0.3, 0.5, and 0.7. The corresponding FCGR curves and crack length curves are provided in Figure 6.24 and Figure 6.25, respectively. Figure 6.24 displays the FCGR curves of these four R ratio levels in an electrochemical corrosion of 1 mA and in the reference – 0.6 M Cl mixed SPS. The FCGR curves show that R ratio had a great effect on the FCGR: the higher the stress ratio, the lower the stress intensity factor range. In Figure 6.24, the entire ΔK range of the R=0.1 test was from 10.3 MPa√m to 32.2 MPa√m, while it ranged from 3.5 MPa√m to 9.9 MPa√m for R=0.7. Moreover, both ΔK_{th} and fracture toughness were observed to descend along with the increase of R ratios in the FCGR curves. In other words, the entire FCGR curve shifted left to a smaller ΔK region as an R ratio increased, which agreed with the divergence phenomenon provided in the literature (Crooker, 1971; Crooker & Krause, 1972; Milella, 2013; Miller & Gallagher, 1981).

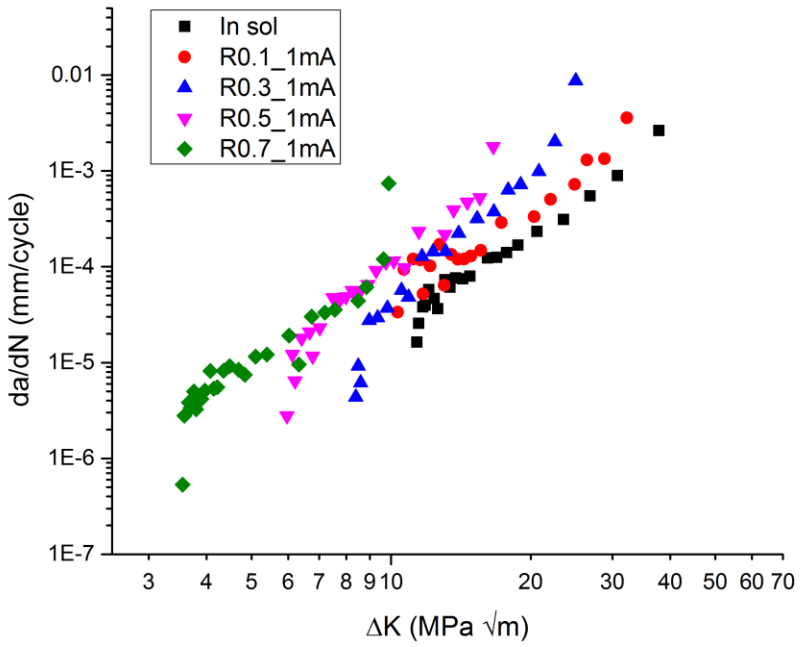

Figure 6.24. FCGR at different R ratios (0.1, 0.3, 0.5, and 0.7) for a maximum load of 1.6 kN.

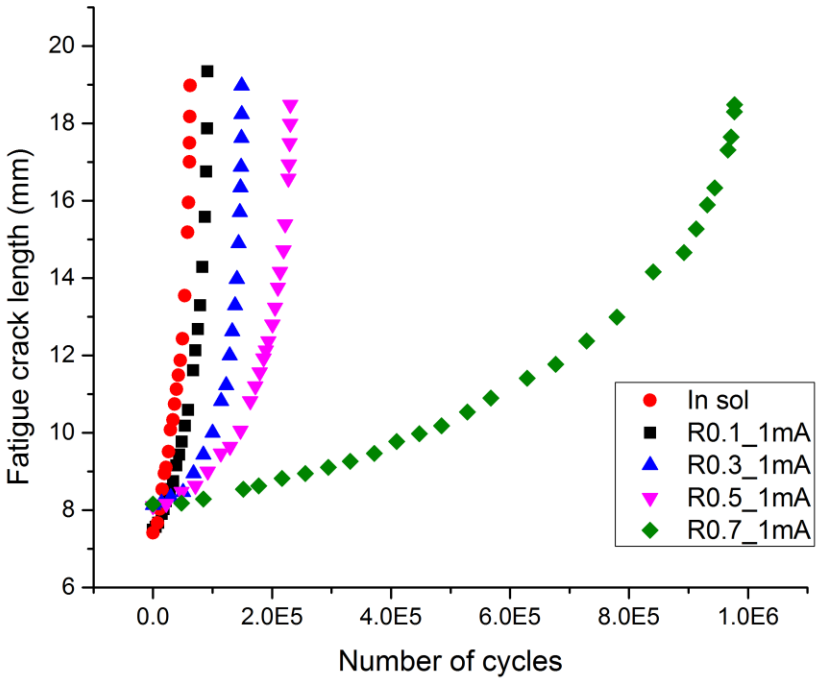

Figure 6.25. Fatigue crack length vs. elapsed cycles recorded at different R ratios under a maximum load amplitude of 1.6 kN and an electrochemical corrosion of 1 mA.

The effect of R ratio on the threshold stress intensity factor range ΔK_{th} can be modified by the equation below (Weng et al., 2013)

$$\Delta K_{th} = \Delta K_{th0}[1 - \langle R \rangle]^{\gamma_{th}} \tag{6.4}$$

where $\langle R \rangle$ = R when R ≥ 0 and R = 0 when R < 0; ΔK_{th0} is the threshold stress intensity factor range at R = 0; γ_{th} is a material constant.

Plotting the 1–R value against ΔK_{th} in Figure 6.24, Figure 6.26 provided $\Delta K_{th} = \Delta K_{th0}(1 - \langle R \rangle)^{1.15}$, hence, the material constant γ_{th} in Eq. (6.4) is 1.15.

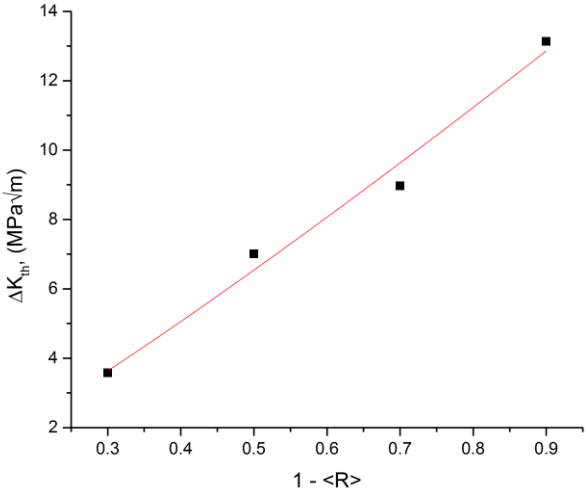

Figure 6.26. R ratio effect on the ΔK_{th} in SPS mixed with 0.6 M Cl.

Despite the fact that the ΔK_{th} decreased with the ascending of R ratio, the total number of fatigue cycles at a higher R-ratio was higher than that at a lower R-ratio as shown in Figure 6.25. This is probably due to the effective stress intensity factor range. In the fatigue crack growth of metal, there appears to be an opening stress intensity factor K_o, below which a crack will not propagate. Moreover, in the low ΔK region, both K_{max} and K_{min} are rather low. Thus, the effective stress intensity factor range from K_o to K_{max} is also smaller in comparison with a high ΔK, which causes a slow crack propagation.

Figure 6.27 displays the logarithmic FCGR curves affected by the coupled effects of R ratio – 0.1 and 0.3 – and corrosion – electrochemically applied 1 mA and 5 mA, and the correspondent linear fittings of the Paris-postulation-governed regions are shown in Table 6.9. Figure 6.27 shows that the R = 0.1 FCGR curve seemed to have a higher crack growth rate in 1 mA corrosion than in 5 mA. However, the R=0.3 FCGR curve in 1 mA corrosion had a lower crack growth rate than that in 5 mA. In Table 6.9, the slope differences between the two acceleration rates at the same R-ratio were within 0.87. Nevertheless, considering the large standard errors in the FCGR diagrams and the experimental error of a fatigue test, little differences were seen at various corrosion environments. At a high ΔK which approaches K_{Ic}, cracks grow at a high rate that corrosion has

little effect on crack development. The effect of R-ratios, on the other hand, was significantly greater than that of corrosion rate and this effect was observed in both Figure 6.27 and Figure 6.28.

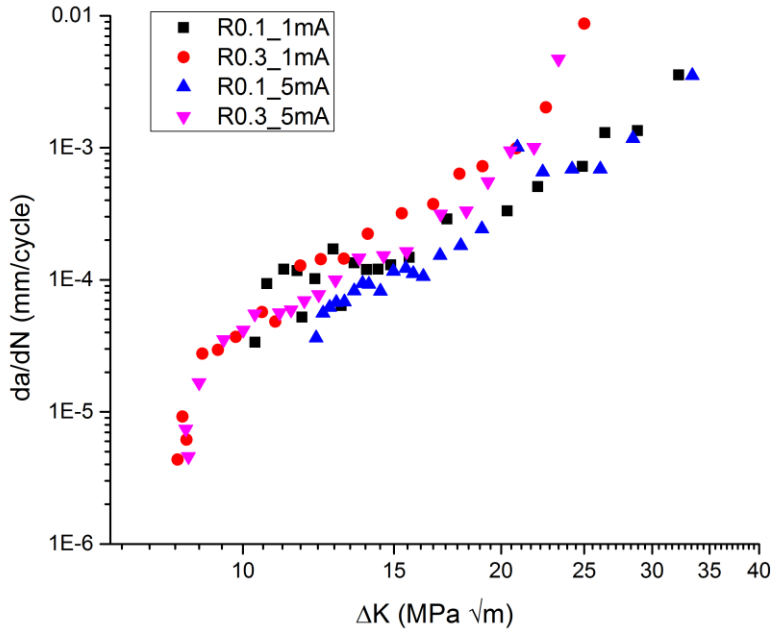

Figure 6.27. FCGR curves of two corrosion acceleration rates – 1 mA and 5 mA – tested in the R ratio of 0.1 and 0.3 at a maximum load amplitude of 1.6 kN.

Table 6.9. Coupled effects of R ratio (0.1 and 0.3) and corrosion (electrochemically applied 1 mA and 5 mA) affecting the Paris postulation governed region in the logarithmic FCGR curves the maximum load amplitude of 1.6 kN.

CF conditions	Intercept		Slope		Statistics
	Value	Standard Error	Value	Standard Error	Adj. R-Square
R 0.1, 1 mA	-7.29	0.31	2.99	0.26	0.883
R 0.1, 5 mA	-8.50	0.38	3.86	0.31	0.907
R 0.3, 1 mA	-8.95	0.27	4.59	0.25	0.969
R 0.3, 5 mA	-8.33	0.21	3.92	0.19	0.969

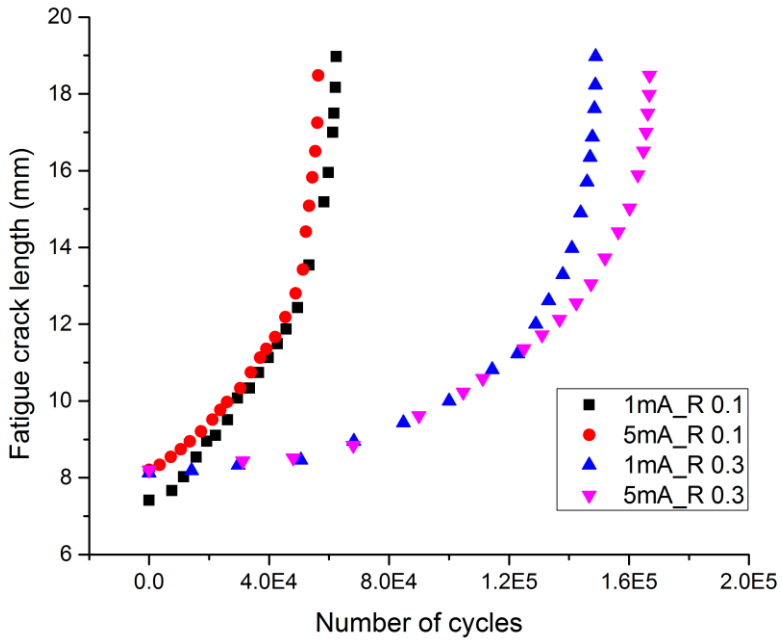

Figure 6.28. Fatigue crack length vs. elapsed cycles tested at a maximum load amplitude of 1.6 kN with the combinations of R ratios (0.1 and 0.3) and electrochemical corrosion (1 mA and 5 mA).

6.2.5 Rebar crack growth of CF under acidic solutions

The effect of electrochemical corrosion on FCGR curves are discussed in Section 6.2.4, and the results revealed that electrochemical corrosion had a minor effect on fatigue crack growth of rebar. In this section, the results of fatigue crack growth tested in acidic solutions were introduced.

Figure 6.29 displays the relationship of da/dN against stress intensity factor range ΔK under an increasing order of acidity in the SPSs mixed with 0.6 M NaCl (reference), 0.6 M NaCl + DDW, 0.1 M H_3PO_4, and 1.0 M H_3PO_4. Figure 6.29 shows that the acidity of corrosives had a great effect on the FCGR curves. The curves show that the FCGR of rebar increased with the increase in acidity of the solution, as the crack started to grow. The FCGR curve in 1.0 M H_3PO_4 presents a steady increase of da/dN from 6.7 MPa√m to 24.0 MPa√m, suggesting that corrosion governed the fatigue growth rate during the testing instead of a synergetic effect of corrosion and fatigue. In other words, for a rather aggressive corrosive, the FCGR curves presented the tendency of the curve shape to change from an interaction of corrosion and fatigue to a purely corrosion-controlled fatigue growth.

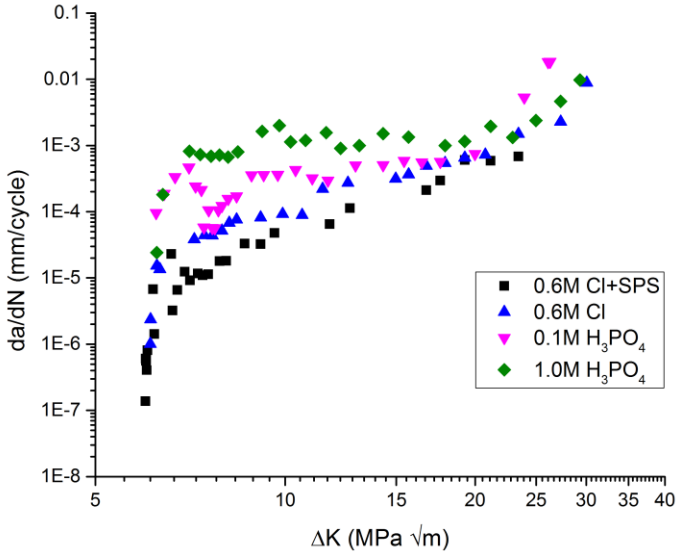

Figure 6.29. FCGR curves generated in acidic corrosives.

6.2.6 Fractographic observation of crack propagation specimens

In order to study the corrosion effect on the crack propagation under CF, the fractographic examination was performed on the fracture surface of the tested specimens. A schematic of the fracture surface is provided in Figure 6.30, in which the locations that were scanned by SEM are indicated on the right side.

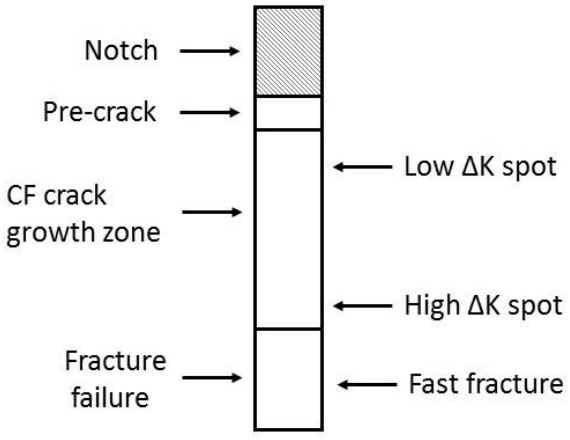

Figure 6.30. A schematic of the specimen surface completing crack propagation.

During a test, the crack fronts were observed growing step by step rather than continuously in all environments, including in air, SPS mixed with chloride, SPS applied with current, and acidic solutions. Many marks of the crack front along the longitudinal direction of rebar were observed on the fracture surface; an example is provided in Figure 6.31, where the crack grows from left to right.

A 2000X magnification image of the crack front is provided in Figure 6.31 (b) and (d) corresponds to the ΔK of 15 MPa√m and 25 MPa√m. Both pictures clearly show that striations cover the fracture surface. The spacing of two consecutive striations looks more consistent in the low ΔK region than in the high district, and this may be attributed to the rapid crack propagation at ΔK=25 MPa√m.

Another feature – crack branching – could be detected in the comparison of fracture surfaces in Figure 6.31 (a) and (c). At the ΔK of 15 MPa√m in Figure 6.31 (a), cracks propagated slower than that in 25 MPa√m, thus the crack usually propagated along the crack front as indicated by the black arrows. In ΔK=25 MPa√m in Figure 6.31 (c), on the other hand, a crack developed violently. This behavior caused branched cracks that were perpendicular or angular to the fracture surface and highly elongated in the direction of fatigue crack propagation.

The typical fracture types without and with corrosion are presented in Figure 6.32 and Figure 6.33, both of which indicate that the fracture in the reinforcing steel was transgranular. An aggressive environment corrodes the sharp edges in the fracture but not the type of fracture.

The final rapid fracture propagation was also transgranular fracture as shown in Figure 6.34. Comparing Figure 6.34 (b) and (d) at a magnification of 2000X, Figure 6.34 (b) shows clear cleavage fracture and corrosion only blurs the surface as seen in Figure 6.34 (d).

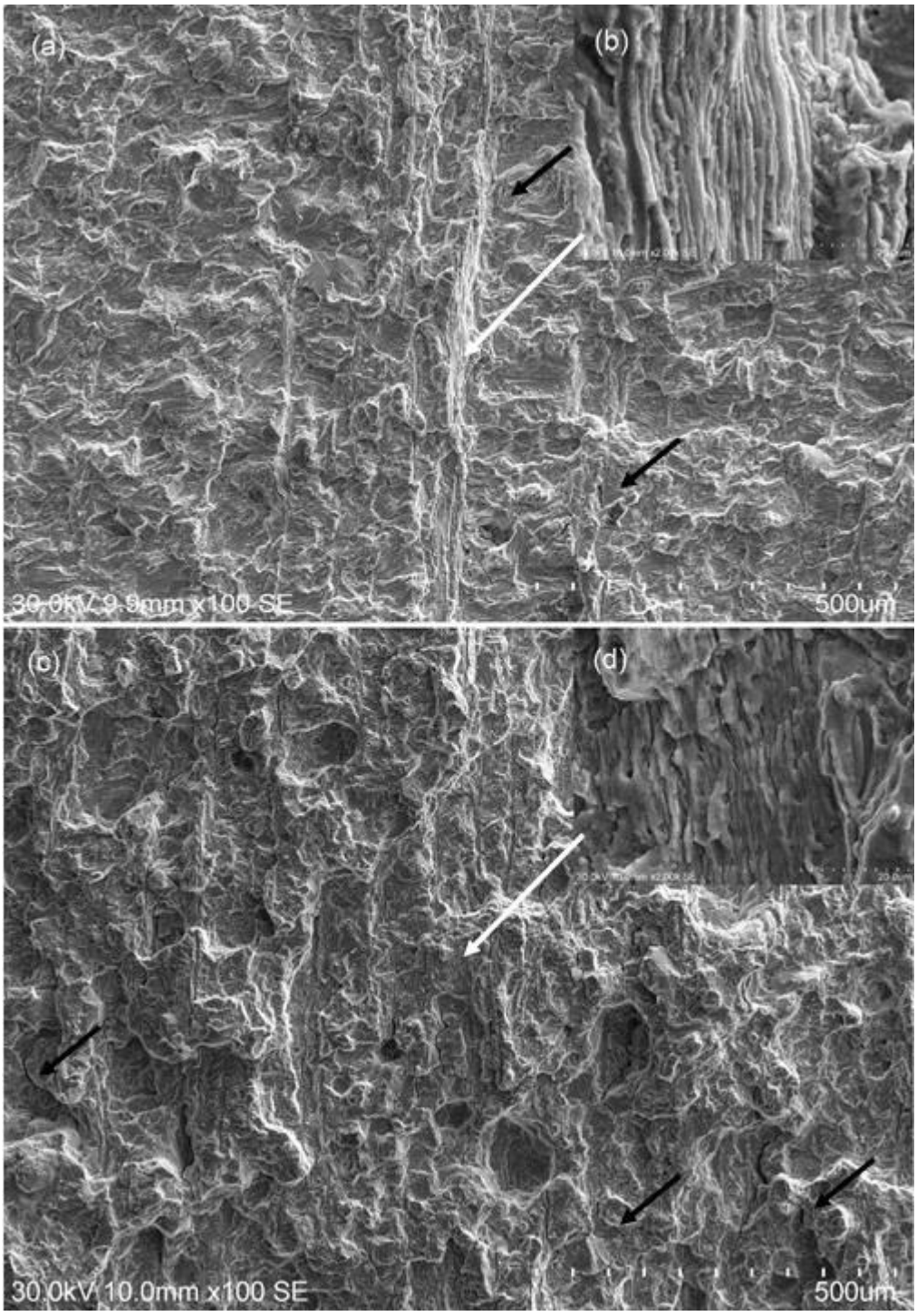

Figure 6.31. SEM graphs of the specimen tested in high SPS applied with 5mA current: (a), low ΔK, ≈ 15 MPa√m; (b) 2000X magnification of the central point in (a); (c), high ΔK, ≈ 25 MPa√m; (d) 2000X magnification of the central point in (c).

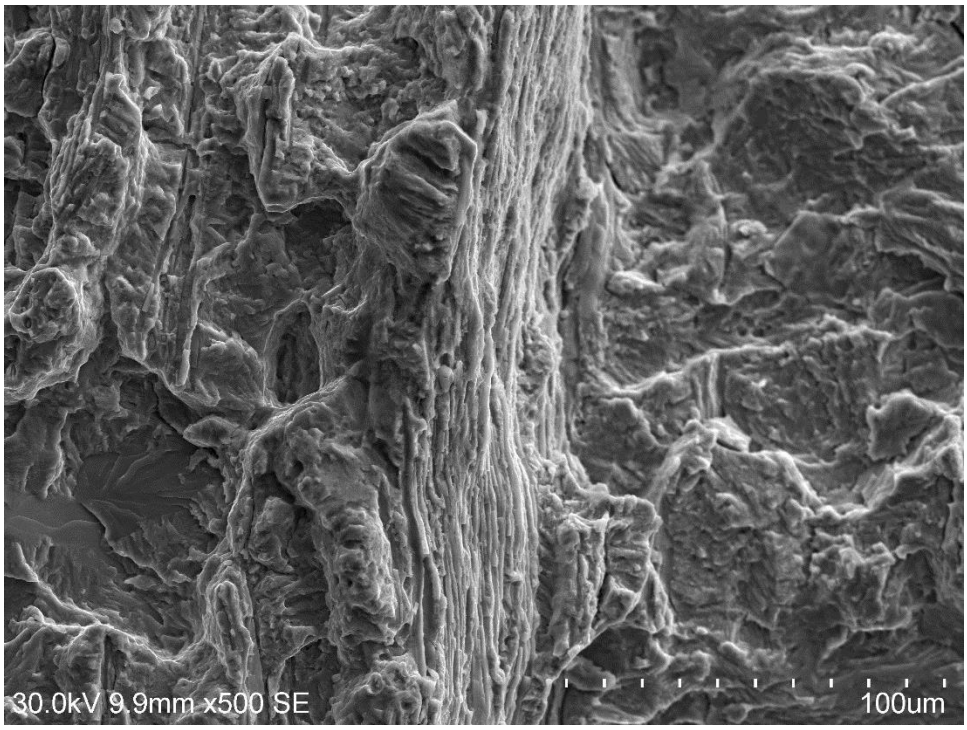

Figure 6.32. Transgranular fracture in the specimen tested in high pH SPS applied with 5mA current (500X).

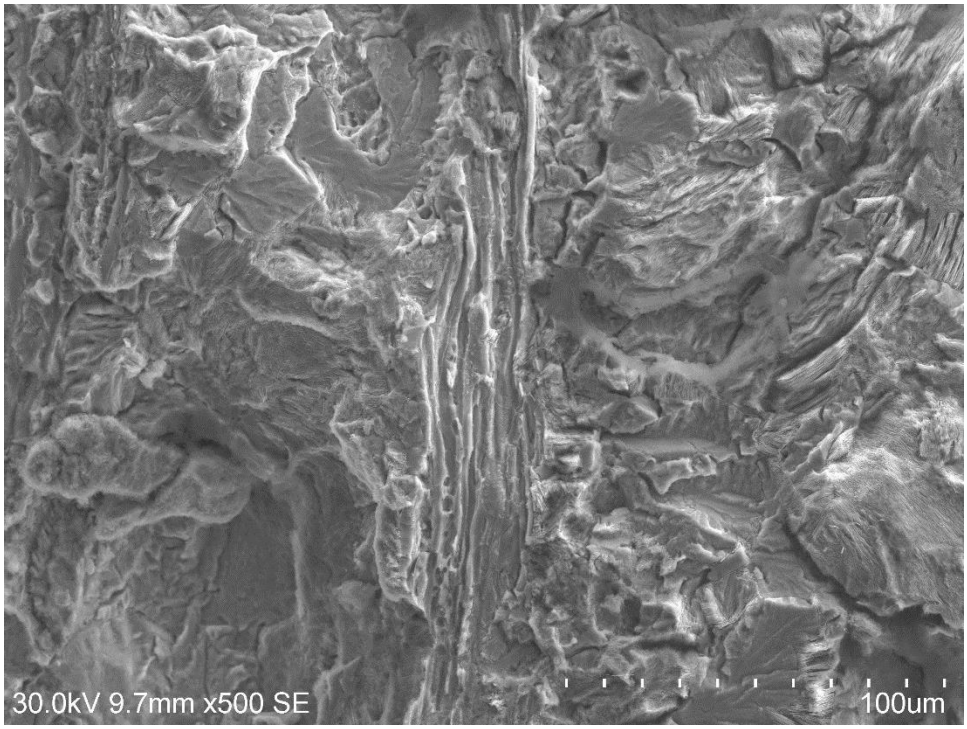

Figure 6.33. Transgranular fracture in the specimen tested in 0.1 M H_3PO_4 (500X).

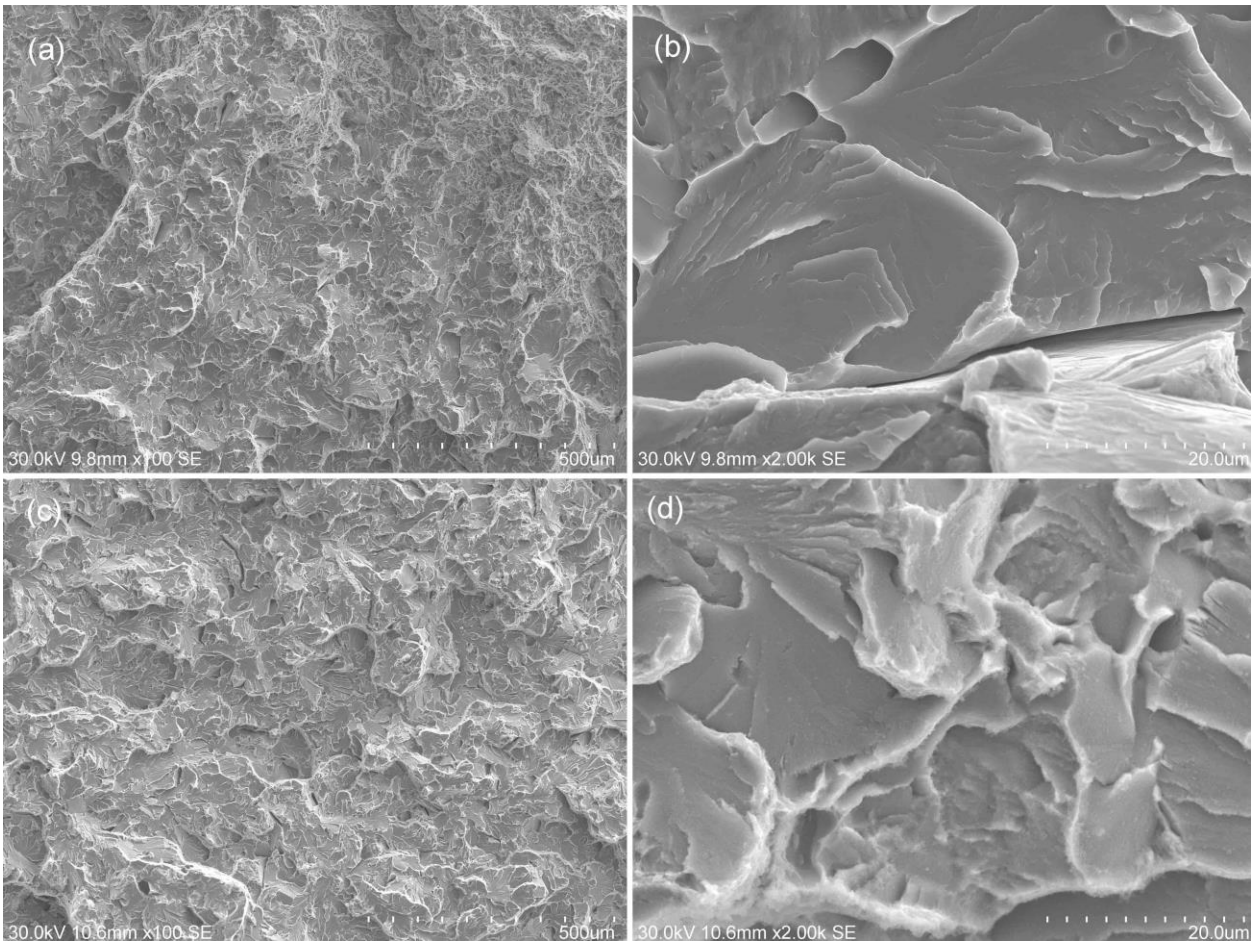

Figure 6.34. Rapid fracture surface of fatigue fractured specimens: (a), in air, 100X; (B), in air, 2000X; (c), in 0.1 M H_3PO_4, 100X; (d), in 0.1 M H_3PO_4, 2000X.

6.3 Rebar fatigue life evaluation under Fractural Mechanics model

Pit nucleation and growth

In a concrete environment, pit nucleation consists of two parts: the penetration of chloride through the concrete cover, and the accumulation of chloride that initiates pitting on rebar. In a solvent circumstance, on the other hand, pit nucleation is defined as the breakdown of the passive film and the initiation of pitting (Missert, Virtanen, Davenport, & Ryan, 2007).

Pit nucleation and growth could be estimated by the empirical pit growth equations generated in Section 6.1.2. In Sections 6.1.1 and 6.1.2, the incubation time of pitting was regressed at zero and the growth of the maximum pit depth was estimated from the curves in Figure 6.13 (a) in high pH SPS because of the general concrete environment. The fitted parameters of Eq. (6.1) in these curves are provided in Table 6.10. The relations between the corrosion current density and the fitted equation constants – A and B – were linearly fitted as Figure 6.35 and Figure 6.36. Since the corrosion current densities of both constants were known, both graphs could be used to extrapolate A and B values at other corrosion current densities.

$$d = At^B \tag{6.1}$$

Table 6.10. Fitting parameters of pit growth data in high pH SPS.

Corrosion conditions	A		B		Statistics
	Value	Standard Error	Value	Standard Error	Adj. R-Square
0.1 M Cl, high pH SPS	0.047	0.004	0.670	0.044	0.983
0.6 M Cl, high pH SPS	0.051	0.004	0.707	0.043	0.980
1.5 M Cl, high pH SPS	0.053	0.005	0.719	0.042	0.991

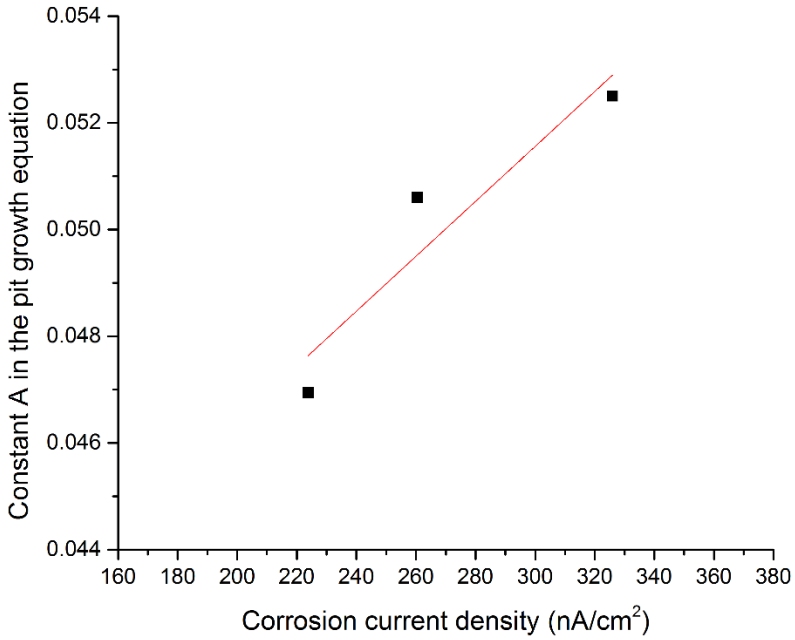

Figure 6.35. Constant A in the pit growth equation against corrosion current density.

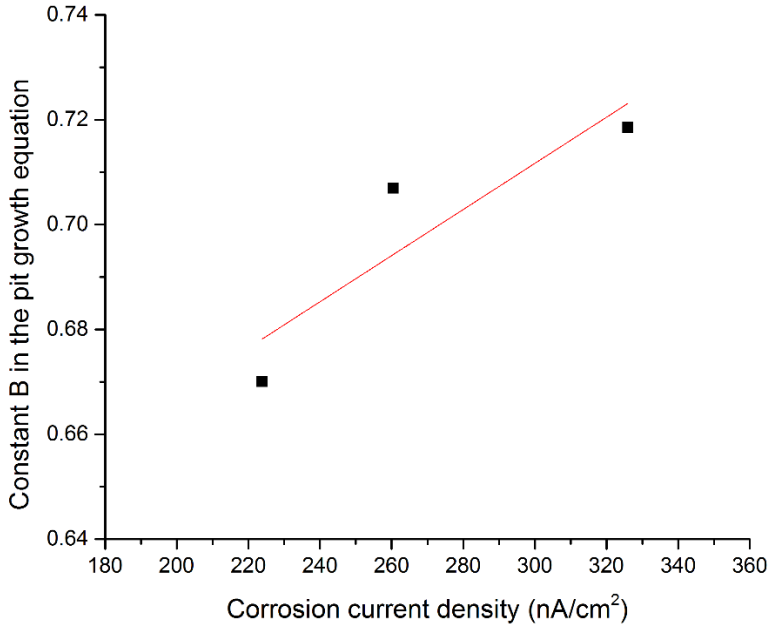

Figure 6.36. Constant B in the pit growth equation against corrosion current density.

Pit-to-crack transition

In Sections 6.2.3 and 6.2.1, the threshold stress intensity factor range ΔK_{th} and the fracture toughness K_{Ic} were measured as 5.70 MPa√m and 29.92 MPa√m. The FCGR curves under acidic corrosion in Figure 6.29 covered a ΔK range from 6.00 MPa√m to 29.98 MPa√m, which generally fit in the measured stress intensity factor range from ΔK_{th} to K_{Ic}. Hence, the FCGR curves under various corrosion rates were reasonably used to predict fatigue cycles at a selected corrosion current density.

Due to the fact that the rebar used in the field has ribs, this study assumed that the reinforcing steel was round bar without ribs. The corresponding stress intensity factor equation citied from Eq. (3.13) is repeated here.

$$K_I = \sigma\sqrt{\pi S}\, f(\frac{a}{c}) \tag{3.13}$$

$$S = r \cdot arcsin(\frac{c}{r}) \tag{3.14}$$

$$f\left(\frac{a}{c}\right) = 0.7433(\frac{a}{r})^2 - 0.2194\left(\frac{a}{r}\right) + 0.6757 \tag{3.15}$$

Eq. (3.13) requires a crack shape function $f(\frac{a}{c})$ in the equation; therefore, a constant a/c ratio has to be selected during the pit growth and the crack propagation. Then, the critical pit size that transits to a crack is calculated by the a/c aspect ratio and the applied tensile stress. The confirmation of using ΔK_{th} to calculate the critical pit size has to be conducted since the crack growth rate at ΔK_{th} might be smaller than its pit growth rate. If the calculated da/dN is less than the pit growth rate at ΔK_{th}, a larger crack size a is required to assure that the correspondent da/dN equals to the corresponding pit growth rate. The crack size a is considered as the initial crack which defines the pit-to-crack transition. Then, providing the pit growth curves and the corrosive environment of a rebar, the time needed to develop a critical pit depth could be estimated. Finally, the fatigue cycles are approximated by the division of the calculated pitting corrosion time and the cyclic loading frequency.

Crack propagation

The crack propagation stage covers the initiation of a crack until its fracture failure. There are two approaches to estimate fatigue cycles by the da/dN vs ΔK curves in Figure 6.29: direct approach and indirect approach.

Direct approach: This approach directly uses the da/dN vs ΔK equation seen in Eq. (6.5) to predict fatigue cycles at different corrosion rates (Weng et al., 2013).

$$da/dN = A(\Delta K - \Delta K_{th})^B \tag{6.5}$$

where da/dN is the crack propagation rate, in mm/cycle; ΔK is the applied stress intensity factor range, in MPa√m; ΔK_{th} is the threshold stress intensity factor range, in MPa√m; A and B are constants depending on the material and the testing environment.

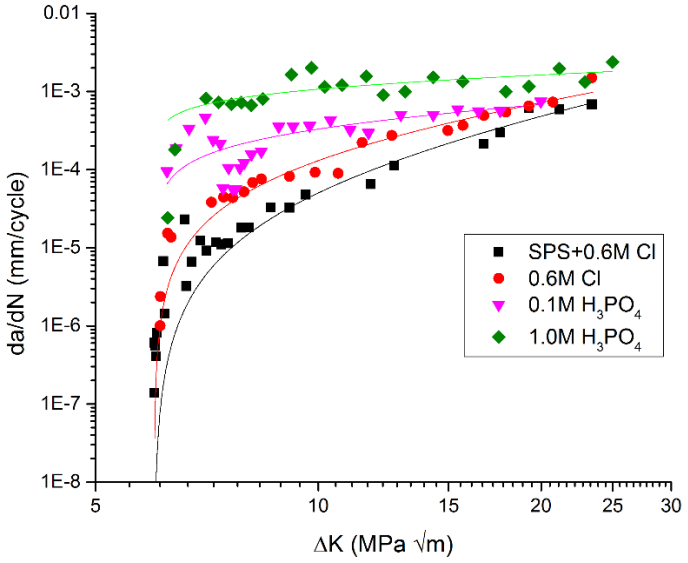

Figure 6.37. Power equation fitting of the da/dN vs ΔK curves under corrosion.

Since A and B depend on the tested metal and the corrosive environment, both constants were generated by the four da/dN vs ΔK curves in Figure 6.29, which were produced in corrosive environments from almost non-aggressive to extremely aggressive. Both constants A and B are plotted against the corrosion current density in Figure 6.38 and Figure 6.39, respectively; hence,

A and B for a corrosion current density located within the plot range could be projected from both graphs. The fatigue cycles of that current density were then reversely integrated by the obtained crack growth curve and the stress intensity factor equation.

Table 6.11. Parameters of fitted power equation of the the da/dN vs ΔK curves under corrosion.

Corrosive environment	Corrosion current density / μA/cm^2	Constant A		Constant B	
		Value	Standard error	Value	Standard error
SPS + 0.6 M Cl	0.26	4.12E-6	1.07E-6	1.80	0.15
0.6 M Cl	242.68	1.96E-5	0.42E-5	1.37	0.10
0.1 M H_3PO_4	1570.00	1.48E-4	0.60E-4	0.58	0.09
1.0 M H_3PO_4	5047.50	6.72E-4	1.22E-4	0.34	0.08

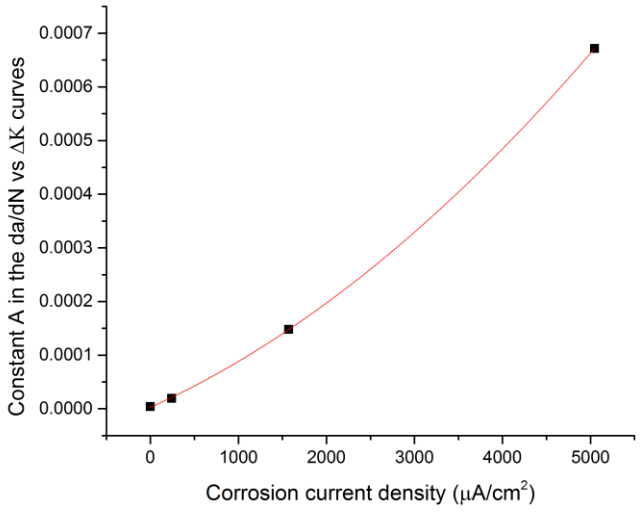

Figure 6.38. Constant A fitting in the da/dN vs ΔK curves.

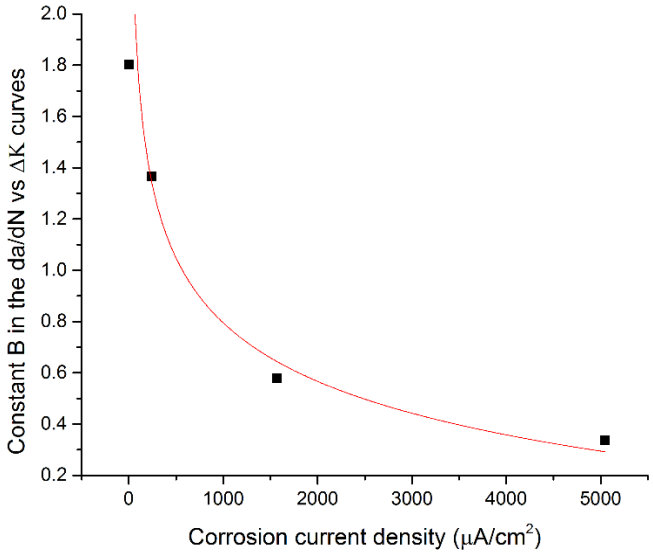

Figure 6.39. Constant B fitting in the da/dN vs ΔK curves.

Indirect approach: In this approach, a CF prediction model is used and shown in Eq. (6.6) (Weng et al., 2013):

$$(da/dN)_{CF} = [\left(\frac{da}{dN}\right)_{LCR}]^{(1-\beta)}((da/dN)_{LCR} + (da/dN)_{HCR})^{\beta} \quad (6.6)$$

$$\beta = \lambda(\Delta K_{th}/K_{max})^{h\Delta K_{th}/\Delta K_{th0}} \quad (6.7)$$

$$\Delta K_{th} = \Delta K_{th0}[1 - \langle R\rangle]^{\gamma_{th}} \quad (6.8)$$

where $\left(\frac{da}{dN}\right)_{LCR}$ and $\left(\frac{da}{dN}\right)_{HCR}$ are the crack growth rates at a rather low corrosion rate and extremely high corrosion rate; λ and h are the model constants defined by material and environment combination; ΔK_{th} is the threshold stress intensity factor of rebar under corrosion; K_{max} is the maximum stress intensity factor in a loading cycle; R is the stress ratio; $\langle R\rangle$ = R when R ≥ 0 and R = 0 when R < 0; ΔK_{th0} is the threshold stress intensity factor range at R = 0; γ_{th} is a material constant and found at 1.15 from Figure 6.26.

The main idea of the CF model involves two extremes of corrosion current densities (rather low and significantly high) in the crack growth, and uses the ΔK against da/dN curves of both current densities to predict the crack propagation curve within these two extremes.

$\left(\frac{da}{dN}\right)_{LCR}$ and $\left(\frac{da}{dN}\right)_{HCR}$ represent the crack growth curves generated in high pH SPS+0.6 M Cl and 1.0 M H_3PO_4, respectively. Table 6.12 provides the parameters in Eq. (6.5) of both growth curves.

Except for λ and h, other parameters in Eq. (6.7) are material-dependent or constant during a CF test. Therefore, λ and h , governed by material/environment, control the crack propagation curve of a specimen in a specific metal/environment condition. All four groups of λ and h were computed by Origin software and the fitted values are provided in Table 6.12. Figure 6.40 plots the corrosion current density against λ or h and the correspondent fitting equations are presented in Eq. (6.9) and Eq. (6.10), respectively:

$$\lambda = 0.02583(i_{corr})^{0.441} \tag{6.9}$$

$$h = -0.74 + 0.000704\, i_{corr} - 0.0000001113(i_{corr})^2 \tag{6.10}$$

Table 6.12. Fitted λ and h for crack growth curves in four corrosives.

Corrosive environment	Corrosion current density / μA/cm^2	Constant λ		Constant h	
		Value	Standard error	Value	Standard error
SPS + 0.6 M Cl	0.26	0.017	0.004	-0.732	0.108
0.6 M Cl	242.68	0.218	0.074	-0.586	0.096
0.1 M H_3PO_4	1570.00	0.743	0.110	-0.092	0.009
1.0 M H_3PO_4	5047.50	1.076	0.113	-0.025	0.005

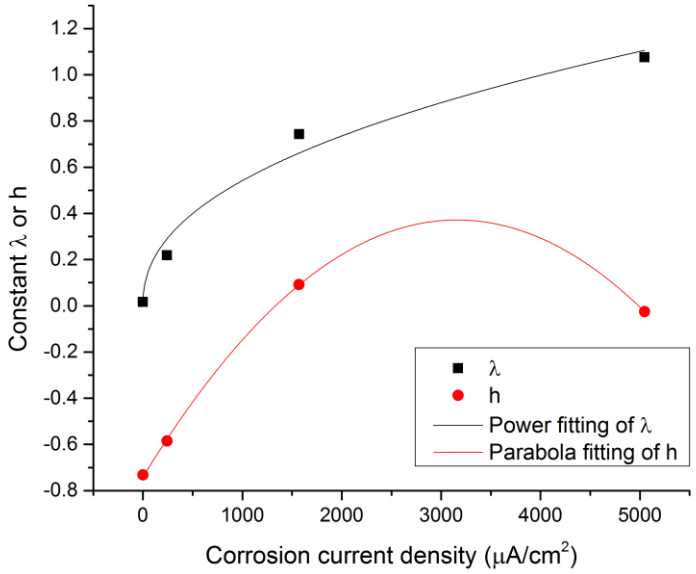

Figure 6.40. λ and h vs corrosion current density fitting in the crack growth curves.

Therefore, the CF model could be generated provided that the corrosion current density i_{corr} is known. Finally, the obtained CF model could reversely estimate the fatigue cycles during the crack propagation in a rebar as indicated in the direct approach.

7 Corrosion-fatigue in RC beams and the prediction of their service lives by both S-N approach and fracture mechanics approach

Chapter 5 and Chapter 6 have introduced two approaches to evaluate fatigue life of reinforced concrete (RC) structures under corrosion-fatigue (CF) – the S-N approach and the fracture mechanics approach. However, these two methods have not yet been verified.

In this chapter, the corrosion-fatigue behavior of RC beams is studied first. Four RC beams were tested under a cyclic loading with varied electrochemical corrosion current densities: 0 $\mu A/cm^2$, 0.05 $\mu A/cm^2$, 0.15 $\mu A/cm^2$, and 0.32 $\mu A/cm^2$. The maximum load amplitude was set to be half the capacity of the designed RC beams at a stress ratio of 0.1. Then, the corresponding fatigue lives at each of the corrosion rates were recorded and compared, and the cracking maps of each face of the RC beam were collected and analyzed.

Furthermore, both S-N method and fracture mechanics method were applied to predict the fatigue cycles of the tested RC beams at the same CF conditions. Then, the predicted cycles were compared with the actually tested values in order to determine the accuracy of each approach.

7.1 RC beams fatigue life under different corrosion degrees

Table 7.1 presents the fatigue cycles of the four RC beams that have been tested with a combination of an applied stress and a corrosion rate. The results show that the fatigue life declined with an increase of corrosion rate with the applied load range of 0.9 – 9 kN. This observation is consistent with many studies performed with an uncoupled corrosion and fatigue (Rteil, 2007; Song & Yu, 2015; Yi et al., 2011). For instance, Song and Yu (Song & Yu, 2015) reported the number of fatigue cycles to be 968,000 and 537,000 at a pre-corroded corrosion degree of 4.7 % and 8.1%, respectively. These results are in good agreement with those acquired in the corrosion degrees of 4.71% and of 7.72% in Table 7.1. At 4.71% of corrosion in this study, fatigue cycles with a coupled corrosion-fatigue effect reached 601,779, significantly lower than 968,000 cycles with an uncoupled corrosion-fatigue effect. These measured results indicate that a more severe damage

could occur under a combined corrosion and fatigue than that with an individual corrosion and fatigue.

Table 7.1 reflects great consistency between the theoretical mass losses and the measured mass losses. Nevertheless, a negative mass loss in the non-corroded RC beam indicated that the rebar actually gained weight after the test. This behavior might be attributed to experimental error caused by the evaluation method of mass loss, or due to the sticking of concrete on the rebar.

Figure 7.1 (a) presents a typical mode of rebar fracture, while Figure 7.1 (b) shows that a crack could initiate from the bottom and propagate upward until the final rupture. During the CF test of an RC beam, the bottom side of rebar tended to corrode first because of the easy access to reaction. Moreover, the bottom edge of the rebar undertakes higher tensile loading during the bending of RC beams. As a result, stress concentrated on the corroded spots, which usually nucleated a crack and further propagated until fracture failure. The fracture surface in Figure 7.1 (b) agreed well with this explanation of pitting-induced fracture failure.

Table 7.1. Fatigue cycles of the five beams tested at the combination of applied stress and corrosion rate

Beam No.	Applied load range / kN	Designed corrosion rate / $\mu A/cm^2$	Theoretical mass loss percentage/ %	Actual mass loss percentage/ %	Fatigue life / cycles	Failure mode
L0	0.9 – 9	0	0	-0.17	> 2 million	N/A
L1	0.9 – 9	0.05	2.90	2.58	1,017,605	Steel rupture
L2	0.9 – 9	0.15	4.71	5.71	601,779	Steel rupture
L3	0.9 – 9	0.32	7.72	8.74	569,840	Steel rupture

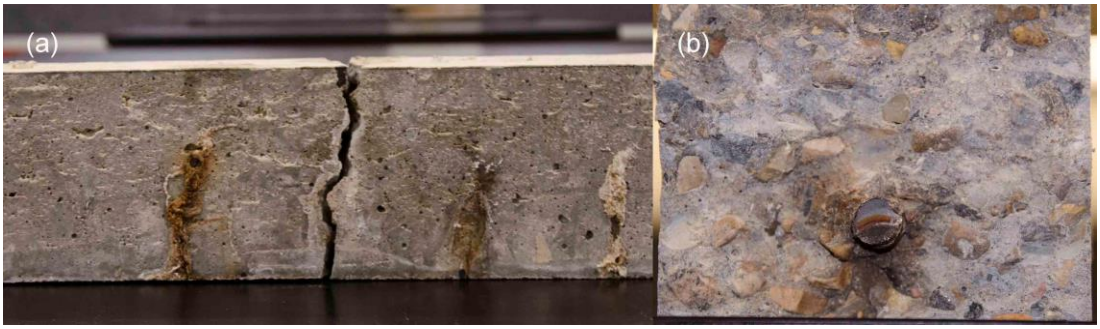

Figure 7.1. RC beam failure: (a), central crack side view; (b), fracture view.

7.2 Crack mapping and cross section loss of rebar in RC beams under corrosion-fatigue

7.2.1 Crack mapping analysis

Figure 7.2 gives the crack mapping of specimens under a non-corrosive environment with a cyclic loading ranging from 0.9 kN to 9.0 kN. The mapping shows that only two continuous cracks were observed in the center. Both cracks vertically crossed the tension zone in the beam and propagate until the compression zone at the top of the beam. This behavior meant that the applied load could result in concrete fracture due to tensile failure. Moreover, the RC beam bends in the center of the beam after the test, which agreed with the designed failure mode in this study – the yielding of reinforcement.

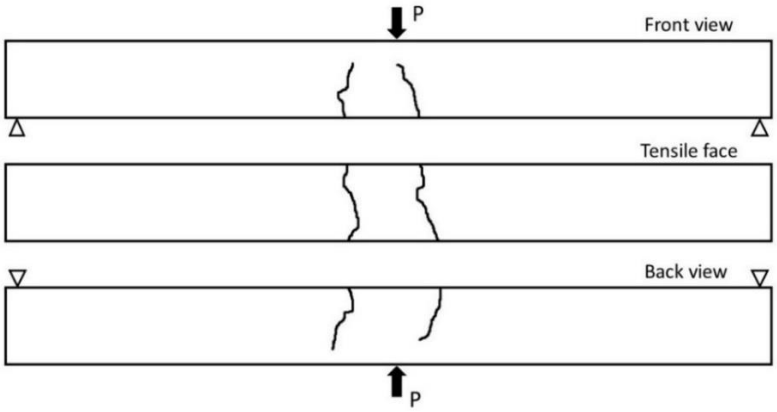

Figure 7.2. RC beam cracks mapping at non-corrosion fatigue test, load range 0.9 – 9.0 kN.

Figure 7.3 demonstrates the crack mapping of an RC beam tested in an accelerated corrosion current density of 0.32 μA/cm^2 with the load range of 0.9 – 9.0 kN. Although the beam tested in a corrosion environment had the similar front and back crack mappings when compared to that tested in air, their mapping was completely different at the tensile face. The in-air beam only had tensile failure cracks across the beam. By contrast, the beam tested under CF had massive cracks. Since the rebar had a concrete cover thickness of 1.5 cm from the bottom (tensile face) and 4.5 cm from the side (front or back face), corrosion product should have fractured the bottom concrete cover prior to the side cover. This explains the similarity in crack mappings at the front and back, as shown in Figure 7.2 and Figure 7.3. Besides the cracks across the tension zone in the corroded portion of the beam in Figure 7.3, multiple cracks also appeared along the rebar, which suggests that the corrosion of rebar could have generated sufficient pressure to overcome the tensile strength of the concrete cover and lead to the occurrence of cracks.

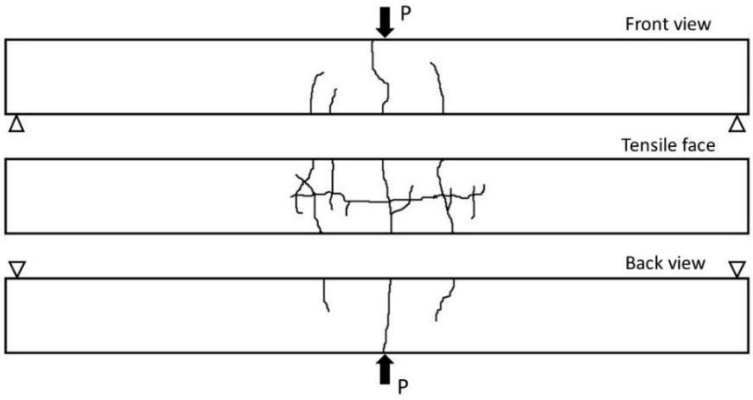

Figure 7.3. RC beam crack mapping under CF, 0.32 μA/cm^2, load range 0.9 – 9.0 kN

7.2.2 Cross section loss of rebar

Figure 7.4 gives the distribution of cross section loss along 20 cm of the corroded rebar. The maximum cross section loss in a rebar is mainly occurred near the center of a beam. This phenomenon could result from two reasons. On the one hand, the central part of an RC beam experiences the maximum bending moment, which produces the maximum tensile stress in the rebar. On the other hand, from the fracture mechanics point of view, the tensile load greatly facilitates pit nucleation of a crack, that probably further develops to a fracture failure.

In the three beams tested from 0.9 – 9.0 kN with the corrosion current densities of 0.05 μA/cm^2, 0.15 μA/cm^2, and 0.32 μA/cm^2, respectively, the data demonstrated that specimens under higher corrosion rates failed at a shorter service life with a higher cross section reduction in rebar.

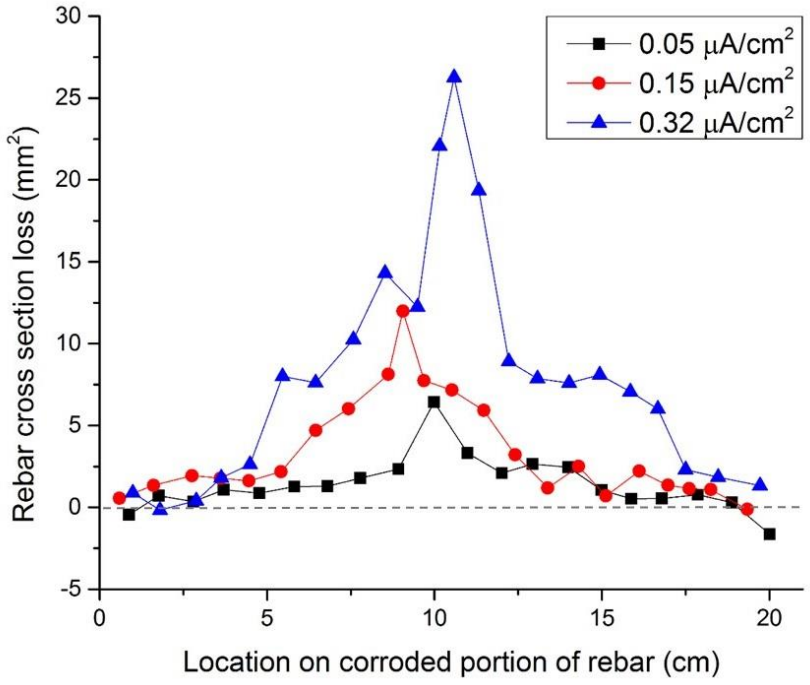

Figure 7.4. Rebar cross section loss at the specific locations in rebar.

7.3 Rebar fracture surface examination

Figure 7.5 presents a typical fracture surface of the tested rebar in RC under CF. Figure 7.5 (a) gives the final fracture failure of rebar that stems from multiple pits on the edge of spot A. The radial lines along the white arrows signify that at least two pits initiated cracks appeared during the fatigue process. This behavior was further confirmed by the existence of two ratchet marks demonstrated by the black arrows, and their presence denoted the junction of two adjacent crack origins. Figure 7.5 (b) displays three main origins initiating the fracture. As the crack initiated and propagated, it grew at an accelerated rate, and then transited from the critical crack to the final ductile failure of rebar as shown in Figure 7.5 (c). Figure 7.5 (d) exhibits that Spot C was filled with micro-voids – known as dimples. They imply that the rebar failed because of ductile rupture, which is consistent with the ductile property of reinforcing steel.

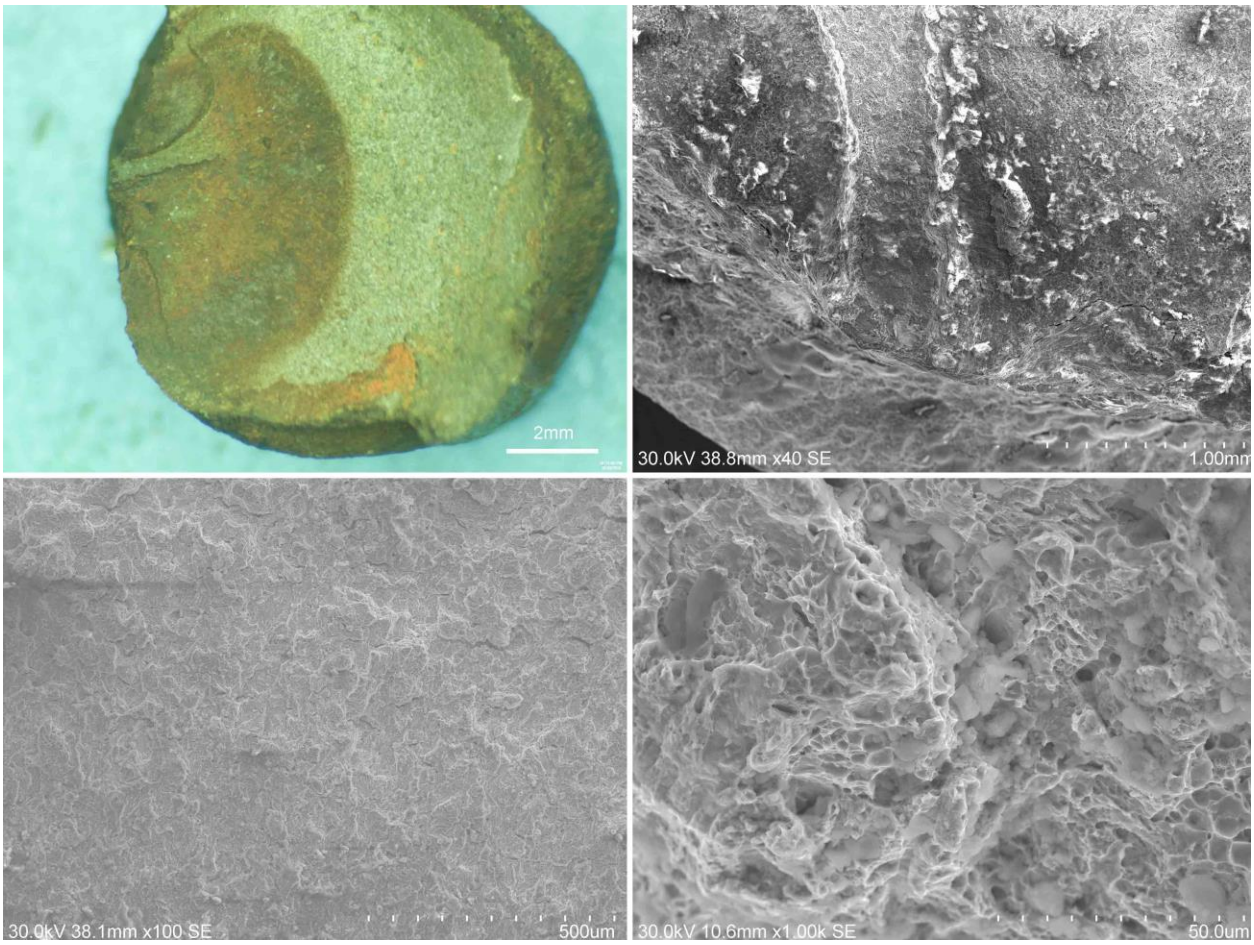

Figure 7.5. Stereo microscope and SEM graphs of rebar fracture surface: (a), entire rebar fracture surface examined by stereo microscope; (b), two main pits in spot A (40X); (c), crack to fracture transition at spot B (100X); (d), final ductile fracture at spot C (1000X).

7.4 The service life prediction of the RC beams under corrosion-fatigue by the S-N curve approach

Service life prediction by the S-N approach has been introduced in Chapter 5, however, the validation of this approach in RC beams has not been introduced. Since corrosion-fatigue test in RC beams has been conducted, the S-N approach can be validated by the obtained fatigue cycles of RC beams in various CF environments.

The RC beams in a CF environment were initially designed with the maximum fatigue cycles of 2 million; thus, the S-N curves in Figure 5.3 (a) can be used for the prediction. As both RC beams CF tests and S-N curves share the same three corrosion levels, 0.05 μA/cm^2, 0.15 μA/cm^2, and 0.32 μA/cm^2, the three S-N curves could be used for the data correction at the CF condition in the RC beam test. In the fatigue testing of RC beams, the applied load ranged from 0.9 kN to 9.0 kN with a mean load of 4.95 kN, which suggested a positive tensile stress existed during the test. However, the mean stress equaled zero in the S-N curves, thus the data transformation required a correction of mean stress effect. Moreover, RC beams tested in a chloride environment are very likely to cause an effect on the reduction of fatigue life because of chloride-induced pitting. The presence of pits on rebar in RC might act as tiny notches; thus, the resultant notch effect should be taken into account in the correction of fatigue life.

Correction of mean stress effect

Mean stress effect was modified by two empirical equations, Goodman line and Gerber parabola, which are cited from Chapter 3 and listed below:

$$\text{Goodman relation: } \sigma_a = \sigma_{fat}\left(1 - \frac{\sigma_m}{\sigma_{ts}}\right) \tag{3.9}$$

$$\text{Gerber relation: } \sigma_a = \sigma_{fat}\left(1 - \left(\frac{\sigma_m}{\sigma_{ts}}\right)^2\right) \tag{3.10}$$

In Section 3.4.1, the ultimate tensile strength σ_{ts} of rebar was 666 MPa in both the RC beam CF test and the rotating bending test. Provided that the load range in RC beam testing was 0.9 – 9.0 kN and the beam dimensions in Section 3.4.5, structural analysis gave a calculated mean stress σ_m of 121 MPa applied on the rebar. Given the ultimate tensile strength and the mean stress, the corrected fatigue stresses were calculated by substituting σ_{fat} in Eq. (3.9) and (3.10) with the fatigue stress levels in Figure 5.3 (a). Figure 7.6 plots these corrected stresses with the fatigue cycles obtained from Figure 5.3 (a). Figure 7.6 (a), (b), and (c) clearly demonstrate that a positive mean stress reduced the required stress amplitude and generated the same amount of failure cycles.

Moreover, the Goodman line was more conservative than the Gerber parabola since specimens survived longer in Gerber correction than Goodman line at the same stress amplitude.

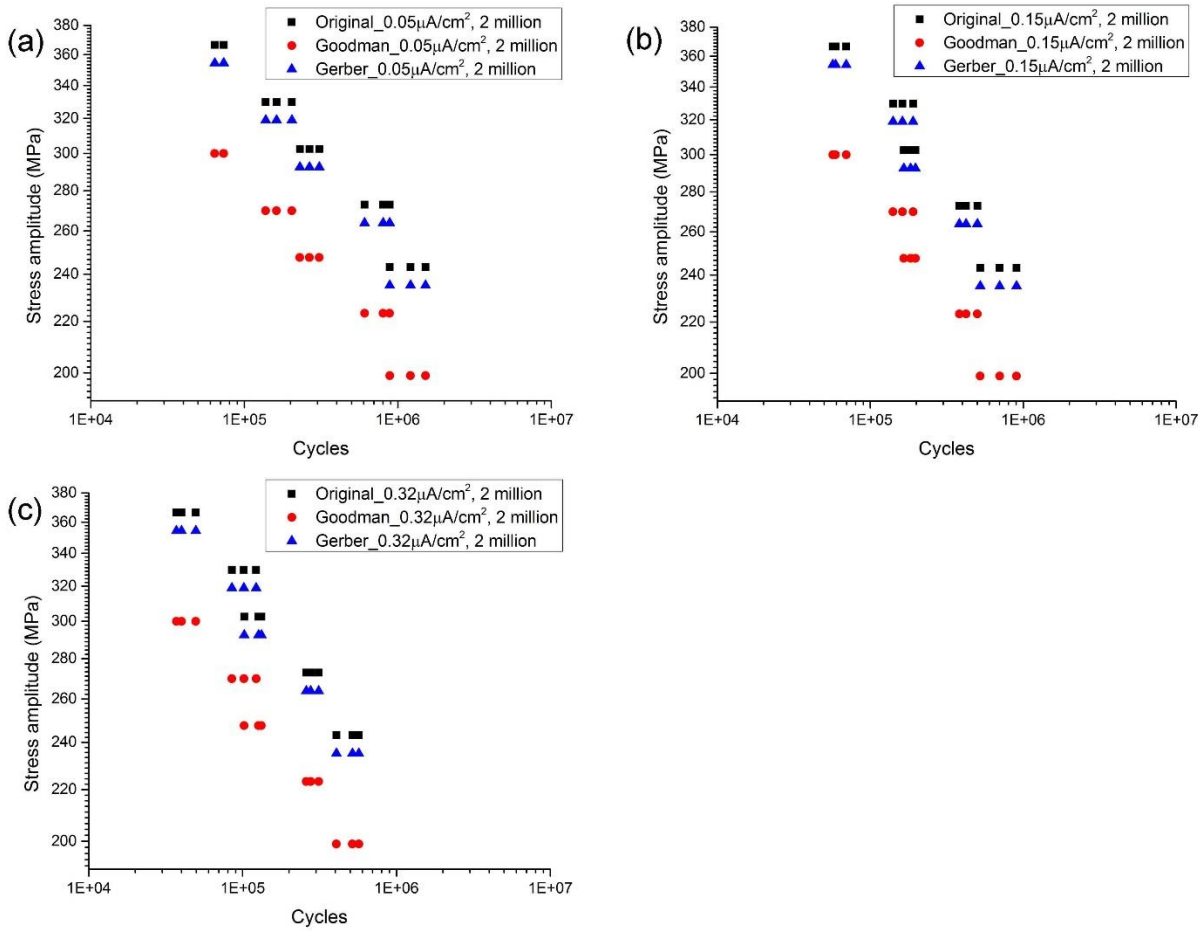

Figure 7.6. Mean stress correction of S-N curves through Goodman and Gerber relations: (a), 0.05 μA/cm^2, 0.9 – 9.0 kN; (b), 0.15 μA/cm^2, 0.9 – 9.0 kN; (c), 0.32 μA/cm^2, 0.9 – 9.0 kN.

Correction of pitting

As discussed before, the notch effect should be corrected as the pits serve as notches on the specimen surface. To introduce the notch effect, the most common approach is to add a notch factor for the correction of mean stress. A notch factor represents the ratio of smooth to notched fatigue strengths; the equation format proposed by Peterson (Stephens et al., 2000) is shown in Eq. (3.7):

$$K_f = 1 + \frac{K_t - 1}{1 + a/r} \tag{3.7}$$

$$a = 0.0254\ (\frac{2070}{S_u})^{1.8} \text{ with } S_u \text{ in MPa and } a \text{ in mm} \tag{3.8}$$

The parameters in Eq. (3.7) could be input as below: the elastic stress concentration factor = 3 MPa√m for steel, and the ultimate tensile strength of rebar = 666 MPa. In terms of the radium of notch root, it can be calculated by the stress intensity factor equation shown in Eq. (3.13), and a/2c in the equation is defined as 1.25 for the geometrical discontinuity on rebar surface.

Substituting the calculated K_f to Eq. (3.9) and (3.10), the final corrected mean stress were plotted as a function of the examined fatigue cycles in the rotating bending test. Figure 7.7 gives the final correction of S-N curves and the actually tested fatigue cycles of RC beams under CF:

$$\text{Corrected Goodman relation: } \sigma_a = \frac{\sigma_{fat}}{K_f}\left(1 - \frac{\sigma_m}{\sigma_{ts}}\right) \tag{3.9}$$

$$\text{Corrected Gerber relation: } \sigma_a = \frac{\sigma_{fat}}{K_f}\left(1 - \left(\frac{\sigma_m}{\sigma_{ts}}\right)^2\right) \tag{3.10}$$

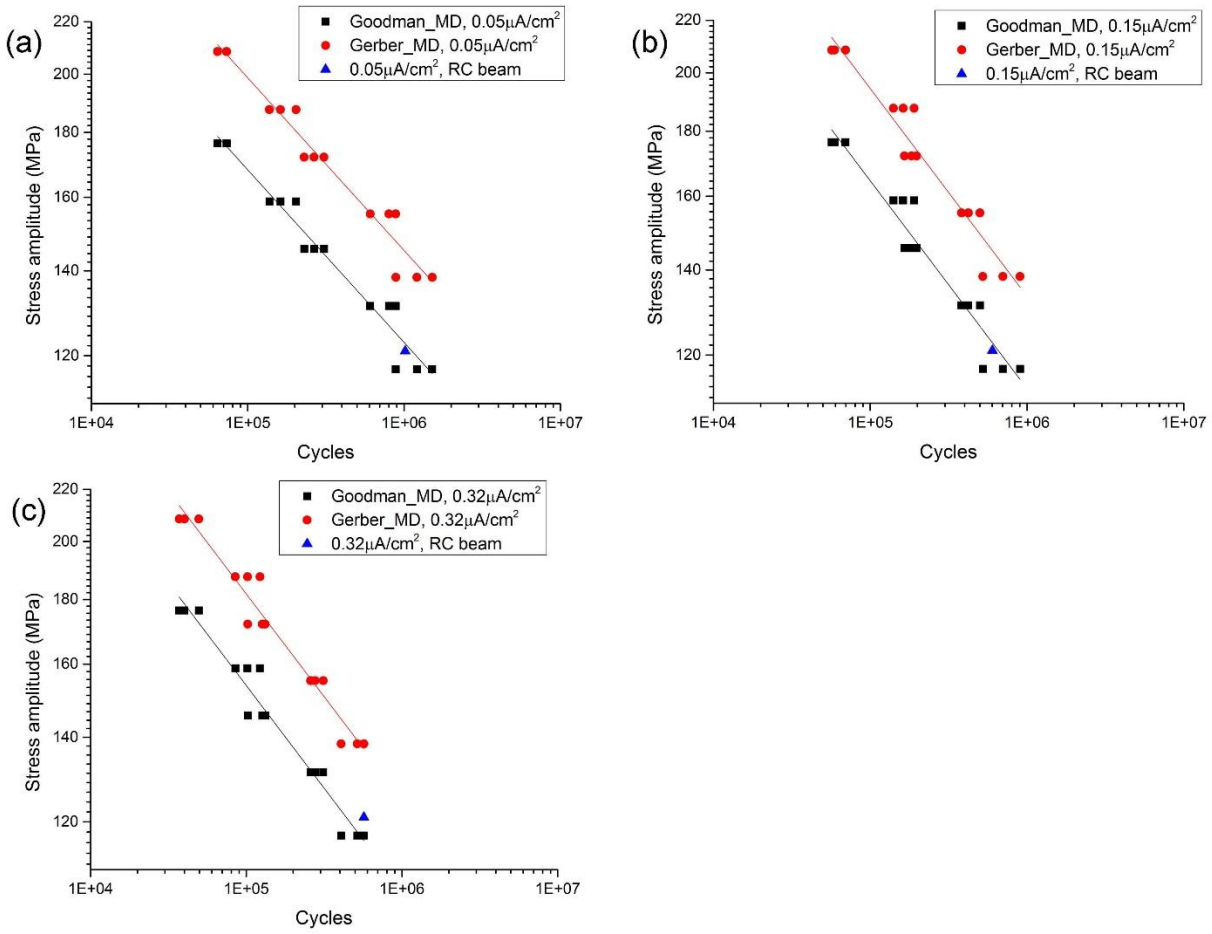

Figure 7.7. Notch effect correction of S-N curves and the comparison between the predicted cycle range and the actual tested life of RC beams: (a), 0.05 μA/cm^2, 0.9 – 9.0 kN; (b), 0.15 μA/cm^2, 0.9 – 9.0 kN; (c), 0.32 μA/cm^2, 0.9 – 9.0 kN.

Instead of providing a specific number of cycles at a stress amplitude, the S-N curve approach predicts the fatigue life of an RC beam in a range between the Goodman line and the Gerber relation. In Figure 7.7, the actual tested fatigue cycles mostly fit the Goodman line rather than fall between the two relations. Due to the fact that corrosion in this project only accounted for the notch effect regardless of many other effects, such as surface roughness and synergetic effects, the prediction of RC CF was more compatible with the conservative relation (Goodman line). According to the Goodman relation, the estimated numbers of fatigue cycles were 1,124,892, 655,865, and 438,822 correspondent to the CF environments of the applied stress at 121 MPa and three corrosion current densities of 0.05 μA/cm^2, 0.15 μA/cm^2, and 0.32 μA/cm^2.

In the reference test, the examination steps were slightly different in the prediction of service life. In Figure 5.2 (a), the fatigue limit of rebar for this project was 326.2 MPa and the mean stress corrected by Eq. (3.9) was 266.9 MPa. Without corrosion, no correction was required for notch effect. Hence, the fatigue limit of reinforcing steel beyond the modified mean stress was 266.9 MPa, significantly higher than the tested stress amplitude – 198 MPa at a load range of 0.9 – 9.0 kN. In other words, the fatigue life of an RC beam tested in the non-corrosion environment was infinite (> 2 million cycles of the design limit).

7.5 The service life prediction of RC beam under corrosion-fatigue by Fracture Mechanics approach

The procedures of the fracture mechanics approach has been introduced in Chapter 6 to estimate the fatigue life of an RC beam under corrosion fatigue. Nevertheless, this method has not been verified yet. After the service life of RC beams under CF has been obtained and the fracture mechanics approach is fully introduced, the validation is performed in this section.

To perform the CF prediction of reinforcement by fracture mechanics, service life estimation in all four stages are required, including pit growth examination, pit-to-crack transition, crack propagation, and fracture failure, as proposed in Section 6.3.

7.5.1 Pit growth in RC under corrosion-fatigue

The development of maximum pit depth d with time t can be estimated by the empirical power equation as shown in Eq. (6.1). The relationship between the constants (A and B) of the equation and corrosion current densities are presented in Figure 6.35 and Figure 6.36. Based on the linear fitting parameters of both constants and corrosion current densities in Table 6.10, Table 7.2 lists the calculated values of A and B in the three designed corrosion rates in the CF testing of RC beams, 0.05 μA/cm^2, 0.15 μA/cm^2, and 0.32 μA/cm^2.

Table 7.2. Constant A and B in the empirical pit growth equation at three corrosion rates during RC CF testing.

Corrosion current density in RC CF test / μA/cm^2	Constant A	Constant B
0.05	0.0387	0.602
0.15	0.438	0.646
0.32	0.0526	0.720

The threshold stress concentration factor range was 6.00 MPa√m that was obtained from the crack growth curves of acidic solutions in Figure 6.29 within the measured ΔK_{th} range 5.70 ± 0.34 MPa√m. Hence, a value of 6.00 MPa√m was used to calculate the critical pit size in crack initiation.

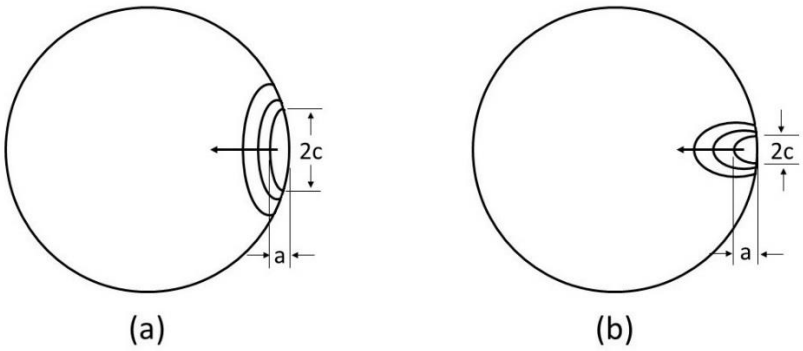

Figure 7.8. Crack shape (a) and pit shape (b) occurring on rebar.

Prior to the calculation of critical pit depth, it was critical to determine the aspect ratio a/c. The crack propagation in a cylindrical rod is usually considered as an elliptical shape as shown in Figure 7.8 (a). While a pit in rebar normally has a longer axis along the pit depth than along the pit mouth as presented in Figure 7.8 (b). By trial and error, the aspect ratio a/c was valued to be 2.5 for the calculations of stress intensity factor range and for the prediction of fatigue cycles.

Substituting ΔK_{th} = 6.00 MPa√m and the a/c=2.5 into the stress intensity factor equations, Eq. (3.13) to Eq. (3.15), the critical pit depth was calculated to be 1.61 mm for the load range of 0.9-

9.0 kN, and the required time to create such a pit is listed in Table 7.3 for different aggressiveness of the corrosives. Provided that the RC beams in the CF test were initially designed to serve a lifespan of 75 years in field, the required time in field to nucleate the critical pit depth could be estimated by the empirical pit growth equation with the constants listed in Table 7.2. Moreover, because the RC beams were designed to survive 2 million cycles in the 75-year lifespan, the required cycles to create such a critical pit depth could be estimated as listed in Table 7.3. The results illustrate that a high corrosion rate in pitting could greatly reduce the necessary fatigue cycles to nucleate the critical pit depth.

Table 7.3. Time to develop the critical pit depth and the correspondent fatigue cycles.

Combination of corrosion current density and load range in RC CF test	Time to create the critical pit depth / month	Total cycles during the pit nucleation period
0.05 μA/cm^2, 0.9-9.0 kN	630.2	1,400,304
0.15 μA/cm^2, 0.9-9.0 kN	337.8	750,592
0.32 μA/cm^2, 0.9-9.0 kN	150.2	333,744

7.5.2 Crack propagation of rebar in RC

The direct approach and the indirect approach were used to evaluate the crack propagation of rebar in RC. Using the relations between the constants of the fitted ΔK vs da/dN curves in Figure 6.29 and the corrosion current densities, the direct approach predicted the values of these constants according to the aggressiveness of corrosion in the CF testing of RC beams. While the indirect approach estimated the crack propagation by applying a CF propagation model, which combined the two extreme crack growth curves (significantly low and rather high corrosion rates) in Figure 6.29.

Direct approach

This approach fits the crack propagation curves in Figure 6.29 with the ΔK vs da/dN equation:

$$da/dN = A(\Delta K - \Delta K_{th})^B \quad (6.5)$$

The relations of the constants (A and B) and the corrosion current densities i_{corr} in the acidic solutions were fitted in Figure 6.38 and Figure 6.39, respectively. The regressed equations are provided below:

$$A = -2.39 \ln(0.104 \ln(i_{corr})) \quad (7.1)$$

$$B = 0.0000027 + 0.000000074\, i_{corr} + 0.0000000000116\, (i_{corr})^2 \quad (7.2)$$

Since the loading frequency of a beam undertaking 2 million cycles in 75 years is 0.000846 Hz in field and the loading frequency of RC beams in the CF test is 1 Hz, all three designed corrosion levels, 0.05 μA/cm^2, 0.15 μA/cm^2, and 0.32 μA/cm^2, could be converted to the laboratory current densities with the values of 59.13 μA/cm^2, 177.39 μA/cm^2, and 378.43 μA/cm^2, respectively. Substituting i_{corr} in Eq. (7.1) and (7.2) with the converted corrosion current densities, the corresponding A and B in Eq. (6.5) were obtained as shown in Table 7.4. The error of the fitted A values in the power equation was 9.0E-4; however, the predicted A values for all three corrosion levels in Table 7.4 were less than 1.62E-05. In other words, the predicted cycles in crack propagation would introduce tremendous errors.

Table 7.4. Constants A and B of the crack growth curve fitting at a designed corrosion rate in RC beam test.

Constants	Corrosion current density / μA/cm^2		
	0.05	0.15	0.32
A	7.12E-06	1.62E-05	3.24E-05
B	2.05	1.48	1.16

Based on these constants A and B listed in Table 7.4 and the crack propagation step of 0.02 mm, Table 7.5 presents the fatigue life estimation steps of an RC beam in 0.32 μA/cm^2. Table 7.6 displays the estimated fatigue cycles in two stages (pit growth and crack propagation) and the summed fatigue life of the three RC beams by fracture mechanics.

Table 7.5. The fatigue life evaluation of RC beam in an accelerated corrosion rate of 0.32 μA/cm^2

Crack length / m	ΔK/MPa√m	(da/dN) / mm/cycle	ΔN	Total cycles
0.00171	6.453	3.92E-06		
0.00173	6.498	5.47E-06	4,499	4,499
0.00175	6.543	1.62E-05	1,846	6,790
0.00177	6.588	2.47E-05	978	7,768
⋮	⋮	⋮	⋮	⋮
0.00699	29.021	9.45E-03	21	25,421
0.00701	29.179	9.52E-03	21	25,442
0.00703	29.238	9.60E-03	20	25,462

Table 7.6 implies that the fatigue life in both pit growth and crack propagation stage was lower in a highly aggressive corrosion. Moreover, the overall fatigue cycles decreased with the increase of corrosion rate. Furthermore, the pit growth stage contributed over 95% of the total fatigue cycles. As indicated in the constants estimation of crack propagation, the evaluation error in the constants of the power equation was far higher than the constants themselves; therefore, this would trigger huge errors in the estimation of fatigue cycles at the crack propagation stage. Such tremendous errors can be attributed to the uncertainty of the direct approach.

Figure 6.39 shows that the predicted B value was much larger than the original data at a corrosion current density below 500 μA/cm^2. Referring to Eq. (6.5), at the same A value, an elevated B would increase the crack propagation rate that reduces the integrated cycles at a fixed crack length. Therefore, in the direct approach, the predicted cycles in the crack propagation stage would be less than the real value. Therefore, this explains why the estimated cycles in the crack propagation stage represented such a small proportion.

In the non-corrosive condition, because of the infinite time demanded in the pit growth, the fatigue life could easily exceed the designed limit of two million cycles for an RC beam under CF. However, without a reasonable corrosion prediction at low corrosion current densities, the application of this approach in life estimation was limited.

Table 7.6. Predicted fatigue cycles of RC beams by the direct approach.

Fatigue cycles	Corrosion current density / μA/cm^2			
	0	0.05	0.15	0.32
Pit growth	>2,000,000	1,400,304	750,592	333,744
Crack propagation	N/A	39,356	36,717	25,462
Total	>2,000,000	1,439,660	787,309	359,206

Indirect approach

In Table 6.11, the constants in the power equation of the ΔK vs da/dN curves were obtained for the specimens tested in high pH SPS + 0.6 M Cl and in 1.0 M H_3PO_4. The key parameters, λ and h, controlling the crack growth curve in a combined environment of corrosion and fatigue, have been plotted as a function of the corrosion current densities in all acidic solutions, as shown in Figure 6.40. Given the converted corrosion rates of RC beam testing at 59.13 μA/cm^2, 177.39 μA/cm^2, and 378.43 μA/cm^2, respectively, Eq. (6.9) and (6.10) were used to calculate the correspondent values of λ and h as shown in Table 7.7.

Table 7.7. The predicted λ and h for the three corrosion levels in RC CF.

Parameters	Designed corrosion current density / μA/cm^2		
	0.05	0.15	0.32
λ	0.158	0.251	0.345
h	-0.699	-0.619	-0.490

With the parameters - λ and h, stress ratio R=0.1, and the modelled crack growth curves in high pH SPS + 0.6 M Cl and in 1.0 M H_3PO_4, the crack propagation curves in the three corrosion environments of tested RC beams could be generated, and the fatigue cycles of rebar could be reversely integrated as in the direct approach.

Table 7.8 gives the predicted cycles in both pit growth and crack propagation. Compared to the direct approach, the indirect approach similarly exhibited a decreasing fatigue life with an increasing corrosion rate. Likewise, the two approaches had the same mechanisms in the non-corrosion conditions – requiring infinite time to generate a critical pit. However, the crack propagation stage in the indirect approach served a longer life in comparison with that in the direct approach, which indicated that the indirect approach was more accurate than the direct approach.

Table 7.8. Predicted fatigue cycles of RC beams by the indirect approach.

Fatigue cycles	Corrosion current density / μA/cm^2			
	0	0.05	0.15	0.32
Pit growth	>2,000,000	1,400,304	750,592	333,744
Crack propagation	N/A	168,700	146,902	84,107
Total	>2,000,000	1,569,004	897,494	417,851

Moreover, Table 7.8 exhibits that pit nucleation and growth consumed most of the service life in corrosion-fatigue, from 79.9 % to 89.2% in a decrease of corrosion current densities. In other words, the service life of a structure approaches the end once a crack is nucleated. This indicates that it would be difficult to monitor fatigue since the crack propagation phase is relatively short. Therefore, routine maintenance, especially corrosion prevention, is essential to reinforced concrete structures that are under corrosion-fatigue. Moreover, special attention must be paid if the appearance of fracture on rebar is detected.

7.6 Comparison of the S-N curve approach and the fracture mechanics methods

Table 7.9 lists the tested fatigue cycles in RC beams and the predicted numbers, which are estimated using the Goodman line approach and the fracture mechanics method. Without corrosion, all models performed the same and gave a fatigue life over two million cycles.

Compared with the tested cycles of RC beams, S-N curves produced a close prediction in all three corrosion levels. The predicted errors were 10.5% in 0.05 $\mu A/cm^2$, 9.0% in 0.15 $\mu A/cm^2$, 23.0% in 0.32 $\mu A/cm^2$, which were rather small in contrast to the errors typical in a common fatigue prediction. These two fracture mechanics methods, direct approach and indirect approach, had errors ranging from 30.8% to 41.5% and from 26.7% to 54.2%, respectively. The error in either case was much higher than that in the S-N method, ranging from 9.0% to 23.0%.

Theoretically, the direct approach in fracture mechanics is supposed to produce a precise prediction since the crack growth curve is directly governed by the power equation. Even though the total cycles in Table 7.9 suggest that the direct approach overall produced a more accurate estimation than the indirect approach at the corrosion levels of 0.05 $\mu A/cm^2$ and 0.15 $\mu A/cm^2$, the predicted cycles at the crack propagation stage remained unreliable because of the significant error in the estimated parameters at low current densities in the fitting formula.

In comparison with the tested cycles, the indirect approach of fracture mechanics had the errors of 54.2%, 49.1%, and 26.7% corresponding to corrosion levels of 0.05 $\mu A/cm^2$, 0.15 $\mu A/cm^2$, and 0.32 $\mu A/cm^2$, respectively. Compared to the S-N curves, the indirect method of fracture mechanics had larger errors than the tested cycles in all corrosion levels. Therefore, it could be concluded that

the S-N curve approach can offer a more precise approximation on the corrosion-fatigue of RC beams than the fracture mechanics method. The reason might be attributed to the fact that the S-N curves approach evaluates CF based on the relationships between the applied stress and the resulting cycles. Besides, life prediction by the S-N approach involves a general relation rather than tracking the possibly detailed development from the crack origin to final failure. However, the fracture mechanics divides the CF process into stages that could introduce larger errors. Moreover, the accumulated error of all stages could be large even if each stage induces only a small error.

Table 7.9. Comparison of the predicted cycles and the actually tested fatigue life.

Approach	Corrosion current density / $\mu A/cm^2$			
	0	0.05	0.15	0.32
Actual tested cycles	>2,000,000	1,017,605	601,779	569,840
S-N curves	>2,000,000	1,124,892	655,865	438,822
Fracture Mechanics – direct approach	>2,000,000	1,439,660	787,309	359,206
Fracture Mechanics – indirect approach	>2,000,000	1,569,004	897,494	417,851

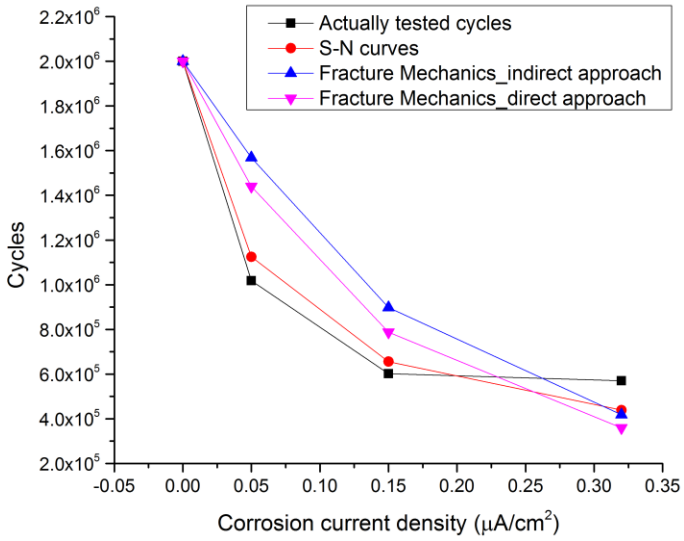

Figure 7.9. The examined and predicted service cycles at corrosion current densities.

Figure 7.9 shows that the fatigue cycles decreased with the increase of corrosion current densities. From non-corrosion to 0.32 μA/cm^2, the decreasing rate of cycles was declining, indicating that the synergetic effect of corrosion and fatigue had a high influence at a low corrosion current density. In other words, from non-corrosion to light corrosion, the effect of CF could cause great damage to the service life loss. As the corrosion current density increased, the contribution of CF to the loss of fatigue cycles rose even though the corresponding driving force was declining. In terms of RC structures in field, corrosion prevention is essential in non-corroded structures involved with cyclic loadings because a slight CF effect tremendously reduces the service life of a structure.

Errors introduced in the prediction were analyzed. In terms of S-N curves, this project accounts for two types of corrections: mean stress and notch effect. As mentioned before, other factors may also contribute to fatigue life reduction in the stress-life relationships, such as the change in surface roughness during the corrosion period, the diameter reduction during testing, and the synergetic effects of all influences.

The sources of errors in fracture mechanics may refer to different stages in the model. The data in pit growth were collected at surface roughness of 1 μm and 15 μm, however, the surface of actual used rebar is usually rougher and that might trigger distinct pit nucleation and propagation. Moreover, crack initiation might not occur in the deepest pit in the field. Furthermore, at a ΔK

near ΔK_{th}, researchers (Lee, Nishikawa, Oda, & Noguchi, 2012; Newman Jr, 1983; Tokaji, Ogawa, & Aoki, 1990) observed small crack behavior in metals, whereas this observation is beyond the consideration of this project.

The direct prediction of fracture mechanics significantly depends on the fitting of the constants A and B, and a small difference in the fitting could introduce a huge error in the forecasted constant A of low corrosion rates. Although different models were tried in order to improve the fit, the improvement was negligible.

The fracture mechanics are irrelevant with the corrosion effect of threshold stress intensity factor ΔK_{th}, which may cause an error in the estimation of fatigue cycles at the early stage of a crack. Some studies (Hertzberg, 2012; Milella, 2013) noted that, in the presence of corrosion, ΔK_{th} often shifts to a lower value as corrosion facilitates the initiation of cracks; besides the ΔK_{th}, the slope of the ΔK vs da/dN curve changes as well. The modification of the corrosion effect on ΔK_{th} reduces the pitting period and increases the crack propagation at a smaller ΔK. This could further reduce the service life; hence, more precise predictions could be expected in 0.05 $\mu A/cm^2$ and 0.15 $\mu A/cm^2$.

8 Conclusions and future work

8.1 General Summary

The study presented in this thesis was carried out to provide a better understanding of the corrosion fatigue of carbon steel reinforcement in concrete and to develop constitutive laws that can be used for predicting the long-term performance of RC structures under corrosion fatigue without favoring one degradation mechanism (corrosion or fatigue) over the other. The novelty of the proposed constitutive models resides in their ability to mimic realistic field conditions because they were developed for wide ranges of corrosion rates and fatigue loadings.

In order to achieve these goals, a three-stage approach was carried out. In the first stage a novel testing procedure was developed for accelerating corrosion in such a way that CF tests can be carried out in reasonable periods of time without distortion of the relative importance of corrosion and fatigue. In the second stage, the accelerated testing procedure that was developed in Stage 1, was used to study the corrosion fatigue of a carbon steel rebar in a synthetic concrete pore solution. Finally, in the third stage, the constitutive models developed in Stage 2 (for a rebar inside a synthetic pore solution) were used to predict the response of RC beams under corrosion-fatigue.

The present study considered developing models using two well-established frameworks – the stress-life method and the fracture mechanics method – to assess the corrosion-fatigue life of RC structures. This chapter summarizes the most important conclusions of the research carried out in this study, and proposes potential future study in this field of research.

8.2 Conclusions

In accordance with the objectives in this project, the following conclusions can be drawn:

1. A novel Corrosion-Fatigue testing procedure, capable of achieving reliable highly accelerated corrosion rates through a combination of pore solution chemistry and electrochemical corrosion means, was developed. Potentiostatic and Galvanostatic modes of control were investigated and compared. Although both electrochemical approaches can

rapidly accelerate corrosion, the use of the Galvanostatic mode of control was shown to be the preferred method in the laboratory:

- The Potentiostatic method is unable to control the output current and requires an output current recording system to precisely collect the total corrosion current.
- The Galvanostatic method can control the output current and a given accelerated corrosion rate can be easily achieved through this feature.

2. A versatile constitutive model, that can accommodate relatively wide ranges of corrosion fatigue field conditions, was developed in this study based on stress-life approach (S-N curve). The model works equally well in situations where the corrosion rate is low enough that a fatigue limit is observed as well as in situations where the corrosion rate is high enough to cause a significant departure from the pure fatigue case (for a non-corroding rebar). The generated S-N curves are dependent on the corrosion rate and can capture the loss of the fatigue limit under severe corrosion rates or moderate corrosion under extended periods of time. Also, a higher corrosion rate generates a lower fatigue life at the same applied stress amplitude.

3. A Fracture-Mechanics based constitutive model, that can accommodate relatively wide ranges of corrosion fatigue field conditions, was also developed in this study. The key idea behind the development of this second model was mainly related to the inherent inability of all S-N models to give enough insight into the evolution of damage in the reinforcement, as a function of time or number of cycles. This model was able to account for the four main stages of the metal degradation process: pit nucleation and growth, pit-to-crack transition, crack growth state, and ultimate fracture failure. More specifically, this model can capture the effect of corrosion on the shape of the ΔK vs da/dN curves used to represent this type of model. An increase in the corrosion rate promotes a faster increase of the crack length, as a function of time or the equivalent number of cycles, and hence, reduces the fatigue life of a specimen. Corrosion alone could dominate the coupled effect of corrosion-fatigue provided that the service environment is “highly aggressive”. Under such conditions, the crack growth rate, da/dN, becomes independent of the growth of stress intensity factor range ΔK.

4. The service life of RC beams, tested under CF in the laboratory, was successfully estimated by both the S-N approach and the fracture mechanics approach developed in this study.
    - The S-N approach was able to exhibit a higher precision in the prediction of RC beams under CF than the fracture mechanics approach. The error ranges of the S-N curves and the fracture mechanics were from 9.0% to 23.0% and from 26.7% to 54.2%, respectively. However, it is important to keep in mind that those errors are rather reasonable compared to errors typically encountered in CF life estimations.
    - Both approaches predict that the higher the corrosion rate, the lower the service life of an RC structure. Comparing the predicted fatigue lives at different corrosion rates, the results suggest that even a relatively light corrosion could result in a great reduction of the service life of an RC structure under fluctuating loads.
    - The four main stages of damage development in the steel reinforcement (chloride-induced pit nucleation and growth, pit-to-crack transition, crack propagation, and fracture failure) were evaluated using the fracture mechanics model. The fraction of the service life that covers the pit nucleation and growth stage ranges from 79.9% to 89.2%. This result suggests that most of the service life of the rebar is governed by the formation and growth of corrosion-induced pits rather than by the propagation of cracks right from the start.

5. A failure analysis of the specimens used in the corrosion-fatigue tests for the stress-life method, Fracture Mechanics, and reinforced concrete beams was carried out. Scanning Electron Microscope (SEM) and Energy-Dispersive X-ray Spectroscopy (EDS) were used to examine the nature of the fracture surfaces. This analysis was particularly helpful for identifying the origin of pitting-induced fractures. The fracture analysis of the specimens tested in the rotating bending machine and RC beams show that multiple pits initiate a crack, the growth of which results in the fracture failure. Different stages of the fracturing process have been clearly identified. The constitutive equations were constructed based on pit growth, pit-to-crack transition, and crack propagation. Moreover, the fracture toughness of the rebar was also identified.

8.3 Contributions

- S-N relationships for reinforcing steel were used to characterize the CF behavior and to estimate the service life of rebars in RC beams.

- A Fracture Mechanics approach was thoroughly examined and used to predict a carbon steel rebar fatigue life in RC.

- Specialized CF procedures and tools were developed to perform CF testing for both the S-N curves and the Fracture Mechanics approaches.

- An efficient electrochemical approach was developed in this study to accelerate corrosion of rebar in both simulated concrete pore solution and concrete.

8.4 Future work

1. The S-N curves developed in this research for predicting the Corrosion-Fatigue of RC beams accounts for the mean stress effect and the notch effect. However, other important factors, such as temperature, load type, and surface roughness, etc, were not taken into consideration. Hence, future improved models may consider these factors in the stress-life method to improve the domain of applicability.
2. Short cracks are studied by many scientists. With the recommendation, the short crack model could be further studied to predict the service life of a metal structure. Therefore, this model can be combined with the current fracture mechanics models for a more precise prediction.
3. The threshold stress intensity factor range is reported to decrease with an increase of the severity of the corrosive environment. Adding this threshold dependency to the fracture mechanics model developed in this study would further improve its prediction accuracy.

References

AASHTO. Standard specifications for highway bridges (1977).

Acuña-González, N., González-Sánchez, J. A., Dzib-Pérez, L. R., & Rivas-Menchi, A. (2012). Early corrosion fatigue damage on stainless steels exposed to tropical seawater: a contribution from sensitive electrochemical techniques. In *Applied Fracture Mechanics*. InTech.

Aguayo, M., Yang, P., Vance, K., Sant, G., & Neithalath, N. (2014). Electrically driven chloride ion transport in blended binder concretes: Insights from experiments and numerical simulations. *Cement and Concrete Research*, *66*, 1–10. http://doi.org/10.1016/j.cemconres.2014.07.022

Ahmad, S. (2003). Reinforcement corrosion in concrete structures, its monitoring and service life prediction—a review. *Cement and Concrete Composites*, *25*(4), 459–471. http://doi.org/https://doi.org/10.1016/S0958-9465(02)00086-0

Ahmad, Z. (2006). *Principles of Corrosion Engineering and Corrosion Control*. Butterworth-Heinemann.

Al-hammoud, R., Soudki, K., & Topper, T. H. (2011). Fatigue Flexural Behavior of Corroded Reinforced Concrete Beams Repaired with CFRP Sheets. *Journal of Composites for Construction*, *15*, 42–51. http://doi.org/https://doi.org/10.1061/(ASCE)CC.1943-5614.0000144#sthash.wDyyUDxk.dpuf

Al-Hammoud, R., Soudki, K., & Topper, T. H. (2010). Bond analysis of corroded reinforced concrete beams under monotonic and fatigue loads. *Cement and Concrete Composites*, *32*(3), 194–203. http://doi.org/10.1016/j.cemconcomp.2009.12.001

Alden, T. H., & Backofen, W. A. (1961). The formation of fatigue cracks in aluminum single

crystals. *Acta Metallurgica*, *9*(4), 352–366. http://doi.org/https://doi.org/10.1016/0001-6160(61)90229-2

Alonso, C., Castellote, M., & Andrade, C. (2002). Chloride threshold dependence of pitting potential of reinforcements. *Electrochimica Acta*, *47*(21), 3469–3481. http://doi.org/10.1016/S0013-4686(02)00283-9

Amleh, L., Mirza, M. S., & Ahwazi, B. B. N. (2000). *Bond deterioration of reinforcing steel in concrete due to corrosion*.

Apostolopoulos, C. A. (2007). Mechanical behavior of corroded reinforcing steel bars S500s tempcore under low cycle fatigue. *Construction and Building Materials*, *21*(7), 1447–1456. http://doi.org/10.1016/j.conbuildmat.2006.07.008

Apostolopoulos, C. A., & Michalopoulos, D. (2006). Effect of Corrosion on Mass Loss, and High and Low Cycle Fatigue of Reinforcing Steel. *Journal of Materials Engineering and Performance*, *15*(6), 742–749. http://doi.org/10.1361/105994906X150867

Apostolopoulos, C. A., & Pasialis, V. P. (2009). Effects of Corrosion and Ribs on Low Cycle Fatigue Behavior of Reinforcing Steel Bars S400. *Journal of Materials Engineering and Performance*, *19*(3), 385–394. http://doi.org/10.1007/s11665-009-9502-y

ASTM. Standard Practice for Conducting Force Controlled Constant Amplitude Axial Fatigue Tests of Metallic Materials, 3ASTM 4–8 (2002). http://doi.org/10.1520/E0466-07.2

ASTM. Standard Practice for Preparing , Cleaning , and Evaluating Corrosion Test Specimens (2011). http://doi.org/10.1520/G0001-03R11.2

ASTM. Standard Terminology Relating to Fatigue and Fracture Testing (2013). http://doi.org/10.1520/E1823-13.2

ASTM. Standard Test Method for Determining Threshold Stress Intensity Factor for Environment-

Assisted Cracking of Metallic Materials (2013). http://doi.org/10.1520/E1681-03R08E02.Copyright

ASTM. Standard Test Method for Linear-Elastic Plane-Strain Fracture Toughness KIc of (2013). http://doi.org/10.1520/E0399-12E01.2

ASTM. Standard test method for measurement of fatigue crack growth rates (2013). http://doi.org/10.1520/E0647-13.2

Baker, E. A., Money, K. L., & Sanborn, C. B. (1977). Marine Corrosion Behavior of Bare and Metallic-Coated Steel Reinforcing Rods in Concrete. *ASTM Special Technical Publication*, *629*, 30–50.

Bard, A., & Faulkner, L. (2001). *Electrochemical Methods Fundamentals and Applications*. John Wiley & Sons, Inc. http://doi.org/10.1038/nprot.2009.120.Multi-stage

Bastidas-arteaga, E. (2009). *Probabilistic service life modeling of RC structures subjected to the combined effect of chloride-induced corrosion and cyclic loading*. Universidad De Los Andes.

Bastidas-Arteaga, E., Bressolette, P., Chateauneuf, A., & Sánchez-Silva, M. (2009). Probabilistic lifetime assessment of RC structures under coupled corrosion–fatigue deterioration processes. *Structural Safety*, *31*(1), 84–96. http://doi.org/10.1016/j.strusafe.2008.04.001

Bastidas-Arteaga, E., Sánchez-Silva, M., Chateauneuf, A., & Silva, M. R. (2008). Coupled reliability model of biodeterioration, chloride ingress and cracking for reinforced concrete structures. *Structural Safety*, *30*(2), 110–129. http://doi.org/10.1016/j.strusafe.2006.09.001

Bertolini, L. (2008). Steel corrosion and service life of reinforced concrete structures. *Structure and Infrastructure Engineering*, *4*(2), 123–137. http://doi.org/10.1080/15732470601155490

Bertolini, L., & Polder, R. (2013). *Corrosion of Steel in Concrete*. WILEY-VCH.

Bertolini, L., & Redaelli, E. (2009). Depassivation of steel reinforcement in case of pitting corrosion: detection techniques for laboratory studies. *Materials and Corrosion*, *60*(8), 608–616. http://doi.org/10.1002/maco.200905276

Blom, A. F., Hedlund, A., Zhao, W., Fathulla, A., Weiss, B., & Stickler, R. (1986). Short fatigue crack growth behaviour in Al 2024 and Al 7475. In *The behaviour of short fatigue cracks* (pp. 37–66).

Boulfiza, M., Sakai, K., Banthia, N., & Yoshida, H. (2003). Prediction of chloride ions ingress in uncracked and cracked concrete. *ACI Materials Journal*, *100*(1), 38–48.

Broomfield, J. P. (1997). *Corrosion of Steel in Concrete, Understanding, investigation and repair*. Abingdon, UK: Taylor & Francis. http://doi.org/10.4324/9780203414606

Bullen, F. P., Head, A. K., & Wood, W. A. (1953). Structural changes during the fatigue of metals. In *Proceedings of the Royal Society of London A: Mathematical, Physical and Engineering Sciences* (Vol. 216, pp. 332–343).

Burstein, G. T., & Pistorius, P. C. (1995). Surface Roughness and the Metastable Pitting of Stainless Steel in Chloride Solutions. *Corrosion*, *51*, 380–385. http://doi.org/https://doi.org/10.5006/1.3293603#sthash.Xl2turiS.dpuf

Burstein, G. T., & Sasaki, K. (2000). The birth of corrosion pits as stimulated by slurry erosion. *Corrosion Science*, *42*(5), 841–860. http://doi.org/10.1016/S0010-938X(99)00100-6

Chen, G. S., Wan, K.-C., Gao, M., Wei, R. P., & Flournoy, T. H. (1996). Transition from pitting to fatigue crack growth—modeling of corrosion fatigue crack nucleation in a 2024-T3 aluminum alloy. *Materials Science and Engineering: A*, *219*(1–2), 126–132. http://doi.org/10.1016/S0921-5093(96)10414-7

Chen, T. (2014). *Pitting corrosion and corrosion fatigue crack growth behavior of oil-grade alloy 718 in sodium chloride solution*. West Virginia University.

Clark, P. N. (2001). *The Transition of Corrosion Pitting to Surface Fatigue Cracks in 2024-T3 Aluminum Alloy*. The University of Utah.

Coca, F. J. O., Tello, M. U. L., Romero, J. A., & Villafañe, A. M. (2011). Corrosion Fatigue of Road Bridges : a review. *International Journal of Electrochemical Science*, *6*, 3438–3451.

Crooker, T. W. (1971). Effects of tension-compression cycling on fatigue crack growth in high strength alloys. *Journal of Engineering for Industry*, *93*(4), 893–896. http://doi.org/http://doi.org/10.1115/1.3428081

Crooker, T. W., & Krause, D. J. (1972). *Influence of stress ratio and stress level on fatigue crack growth-rates in 140-ksi YS steel*. *National Technical Information Service*. Springfield: NAT Technical Inform Service UP Dept of Commerce.

Das, S., Cheng, J. J. R., & Murray, D. W. (2006). A test method to determine low-cycle-fatigue behavior of wrinkled pipe. *Journal of Testing and Evaluation*, *35*(1), 1–9.

DeJong, S. J., Heffernan, P. J., & MacDougall, C. (2009). Periodic Overload Corrosion Fatigue of MMFX and Stainless Reinforcing Steels. *Journal of Materials in Civil Engineering*, *21*(1), 1–9. http://doi.org/10.1061/(ASCE)0899-1561(2009)21:1(1)

Dolley, E.J.; Lee, B.; Wei, R. P. (2000). The effect of pitting corrosion on fatigue life. *Fatigue & Fracture of Engineering Materials & Structures*, *23*, 555–560. http://doi.org/http://doi.org/10.1046/j.1460-2695.2000.00323.x

El-Zeghayar, M., Topper, T. H., & Soudki, K. a. (2011). A model of crack opening stresses in variable amplitude loading using smooth specimen fatigue test data for three steels. *International Journal of Fatigue*, *33*(10), 1337–1350. http://doi.org/10.1016/j.ijfatigue.2011.04.011

El, M., Palin-luc, T., Saintier, N., & Devos, O. (2013). Effect of corrosion on the high cycle fatigue strength of martensitic stainless. *International Journal of Fatigue*, *47*, 330–339.

http://doi.org/10.1016/j.ijfatigue.2012.09.018

El May, M., Palin-Luc, T., Saintier, N., & Devos, O. (2013). Effect of corrosion on the high cycle fatigue strength of martensitic stainless steel X12CrNiMoV12-3. *International Journal of Fatigue*, *47*, 330–339. http://doi.org/10.1016/j.ijfatigue.2012.09.018

Ettouney, M. M., & Alampalli, S. (2016). *Infrastructure health in civil engineering: Theory and components* (Vol. 1). CRC Press.

Feldman, L., Boulfiza, M., Zacaruk, J., Christensen, P., & Sparks, G. (2008). Life cycle deterioration and cost comparison of bridge deck designs including rehabilitation strategies. In *Life-Cycle Civil Engineering: Proceedings of the International Symposium on Life-Cycle Civil Engineering* (pp. 143–148).

Fernandez, I., Bairan, J. M., & Mari, A. R. (2015). Corrosion effects on the mechanical properties of reinforcing steel bars. Fatigue and stress-strain behavior. *Construction and Building Materials*, *101*, 772–783. http://doi.org/10.1016/j.conbuildmat.2015.10.139

Ferro, G., Carpinteri, A., & Ventura, G. (2007). Minimum reinforcement in concrete structures and material/structural instability. *International Journal of Fracture*, *146*(4), 213–231. http://doi.org/10.1007/s10704-007-9162-6

Fontana, M. G. (1987). *Corrosion Engineering* (III). McGraw Hill Book Company.

Frangini, S., & De Cristofaro, N. (2003). Analysis of the galvanostatic polarization method for determining reliable pitting potentials on stainless steels in crevice-free conditions. *Corrosion Science*, *45*(12), 2769–2786. http://doi.org/10.1016/S0010-938X(03)00102-1

G. E. Coates. (1990). Effect of some surface treatments on corrosion of stainless steel. *Material Performance*, *29*(8), 61–65.

Ghods, P., Isgor, O. B., McRae, G., & Miller, T. (2009). The effect of concrete pore solution

composition on the quality of passive oxide films on black steel reinforcement. *Cement and Concrete Composites*, *31*(1), 2–11. http://doi.org/10.1016/j.cemconcomp.2008.10.003

Gregory, J. K. (1999). Corrosion-fatigue crack growth in titanium alloys. *Materials and Corrosion*, *50*(1), 7–11. http://doi.org/10.1002/(SICI)1521-4176(199901)50:1<7::AID-MACO7>3.0.CO;2-3

Harlow, D. G., & Wei, R. P. (1993). A mechanistically based approach to probability modeling for corrosion fatigue crack growth. *Engineering Fracture Mechanics*. http://doi.org/10.1016/0013-7944(93)90009-H

Harlow, D. G., & Wei, R. P. (1998). A probability model for the growth of corrosion pits in aluminum alloys induced by constituent particles. *Engineering Fracture Mechanics*, *59*(3), 305–325. http://doi.org/10.1016/S0013-7944(97)00127-6

Hartt, W. H. (2012). Service Life Projection for Chloride-Exposed Concrete Reinforced with Black and Corrosion- Resistant Bars, *9312*, 754–761. http://doi.org/https://doi.org/10.5006/0489#sthash.7acI0nDM.dpuf

Hausmann, D. A. (1967). Steel corrosion in concrete--How does it occur? *Materials Protection*, *6*(11), 19–23.

Hertzberg, R. W. (2012). *Deformation and fracture mechanics of engineering materials.pdf* (Fifth). Wiley.

Hoeppner, D. W. (1979). Model for Prediction of Fatigue Lives Based Upon a Pitting Corrosion Fatigue Process. In *Fatigue Mechanisms of ASTM- NSF symposium* (pp. 841–870).

Hoeppner, D. W. (2011). Modelling pitting corrosion fatigue: pit growth and pit/crack transition issues. In *Corrosion Fatigue and Environmentally Assisted Cracking in Aging Military Vehicles* (pp. 1–20). The Research and Technology Organisation (RTO) of NATO.

Hu, D., Meng, F., Liu, H., Song, J., & Wang, R. (2015). Experimental investigation of fatigue crack growth behavior of GH2036 under combined high and low cycle fatigue. *International Journal of Fatigue*, *85*, 1–10. http://doi.org/10.1016/j.ijfatigue.2015.10.027

Huang, X., & Xu, J. (2013). 3D analysis for pit evolution and pit-to-crack transition during corrosion fatigue. *Journal of Zhejiang University SCIENCE A*, *14*(4), 292–299. http://doi.org/10.1631/jzus.A1200273

Ishida, T. (2009). Life-Span Simulation of Reinforced Concrete Structures: Toward Rational Stock Management. In *Stock Management for Sustainable Urban Regeneration* (pp. 81–100). Springer.

Islam, G. M. S., & Sugiyama, T. (2010). Determination of corrosion initiation of rebar in cocnrete by monitoring half-cell potential, *22*(2), 186–201.

Janik-Czachor, M., Szummer, A., & Szklarska-Smialowska, Z. (1975). Electron microprobe investigation of processes leading to the nucleation of pits on iron. *Corrosion Science*, *15*(6–12), 775–778. http://doi.org/https://doi.org/10.1016/0010-938X(75)90041-4

Jarrah, A., Bigerelle, M., Guillemot, G., Najjar, D., Iost, A., & Nianga, J. M. (2011). A generic statistical methodology to predict the maximum pit depth of a localized corrosion process. *Corrosion Science*, *53*(8), 2453–2467. http://doi.org/10.1016/j.corsci.2011.03.026

Jaske, C. E., Payer, J. H., & Balint, V. S. (1981). *Corrosion fatigue of metals in marine environments*. Metals and Ceramics Information Center.

Jiang, L., Huang, G., Xu, J., Zhu, Y., & Mo, L. (2012). Influence of chloride salt type on threshold level of reinforcement corrosion in simulated concrete pore solutions. *Construction and Building Materials*, *30*, 516–521. http://doi.org/10.1016/j.conbuildmat.2011.12.044

Kalnaus, S., Zhang, J., & Jiang, Y. (2010). Stress-Corrosion Cracking of AISI 4340 Steel in Aqueous Environments. *Metallurgical and Materials Transactions A*, *42*(2), 434–447.

http://doi.org/10.1007/s11661-010-0335-y

Katwan, M. J. (1988). *Corrosion fatigue of reinforced concrete*. University of Glasgow.

Kawai, S., & Kasai, K. (1985). Considerations of allowable stress of corrosion fatigue (focused on the influence of pitting). *Fatigue & Fracture of Engineering Materials & Structures, 8*(2), 115–127. http://doi.org/http://doi.org/10.1111/j.1460-2695.1985.tb01198.x

Khan, Z., & Younas, M. (1996). Corrosion-fatigue life prediction for notched components based on the local strain and linear elastic fracture mechanics concepts. *International Journal of Fatigue, 18*(7), 491–498. http://doi.org/https://doi.org/10.1016/0142-1123(95)00054-2

Kim, B., Boyd, A. J., Kim, H.-S., & Lee, S.-H. (2015). Steel and synthetic types of fibre reinforced concrete exposed to chemical erosion. *Construction and Building Materials, 93*, 720–728. http://doi.org/https://doi.org/10.1016/j.conbuildmat.2015.06.023

Kondo, Y. (1989). Prediction of Fatigue Crack Initiation Life Based on Pit Growth. *Corrosion, 45*(1), 7–11. http://doi.org/10.5006/1.3577891

Landolt, D. (2007). *Corrosion and surface chemistry of metals*. *EPFL Press*. http://doi.org/10.1016/S1369-7021(07)70081-0

Lankford, J. (1982). The growth of small fatigue cracks in 7075--T6 aluminum. *Fatigue & Fracture of Engineering Materials & Structures*, *5*(3), 233–248. http://doi.org/http://doi.org/10.1111/j.1460-2695.1982.tb01251.x

Larsen, J. M., & Allison, J. E. (1992). *Small-Crack Test Methods*. ASTM International. http://doi.org/http://doi.org/10.1520/STP1149-EB

Lee, D., Nishikawa, H., Oda, Y., & Noguchi, H. (2012). Small fatigue crack growth characteristics and fracture surface morphology of low carbon steel in hydrogen gas. *International Journal of Fracture*, *179*(1–2), 147–156. http://doi.org/10.1007/s10704-012-9783-2

Li, C. Q., Yang, Y., & Melchers, R. E. (2008). Prediction of reinforcement corrosion in concrete and its effects on concrete cracking and strength reduction. *ACI Materials Journal*, *105*(1), 3–10.

Li, S., Zhang, W., Gu, X., & Zhu, C. (1998). Analysis on Fatigue of Natural Corrosion Steel Bars. In *Advanced Materials Research* (pp. 163–167). http://doi.org/http://doi.org/10.4028/www.scientific.net/AMR.163-167.3237

Liu, Y., & Weyers, R. E. (1998). Modeling the Time-to-Corrosion Cracking in Chloride Contaminated Reinforced Concrete Structures. *ACI Materials Journal*, *95*(6), 675–681.

Liu, Z., Diao, B., & Zheng, X. (2015). Effects of Seawater Corrosion and Freeze-Thaw Cycles on Mechanical Properties of Fatigue Damaged Reinforced Concrete Beams. *Advances in Materials Science and Engineering*, *2015*, 1–16. http://doi.org/http://dx.doi.org/10.1155/2015/536487

Loo, Y. M., Foster, S. J., & Smith, S. T. (2013). Fatigue Behavior of Carbon Fiber-Reinforced Polymer- Repaired Corroded Reinforced Concrete Beams. *ACI Structural Journal*, (109), 795–804.

Maaddawy, E., Soudki, K., & Topper, T. (2006). Long-Term Performance of Corrosion-Damaged Reinforced Concrete Beams. *ACI Structural Journal*, (102), 649–656.

Maaddawy, T. A. El, & Soudki, K. A. (2003). Effectiveness of Impressed Current Technique to Simulate Corrosion of Steel Reinforcement in Concrete. *Journal of Materials in Civil Engineering*, *15*, 41–47. http://doi.org/https://doi.org/10.1061/(ASCE)0899-1561(2003)15:1(41)#sthash.62g9YYvi.dpuf

Marcus, P. (2002). *Corrosion Mechanisms in Theory and Practice*. CRC Press.

Martın-Pérez, B., Pantazopoulou, S. J., & Thomas, M. D. A. (2001). Numerical solution of mass transport equations in concrete structures. *Computers & Structures*, *79*(13), 1251–1264.

Maslehuddin, M., Al-Zahrani, M. M., Ibrahim, M., Al-Mehthel, M. H., & Al-Idi, S. H. (2007). Effect of chloride concentration in soil on reinforcement corrosion. *Construction and Building Materials*, *21*(8), 1825–1832. http://doi.org/10.1016/j.conbuildmat.2006.05.019

Masoud, S., & Soudki, K. (2006). Evaluation of corrosion activity in FRP repaired RC beams. *Cement and Concrete Composites*, *28*(10), 969–977. http://doi.org/10.1016/j.cemconcomp.2006.07.013

Medved, J. J., Breton, M., & Irving, P. E. (2004). Corrosion pit size distributions and fatigue lives - A study of the EIFS technique for fatigue design in the presence of corrosion. *International Journal of Fatigue*, *26*(1), 71–80. http://doi.org/10.1016/S0142-1123(03)00069-0

Melchers, R. E. (2004). Pitting Corrosion of Mild Steel in Marine Immersion Environment—Part 2: Variability of Maximum Pit Depth. *Corrosion*, *60*(10), 937–944. http://doi.org/10.5006/1.3287827

Melchers, R. E. (2005). Representation of uncertainty in maximum depth of marine corrosion pits. *Structural Safety*, *27*(4), 322–334. http://doi.org/10.1016/j.strusafe.2005.02.002

Melchers, R. E. (2005). Statistical characterization of pitting corrosion - Part 1: Data analysis. *Corrosion*, *61*(7), 655–664. http://doi.org/10.5006/1.3278211

Melchers, R. E. (2006). Pitting Corrosion of Mild Steel under Marine Anaerobic Conditions—Part 1: Experimental Observations. *Corrosion*, *62*(11), 981. http://doi.org/10.5006/1.3278236

Melchers, R. E. (2012). Modeling and prediction of long-term corrosion of steel in marine environments. *International Journal of Offshore and Polar Engineering*, *22*(4), 257–263.

Melchers, R. E., & Jeffrey, R. J. (2008). Probabilistic models for steel corrosion loss and pitting of marine infrastructure. *Reliability Engineering and System Safety*, *93*(3), 423–432. http://doi.org/10.1016/j.ress.2006.12.006

Menan, F., & Hénaff, G. (2010). Synergistic action of fatigue and corrosion during crack growth in the 2024 aluminium alloy. *Procedia Engineering*, *2*(1), 1441–1450. http://doi.org/10.1016/j.proeng.2010.03.156

Milella, P. P. (2013). *Fatigue and Corrosion in Metals*. Springer Milan.

Miller, M. S., & Gallagher, J. P. (1981). An analysis of several fatigue crack growth rate (FCGR) descriptions. In *Fatigue Crack Growth Measurement and Data Analysis*. ASTM International. http://doi.org/http://doi.org/10.1520/STP33462S

Missert, N., Virtanen, S., Davenport, A. J., & Ryan, M. P. (2007). Critical Factors in Localized Corrosion 5: A Symposium in Honor of Hugh Isaacs. *ECS Transactions*, *3*(31), 81.

Moayed, M. H., Laycock, N. J., & Newman, R. C. (2003). Dependence of the Critical Pitting Temperature on surface roughness. *Corrosion Science*, *45*, 1203–1216. http://doi.org/10.1016/S0010-938X(02)00215-9

Mohamed, N. (2009). *Comparative Study of the Corrosion Behaviour of Conventional Carbon Steel and Corrosion Resistant Reinforcing Bars*. University of Saskatchewan.

Moreno, M., Morris, W., Alvarez, M. G., & Duffó, G. S. (2004). Corrosion of reinforcing steel in simulated concrete pore solutions - Effect of carbonation and chloride content. *Corrosion Science*, *46*(11), 2681–2699. http://doi.org/10.1016/j.corsci.2004.03.013

Mori, Y., & Ellingwood, B. R. (1993). Reliability-based service-life assessment of aging concrete structures. *Journal of Structural Engineering*, *119*(5), 1600–1621. http://doi.org/https://doi.org/10.1061/(ASCE)0733-9445(1993)119:5(1600)#sthash.HipnJ3MQ.dpuf

Murtaza, G., & Akid, R. (2000). Empirical corrosion fatigue life prediction models of a high strength steel, *67*(263). http://doi.org/https://doi.org/10.1016/S0013-7944(00)00057-6

Narasaiah, N., & Ray, K. K. (2005). Small crack formation in a low carbon steel with banded ferrite–pearlite structure. *Materials Science and Engineering: A*, *392*(1–2), 269–277. http://doi.org/10.1016/j.msea.2004.09.058

Newman, J. (1999). Fatigue-life prediction methodology using small-crack theory. *International Journal of Fatigue*, *21*(2), 109–119. http://doi.org/10.1016/S0142-1123(98)00058-9

Newman, J. C., & Annigeri, B. S. (2012). Fatigue-Life Prediction Method Based on Small-Crack Theory in an Engine Material. *Journal of Engineering for Gas Turbines and Power*, *134*(3), 32501. http://doi.org/10.1115/1.4004261

Newman Jr, J. C. (1983). A nonlinear fracture mechanics approach to the growth of small cracks. In *AGARD Behaviour of Short Cracks in Airframe Components* (pp. 22–31).

Oh, B. H., Asce, M., Lew, Y., & Choi, Y. C. (2007). Realistic Assessment for Safety and Service Life of Reinforced Concrete Decks in Girder Bridges. *Journal of Bridge Engineering*, *12*(4), 410–418. http://doi.org/https://doi.org/10.1061/(ASCE)1084-0702(2007)12:4(410)#sthash.So6CekoG.dpuf

Okada, T. (1984). Halide nuclei theory of pit initiation in passive metals. *Journal of the Electrochemical Society*, *131*(2), 241–247. http://doi.org/http://doi.org/10.1149/1.2115556

Organization, R. and T. (2011). *Corrosion Fatigue and Environmentally Assisted Cracking in Aging Military Vehicles*. North Atlantic Treaty Organization.

Ostash, O., Kostyk, E., & Makoviichuk, I. (1999). Initiation and growth of corrosion-fatigue cracks near stress concentrators in V95pchT2 aluminum alloy. *Materials Science*, *35*(1), 7–15. http://doi.org/http://doi.org/10.1007/BF02355595

Oyado, M., Kanakubo, T., Sato, T., & Yamamoto, Y. (2011). Bending performance of reinforced concrete member deteriorated by corrosion. *Structure and Infrastructure Engineering*, *7*(1–2), 121–130. http://doi.org/10.1080/15732471003588510

Pacheco, J., Polder, R. B., Fraaij, A. L. A., & Mol, J. M. C. (2011). Short-term benefits of cathodic protection of steel in concrete. *Proceedings of Concrete Solutions. Taylor and Francis, Dresden*, 147–156.

Palin-luc, T., Pérez-mora, R., Bathias, C., Domínguez, G., Paris, P. C., & Luis, J. (2010). Fatigue crack initiation and growth on a steel in the very high cycle regime with sea water corrosion. *Engineering Fracture Mechanics*, *77*(11), 1953–1962. http://doi.org/10.1016/j.engfracmech.2010.02.015

Pao, P. ., Gill, S. ., & Feng, C. . (2000). On fatigue crack initiation from corrosion pits in 7075-T7351 aluminum alloy. *Scripta Materialia*, *43*(5), 391–396. http://doi.org/10.1016/S1359-6462(00)00434-6

Poursaee, A. (2010). Corrosion of steel bars in saturated Ca(OH)2 and concrete pore solution. *Concrete Research Letters*, *1*(September), 90–97.

Radian, T. A. (1989). *Effect of corrosion , freeze-thaw cycles , and their combined effects on the fatigue behavior of reinforced concrete*. University of Rhode Island.

Rahman, M. K., Al-Kutti, W. a., Shazali, M. a., & Baluch, M. H. (2012). Simulation of Chloride Migration in Compression-Induced Damage in Concrete. *Journal of Materials in Civil Engineering*, *24*(7), 789–796. http://doi.org/10.1061/(ASCE)MT.1943-5533.0000458

Ravikumar, D., & Neithalath, N. (2013). Electrically induced chloride ion transport in alkali activated slag concretes and the influence of microstructure. *Cement and Concrete Research*, *47*, 31–42. http://doi.org/10.1016/j.cemconres.2013.01.007

Rodriguez, J., Ortega, L. M., & Casal, J. (1997). Load carrying capacity of concrete structures with corroded reinforcement. *Construction and Building Materials*, *11*(4), 239–248. http://doi.org/https://doi.org/10.1016/S0950-0618(97)00043-3

Rokhlin, S. I., Kim, J., Nagy, H., & Zoofan, B. (1999). Effect of pitting corrosion on fatigue crack

initiation and fatigue life. *Engineering Fracture Mechanics*, *62*, 425–444. http://doi.org/https://doi.org/10.1016/S0013-7944(98)00101-5

Rteil, A. (2007). *Fatigue bond behaviour of corroded reinforcement and CFRP confined concrete*. University of Waterloo.

Sankaran, K. K., Perez, R., & Jata, K. V. (2001). Effects of pitting corrosion on the fatigue behavior of aluminum alloy 7075-T6: modeling and experimental studies. *Materials Science and Engineering: A*, *297*(1–2), 223–229. http://doi.org/10.1016/S0921-5093(00)01216-8

Sasaki, K., & Burstein, G. T. (1996). The generation of surface roughness during slurry erosion-corrosion and its effect on the pitting potential. *Corrosion Science*, *38*(12), 2111–2120. http://doi.org/10.1016/S0010-938X(96)00066-2

Sastri, V. S. (2012). *Green corrosion inhibitors: theory and practice*. John Wiley & Sons.

Schijve, J. (2009). *Fatigue of Structures and Materials*. Springer Milan.

Schmidt, F., & Rostasy, F. S. (1993). A method for the calculation of the chemical composition of the concrete pore solution. *Cement and Concrete Research*, *23*(5), 1159–1168. http://doi.org/https://doi.org/10.1016/0008-8846(93)90176-A

Scott, P. M. (1983). The effects of seawater on corrosion fatigue in structural steels. *The Metals Society*, *8*(6), 89–100.

Seifert, H. P., Ritter, S., & Leber, H. J. (2012a). Corrosion fatigue crack growth behaviour of austenitic stainless steels under light water reactor conditions. *Corrosion Science*, *55*, 61–75. http://doi.org/10.1016/j.corsci.2011.10.005

Seifert, H. P., Ritter, S., & Leber, H. J. (2012b). Corrosion fatigue initiation and short crack growth behaviour of austenitic stainless steels under light water reactor conditions. *Corrosion Science*, *59*, 20–34. http://doi.org/10.1016/j.corsci.2012.02.008

Sivaprasad, S., Tarafder, S., Ranganath, V. R., Tarafder, M., & Ray, K. K. (2006). Corrosion fatigue crack growth behaviour of naval steels. *Corrosion Science*, *48*(8), 1996–2013. http://doi.org/10.1016/j.corsci.2005.08.005

Slater, J. (1983). *Corrosion of metals in association with concrete*. ASTM International.

Sohail, M. G. (2013). Corrosion of Steel in Concrete: Development of an Accelerated Test by Carbonation and Galvanic Coupling, (Lmdc), 1–143.

Sonali, S. (1993). *Computer simulation of corrosion fatigue of reinforced concrete beams in marine environment*. Florida Atlantic University.

Song, L., & Yu, Z. (2015). Fatigue performance of corroded reinforced concrete beams strengthened with CFRP sheets. *Construction and Building Materials*, *90*, 99–109. http://doi.org/10.1016/j.conbuildmat.2015.05.024

Soudki, K. A., Rteil, A. A., Al-hammoud, R., & Topper, T. H. (2007). Fatigue strength of fibre-reinforced-polymer- repaired beams subjected to mild corrosion 1. *Canadian*, *421*, 414–421. http://doi.org/10.1139/L06-153

Starke, E. A. (1996). *Accelerated aging of materials and structures, the effects of long-term elevated-temperature exposure*. *National Materials Advisory Board, National Research Council, Washington, DC NMAB-479*.

Stephens, R. I., Fatemi, A., Stephens, R. R., & Fuchs, H. O. (2000). *Metal fatigue in engineering*. John Wiley & Sons.

Strength, R. B., Concrete, O. F., & Fly, C. (2010). Effects of Rebar Temperature and Water to Cement Ratio on Rebar Concrete-Bond Strength of Concrete Containing Fly Ash.

Sundaresan, R. (1989). *Influences of chlorides, pH and surface films on the corrosion of reinforcing steel in alkaline solutions*. Florida Atlantic University.

Suresh, S. (1998). *Fatigue of Materials* (Second). Cambridge University Press.

Suwito, C., & Xi, Y. (2008). The effect of chloride-induced steel corrosion on service life of reinforced concrete structures. *Structure and Infrastructure Engineering*, *4*(3), 177–192. http://doi.org/10.1080/15732470600688699

Szklarska-Smialowska, Z. (2005). *Pitting and Crevice Corrosion*. NACE Press.

Szklarska-Smialowska, Z., & Janik-Czachor, M. (1971). The analysis of electrochemical methods for the determination of characteristic potentials of pitting corrosion. *Corrosion Science*, *11*(12), 901–914. http://doi.org/10.1016/S0010-938X(71)80035-5

Thomas, C. J., Edyvean, R. G. J., & Brook, R. (1988). Biologically enhanced corrosion fatigue. *Biofouling*, *1*(1), 65–77. http://doi.org/http://dx.doi.org/10.1080/08927018809378096

Tilly, G. P. (1979). Fatigue of Steel Reinforcement Bars in Concrete: a Review. *Fatigue & Fracture of Engineering Materials and Structures*, *2*(3), 251–268. http://doi.org/10.1111/j.1460-2695.1979.tb01084.x

Tokaji, K., Ogawa, T., & Aoki, T. (1990). Small Fatigue Crack Growth in a Low Carbon Steel Under Tension?Compression and Pulsating-Tension Loading. *Fatigue & Fracture of Engineering Materials and Structures*, *13*(1), 31–39. http://doi.org/10.1111/j.1460-2695.1990.tb00574.x

Vonezawa, T., Ashworth, V., & Procter, R. P. M. (1988). Pore Solution Composition and Chloride Effects on the Corrosion of Steel in Concrete. *Corrosion Engineering*, *44*(7), 489–499. http://doi.org/https://doi.org/10.5006/1.3583967#sthash.zHswASYH.dpuf

Wahab, M. A., & Sakano, M. (2001). Experimental study of corrosion fatigue behaviour of welded steel structures. *Journal of Materials Processing Technology*, *118*(1), 116–121. http://doi.org/https://doi.org/10.1016/S0924-0136(01)00902-5

Wang, Q. (2003). Effect of pitting corrosion on very high cycle fatigue behavior. *Scripta Materialia*, *49*(7), 711–716. http://doi.org/10.1016/S1359-6462(03)00365-8

Wei, R. P., & Gangloff, R. P. (1989). Environmentally assisted crack growth in structural alloys: Perspectives and new directions. *Fracture Mechanics: Perspectievs and Directions, ASTM STP 1020*, 233–264. http://doi.org/http://doi.org/10.1520/STP18827S

Weng, L., Zhang, J., Kalnaus, S., Feng, M., & Jiang, Y. (2013). Corrosion fatigue crack growth of AISI 4340 steel. *International Journal of Fatigue*, *48*, 156–164. http://doi.org/10.1016/j.ijfatigue.2012.10.015

Werner, K., & Koliasinsky, Z. (2003). Effect of the strength and structure of low-alloy steel on the near-threshold growth of corrosion-fatigue cracks. *Materials Science*, *39*(2), 282–284. http://doi.org/10.1023/B:MASC.0000010281.86414.c4

Yi, W., Kunnath, S. K., Sun, X., Shi, C., & Tang, F. (2011). Fatigue Behavior of Reinforced Concrete Beams with Corroded Steel Reinforcement. *ACI Structural Journal*, (107), 526–533.

Yu, L., Francois, R., Dang, V. H., L'Hostis, V., & Gagne, R. (2015). Structural performance of RC beams damaged by natural corrosion under sustained loading in a chloride environment. *Engineering Structures*, *96*, 30–40. http://doi.org/10.1016/j.engstruct.2015.04.001

Zhang, R., & Mahadevan, S. (2001). Reliability-based reassessment of corrosion fatigue life. *Structural Safety*, *23*(1), 77–91. http://doi.org/10.1016/S0167-4730(01)00002-9

Zhao, W., Wang, Y., Zhang, T., & Wang, Y. (2012). Study on the mechanism of high-cycle corrosion fatigue crack initiation in X80 steel. *Corrosion Science*, *57*, 99–103. http://doi.org/10.1016/j.corsci.2011.12.029